

**Hot corrosion behavior of Pt-modified Ni- and Co-based alloys and coatings**

by

**Vinay Prakash Deodeshmukh**

A dissertation submitted to the graduate faculty  
in partial fulfillment of the requirements for the degree of

DOCTOR OF PHILOSOPHY

Major: Materials Science and Engineering

Program of Study Committee:  
Brian Gleeson, Major Professor  
Daniel Sordelet  
Matthew Kramer  
Scott Chumbley  
Palaniappa A. Molian

Iowa State University

Ames, Iowa

2007

Copyright © Vinay Prakash Deodeshmukh, 2007. All rights reserved.

UMI Number: 3287421

Copyright 2008 by  
Deodeshmukh, Vinay Prakash

All rights reserved.

UMI<sup>®</sup>

---

UMI Microform 3287421

Copyright 2008 by ProQuest Information and Learning Company.  
All rights reserved. This microform edition is protected against  
unauthorized copying under Title 17, United States Code.

---

ProQuest Information and Learning Company  
300 North Zeeb Road  
P.O. Box 1346  
Ann Arbor, MI 48106-1346

## TABLE OF CONTENTS

<b>ACKNOWLEDGEMENTS</b> .....	vi
<b>ABSTRACT</b> .....	vii
<b>1. INTRODUCTION</b> .....	9
<b>2. TECHNICAL BACKGROUND</b> .....	12
2.1 Superalloys in Gas-Turbine Engine .....	12
2.2 High-Temperature Protective Coating Systems .....	12
2.2.1 High-Temperature Surface Protection .....	12
2.2.2 Coating Processes .....	14
2.2.2.1 Diffusion Coatings .....	15
2.2.2.2 Overlay Coatings .....	17
2.2.2.3 Miscellaneous Coatings .....	20
2.3 Background on Hot Corrosion .....	20
2.3.1 Mixed Oxidant Corrosion .....	20
2.3.2 Formation of Na <sub>2</sub> SO <sub>4</sub> in a Gas Turbine Engine Environment .....	21
2.3.3 Hot Corrosion Characteristics: Temperature Dependence and Microstructural Appearance .....	22
2.3.3.1 High Temperature Hot Corrosion (HTHC-Type I HC) .....	23
2.3.3.2 Low Temperature Hot Corrosion (LTHC-Type II HC) .....	24
2.3.4 Deposit Induced Degradation-Salt Fluxing Reactions .....	26
2.3.5 Basic and Acidic Fluxing Model .....	28
2.3.5.1 Goebel-Pettit Model for Basic Fluxing .....	28
2.3.5.2 Rapp-Goto Criterion of Oxide Fluxing .....	30
2.3.5.3 Gas Phase Induced Acidic Fluxing .....	33
2.3.5.4 Alloy Phase Induced Acidic Fluxing .....	36
2.3.6 Fluxing of NiO and Protective Nature of Cr <sub>2</sub> O <sub>3</sub> and Al <sub>2</sub> O <sub>3</sub> .....	37
2.3.7 Hot Corrosion Degradation Sequence .....	42
2.3.7.1 Initiation Stage of Hot Corrosion .....	42
2.3.7.2 Propagation Stage of Hot Corrosion .....	44
2.3.8 Hot Corrosion of Pt-modified Alloys/Coatings and MCrAlY-Based Coatings .....	45

2.4 Oxidation Behavior of Pt-Modified Ni-Based Alloys and Coatings: An Overview .....	46
2.5 Aims of Research.....	51
<b>3. EXPERIMENTAL APPROACH .....</b>	<b>52</b>
3.1 Materials: Alloys and Coatings.....	52
3.2 High Temperature (Type I) Hot Corrosion Dean-rig Testing.....	52
3.3 Low Temperature (Type II) Hot Corrosion Dean-rig Testing.....	54
3.4 Isothermal and Cyclic Oxidation Testing .....	55
3.5 Characterization and Analysis .....	56
<b>4. HOT CORROSION BEHAVIOR OF COMMERCIAL METALLIC COATINGS .</b>	<b>58</b>
4.1 Comparative Study of Low- and High-Temperature Hot Corrosion Resistance of Various Aluminide Coatings.....	58
4.1.1 High Temperature Hot Corrosion Results (900 °C).....	59
4.1.2 Comparison Between Dean Rig and Burner Rig Testing .....	65
4.1.3 Low Temperature Hot Corrosion Results (705 °C and 750 °C).....	68
4.1.4 Summary of Hot Corrosion Results.....	79
4.2 Structural and Compositional Effects on the Hot Corrosion Resistance of Al- Pt- rich $\beta$ Aluminides and their Performance Compared with a Standard CoCrAlY Coating ..	80
4.2.1 Low Temperature Hot Corrosion (705 °C) Results .....	83
4.2.2 High Temperature Hot Corrosion (900 °C) Results.....	90
4.2.3 Summary and Conclusions .....	91
4.3 Effects of Pt on the LTHC Behavior of Co-and Ni-Based Coatings .....	92
<b>5. HOT CORROSION AND OXIDATION BEHAVIOR OF NOVEL <math>\gamma'</math>-Ni<sub>3</sub>Al + <math>\gamma</math>-Ni ALLOYS .....</b>	<b>97</b>
5.1 Optimization of the High Temperature Hot Corrosion and Oxidation Resistance of Pt+(Cr+Si)+Hf-modified $\gamma'$ -Ni <sub>3</sub> Al + $\gamma$ -Ni Alloys Containing 22 at.% Al .....	97
5.1.1 Introduction.....	97
5.1.2 Experimental .....	97
5.1.3 Results and Discussion .....	100
5.1.3.1 Improving the HTHC Resistance of $\gamma'$ + $\gamma$ Alloys by Alloying Additions and with a Pre-oxidation Treatment .....	100

5.1.3.2 Effects of Alloying Additions on the Oxidation Behavior of Modified $\gamma' + \gamma$ Alloys.....	111
5.1.3.2A Isothermal Oxidation (1150°C).....	111
5.1.3.2B Cyclic Oxidation (1150°C).....	117
5.1.3.3 Optimizing the HTHC and Oxidation Resistance of $\gamma' + \gamma$ Alloys.....	130
5.1.4 Summary and Conclusions .....	134
5.2 Effects of Alloying Additions on the LTHC Resistance of $\gamma' + \gamma$ and $\beta$ -Based Alloys	135
5.2.1 Introduction.....	135
5.2.2 Experimental.....	135
5.2.3 Results and Discussion .....	137
5.2.3.1 Effect of Pt on the LTHC Resistance of Hf-Modified $\gamma' + \gamma$ Alloys.....	137
5.2.3.2 Effect of Cr on the LTHC Resistance of Pt+Hf-Modified $\gamma' + \gamma$ Alloys .....	139
5.2.3.3 Effect of Si on the LTHC Resistance of Pt+Hf-Modified $\gamma' + \gamma$ Alloys.....	143
5.2.3.4 Effect of Al and Pt Content in $\beta$ -NiAl Alloys and their LTHC Resistance Compared with $\gamma' + \gamma$ Alloys.....	145
5.2.3.5 Effects of Co and Refractory Elements on the LTHC Resistance of $\beta$ Alloys	147
5.2.3.6 Summary and Conclusions .....	150
5.3 Effects of Pre-oxidation on the Hot Corrosion Resistance of Pt+Cr+Hf-Modified $\gamma' + \gamma$ Alloys.....	151
5.3.1 Introduction.....	151
5.3.2 Experimental.....	151
5.3.3 Results and Discussion .....	152
5.3.3.1 Effects of Pre-oxidation on the Ni-22Al-20Pt-5Cr-0.4Hf Alloy .....	152
5.3.3.2 Effect of Pre-oxidation on the Ni-22Al-5Pt-5Cr-0.4Hf $\gamma' + \gamma$ Alloy .....	159
5.3.4 Summary and Conclusions .....	161
<b>6. HOT CORROSION EVALUATION OF DEVELOPMENTAL <math>\gamma' + \gamma</math> COATING AND COMMERCIALY AVAILABLE METALLIC COATINGS .....</b>	<b>162</b>
6.1 Introduction.....	162
6.2 Experimental.....	162

6.3 Results and Discussion .....	165
6.3.1 LTHC (700 °C) Testing with Pre-oxidation Treatment (Air-1080°C-6h).....	165
6.3.2 LTHC (705 °C) with No Pre-oxidation Treatment .....	174
6.3.3 HTHC (900 °C) with Pre-oxidation Treatment (Air-1080°C-6h) .....	178
6.3.4 HTHC (900 °C) with No Pre-oxidation Treatment.....	185
6.3.5 Hot Corrosion Resistance: Pt+Hf-Modified $\gamma'+\gamma$ vs. $\gamma+\beta$ -CoCrAlY .....	189
6.4 Summary and Conclusions .....	191
<b>7. SUMMARY AND OUTCOMES .....</b>	<b>193</b>
7.1 Hot Corrosion Behavior of Commercial Ni- and Co-Based Metallic Coatings .....	193
7.2 Hot Corrosion and Oxidation Behavior of Novel $\gamma'+\gamma$ Alloys.....	193
7.3 Hot Corrosion Evaluation of Developmental $\gamma'+\gamma$ Coating and Commercially Available Coatings.....	195
<b>References.....</b>	<b>197</b>

## ACKNOWLEDGEMENTS

I would like to dedicate this dissertation to my brother Vikas Deodeshmukh who is a source of continuous inspiration to me. I would like to thank my major professor, Brian Gleeson for his continued support, guidance, and encouragement throughout my studies. I also appreciate his patience and understanding during my difficult times. I consider myself very lucky to have worked with him for my PhD work. I express my thanks to Dan Sordelet for his help and support during this study. I would also like to thank my officemates: Joe Schramm, Bingtao Li, Shigenari Hayashi, Wen Wang, Nan Mu, Benjamin Zimmerman, Takeshi Izumi, Joe Henderkott, Andy Heidloff, and Liming Zhang, for their assistance and general discussions throughout this work. I also thank Matt Besser for the technical assistance. I am grateful to Dr. David Shifler at Office of Naval Research (ONR) for providing the burner rig hot corrosion test samples and Dr. Evan Copland at NASA Glenn Research Center for performing the activity measurements. The financial support for this work by ONR, with Dr. Airan Perez being the program manager, and Rolls Royce Corporation USA, is gratefully acknowledged. The close collaboration, which includes providing samples and technical information, with George Creech, Dr. Kang Lee, and Dr. Mike Cybulsky at Rolls Royce Corporation and Dr. Ram Darolia at General Electric Aircraft Engines, is also gratefully acknowledged. Finally, I wish to thank my parents Prakash and Sudha Deodeshmukh, and my wife Rashmi, and my family for their continued encouragement and endless support.

**ABSTRACT**

High temperature degradation by hot corrosion (650-1000°C) and/or oxidation (>1000°C) can severely reduce the longevity of advanced gas turbine engine components. The protection of high-temperature components against hot corrosion or oxidation is typically conferred by the application of either a diffusion or overlay metallic coating that is able to form a continuous, adherent, and slow-growing oxide scale. There are currently no coatings that provide adequate protection to *both* hot corrosion and oxidation. Indeed, there is a particular need for such protective coatings because many advanced aero, marine, and industrial gas-turbines operate in both hot corrosion and oxidation regimes in their duty cycle. Recent work at Iowa State University (ISU) has showed that a wide range Pt+Hf-modified  $\gamma'$ -Ni<sub>3</sub>Al +  $\gamma$ -Ni alloy compositions form a very adherent and slow-growing Al<sub>2</sub>O<sub>3</sub> scale. In fact, the results reported suggest that Pt+Hf-modified  $\gamma' + \gamma$  coatings offer a viable superior alternative to  $\beta$ -NiAl(Pt)-based coatings. The main thrust of this study was to assess and establish optimum target  $\gamma' + \gamma$  coating compositions for extending the service life of high-temperature gas turbine components exposed to hot corrosion and oxidation conditions. Both high temperature hot-corrosion (HTHC-900°C) and low temperature hot-corrosion (LTHC-705°C) behaviors of the Pt+Hf-modified  $\gamma' + \gamma$  alloys were assessed. The salt used to bring about hot corrosion was Na<sub>2</sub>SO<sub>4</sub>. Quite interestingly, it was found that the HTHC resistance of  $\gamma' + \gamma$  alloys improved with up to about 10 at.% Pt addition, but then decreased significantly with increasing Pt content up to 30 at.% (the maximum level studied); however, under LTHC conditions the resistance of  $\gamma' + \gamma$  alloys improved with increasing Pt content up to 30 at.%. To further improve hot corrosion resistance of Pt+Hf-modified  $\gamma' + \gamma$  alloys, the effects of systematic additions of Cr, Si, and Cr+Si were assessed. The effects pre-oxidation treatments were also studied to further improve the hot corrosion resistance. In addition, high-temperature oxidation behavior of various modified of  $\gamma' + \gamma$  alloys was studied in air at 1150°C under both isothermal and cyclic oxidation conditions. Certain modified versions of  $\gamma' + \gamma$  coating composition(s) exhibited excellent resistance to both hot corrosion and oxidation. Finally, the HTHC and LTHC resistance of novel Pt+Hf-modified  $\gamma' + \gamma$ -based

diffusion coatings using a pack cementation process developed at ISU were studied and compared with state-of-the-art commercial coatings. It was found that the Pt+Hf-modified  $\gamma'+\gamma$  coating exhibited superior resistance to both types of hot corrosion with the pre-oxidation treatment; while, only Pt-modified  $\beta$  exhibited excellent LTHC resistance with no pre-oxidation treatment. This study also involved evaluating the hot corrosion resistance of various commercially available Pt-modified  $\beta$ -NiAl diffusion aluminides and CoCrAlY-based overlay coatings for marine gas turbine engine components under both HTHC and LTHC conditions. The Al-Pt-rich  $\beta$  aluminide exhibited improved resistance to both types of hot corrosion compared to the various Ni-rich  $\beta$  aluminide and CoCrAlY coatings.

## 1. INTRODUCTION

The advancement in high-temperature engineering alloys and coating systems has led to increases in both power and efficiency of gas-turbine engines over the past 60 years. Aero, industrial, and marine gas-turbines also face extreme (*i.e.* greater than  $\sim 1000^{\circ}\text{C}$ ) and harsh (*i.e.* with aggressive deposits and mixed gas mixture) operating conditions; hence, surface degradation often occurs by high temperature oxidation ( $>1000^{\circ}\text{C}$ ) and hot corrosion ( $\sim 850$ - $1000^{\circ}\text{C}$  for Type I and  $600$ - $800^{\circ}\text{C}$  for Type II) [1]. Of particular concern in this study is hot corrosion, which is an accelerated degradation process that involves deposition of corrosive species (*e.g.*, sulfates, chlorides) from the surrounding environment (*e.g.*, combustion gas to the surface of hot components). The deposition of molten corrosive species is then followed by destruction of the protective thermally grown oxide (TGO) scale, which had formed on the component surface. Salt-induced hot corrosion can be a particularly significant degradation mechanism in marine environments and when a contaminated lower-grade fuel is used. The severity of oxidation and hot corrosion processes in aircraft, land-based power generation, and marine gas-turbines is summarized in Table 1 [2].

Advanced gas-turbines consist of low-pressure turbine (LPT) and high-pressure turbine (HPT) sections and hot corrosion attack is more frequently observed in the LPT than in the HPT. This is because the LPT sections operate at lower temperatures compared to HPT, thus allowing a significant amount of corrosive contaminants to accumulate on the blade surface [3]. It has also been observed that hot corrosion is usually greatest at the hottest point on the concave surface of the blade, which is about mid-way along the length of the blade [3]. Hot corrosion attack on gas-turbine materials can be reduced to a certain extent with the use of high quality fuels and improved filtration systems. However, it would be extremely costly to provide fuel of excellent quality to give a significant resistance. The other option is to improve the hot corrosion resistance of turbine blade material itself. Superalloys used for gas turbine blades and vanes encompass a large group of metals which have improved strength at higher operating temperatures. The improvements in the strength of superalloys corresponded to additions of elements such as W, Mo, Ta, Ti, which confer poor hot corrosion and oxidation resistance. Hence, in gas-turbines the superalloy components are

usually protected by a diffusion or overlay metallic coating that is able to form a protective  $\alpha$ -Al<sub>2</sub>O<sub>3</sub> scale [4].

The most widely used diffusion coatings are based on the aluminide  $\beta$ -NiAl, while overlay coatings are typically based on an MCrAlY composition in which M represents Ni, Co, or Ni + Co. The performance of coatings depends upon their chemical composition and microstructure. The use of protective coatings and high-quality aviation fuels does not usually cause extensive degradation of the coated superalloy systems below about 5,000 hours, at least in aircraft engines [5]. However, for flights in marine atmosphere at lower altitude the life expectancy dramatically drops below 5,000 hours.

**Table 1.** Comparison of severity of degradation mechanisms for various gas-turbine engine applications [2].

<b>Gas-turbine engine application</b>	<b>Oxidation</b>	<b>Hot corrosion</b>	<b>Interdiffusion</b>
Aircraft engines	Severe	Moderate	Severe
Land-based industrial power generation engines	Moderate	Severe	Moderate
Marine gas-turbine engines	Moderate	Very Severe	Light

The quest for higher component operating temperatures in gas-turbine engines was mostly dominated by superalloy processing technology until the past 20 years. The development of thermal barrier coating (TBC) systems coupled with modern cooling systems has allowed for an almost 150°C reduction at the superalloy blade surface temperature thereby allowing the gas-turbine engine combustion temperature to be above the melting temperatures of superalloys [6]. The technological developments in superalloys over the time providing an increase in the operational temperatures are shown in figure 1 [7]. The major mode of TBC failure is delamination of the outermost ceramic layer from metallic bond coat [6]. The hot corrosion and oxidation behavior of the metallic bond coats has a major impact on the life of a TBC. In many cases, the protective metallic coating is often applied to a

superalloy substrate without a ceramic top coat and protection from oxidation and hot corrosion is provided just from the coating that is able to form a protective TGO scale.

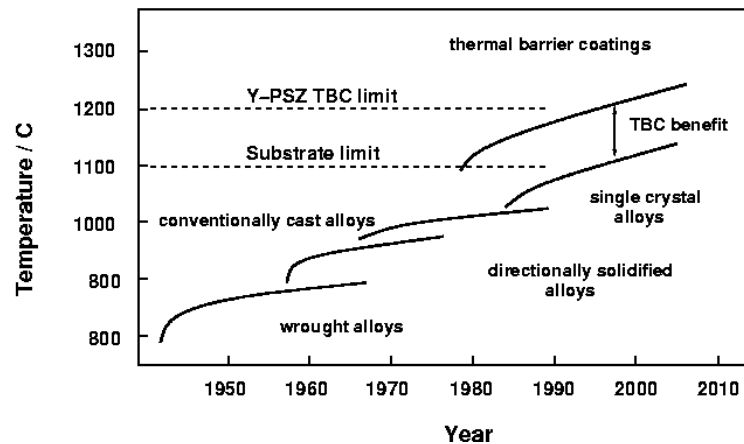


**Figure 1.** Increase in operational temperature of turbine components [7].

This dissertation compares and ranks the hot corrosion resistance of various commercially available metallic coatings applied to Ni-based superalloy substrates. Specifically, coating performances under hot corrosion conditions were ranked by assessing the extents of attack around the circumference of each coated sample together with maximum depth of attack. Recent work at Iowa State University (ISU) has showed that a wide range Pt+Hf-modified  $\gamma'$ -Ni<sub>3</sub>Al +  $\gamma$ -Ni alloy compositions form a very adherent and slow-growing Al<sub>2</sub>O<sub>3</sub> scale and offer a viable superior alternative to  $\beta$ -NiAl(Pt)-based coatings [8]. The primary goal of this research was to study high temperature degradation of various commercially available coatings and developmental  $\gamma'+\gamma$  alloys and coatings. It includes hot corrosion and oxidation behavior of novel Pt+Hf-modified  $\gamma'+\gamma$  alloys and coatings in detail to gain a better fundamental understanding of the effects of  $\gamma'+\gamma$  composition and assemblage on degradation behavior. A targeted significant outcome of this study is the establishment of an optimum coating composition(s) that is highly resistant to both hot corrosion and oxidation. Alternative  $\gamma'+\gamma$  coating compositions are proposed to current state-of-the-art Pt-modified  $\beta$ -NiAl coatings. The hot corrosion behavior of developmental  $\gamma'+\gamma$  metallic coating was also studied and compared with state-of-the-art diffusion and overlay coatings.

## 2. TECHNICAL BACKGROUND

### 2.1 Superalloys in Gas-Turbine Engine

Superalloys are Ni-, Co-, and Fe-based alloys based on the face centered cubic (FCC) crystal structure and are generally used at elevated temperatures as the blades and vanes in the turbine section of an engine. Ideally, they provide high-temperature strength and resistance to both hot corrosion and oxidation. Superalloys have solubility for various elements, thus allowing a wide range of alloys with different properties. Strengthening of superalloys is achieved by solid-solution hardening (by substituting elements with slightly different atomic diameter, *e.g.* Co, Fe, Mo, W, V, Ti, Al), precipitation hardening (by forming precipitates such as  $\gamma'$ -Ni<sub>3</sub>(Al, Ti)), and by formation of a carbide-dispersion (by favorable distribution of carbides). The latter is particularly case for Co-based alloys. The upper temperature limit of superalloys depends upon the melting temperature and dissolution of the strengthening phases. Superalloys are available in cast or wrought (usually heat treated or processed) forms. Developments in casting technologies made it possible to produce directionally-solidified and single-crystal superalloys (figure 1).

### 2.2 High-Temperature Protective Coating Systems

#### 2.2.1 High-Temperature Surface Protection

The goal of continuous improved performance of gas-turbine engine components has led to the evolution of superalloy processing technology along with the development of high-temperature protective coatings. A metallic coating improves reliability and durability of turbine blades in harsh operating temperatures, under thermal cycling and in aggressive environments, thus enabling higher efficiencies and longer operating lifetimes [5]. Metallic coatings are preferred for the surface protection of superalloys because coatings can be tailored for the surrounding aggressive environment. This in turn allows for the development of superalloy substrates with much improved strength. Application of a coating also provides an opportunity to refurbish worn surfaces after some time in service, allowing the use of superalloy substrate for extended operating lifetimes before replacement.

Advanced high-temperature protective coatings must provide adequate resistance to both oxidation and hot corrosion, while being chemically and mechanically compatible with the superalloy substrate. Apart from providing environmental protection, coatings should exhibit the following characteristics [1-15]:

- Coatings should be well bonded to the substrate.
- Coatings should form thin, continuous, slow-growing, and adherent thermally grown oxide (TGO) scale.
- Coatings usually have lower strength than the superalloy substrate; hence they should be thin, continuous and should have uniform composition.
- Coatings should be self-healing in forming a protective TGO scale.
- Coatings should not degrade the mechanical properties of the superalloy substrate.
- Coatings should have high-temperature diffusional stability.
- Coatings should be ductile enough to withstand substrate deformation without cracking.

Protective coatings on superalloys do not function as inert barriers but rather they provide protection by interacting with oxygen in the aggressive environments to form a dense, continuous and adherent TGO scale. The TGO layer often acts as a diffusion product layer that inhibits inward diffusion of oxidizing species such as oxygen and sulfur and outward diffusion of metal species. It is important that, the TGO layer should not crack or spall during thermal cycling. Therefore, protective coatings must be rich in the elements (Al, Cr, and Si) that participate in the formation of protective oxide scales ( $\text{Al}_2\text{O}_3$ ,  $\text{Cr}_2\text{O}_3$ , and  $\text{SiO}_2$ ). Among these oxides,  $\text{Cr}_2\text{O}_3$  is not suitable above about  $950^\circ\text{C}$ , especially in high-velocity gases, due to formation of volatile  $\text{CrO}_3$  [9]. Silica-forming ceramic coatings ( $\text{SiC}$ ,  $\text{Si}_3\text{N}_4$ ) are deposited on carbon-based materials at higher temperatures ( $> 1000^\circ\text{C}$ ) [10]; however, the use of silica-forming metallic coating on superalloys is limited. A metallic coating must contain a large amount of silicon in order to form  $\text{SiO}_2$  scale. Silicon in a coating tends to diffuse rapidly into the substrate, forming low melting phases and brittle silicides by interacting with the superalloy substrate. Hence, most of the high-temperature protective coatings are  $\text{Al}_2\text{O}_3$  formers. The growth rates of  $\text{Al}_2\text{O}_3$  scales generally determine the life for coatings, since this controls the rate and extent of aluminum depletion from the coating in forming the scale.

In Al<sub>2</sub>O<sub>3</sub>-forming coatings, silicon and chromium additions have been found to be beneficial in improving oxidation and hot corrosion resistance [1-4], [13-15]. Chromium addition in the coating decreases the amount of aluminium required for the formation of an Al<sub>2</sub>O<sub>3</sub> scale [17]; but the development of advanced single crystal superalloys with improved strength meant reductions in chromium and silicon contents. The scale growth and spallation rates can be controlled by small additions of reactive elements such as yttrium, cerium, hafnium and zirconium [18-20]. Precious-metal additions such as platinum, palladium, and ruthenium are also known to improve oxidation and hot corrosion resistance [21-24]. Addition of platinum in the diffusion aluminide coating promotes the formation of a slow growing, continuous, and adherent oxide scale [20].

### 2.2.2 Coating Processes

Superalloy coating processes are often divided into two main categories: one involves the reaction of an outer surface layer from reactive chemical vapor deposition with the selective chemical species (*i.e.* diffusion coating process) and the other involves deposition of metallic species with desired protective compositions onto the substrate (*i.e.* overlay coating process). There are various factors that influence the coating selection process in advanced gas turbine, and these include [1-16]:

1. Gas and deposit composition
2. Gas and/or deposit and superalloy temperature
3. Thermal cycling
4. Superalloy specimen geometry, since overlay coatings are line-of-sight process
5. Superalloy composition
6. Required protection time and cost of the coating deposition process
7. Gas pressure and velocity
8. Possible effects of the coating process on the mechanical and thermal properties of the superalloy substrate
9. Effects of interdiffusion between the coating and superalloy substrate during the high-temperature exposure

Conventionally cast, directionally solidified or single crystal superalloy substrates in high- and low-pressure turbine components are often protected against oxidation and hot corrosion using a Pt-modified diffusion aluminide or a MCrAlY (where M is Ni, Co or Ni + Co) overlay coatings. A short summary of these coatings is presented in the next section, while more comprehensive reviews about the various types of coatings can be found in the references [11-15].

#### 2.2.2.1 Diffusion Coatings

Coating processes which involve enrichment of Al, Cr, and Si via diffusion process into the superalloy surface are widely used in industry. Diffusion coatings can be applied on gas turbine engine components using various techniques such as slurry cementation, powder pack cementation, and chemical vapor deposition (CVD).

A pack cementation process is itself a type of CVD process that involves both the component and the powder reactants in a same semi-sealed retort. The “pack” of powder reactants mixture consists of Al/Cr/Si and/or other element-powder, a halide (*e.g.*  $\text{NH}_4\text{Cl}$ ) as a chemical activator, and inert filler (*e.g.*  $\text{Al}_2\text{O}_3$ ). The retort is then placed in the furnace in an inert atmosphere and on heating the metal powder reacts with the activator to form a vapor that in turn reacts with the surface of the superalloy thereby enriching it with the metal to be coated [5]. The most commonly used diffusion based  $\beta$ -NiAl coatings by pack cementation process can be classified as either low-activity (outward growing) or high-activity (inward growing) coatings. Low-activity  $\beta$ -NiAl coatings are formed by the predominant outward diffusion of nickel, while high-activity coatings are formed by the predominant inward diffusion of aluminium [5]. In pack aluminizing of Ni-based alloys the phases of interest are NiAl,  $\text{Ni}_3\text{Al}$ , and  $\text{Ni}_2\text{Al}_3$ . The final phase structure of the coating can be controlled by the concentration and temperature of the pack constituents and the time and temperature of the post-heat treatment. A further factor that influences the properties of aluminide coating is the variation in the substrate composition. As a consequence a different processing methodology is often required for each superalloy to obtain desired coating results.

Modified aluminide coating can be prepared by depositing another layer prior to the aluminizing process or by co-depositing elements from pack or slurry. For example,

chromizing is performed prior to the aluminizing process to develop chrome-modified aluminide coatings with improved hot corrosion resistance; however, their oxidation resistance is rather poor [70]. Similarly Si-modified aluminide coatings can be produced using slurry or process to produce CrSi<sub>2</sub>-dispersed  $\beta$ -NiAl coatings, which exhibit improved hot corrosion resistance [25]. A significant advancement in the diffusion coating processes was made with the inclusion of noble metal-Pt in the aluminide coatings (Pt-modified  $\beta$ -NiAl coatings). Platinum-modified aluminide coatings are now widely used in the gas turbine industry, outperforming most of the other diffusion aluminide coatings under the cyclic oxidation and hot corrosion conditions [1-4]. A commercially used Pt-modified  $\beta$  coating is prepared by electroplating 5-10  $\mu\text{m}$  platinum into the superalloy surface followed by heat treatment process prior to the pack cementation aluminizing treatment. A typical coating composition of Al-rich Pt-modified  $\beta$ -NiAl coating is Ni-(38-42 at%)Al-(8-10 at%)Pt and its microstructure is shown in figure 2 (a). Pt-modified aluminides are also widely used in thermal barrier coatings as the bond-coat with an electron beam physical vapour deposition (EBPVD) ceramic coat as the top-coat. More detailed discussion about the pack cementation process can be found elsewhere [5, 16]. Recently, Gleeson *et al.* [26] developed a novel Pt(+Hf)-modified  $\gamma'$ -Ni<sub>3</sub>Al +  $\gamma$ -Ni coating using the pack cementation deposition technique. The coating has a nominal composition of Ni-(20-22 at%)Al-(15-20at%)Pt-1wt%Hf and consists primarily of  $\gamma'$ , figure 2 (b). The phase structure of the coating is more compatible with the substrate ( $\gamma$ + $\gamma'$ ), thus reducing the undesired topologically closed packed (TCP) phases in the interdiffusion zone. The brittle TCP phase in the coatings decreases the strength of the superalloy-coating system. Therefore, Pt(+Hf)-modified  $\gamma'$ -Ni<sub>3</sub>Al +  $\gamma$ -Ni coatings are more suitable for advanced gas-turbine engine components from a mechanical standpoint. Preliminary results indicate that the Pt(+Hf)-modified  $\gamma'$ -Ni<sub>3</sub>Al +  $\gamma$ -Ni coatings exhibit excellent oxidation resistance and offer superior viable alternative to the current state-of-art  $\beta$ -NiAl(Pt)-based diffusion coatings. However, hot corrosion resistance of these coatings is not established and is the main focus of the current research.

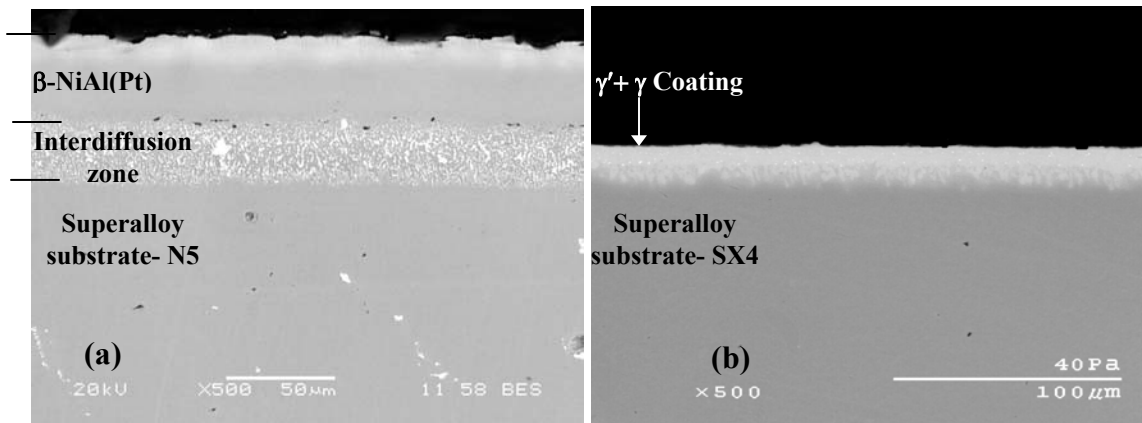


**Figure 2.** As-deposited diffusion aluminide coatings: (a) Commercially used Pt-modified  $\beta$ -NiAl coating [Ni-(38-42 at%)Al-(8-10 at%)Pt] (b) Pt+(Hf)-modified  $\gamma$ -Ni+  $\gamma'$ -Ni<sub>3</sub>Al coating [Ni-(20-22at%)Al-(15-20 at%)Pt-0.5 at%Hf] developed at ISU.

#### 2.2.2.2 Overlay Coatings

Diffusion based coatings have excellent oxidation resistance, but rather poor high temperature hot corrosion resistance. To combat this problem, research led to the development of MCrAlY overlay coatings. The final composition of a diffusion coating is dependent on the substrate composition; hence it is intrinsically difficult to obtain an ideal coating composition of optimum oxidation and hot corrosion resistance with improved ductility. In MCrAlY type overlay coating a pre-alloyed material with composition required to form protective TGO layer is applied to the superalloy surface by processes that require interdiffusion to ensure that the coating is metallurgically bonded to the substrate. In MCrAl overlay coating composition is selected to give optimum environmental resistance and ductility, while the active element Y is added to improve the oxide scale adhesion and to decrease oxidation rates. Most commonly used overlay coating processes are EBPVD and plasma spraying.

In physical vapor deposition, the required deposit composition is achieved from the vapor of a source and there is no need for chemical reaction between the substrate and the coating. The EBPVD process specifically involves vaporization of an ingot of the selected coating composition in a vacuum using focused electron beam as the evaporation source. The

composition of the deposited coating will often be different from the ingot due to the differences in vapor pressures of the elements and the composition of the ingot must therefore be adjusted accordingly. With the advancements in EBPVD coating technology, elements with a wide range of vapor pressure can be evaporated from a single source. More detailed information about the EBPVD process is presented elsewhere [27]. A typical coating microstructure of as-deposited CoCrAlY with nominal coating composition of Co-25Cr-14Al-0.5Y is shown in figure 3. The phase structure of CoCrAlY coating shows the precipitation of  $\beta$ -CoAl in a  $\gamma$ -matrix the cobalt solid-solution. The post-heat treatment is used to bond the coating and the substrate with the creation of a limited interdiffusion zone. The structure and composition of the CoCrAlY coating is constant throughout its thickness. The phase orientation in the as-deposited EBPVD coating is perpendicular to the substrate due to the nature of the process.

Air plasma spraying is a thermal spray method in which an electric arc creates plasma that can reach temperatures of more than 1600°C. The plasma spraying process involves injection of pre-alloyed coating material into a high-temperature plasma where it is fully melted and propelled towards the substrate. The molten particles impact the substrate surface and are rapidly solidified, forming a continuous but typically porous coating. With the help of high-temperature plasma it is possible to spray any material of tailored compositions and microstructures. The structure, composition and properties of a given coating are influenced by various factors such as the amount of preheat, plasma gun characteristics and gun to workpiece distance. Advancements in plasma spraying technology have made it possible to spray coatings in low-pressure vacuum chambers. This type of technique is known as low-pressure plasma spraying (LPPS) and is used for spraying MCrAlY coatings, as it minimizes the formation of oxide defect within the as-deposited coating structure. The advantages of LPPS also include higher powder particle velocities and broader spraying patterns. Plasma spraying coatings can also be applied in an inert gas shroud, especially Ar. A typical structure of NiCrAlY coating with a YSZ top coat is shown in figure 4. Plasma spraying process gives more compositional flexibility compared to the EBPVD process because vapor pressure of the coating elements is not an issue in the plasma spaying process. A detailed overview of plasma spraying process can be obtained from the reference [28].

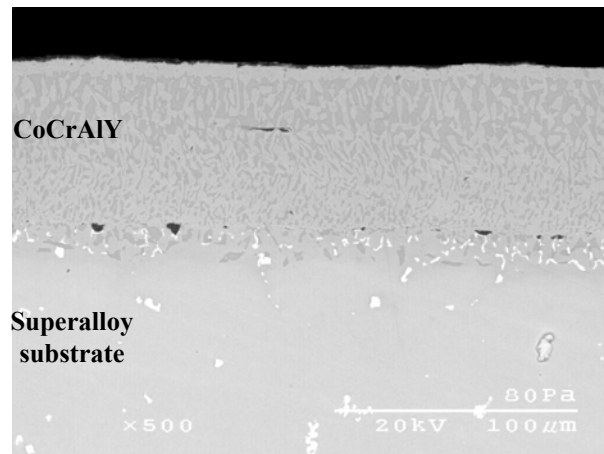


**Figure 3.** As-deposited CoCrAlY (Co-25Cr-14Al-0.5Y) overlay coating deposited by EBPVD process.

As-deposited overlay coatings when compared to diffusion coatings have little or no interdiffusion zone between the coating and the substrate, hence mechanical properties of the superalloy substrate are initially unaffected in the case of overlay coatings. Overlay coatings by plasma spraying or EBPVD show improved hot corrosion resistance than diffusion aluminides [2-4, 11-15]; however, both types of overlay coatings are line of sight processes and it is quite difficult to obtain uniform coating thickness for the complex shapes of turbine blades or vanes. Moreover, the internal cooling passages of the airfoils can not be coated using the overlay coating processes. Another disadvantage of overlay coatings is that coating processes are more expensive than the diffusion coating processes.

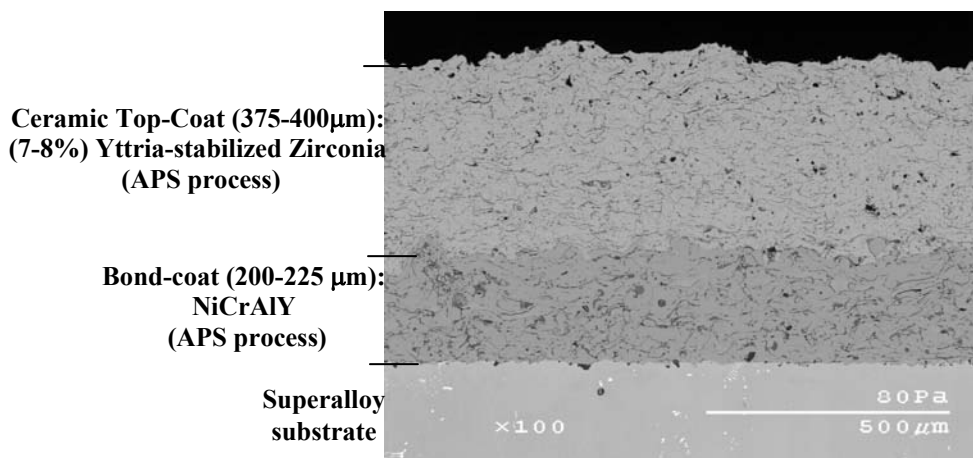


**Figure 4.** As-deposited NiCrAlY (Ni-25Cr-14Al-0.5Y) overlay coating (LPPS) with YSZ top coat (APS) both deposited using plasma spraying processes.

### 2.2.2.3 Miscellaneous Coatings

Coatings similar to the diffusion type can also be produced by an electrophoretic deposition process. In this process fine metal particles of desired composition are electrodeposited by immersion of substrate into the solution. The coated substrate is then subjected to a diffusion heat treatment in a protective atmosphere to produce a coating structure similar to diffusion aluminides (figure 5). Creech *et al.* [29] developed an electrophoretic process for the co-deposition of Pt and Si on Ni-based superalloys with or without additions of other minor elements. Electrophoretic deposition differs from electroplating in that particles of any composition rather than just ions can be deposited. Compared with physical vapor deposition, electroplating, spraying or dipping, the electrophoretic process is deemed to be the most suitable method for coating non-uniform geometries; however, it is still not better than diffusion aluminide coatings for depositing internal passages of airfoils.

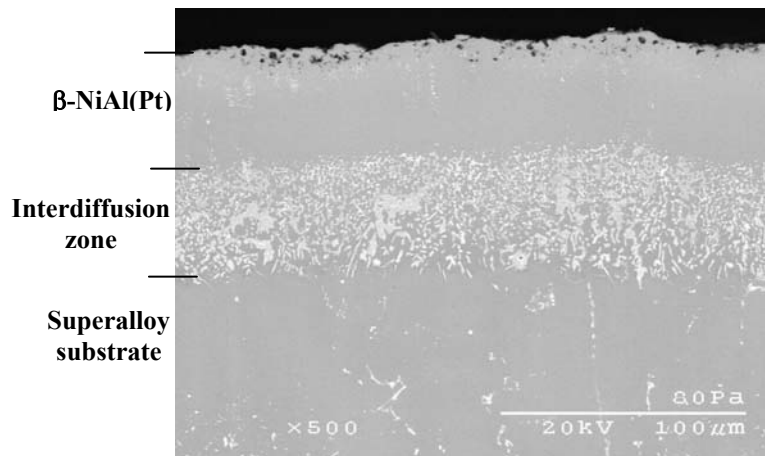


**Figure 5.** As-deposited Pt-modified  $\beta$ -NiAl coating [Ni-(36-40 at%)Al-(6-8 at%)Pt] deposited by electrophoretic process.

## **2.3 Background on Hot Corrosion**

### 2.3.1 Mixed Oxidant Corrosion

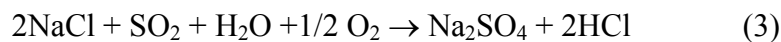
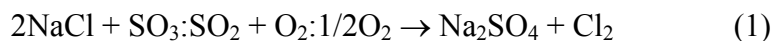
Materials used in high temperature applications encounter variety of corrosive environments containing two or more oxidizing components. CO, CO<sub>2</sub>, H<sub>2</sub>O, SO<sub>3</sub>/SO<sub>2</sub>, N<sub>2</sub>,

halogens, and molten alkali salts are the most common types of mixed oxidants other than O<sub>2</sub> that industrial applications encounter. Coking, nitridation, chlorination, sulfidation, and hot corrosion are some of the high temperature degradation mechanisms that occur due to exposure to mixed oxidizing reactants. The presence of these secondary oxidants affects oxidation behavior of an alloy resulting in corrosion products which are less protective than the protective TGO layer.

Molten-salt-induced hot corrosion is the focus of current research. It is an accelerated form of oxidation that is induced by the presence of a thin layer of molten oxidants on the surface of metals and alloys. It occurs in various advanced gas turbine engine components.

### 2.3.2 Formation of Na<sub>2</sub>SO<sub>4</sub> in a Gas Turbine Engine Environment

The molten oxidants in marine gas turbine environments are primarily composed of sulfates of alkaline earth metals. The sea environment is the primary source of these corrosive salts. Sea salt enters gas turbine engines as an aerosol and also as a fuel contaminant. It has been found that Na<sub>2</sub>SO<sub>4</sub> alone or combined with K<sub>2</sub>SO<sub>4</sub>, CaSO<sub>4</sub>, MgSO<sub>4</sub> and NaCl causes hot corrosion attack of gas turbine engine components [1, 34, 35]. Na<sub>2</sub>SO<sub>4</sub> is a minor constituent of sea salt, and is not found easily in air. Both coal and aviation fuel oils contain varying amounts of sulfur, which on combustion forms SO<sub>2</sub> and SO<sub>3</sub>. Dew point calculations showed that NaCl present in the form of vapor under the gas turbine engine conditions [34]. Sodium sulfate is formed when NaCl reacts with SO<sub>2</sub>/SO<sub>3</sub>, oxygen and/or water in the following manners:



DeCrescente and Bornstein [34] studied the formation and thermodynamic stability of Na<sub>2</sub>SO<sub>4</sub> in gas turbine engine environment and calculated equilibrium constants for the above reactions. They showed that the complete conversion of NaCl to Na<sub>2</sub>SO<sub>4</sub> is possible in a gas turbine engine atmosphere.

### 2.3.3 Hot Corrosion Characteristics: Temperature Dependence and Microstructural Appearance

Typically there are two different forms of hot corrosion mechanisms that are reported for gas turbine engine components. Depending upon temperature and their microstructural appearance, hot corrosion is divided into high-temperature hot corrosion (Type I HC) and low-temperature hot corrosion (Type II HC). The temperature dependence and corrosion rates of these forms of hot corrosion are compared with oxidation rate in figure 6 [35]. It is seen that hot corrosion is quite aggressive than oxidation in the temperature range of 650-1000°C; while, above 1000°C salt vaporizes and oxidation becomes a significant degradation process. HTHC occurs above melting temperature of external salt deposit and LTHC occurs below the melting temperature of external salt deposit; however, there can be localized liquid formation that causes LTHC attack at comparatively lower temperature. The localized liquid formation in LTHC is primarily due to a reaction between salt deposit and alloy underneath. Both forms of hot corrosion depend upon various factors such as salt composition and its melting temperature, alloy composition, gas composition, salt flux rate, thickness of salt scale, temperature and thermal cycles, thickness and composition of thermally grown oxide (TGO) scale.

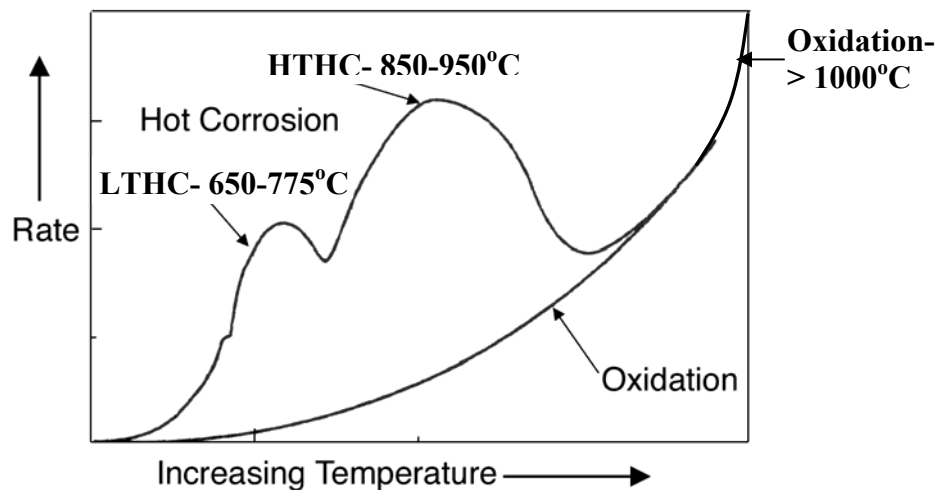


**Figure 6.** Schematic of comparison between temperature dependence and corrosion rates produced by the two forms of hot corrosion and oxidation [35].

### 2.3.3.1 High Temperature Hot Corrosion (HTHC-Type I HC)

HTHC mainly occurs at a higher temperature range between 850-950°C [35, 36]. The microstructural appearance of HTHC is characterized by a broad corrosion front with internal oxides beneath the porous non-protective external oxide scale. Internal sulfides are typically observed below the internally oxidized zone. Depletion of reactive elements (e.g. Al and Cr) and enrichment of noble elements such as Pt (if present) is also observed beneath the oxide scale. A schematic representation of microstructural appearance with various zone distributions is shown in figure 7 (a). SEM image of the Pt-modified  $\beta$  coating after 100 hours of exposure under HTHC conditions at 900°C is shown in figure 7 (b). HTHC is characterized by a change in surface color (e.g. green color in Ni-based alloys due to the formation of NiO), severe cracking and a substantial weight gain. It occurs above the melting temperature of the aggressive salt deposit. One of the most significant source of salt deposit for HTHC is  $\text{Na}_2\text{SO}_4$  ( $T_{\text{melt}} = 884^\circ\text{C}$ ) [39]; however, its melting point can be lowered by addition of other impurities such as vanadium, chlorides and other sulfate mixtures, thus broadening the range of HTHC. For instance,  $\text{Na}_2\text{SO}_4$  combined with dissolved salts like  $\text{CaSO}_4$  and  $\text{MgSO}_4$  forms an eutectic with a melting point as low as 650°C [37].  $\text{Na}_2\text{SO}_4$  also forms an eutectic with  $\text{NaCl}$  ( $T_{\text{melt}} = 620^\circ\text{C}$ ) that is present in the marine atmosphere [35]. Vanadium present as an impurity in low-grade fuel oils forms vanadium oxides upon combustion. Sodium vanadates formed by the reaction between  $\text{V}_2\text{O}_5$  and  $\text{Na}_2\text{SO}_4$  have lower melting point than the pure  $\text{Na}_2\text{SO}_4$ . In gas turbine engine atmosphere, it is possible to form various salt deposits with lower melting temperatures; however, a proto-typical salt,  $\text{Na}_2\text{SO}_4$ , was used in the present study.

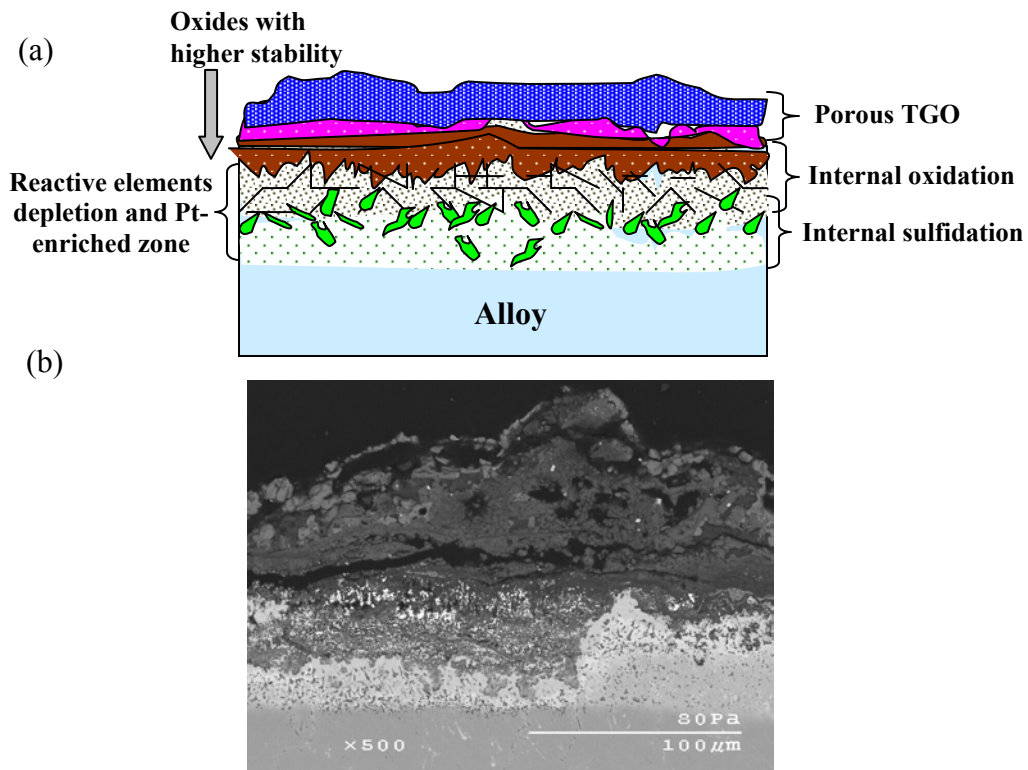


**Figure 7.** (a) Schematic of microstructural appearance showing zone distribution in HTHC  
 (b) SEM image showing HTHC in Pt-modified  $\beta$ -NiAl coating on Ni-based superalloy.

### 2.3.3.2 Low Temperature Hot Corrosion (LTHC-Type II HC)

Typically LTHC occurs at a lower temperature range between 650-775°C [35, 36, 38]. This form of degradation is often characterized by a pitting attack at least during early stages. The microstructural appearance reveals internal voluminous oxides with very little or no internal sulfides and depletion zone. A schematic representation and SEM image of the Pt-modified  $\beta$  coating after LTHC is shown in figure 8. Liquid formation of salt deposit in LTHC depends upon the alloy underneath and on the surrounding gaseous environment. LTHC occurs at least 125°C below melting temperature of external  $\text{Na}_2\text{SO}_4$  salt and liquid formation of deposit is generally believed to be due to eutectic  $\text{Na}_2\text{SO}_4$ - $\text{MSO}_4$  (where M is Co or Ni). The  $\text{Na}_2\text{SO}_4$ - $\text{NiSO}_4$  phase diagram is shown in figure 9. Both eutectic ( $\text{Na}_2\text{SO}_4$ - $\text{NiSO}_4 \rightarrow T_{\text{melt}} = 671^\circ\text{C}$  and  $\text{Na}_2\text{SO}_4$ - $\text{CoSO}_4 \rightarrow T_{\text{melt}} = 565^\circ\text{C}$ ) temperatures are below 700°C.  $\text{CoSO}_4$  and  $\text{NiSO}_4$  can be formed from the following reactions in Co- and Ni-based alloys,

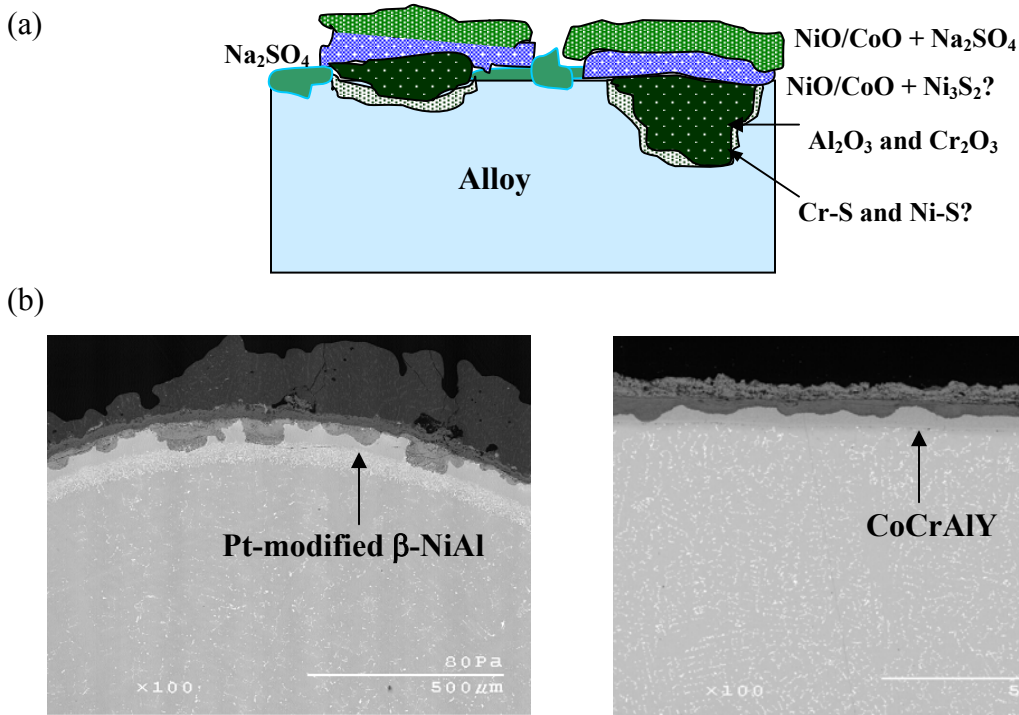
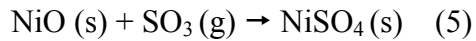
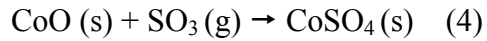


**Figure 8.** (a) Schematic of microstructural appearance showing zone distribution in LTHC

(b) SEM image showing LTHC in Pt-modified  $\beta$ -NiAl and CoCrAlY coating.

In these reactions a higher  $\text{PSO}_3$  is required for the formation of an eutectic  $\text{Na}_2\text{SO}_4$ - $\text{MSO}_4$  at lower temperatures.  $\text{SO}_3$  and  $\text{SO}_2$  are more stable in LTHC than in the HTHC temperature range, as their stability decreases with increase in temperature. It should be noted that  $\Delta G_f^\circ$  for the  $\text{SO}_2 + 1/2 \text{O}_2 \rightarrow \text{SO}_3$  reaction suggests that the reaction is possible only in the LTHC temperature range ( $< 780^\circ\text{C}$ ). Such aggressive high temperature degradation mechanisms (HTHC and LTHC) involve breakdown of protective reaction product barrier followed by dissolution of an oxide by what is referred to as a “fluxing” action. Hot corrosion degradation by such fluxing reactions and models describing these reactions are explained in detail in the next few sections.

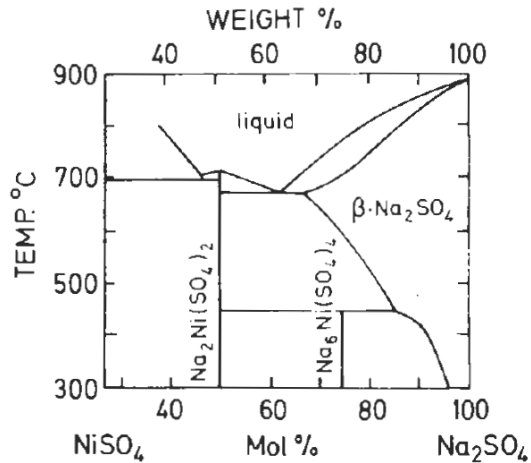


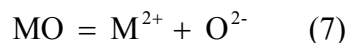
**Figure 9.** Phase diagram of  $\text{Na}_2\text{SO}_4$ - $\text{NiSO}_4$  with eutectic temperature of  $671^\circ\text{C}$  [39].

#### 2.3.4 Deposit Induced Degradation-Salt Fluxing Reactions

Thermodynamic phase stability diagrams are quite useful in describing any compositional changes that may occur in the deposit. For instance, in hot corrosion, metal-sulfur-oxygen stability diagrams delineate the stability regions of the various phases that may exist for different activities of the oxidants. High temperature stability diagrams are quite similar to Pourbaix diagrams used in aqueous environments [39]. The  $900^\circ\text{C}$  phase stability diagram for the Na-O-S [39] system in figure 10 illustrates various phase stability regions that are present when  $\text{Na}_2\text{SO}_4$  is in contact with the oxide or metal. Activities of  $\text{O}_2$  and  $\text{SO}_3$  are used as coordinates, where activity of  $\text{SO}_3$  can be replaced with  $\text{Na}_2\text{O}$  activity in the same figure, in accordance with the equilibrium,



The acidity of the molten salt is expressed as  $\log(\text{PSO}_3)$  and the basicity as  $\log(\text{aNa}_2\text{O})$ . The deposit may become more basic due to an increase in the oxide ions concentration *i.e.* activity of  $\text{Na}_2\text{O}$  is increased or it may turn more acidic if the oxide ion concentration is decreased *i.e.*  $\text{PSO}_3$  is increased. A fluxing mechanism depends upon the oxide ion concentration in the melt. Acidic fluxing occurs when oxide ion concentration in the melt is low compared to the value required to maintain equilibrium. The acidic dissociation reaction is given as,



Similarly in basic fluxing oxide ion activity is high compared to the value required to maintain equilibrium and forms a complex anion as shown below,

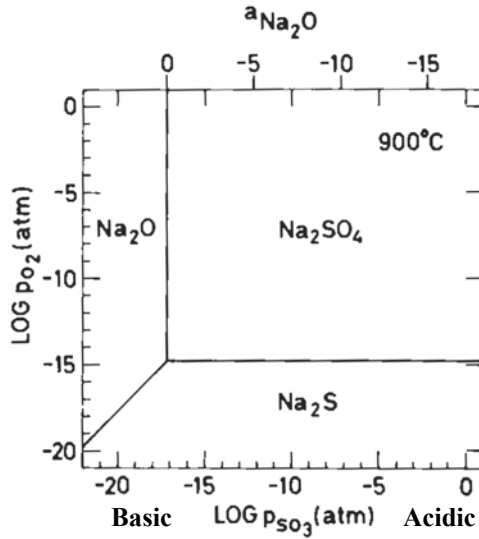
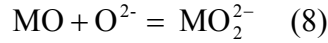
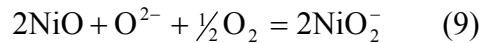
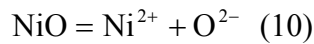


**Figure 10.** Phase stability diagram for Na-S-O system at 900°C [39].

These fluxing reactions are very similar to anodic and cathodic reactions in aqueous environments. Basic and acidic fluxing of an oxide can be explained by considering an example of NiO fluxing in Na<sub>2</sub>SO<sub>4</sub>. Gupta and Rapp [40] measured solubility of NiO in Na<sub>2</sub>SO<sub>4</sub> as a function of log aNa<sub>2</sub>O (or log P<sub>SO<sub>3</sub></sub>) and their results are shown in figure 11. The solubility of NiO has a minimum at log aNa<sub>2</sub>O = -10.3 and it increases with increase in log aNa<sub>2</sub>O (*i.e.* decrease in log P<sub>SO<sub>3</sub></sub>) according to the reaction,



The above reaction corresponds to the basic fluxing of NiO in Na<sub>2</sub>SO<sub>4</sub>. The solubility of NiO also increases below the minimum with decrease in log aNa<sub>2</sub>O (*i.e.* increase in log P<sub>SO<sub>3</sub></sub>) according to the reaction,



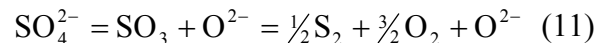
This corresponds to the acidic fluxing of NiO, suggesting that at higher values of  $\log a_{\text{Na}_2\text{O}}$ , NiO dissolves as  $\text{NiO}_2^-$  and at lower values as  $\text{Ni}^{2+}$ .

### 2.3.5 Basic and Acidic Fluxing Model

The concept of fluxing of an oxide is used to interpret various propagation modes in hot corrosion. Researchers have developed fluxing models for each type of fluxing mechanism. The next section discusses fluxing mechanisms and models for various hot corrosion conditions.

#### 2.3.5.1 Goebel-Pettit Model for Basic Fluxing

Bornstein and DeCrescente [41-43] first proposed the concept of basic fluxing. Goebel *et al.* [44, 45] subsequently developed and described the model by a thermochemical approach. This model considers that metal is covered by an oxide scale which is continuously dissolved in the molten deposit. It is also assumed that a compositional gradient is established across the deposit layer. The basic fluxing model is explained here using an example of  $\text{Na}_2\text{SO}_4$  induced hot corrosion in Ni at  $900^\circ\text{C}$ . In basic fluxing, oxide ions are produced in the  $\text{Na}_2\text{SO}_4$  layer due to the removal of oxygen and sulfur from the deposit via reaction with the alloy or metal as shown in equation 11 below,



It should be noted from this equation that an increase in  $\text{O}_2$  or  $\text{O}^{2-}$  activity necessarily means a decrease in sulfur activity and vice versa. From estimated oxygen and sulfur activities in a gas turbine environment, the phase stability diagram suggests that NiO is predominantly formed resulting in depletion of oxygen near the  $\text{Na}_2\text{SO}_4/\text{NiO}$  interface. An oxygen activity gradient is produced by initial oxidation of Ni throughout the  $\text{Na}_2\text{SO}_4$  layer. Decrease in oxygen activity at the  $\text{Na}_2\text{SO}_4/\text{NiO}$  interface results in a higher sulfur activity beneath the NiO layer. An increased sulfur activity promotes formation of nickel sulfide, which decreases sulfur activity and eventually increases oxide ion activity. Higher oxide ion activity would then favor fluxing or dissolution of NiO by oxide ions via reaction 9.

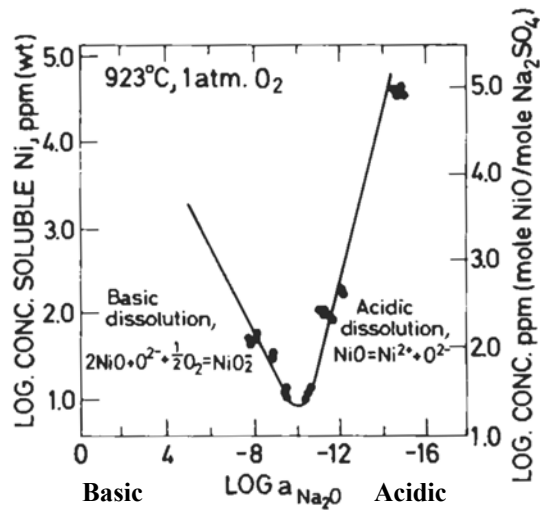


**Figure 11.** The solubility of NiO in Na<sub>2</sub>SO<sub>4</sub> at 1atm O<sub>2</sub> and 927°C as a function of basicity  $a_{\text{Na}_2\text{O}}$  in Na<sub>2</sub>SO<sub>4</sub> [40].

The hot corrosion conditions create a gradient of O<sup>2-</sup> and O<sub>2</sub> activity such that O<sup>2-</sup> activity decreases and O<sub>2</sub> activity increases when going from the Na<sub>2</sub>SO<sub>4</sub>/NiO interface through the Na<sub>2</sub>SO<sub>4</sub>/gas interface. Nickelate ions formed from the above reactions then diffuse away from Na<sub>2</sub>SO<sub>4</sub>/NiO interface to a point where the O<sup>2-</sup> activity is low and O<sub>2</sub> activity is high. This leads to the precipitation of NiO<sub>2</sub> to NiO resulting in a discontinuous, non protective and porous oxide scale increasing the mobility of liquid Na<sub>2</sub>SO<sub>4</sub> through the scale. Basic fluxing explained using this model is maintained until Na<sub>2</sub>SO<sub>4</sub> is consumed. The fluxing model proposed by Goebel and Pettit [44] for hot corrosion of Ni is shown in figure 12. Such a basic fluxing mechanism has distinctive microstructural features of porous, non-protective oxide scale and sulphide particles are found in the alloy substrate below the oxide scale. This form of basic fluxing depends on the production of oxide ions from the molten deposit; hence, a continuous supply of molten deposit is required for the attack to continue. This suggests that basic fluxing hot corrosion is not self-sustaining and is usually restricted to high temperatures (HTHC ~ 900°C).

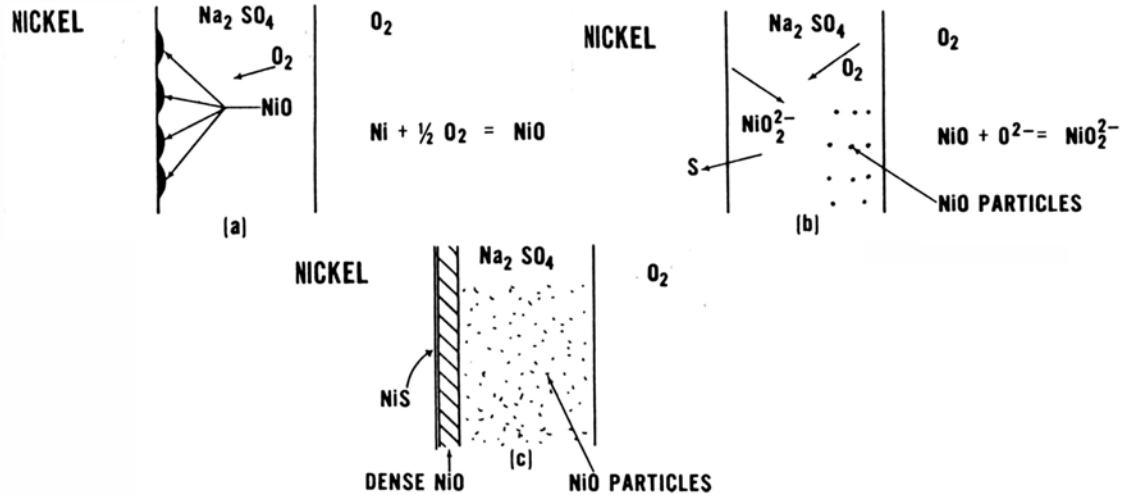


**Figure 12.** Model for Na<sub>2</sub>SO<sub>4</sub>-induced accelerated oxidation of pure nickel. (a) Oxygen activity gradient is produced by initial oxidation of nickel. (b) Sulfur enters alloy and oxygen ions react with NiO to form nickelate ions. (c) Sulfur activity decreases and oxide ions are no longer produced, Na<sub>2</sub>SO<sub>4</sub> becomes saturated with Ni, and a continuous NiO scale is formed [44].

### 2.3.5.2 Rapp-Goto Criterion of Oxide Fluxing

Rapp and Goto [46] considered a fluxing model based on oxide solubilities in the molten deposit. According to these authors, hot corrosion attack is sustained through a dissolution-precipitation mechanism if “negative solubility gradient” of the protective oxide is maintained at some distance from oxide/salt to salt/gas interface. Using this Rapp-Goto model, Shores [47] provided the following quantitative expression for the earlier Goebel-Pettit model of dissolution-precipitation mechanism;

$$\left[ \frac{d [\text{Solubility of oxide}]}{dx} \right]_{x=0} < 0$$

Here  $x = 0$  is the salt/oxide boundary and  $x > 0$  corresponds to the salt layer. This so-called Rapp-Goto criterion does not involve consumption of sulfur or any change of molten deposit with time and is applicable to both acidic and basic fluxing. The negative solubility gradient

of an oxide is a consequence of the negative gradient of  $O^{2-}$  or  $S_2O_7^{2-}$  in the melt. Rapp [48] considered two specific conditions to explain the acidic and basic fluxing using the Rapp-Goto criterion. In basic fluxing, basic solute (*e.g.*,  $O^{2-}$ ) has a higher solubility at the oxide/salt interface than at the salt/gas interface resulting in higher solubility for oxide at the oxide/salt interface than at the salt/gas interface. The concentration gradients produced are also shown in the figure 13. It should be noted that due to oxidation of Ni, oxygen is consumed and  $PO_2$  decreases at the oxide/salt interface but basic fluxing occurs if the solubility of an oxide is higher at oxide/salt interface.

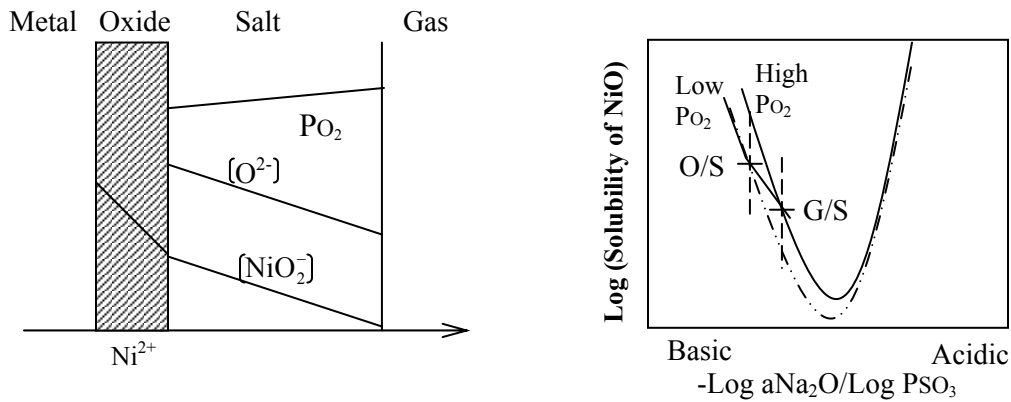
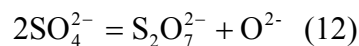


**Figure 13.** A schematic diagram of concentration gradients applying Rapp-Goto criterion of basic fluxing with  $O^{2-}$  as oxidant. For the establishment of “negative solubility gradient” in basic fluxing, solubility of oxide in the melt should be higher at O/S interface than G/S interface.

For acidic fluxing,  $S_2O_7^{2-}$  is formed from the following reaction,



The dominant acidic solute (*e.g.*,  $S_2O_7^{2-}$ ) has a higher solubility at the oxide/salt interface than at salt/gas interface (figure 14). For a constant  $PO_2$  acidic fluxing is sustained if solubility of an oxide is higher at oxide/salt interface than at gas/salt interface *i.e.*, if a negative solubility gradient is maintained. Rapp [48] determined and compiled solubilities of various oxides as a function of melt basicity and oxygen activity for pure fused  $Na_2SO_4$  at

1200 K and at 973 K for  $\text{SiO}_2$  (figure 15). In the range of this study  $\text{SiO}_2$  does not form an ionic solute, and its low solubility is independent of basicity or acidity. According to Rapp [48], under the operating conditions of a gas turbine, the  $\text{PSO}_3$  values produced are in the range where both  $\text{Cr}_2\text{O}_3$  and  $\text{Al}_2\text{O}_3$  exhibit minimum in their solubilities.

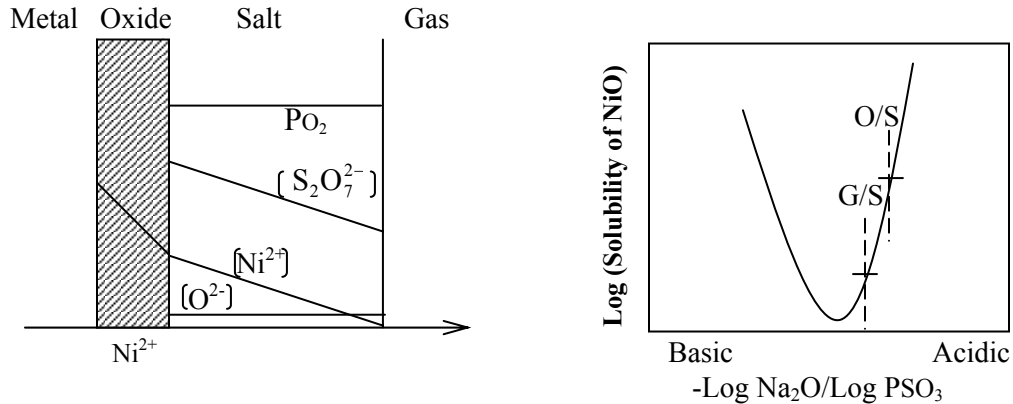


**Figure 14.** A schematic diagram of concentration gradients applying Rapp-Goto criterion of acidic fluxing with  $\text{S}_2\text{O}_7^{2-}$  as oxidant. For the establishment of “negative solubility gradient” in basic fluxing, solubility of oxide in the melt should be higher at O/S interface than G/S interface.

Shores [47] examined the Rapp-Goto criterion for different conditions and confirmed that the reactions are not always self-sustaining. For example, Shores showed that basic fluxing is not self-sustaining and molten deposit becomes more basic over a period of time. Hot corrosion attack eventually stops unless more salt is deposited. This condition is shown in figure 16. Shores [47] considered various possibilities and determined when fluxing would occur. Luthra [49-52] used the Rapp-Goto criterion and developed a model for hot corrosion in LTHC conditions.

Stringer [38] concluded that fluxing by  $\text{Na}_2\text{SO}_4$  is not likely to be important in gas turbine due to following reasons:

1. The salt deposits in gas turbine are very thin and gradients of basic and acidic solute ( $\text{O}^{2-}$  or  $\text{S}_2\text{O}_7^{2-}$ ) can not be expected.
2. Acidic fluxing will not occur because of low  $\text{PSO}_3$  available at high temperatures creating positive or zero solubility gradient. However, Shores [47] showed that the

Rapp-Goto criterion for acidic fluxing is satisfied in the presence of strong acidic refractory metal oxides at higher temperatures.

3. Oxides such as NiO have minimum solubility at  $a_{\text{Na}_2\text{O}} = 10^{-10}$  atm and basic fluxing of NiO occurs at  $a_{\text{Na}_2\text{O}} > 10^{-10}$  atm. Basic fluxing of NiO is not possible in gas turbine atmosphere because salt deposit is too acidic (*i.e.*  $a_{\text{Na}_2\text{O}} < 10^{-10}$  atm), suggesting that acidic solute should be dominant in creating a positive solubility gradient. To address this valid question Otsuka and Rapp [53] conducted a potentiometric experiment to track basicity and the oxygen activity at the substrate/salt interface during hot corrosion of Ni. They found that initially an acidic solute was dominant but after some time salt film was reduced and deposit became less acidic. Nickel sulfides were formed and the coupon was severely corroded while at the same time local salt chemistry shifted towards higher basicity. Their findings suggest that even in acidic gas turbine environment basic fluxing of NiO is possible thus satisfying negative solubility gradient criterion.

As mentioned earlier the Rapp-Goto criterion can be applied to both basic as well as acidic fluxing. This led researchers to develop separate models for acidic fluxing reactions. Acidic fluxing of alloys in a gas turbine engine environment occurs by at least two different processes. One of which is known as “gas phase induced acidic fluxing” where the component that produces acidic conditions can be present in the surrounding gas. Another possibility is that the acidic component can be present as an oxide of an element in the alloy and this type of fluxing is known as “alloy phase induced acidic fluxing”. The models describing these two processes will be discussed in the next section.

#### 2.3.5.3 Gas Phase Induced Acidic Fluxing

In this type of acidic fluxing, component is supplied to the salt deposit from the surrounding gas. Typically, in gas turbine engine environment there are two types of acidic components,  $\text{SO}_3$  and  $\text{V}_2\text{O}_5$ . As discussed earlier,  $\text{SO}_3$  is produced due to the combustion of sulfur in the fuel, while  $\text{V}_2\text{O}_5$  can be present as an impurity in the fuel.

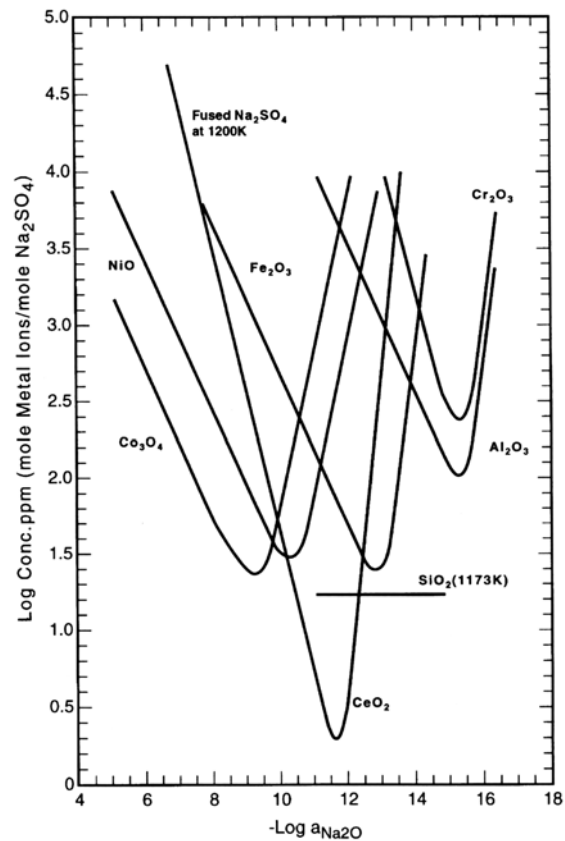
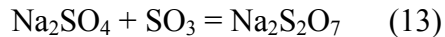


**Figure 15.** Measured solubilities for several oxides in pure fused  $\text{Na}_2\text{SO}_4$  [48].

$\text{SO}_3$ -gas phase induced attack is the focus of this current proposed research. In case of  $\text{SO}_3$ -gas phase induced attack,  $\text{SO}_3$  may react with  $\text{Na}_2\text{SO}_4$  in the following manner to produce lower melting temperature products such as sodium pyrosulfate ( $T_{\text{melt}} = 401^\circ\text{C}$ ),



However, liquid formation of the deposit in  $\text{SO}_3$ -gas phase induced attack is not likely due to sodium pyrosulfate formation, but is instead due to the formation of eutectic  $\text{Na}_2\text{SO}_4$ - $\text{MSO}_4$  (where M is Ni or Co) liquid. Since quite high  $\text{PSO}_3$  is available at the oxide/salt interface, the reaction between oxide (*i.e.* NiO or CoO) and  $\text{SO}_3$  is much faster and more stable than the reaction between  $\text{SO}_3$  and  $\text{Na}_2\text{SO}_4$ . This mode of attack gives LTHC.

$\text{SO}_3$ -gas phase induced acidic fluxing goes through a maximum at  $700^\circ\text{C}$ . As discussed in the earlier section, LTHC or gas-phase induced acidic fluxing depends upon the partial pressure of  $\text{SO}_3$  which decreases with increase in temperature. Therefore,  $\text{SO}_3$ -gas phase induced hot corrosion rate decreases considerably above  $800^\circ\text{C}$  and at  $900^\circ\text{C}$  HTHC or basic fluxing conditions are favored. There are various models developed to explain  $\text{SO}_3$ -gas

phase induced attack. Luthra *et al.* [49-52], proposed that non-protective  $\text{Al}_2\text{O}_3$  and  $\text{Cr}_2\text{O}_3$  oxide scales are formed in presence of salt deposit due to rapid removal of nickel and/or cobalt from the alloy. Nickel and cobalt diffuse outward to react with the deposit not allowing the formation of protective and continuous  $\text{Al}_2\text{O}_3$  and  $\text{Cr}_2\text{O}_3$ . These oxides of nickel and/or cobalt then become soluble in the acidic melt at the salt/oxide interface.

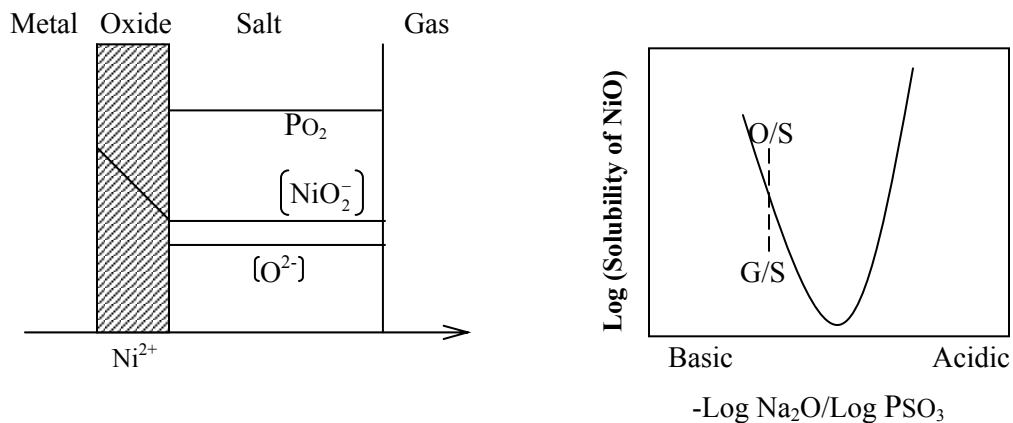
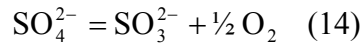


**Figure 16.** A schematic diagram of concentration gradients with no  $\text{O}^{2-}$  gradient because of fast transport. A condition for “negative solubility gradient” of oxide is not satisfied hence fluxing does not occur.

$\text{SO}_3$ -gas phase induced acidic fluxing mechanisms of the Ni- and Co-based alloys are quite similar to the mechanisms explained for pure Ni [39, 54] and Co [55, 56]. The hot corrosion product in Ni- and Co-based alloys also consists of two layers: (i) Eutectic liquid layer of  $\text{Na}_2\text{SO}_4 + \text{MSO}_4$  (where M is Ni or Co) as an outer layer and (ii) inner layer of  $\text{Ni}_3\text{S}_2 + \text{NiO}$  in Ni-based alloys or only  $\text{CoO}/\text{Co}_3\text{O}_4$  in case of Co-based alloys. The pits or internal attack usually consist of sulfate mixture,  $\text{Cr}_2\text{O}_3$  and/or  $\text{Al}_2\text{O}_3$ . The pitting type of attack is because breakdown of protective  $\text{Cr}_2\text{O}_3$  or  $\text{Al}_2\text{O}_3$  scales followed by fluxing of NiO or CoO and their spinels. The sulfate formation of NiO and CoO and even Ni/Co components of spinels above critical  $\text{SO}_3$  pressures causes gas phase induced acidic fluxing in these alloys. Ni-S formed during the corrosion may partially react with Cr to form more stable  $\text{Cr}_2\text{S}_3$ . The outward diffusion of Ni through NiO + Ni-S layer is much faster than the outward diffusion of Co through  $\text{CoO}/\text{Co}_3\text{O}_4$  layer. However, Co-based alloys are more susceptible to LTHC

than Ni-based alloys. The main reason for this is that  $\text{CoSO}_4$  is more stable than  $\text{NiSO}_4$  with respect to  $\text{CoO}$  and  $\text{NiO}$ , respectively. As a consequence,  $\text{CoSO}_4$  can form at a lower  $\text{PSO}_3$  than  $\text{NiSO}_4$ . In addition, the eutectic mixture of  $\text{Na}_2\text{SO}_4 + \text{CoSO}_4$  has a much lower melting temperature ( $565^\circ\text{C}$ ) than that of  $\text{Na}_2\text{SO}_4 + \text{NiSO}_4$  ( $T_{\text{melt}} = 671^\circ\text{C}$ ); hence the Co-based alloys are likely to be more susceptible to LTHC attack than the Ni-based alloys at lower temperatures. Luthra and Shores [57] also showed that  $\text{CoO}$  is a better catalyst for the  $\text{SO}_2 + \frac{1}{2} \text{O}_2 \rightarrow \text{SO}_3$  reactions than  $\text{NiO}$  as this increases  $\text{PSO}_3$  at the  $\text{CoO}$  surface than at the  $\text{NiO}$  surface.

Barkalow and Pettit [58] proposed another model for gas-phase induced acidic fluxing suggesting that the  $\text{PO}_2$  at the oxide/salt interface is too low to form oxides of cobalt and nickel and  $\text{SO}_3^{2-}$  ions are formed from the following reaction,



$\text{Al}_2\text{O}_3$  is assumed not to be stable in such melts because of the following reaction,



A dissolution-precipitation mechanism is followed so that non protective oxide particles are formed at the salt/gas interface where  $\text{PO}_2$  is higher. This model does not assume that the salt deposit will be in liquid form at the low  $\text{SO}_3$  pressures.

#### 2.3.5.4 Alloy Phase Induced Acidic Fluxing

Acidic conditions in the salt deposit are also favored by the incorporation of certain oxides such as  $\text{MoO}_3$  [45] and  $\text{WO}_3$  [59]. These oxides dissolve in the melt in following manner,

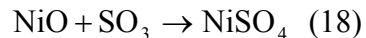


Thermally grown oxides ( $\text{NiO}$ ,  $\text{CoO}$ ,  $\text{Al}_2\text{O}_3$  and  $\text{Cr}_2\text{O}_3$ ) can dissolve into the melt at regions with higher  $\text{MoO}_3/\text{WO}_3/\text{V}_2\text{O}_5$  activity and precipitates where activity of these oxides is low. During initial formation of  $\text{Na}_2\text{MoO}_4/\text{Na}_2\text{WO}_4$  and its dissolution in deposit, an increase in local concentration of  $\text{PSO}_3$  causes rapid sulfate-induced corrosion of an alloy. Alloy-induced acidic fluxing occurs till Mo, W or V component of the alloy is completely consumed

suggesting that alloy induced fluxing is self-sustaining and only one application of salt layer may cause complete destruction of alloy. This type of acidic fluxing occurs at high temperatures where refractory metal oxides are more stable providing sufficient amount of oxides for making the melt acidic.

### 2.3.6 Fluxing of NiO and Protective Nature of Cr<sub>2</sub>O<sub>3</sub> and Al<sub>2</sub>O<sub>3</sub>

The protective nature of Cr<sub>2</sub>O<sub>3</sub> and Al<sub>2</sub>O<sub>3</sub> scales compared to non-protective NiO is discussed in detail in this section. Figure 17 (a) shows phase stability diagram for the Ni-O-S system [45] at 900°C. Acidic and basic fluxing sides are also shown in the figure. NiO is very stable oxide and NiSO<sub>4</sub> (required for acidic fluxing) is stable at quite high PO<sub>2</sub> and PSO<sub>3</sub> (log PSO<sub>3</sub> ~ -1 atm). Since PSO<sub>3</sub> decreases with increase in temperature NiO is unlikely to dissolve by acidic fluxing reaction at 900°C. Similarly stability diagram for the same system Ni-O-S at 700°C is shown in figure 17 (b) [39]. NiSO<sub>4</sub> is stable at much lower PSO<sub>3</sub> (log PSO<sub>3</sub> ~ -3 atm) and PO<sub>2</sub> and NiO is likely to dissolve in Na<sub>2</sub>SO<sub>4</sub> melt by acidic fluxing reaction,



The Ni-O-S stability diagram does not take into consideration the effect of Na<sub>2</sub>SO<sub>4</sub>. In order to understand the phases that may form in presence of Na<sub>2</sub>SO<sub>4</sub>, it is necessary to superimpose Na-O-S diagram (figure 18). Gupta and Rapp [40] concluded that two additional phases Na<sub>2</sub>NiO<sub>2</sub> and NaNiO<sub>2</sub> may form at the Na<sub>2</sub>O/Na<sub>2</sub>SO<sub>4</sub> boundary. This figure suggests that NiO is likely to dissolve in Na<sub>2</sub>SO<sub>4</sub> by reacting with Na<sub>2</sub>O at 900°C by basic fluxing reaction shown below,



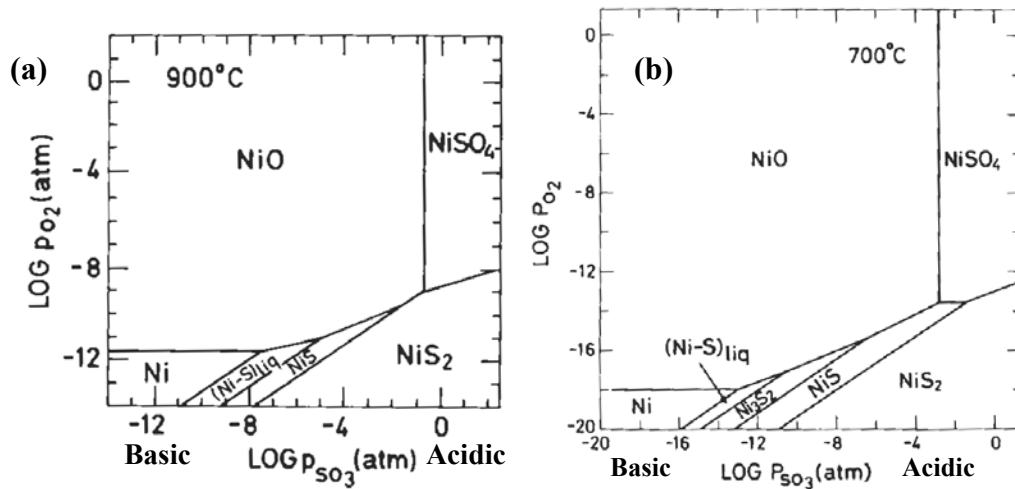


**Figure 17.** Phase stability diagram for Ni-S-O system at (a) 900°C and (b) 700°C [39].

As discussed in the earlier section that in LTHC ( $\text{SO}_3\text{-O}_2$  atmosphere at 700°C) conditions, NiO and  $\text{CoO/Co}_3\text{O}_4$  are susceptible to hot corrosion due to acidic fluxing.  $\text{Al}_2\text{O}_3$  and  $\text{Cr}_2\text{O}_3$  may possibly dissolve in acidic salt deposit in the following manner,



However, for the  $\text{SO}_3$  contents normally found in gas turbine atmosphere, neither  $\text{Cr}_2\text{O}_3$  nor  $\text{Al}_2\text{O}_3$  undergoes acidic fluxing.  $\text{Cr}_2\text{O}_3$  and  $\text{Al}_2\text{O}_3$  are both acidic oxides and sufficiently high  $\text{P}_{\text{SO}_3}$  ( $> 1\text{atm}$ ) is required for Cr and Al sulfate formation. In fact, Luthra constructed Cr-S-O and Al-S-O stability diagrams [50] at 750°C as a function of  $\text{P}_{\text{SO}_3}$  and  $\text{P}_{\text{O}_2}$ . The stability diagrams shown in figure 26 suggest that  $\text{Cr}_2\text{O}_3$  and  $\text{Al}_2\text{O}_3$  are indeed stable in  $\text{O}_2 + 2\%$  ( $\text{SO}_2 + \text{SO}_3$ ) atmosphere (shown by the hatched region).

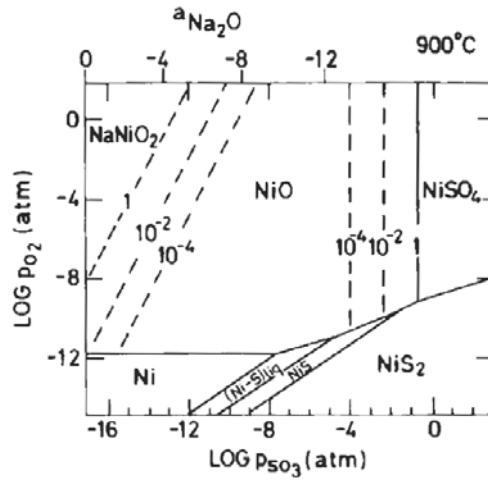
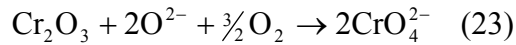
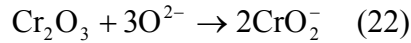
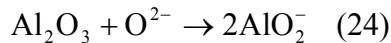


**Figure 18.** Phase stability diagram of the Ni-O-S system in the presence of  $\text{Na}_2\text{SO}_4$  [39].

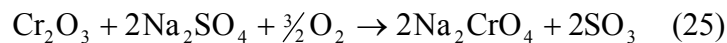
$\text{Al}_2\text{O}_3$  and  $\text{Cr}_2\text{O}_3$  are stable in LTHC conditions, if local equilibrium exists; however, rationale behind the protective nature is quite different in HTHC conditions. The phase stability diagrams of Cr-S-O and Al-S-O shown in figure 19 at  $900^\circ\text{C}$  are quite useful in interpreting their HTHC behavior.  $\text{Cr}_2\text{O}_3$  may dissolve as  $\text{CrO}_2^-$  and  $\text{CrO}_4^{2-}$  at low and high oxygen activities as shown by the following reactions,



Similarly,  $\text{Al}_2\text{O}_3$  dissolves as  $\text{AlO}_2^-$  in a basic melt.



At higher temperatures combustion gases containing  $\text{SO}_2$  do not have sufficiently high  $\text{SO}_3$  to cause acidic fluxing, on the other hand in air or in oxygen containing no  $\text{SO}_3$ , basic fluxing is expected to take place. The minimum solubility of  $\text{Al}_2\text{O}_3$  and  $\text{Cr}_2\text{O}_3$  in  $\text{Na}_2\text{SO}_4$  is at  $\log a_{\text{Na}_2\text{O}} \cong -15$ . Rapp [48] indicated that  $\text{Al}_2\text{O}_3$  and  $\text{Cr}_2\text{O}_3$  both exhibit minimum in their solubilities at  $a_{\text{Na}_2\text{O}}/p_{\text{SO}_3}$  observed in the gas turbine atmosphere suggesting protective nature of alloys with  $\text{Al}_2\text{O}_3$  or  $\text{Cr}_2\text{O}_3$  scales. Rapp further proposed that the protective behavior of  $\text{Cr}_2\text{O}_3$  is because of oxygen-pressure-dependence for the basic fluxing. The reaction (25) can be rewritten as



The above reaction results in consumption of dissolved  $O_2$  and  $O^{2-}$  in the melt. This reaction also increases acidity of melt due to formation of  $SO_3$ . Two cases resulting from the consumption of dissolved  $O_2$  and  $O^{2-}$  that creates positive solubility gradient of the chromate ions. Therefore consumptive re-precipitation of  $Cr_2O_3$  in the salt deposit does not occur. These two simplified transient-state cases for thick and thin salt layers are described here. In case of thick salt layer dissolved  $O_2$  diffuse at much slower rate. As  $CrO_4^{2-}$  is formed,  $O_2$  and  $O^{2-}$  are consumed at the  $Na_2SO_4$ /oxide interface resulting in a positive gradient of both  $PO_2$  and  $O^{2-}$ . From the above reaction a positive solubility gradient of  $CrO_4^{2-}$  is also produced in the salt deposit as shown in figure 20. In case of thin salt layer, due to continuous and fast transport of dissolved  $O_2$  the supply of  $O^{2-}$  to the oxide/salt interface limits the reaction. Formation of  $CrO_4^{2-}$  at the oxide/salt interface decreases  $[O^{2-}]$ . A positive solubility gradient of  $CrO_4^{2-}$  is produced in the salt deposit and no fluxing occurs. This condition is shown in figure 21. The basic dissolution reaction of  $Al_2O_3$  in presence of  $Na_2SO_4$  can be rewritten in the following manner,

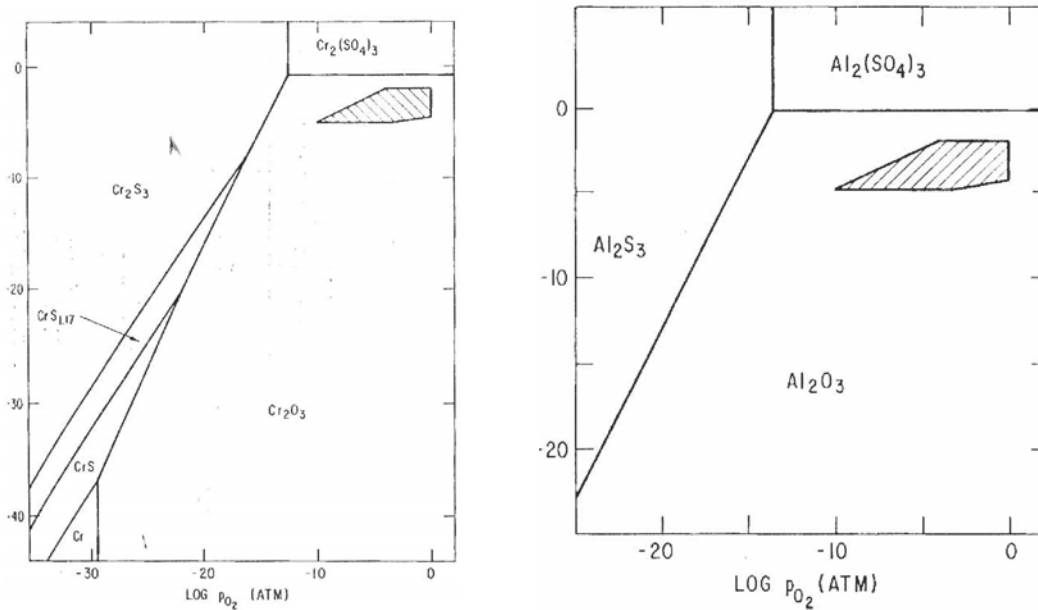
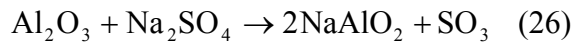


**Figure 19.** Phase stability diagram of Cr-S-O and Al-S-O at 700°C. The hatched region shows thermodynamically calculated phase region in  $O_2 + (2\%SO_2+SO_3)$  gas [50].

The above reaction involves only  $O^{2-}$  as an oxidant, hence dissolved  $O_2$  has no effect on the solubility of  $Al_2O_3$ . Consumption of  $O^{2-}$  at the oxide/salt interface produces positive solubility gradient of  $AlO_2^-$  in the salt deposit. This condition is similar to the transient stage shown for  $Cr_2O_3$  in figure 21.

NiO is more susceptible towards basic fluxing than Cr and Al oxides. The reason for this is explained here. NiO undergoes basic dissolution in the following manner,



The above basic fluxing reaction of NiO is similar to Cr (reaction 23) and Al (reaction 24) oxides but consumes  $O^{2-}$  to a lower extent. In a thin salt layer, due to less consumption of  $O^{2-}$  it is difficult to create and maintain positive gradient of  $O^{2-}$ . The conditions in gas turbine are such that a negative gradient of  $O^{2-}$  is formed resulting in negative solubility gradient of  $NiO_2^-$  in the salt layer (figure 13).

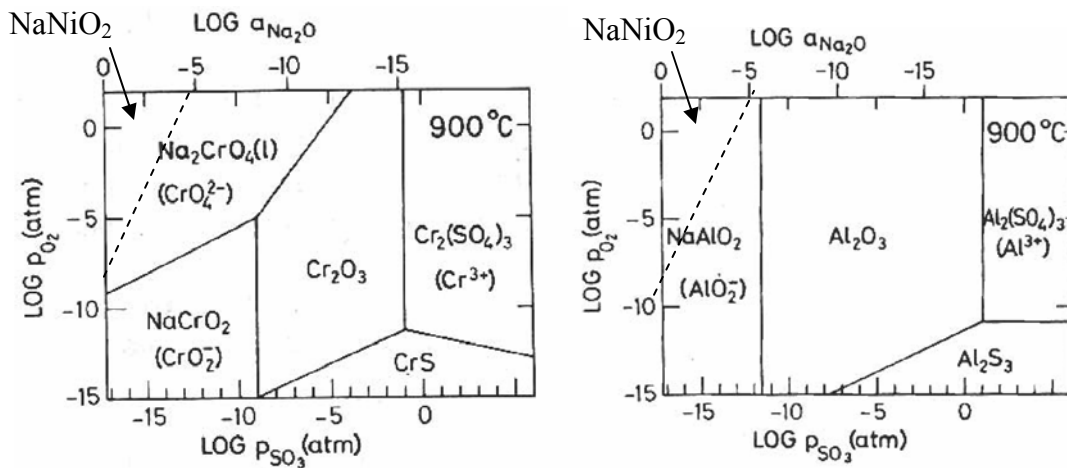


**Figure 20.** Phase stability diagram of Cr-S-O and Al-S-O at 900°C. The broken line shows stable region of  $NaNiO_2$  ( $NiO_2^-$ ) [39].

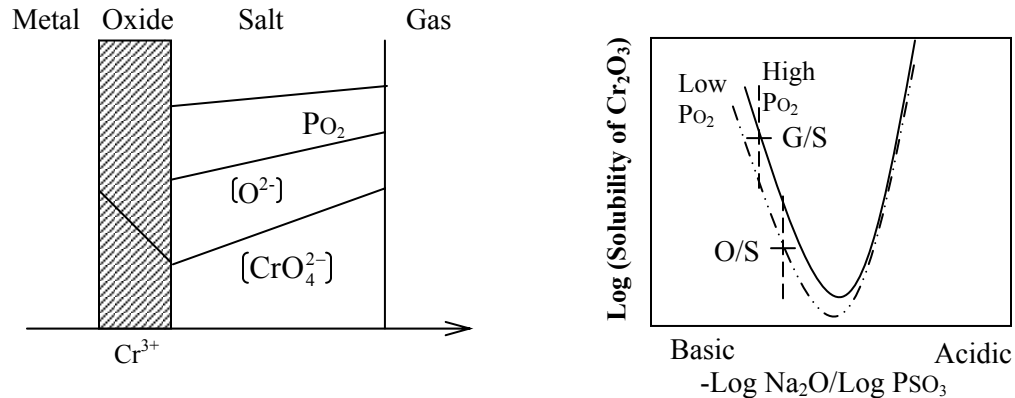


**Figure 21.** In thick salt layer, consumption of  $O_2$  at the oxide/salt interface results in positive oxide solubility gradient, hence no fluxing occurs.

### 2.3.7 Hot Corrosion Degradation Sequence

Hot corrosion rate of an alloy changes with time. Pettit and Meier [1] proposed that hot corrosion follows two stages of degradation, an initiation followed by a propagation stage. A schematic representation of hot corrosion degradation sequence is shown in figure 22. Pettit and Giggins [60] using weight-change kinetics and microstructural analysis showed that hot corrosion underwent a marked change with increase in severity. Hot corrosion resistance for an alloy is often provided by a protective reaction product formation. Initiation stage is slow and involves formation of an oxide scale which would have been formed in the absence of salt deposit; while propagation mode is more catastrophic and involves fluxing or complete breakdown of an oxide barrier. Hot corrosion resistance depends on the extent of protection provided by the protective reaction product thereby prolonging initiation stage and by inhibiting propagation stage. Hot corrosion degradation sequence proceeds by replacing the protective product with a less protective reaction product.

#### 2.3.7.1 Initiation Stage of Hot Corrosion

An alloy forms various oxides during initiation stage and a competition exists for the formation of continuous oxide layer. Under equilibrium conditions, the most stable and slow growing oxide scale is established at the oxide/metal interface. In a gas turbine engine application most alloys form  $Al_2O_3$  and/or  $Cr_2O_3$  as a protective TGO scale. Consequently,

an established protective reaction product offers resistance to the growth of various fast growing external oxides and to the salt penetration. It avoids direct contact between the alloy surface and the salt deposit thereby delaying initiation stage. The composition of a protective layer depends on the chemical composition of the alloy itself. The initiation stage begins in a very similar to the transient oxidation without salt deposit and is also quite similar for both HTHC and LTHC. As the initiation stage progresses, salt deposit begins to affect the reaction product beneath the salt deposit. Initiation stage is evident when some time is lapsed before deposit can form a non- protective reaction product. In HTHC, Cr and Al are sufficiently depleted below subsurface level thus allowing oxide scale to be penetrated. The breakdown of a protective scale is often associated with the transport of secondary oxidant through the scale.

The mechanisms by which secondary oxidant penetrates the oxide scale is not clear. The secondary oxidants could penetrate through pores and cracks present in the oxide scale. Singh and Birks [61] have shown that lattice diffusion could not establish a sufficient sulfur activity to form sulfides below TGO scales. However, Kim *et al.* [62, 63] observed sulfur penetrating through the oxide grain boundaries in pre-existing  $\text{Cr}_2\text{O}_3$  and  $\text{Al}_2\text{O}_3$  scales with no evidence of cracks and pores in the scale. The breakdown of  $\text{Cr}_2\text{O}_3$  and  $\text{Al}_2\text{O}_3$  is possible in high sulfur pressure atmospheres due to developments of sulfide channels through the scales [64, 65]. The initiation stage ends when salt or sulfur penetrates protective scale by forming sulfide particles beneath the scale. This stage is usually more evident for HTHC than LTHC. In LTHC conditions the initiation stage continues by the reaction between external Ni or Co oxides and the solid  $\text{Na}_2\text{SO}_4$  forming eutectic  $\text{Na}_2\text{SO}_4 + \text{MSO}_4$  (where M is Ni or Co) liquid. This reaction is faster in Co-based alloys leading to smaller initiation time compared to Ni-based alloys. It is also possible that the initiation stage may not visibly exist in some alloys with poor hot corrosion resistance. Consequently, degradation directly goes into the propagation stage when molten deposit comes in contact with such alloys. Alloys which are unable to develop a continuous and protective layer of  $\text{Cr}_2\text{O}_3$  or  $\text{Al}_2\text{O}_3$  in the presence of a salt deposit have poor hot corrosion resistance. The duration over which the scale provides protection against hot corrosion is influenced by a number of factors listed below [1, 60]:

1. Alloy composition
2. TGO-reaction product composition and thickness
3. Alloy processing
4. Gas composition
5. Salt composition and its physical state
6. Salt deposition flux
7. Temperature
8. Thermal cycles
9. Erosion
10. Specimen geometry
11. Thickness of the salt scale
12. Pre-oxidation treatment

#### 2.3.7.2 Propagation Stage of Hot Corrosion

Hot corrosion rates are much larger in the propagation stage and the alloy must be replaced from service at this stage. Various types of propagation modes are evident through the microstructural features. The propagation stage proceeds when reactants from the gas diffuse through the deposit or elements from alloy dissolve and diffuse out at the salt/gas interface [1 and 60]. Diffusion of reactants through the deposit often changes composition and such changes play an important role in various types of propagation modes [1]. A reaction between deposit and metal/oxide forms a non protective reaction product during propagation mode. Non-protective reaction product formation is often due to fluxing of an oxide in the molten salt. Fluxing mechanisms have already been discussed in the previous sections.

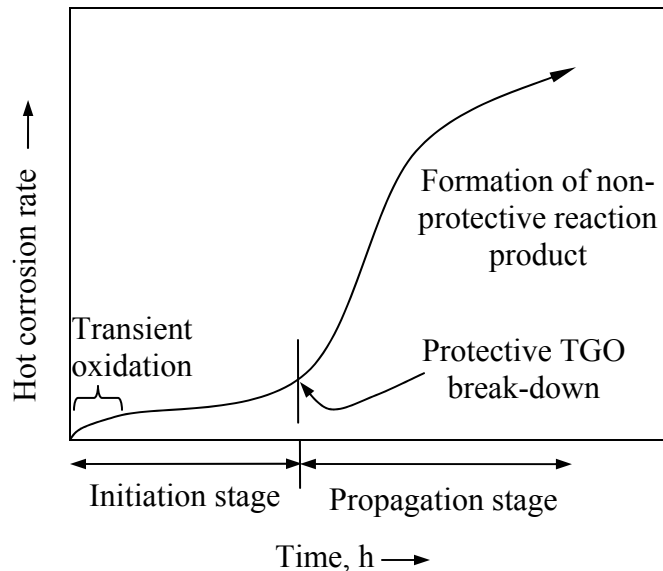


**Figure 22.** Schematic representation of hot corrosion degradation sequence.

### 2.3.8 Hot Corrosion of Pt-modified Alloys/Coatings and MCrAlY-Based Coatings

The hot corrosion resistance of coatings often depends on chemical composition, microstructure, and deposition method. Hot corrosion resistance of aluminide coatings is improved by the addition of modifying elements like Pt [66, 67], Cr [68, 69] and Si [70]. Platinum addition has been found to improve HTHC and oxidation resistance of  $\beta$ -NiAl coatings [66, 67, 71, 72]. Indeed, addition of Pt tends to reduce surface spallation by promoting the slow growth of extremely adherent  $\alpha$ - $\text{Al}_2\text{O}_3$  scale [67]. Haynes *et al.* [73] and Zhang *et al.* [24] found that, along with improved scale adhesion, Pt also helped in decreasing detrimental effects of high S levels in the substrate and reducing the amount of voids at the scale/metal interface. The hot corrosion resistance of Pt-modified  $\beta$ -NiAl coating depends upon the substrate and their behavior has been studied on various substrates by researchers over the past 30 years. Addition of Cr has been shown to improve hot corrosion resistance of aluminide coatings at both low and high temperatures [68, 69]. In addition, Cr can be beneficial by decreasing the amount of Al in the alloy required to form a protective  $\text{Al}_2\text{O}_3$  scale layer [17]. Malush *et al.* [74] and Dust *et al.* [75] found that Cr+Pt modified aluminide coatings exhibited excellent hot corrosion resistance. The MCrAlY overlay

coatings have optimum composition and have excellent hot corrosion resistance. The CoCrAlY-based coating is known to have relatively good resistance to high-temperature HTHC; however, their low-temperature LTHC depends upon the Cr content [52]. Luthra [52, 76] showed that Cr-rich CoCrAlY coatings have better LTHC resistance than conventional CoCrAlY coatings. The NiCrAlY and NiCoCrAlY are other types overlay coatings often used in gas-turbine engines and hot corrosion resistance of these coating was previously studied by the number of researchers [77, 78]. Hot corrosion resistance of various commercial and developmental coatings will be studied and compared in this thesis.

#### **2.4 Oxidation Behavior of Pt-Modified Ni-Based Alloys and Coatings: An Overview**

The effect of alloying addition on the oxidation behavior of Ni-Al system relevant to this proposal will be discussed in detail in this section. Aluminide coatings are used to improve high-temperature oxidation resistance of Ni-based and Co-based superalloys by forming thermally grown protective oxide scale. The addition of platinum group metals (PGM) such as Pd [21], Ir [22] and most commonly Pt [23, 24, 71, 72] to  $\beta$ -NiAl promotes the formation of thin, continuous, and adherent  $\alpha$ -Al<sub>2</sub>O<sub>3</sub> scale. Although Pt has been known to improve oxidation performance of  $\beta$ -NiAl diffusion-aluminide coatings the exact mechanisms by which it helps are unclear. Jackson *et al.* [79] and Schaeffer *et al.* [80] found Pt-enrichment at the surface of the alloy and proposed that Pt retarded the diffusion of refractory elements from the substrate. Recently, Cadoret *et al.* [81, 82] reported increased growth rate of an oxide scale with Pt addition during the initial stages of oxidation of  $\beta$ -NiAl alloys. It was found that transition from  $\theta$ -Al<sub>2</sub>O<sub>3</sub> to  $\alpha$ -Al<sub>2</sub>O<sub>3</sub> was delayed in the presence of Pt leading to thickening of an oxide scale before the transformation. The researchers proposed that prolonged transition favored the relaxation of stresses and slow growth of alumina scale during the transient oxidation. This is attributed to the increase in the Al diffusion in the alloy, thus promoting the oxide growth and limiting the formation of interfacial cavities. In fact, Gleeson *et al.* [8] recently showed using the ternary diffusion couples that the interdiffusion coefficient for Al in its own concentration gradient  $D_{AlAl}$  increases with increasing Pt content.

Both the groups found that Pt improved the alumina scale adherence in  $\beta$ -NiAl and  $\gamma+\gamma'$  alloys.

The beneficial effect of Pt in  $\gamma+\gamma'$  was studied in detail and ascribed that Pt is non-reactive and decreases the chemical activity of aluminum [8]. Pt partitions solely to Ni sites in ordered  $L1_2$  crystal structure of  $\gamma'$  thereby increasing the Al:Ni atom fraction. The Al enrichment at the surface kinetically favors the alumina formation. The short-term oxidation studies by Hayashi *et al.* [83] further showed that Pt-containing  $\gamma'$ -based alloys show subsurface Pt-enrichment thus promoting alumina formation. The beneficial effect of Pt was also seen at lower temperatures around 700°C and 900°C and during transient oxidation [83].

Other ternary alloying additions such as Si and Ti additions promote alumina scale formation in NiCrAlY-based coatings [84]. The beneficial effect of Si on the cyclic oxidation behavior of aluminide coatings was also observed by other researchers [85]. The amount of critical concentration required to form a protective scale in binary alloys can be decreased by additions of elements that form oxide of intermediate thermodynamic stability to the oxides of the elements present in the binary alloy. For instance, it is well known that with additions of Cr in M-Al (where M = Ni, Co or Fe) alloys lower amount of Al is needed to establish and maintain an alumina scale. This phenomenon is known as third element effect or gettering effect [17]. Brumm and Grabke [86] also showed that  $\text{Cr}_2\text{O}_3$  formed during initial stages of oxidation acts as nuclei for the formation of  $\alpha$ - $\text{Al}_2\text{O}_3$ . However, the addition of Cr to NiAl is reported to accelerate  $\theta$ - $\text{Al}_2\text{O}_3$  to  $\alpha$ - $\text{Al}_2\text{O}_3$  phase transformation and leads to higher  $k_p$  values [86]. Pint *et al.* [87] observed that Cr additions up to 10at% in Hf containing NiAl alloys resulted in the faster scale growth as well as scale spallation. Phillips and Gleeson [88] also showed that higher Cr additions were detrimental for the oxidation resistance of NiAl alloys. Unfortunately, higher Cr additions are quite beneficial for improving hot corrosion resistance which led the researchers to conclude that high-temperature oxidation and hot corrosion resistance are not possible to achieve at least in  $\beta$ -NiAl [89].

It is generally known that segregation of sulfur impurities at the oxide/alloy interface significantly decreases the oxide adherence [90, 91]. It has been also observed that detrimental effects of S can be reduced by addition of Pt or by the additions of reactive elements such as Zr, Y, and Hf [18]. Pint *et al.* [19, 20] reported that the addition of 0.05at%

Hf to  $\beta$ -NiAl results in slowest-growing and most adherent alumina scale observed in  $\beta$ -NiAl and proposed that Pt additions in the  $\beta$ -NiAl may be unnecessary with the correct amount of reactive element-Hf additions.

The oxidation behavior of  $\beta$ -NiAl aluminide coatings can be influenced by various factors. Al present in the coating diffuses from the coating into the substrate and also diffuses out to maintain  $\text{Al}_2\text{O}_3$  scale effectively depleting Al in the coating. A recent study by Pint [92] showed the beneficial effect of Pt and Hf for various levels Al in Ni-Al system. However, lower Al ( $> 34.7\text{at } \%$ ) containing alloys ( $\beta+\gamma'$ ) without Pt addition experienced higher mass gain indicating the formation of Ni-rich oxides.

The beneficial effect of Pt in  $\beta$ -NiAl is very well known and the work by Coupland *et al.* [93, 94] and Tatlock *et al.* [95-97] showed that Pt also improves oxidation and hot corrosion resistance of alloys with  $\gamma+\gamma'$  compositions. Felten [98] studied the effect of Pt with Cr addition in low Al (12 at.%) based  $\gamma+\gamma'$  alloys and showed that these alloys were indeed alumina formers. A very recent study of the Ni-Pt-Al system with Hf additions by Gleeson *et al.* [8] led to the foundation for the novel  $\gamma+\gamma'$  coatings as an alternative to  $\beta$ -NiAl aluminide coatings. These authors showed that certain unique Ni-Al-Pt-based alloy compositions, which are sufficiently low in aluminum content (20-22 at%) to be free of  $\beta$ -NiAl, are excellent candidates for the development of novel coatings (and bond coats) that confer significantly improved component oxidation performance. Specifically, was been found that Pt-containing  $\gamma'$ - $\text{Ni}_3\text{Al}+\gamma$ -Ni alloys modified with up to 2.0 wt.% Hf form highly adherent, planar, slow-growing  $\alpha$ - $\text{Al}_2\text{O}_3$  scales during both isothermal and cyclic oxidation at high temperature (maximum temperature studied thus far has been  $1150^\circ\text{C}$ ). Moreover, the presence of platinum in the alloys decreases the thermodynamic activity of aluminum to the extent that it is below the aluminum activity in common Ni-base superalloys used for aero-engine turbine applications. As a consequence, and in complete contrast to  $\beta$ -NiAl-containing coatings, aluminum diffuses from the substrate alloys to the novel  $\gamma'+\gamma$  coating compositions. This is a significant development in that the novel coating compositions offer the combined beneficial properties of (1) forming a slow-growing, planar and adherent TGO scale of  $\alpha$ - $\text{Al}_2\text{O}_3$ , (2) not depleting in aluminum due to coating/substrate interdiffusion during

service, and (3) being compatible with a superalloy substrate in terms of phase constitution and, hence, coefficient of thermal expansion. Figure 23 (a) compares the 1150°C cyclic oxidation kinetics of bulk alloys of the following Pt-modified alloys:  $\beta$ -NiAl (50 at.% Al),  $\gamma'$ -Ni<sub>3</sub>Al+ $\gamma$ -Ni (22 at.% Al), and Hf-modified  $\gamma'$ -Ni<sub>3</sub>Al+ $\gamma$ -Ni (22 at.% Al). It is seen that the  $\beta$  alloy (based on the commonly used bond coat composition) underwent weight loss, which is indicative of TGO spallation, while the better performing  $\gamma'+\gamma$  alloys did not show notable evidence of scale spallation. The performance of the Pt+Hf-modified alloy is particularly superior, undergoing minimal weight gain and, therefore, an exceptionally slow rate of TGO scale thickening. The TGO scales that formed on the  $\gamma'+\gamma$  alloys with and without Hf addition were found to be an adherent, continuous, compact and planar layer of  $\alpha$ -Al<sub>2</sub>O<sub>3</sub>. In the same figure 23 (b) the best performing Hf-modified  $\beta$ -NiAl (Ni-50Al-0.05at% Hf) data by Pint *et al.* [99] is compared. An almost similar weight gain is observed for the best performing Pt+Hf-modified  $\gamma'$ -Ni<sub>3</sub>Al+ $\gamma$ -Ni (Ni-22Al-30Pt-1wt%Hf) and Hf-modified  $\beta$ -NiAl (Ni-50Al-0.05at% Hf).

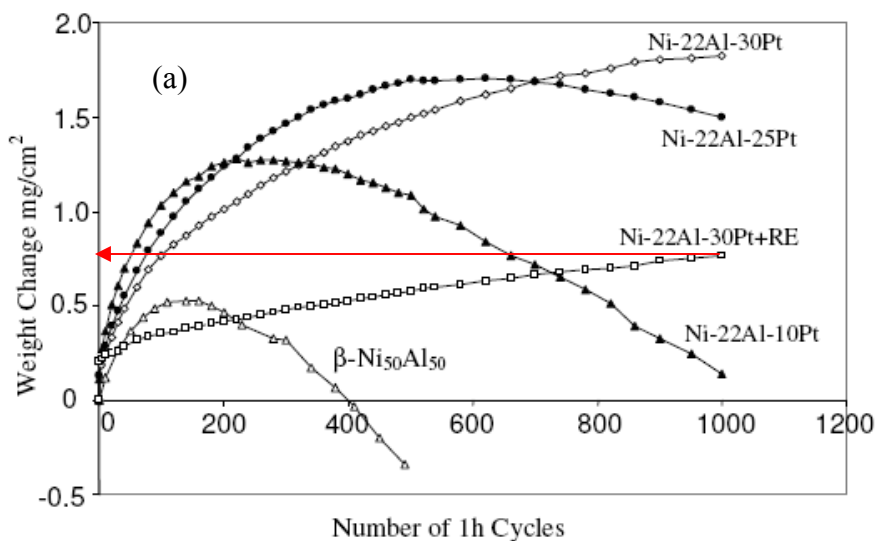


**Figure 23.** Comparison of cyclic oxidation behavior of (a) modified  $\gamma'$ -Ni<sub>3</sub>Al+ $\gamma$ -Ni [8] (carried out in air) and (b) modified  $\beta$ -NiAl [99] (carried out in flowing O<sub>2</sub>) both at 1150°C.

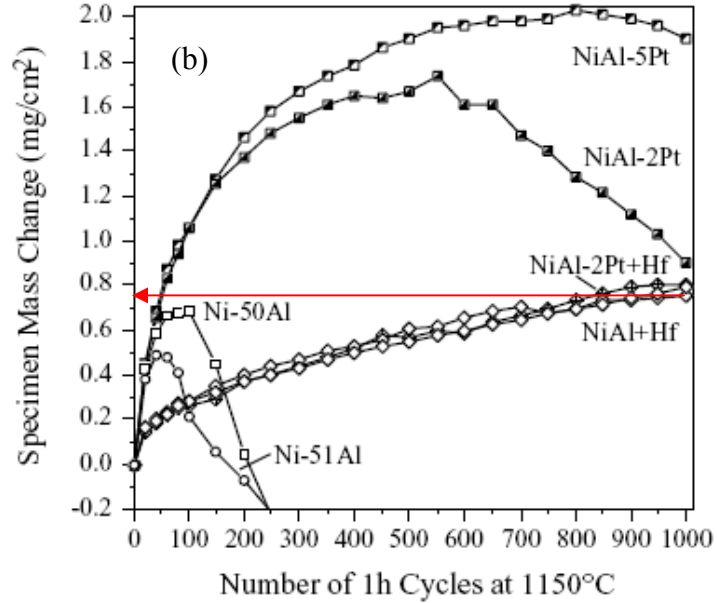


**Figure 23.** Continued.

Zhang *et al.* [100] studied and compared oxidation behavior of Pt-modified  $\gamma'+\gamma$  coating with the Pt-modified  $\beta$ -NiAl coating and found slightly better performance within the  $\beta$ -NiAl(Pt) coatings; however, it was inferred that minor element variations (*e.g.* sulfur and refractory metals) exacerbated the poorer performance of the  $\gamma'+\gamma$  coatings. Hot corrosion resistance of Pt(+Hf)-modified  $\gamma'+\gamma$  coatings will be evaluated in this thesis.

## 2.5 Aims of Research

The primary objective of this research is to gain fundamental understanding of the hot corrosion behavior of novel  $\gamma'+\gamma$  coating compositions. The specific goals of the research are summarized as follows:

1. To assess the hot corrosion behavior of commercially available Pt-modified  $\beta$ -NiAl aluminides and CoCrAlY coatings for marine gas turbine engine components on a case-by-case basis and rank their performance against both types of hot corrosion.
2. To confirm the reliability of Dean rig testing by comparing the results with the burner rig hot corrosion testing, which is often purported to better simulate the actual operating conditions in gas turbine engines.
3. The proposed study seeks to determine and even improve the hot corrosion resistance (HTHC and LTHC) of novel  $\gamma'+\gamma$  coating compositions with the alloying additions of Pt, Cr, and Si. It also includes effects of pre-oxidation to further improve hot corrosion resistance. As a part of this research various modified  $\gamma'+\gamma$  coating compositions were also examined for high temperature oxidation behavior under isothermal and cyclic conditions.
4. A novel  $\gamma'+\gamma$  coating compositions having optimum resistance to both types of hot corrosion and oxidation will be proposed from this study.
5. Finally, hot corrosion resistance of diffusion based Pt+Hf modified  $\gamma+\gamma'$  coating developed at ISU using pack-cementation process will be tested and compared with commercially available diffusion based Pt-modified  $\beta$ -NiAl coating and MCrAlY coatings.

### 3. EXPERIMENTAL APPROACH

Hot corrosion tests were conducted on various commercially available coatings and modified developmental  $\gamma+\gamma'$  bulk alloys and coatings. The laboratory-scale testing rig referred to as a “Dean rig” was used for hot corrosion testing. It consists of two temperature zones: a hot end where the  $\text{Na}_2\text{SO}_4$  salt is heated above its melting temperature and evaporates into atmosphere and a cool end where the salt condenses on the test specimens. The kinetics and extent of the salt-induced attack were monitored by measuring weight change, surface loss or extents of attack, and maximum depth of penetration as a function of time. In a separate set of oxidation tests, alloys were exposed to air under thermal-cycling conditions at  $1150^\circ\text{C}$  for up to 500 h. Each cycle consists of one-hour exposure at high temperature, rapid cooling to room temperature and then raising to the oxidation temperature again. Cyclic oxidation kinetics will be determined on the basis of weight change. More specific details of the tests are provided in the following section. The hot corrosion and oxidation results would be combined to down-select and guide the establishment of modified  $\gamma+\gamma'$  coating compositions and structures having optimum resistance to high-temperature degradation.

#### 3.1 Materials: Alloys and Coatings

The various commercially available coatings tested for hot corrosion resistance were provided by Roll-Royce Corporation, USA. The bulk alloys of  $\gamma\text{-Ni}+\gamma'\text{-Ni}_3\text{Al}$ ,  $\beta\text{-NiAl}$ , and  $\gamma\text{-Ni}+\beta\text{-NiAl}$  in phase constitution were drop-casted at the Materials Preparation Center, Ames Laboratory. The developmental  $\gamma\text{-Ni}+\gamma'\text{-Ni}_3\text{Al}$  coatings were deposited here at Iowa State University by a proprietary Al+Hf co-deposition process. More details of the alloys and coatings used in this study are provided in each chapter as they were studied.

#### 3.2 High Temperature (Type I) Hot Corrosion Dean-rig Testing

An alumina tray (5 x 4 cm) was used for holding the test samples. Just prior to hot-corrosion testing, the samples were placed on a hot plate or in furnace at  $200^\circ\text{C}$  and a

saturated solution of sodium sulfate was dropped on the samples using an eyedropper. The target salt deposition was 2-3 mg/cm<sup>2</sup>. A comparable salt deposit level has been used in many previous studies [66, 69, 74].

The Dean rig [101] for hot-corrosion testing consists of a hot zone where a salt reservoir is heated above its melting point and a cooler zone downstream where the evaporated salt condenses onto the test specimens. A carrier gas of O<sub>2</sub>-0.1%SO<sub>2</sub> is passed through a platinized honeycomb catalyst to form an equilibrium amount of SO<sub>3</sub> which, in turn, stabilizes the salt activity. The controlled atmosphere provides conditions that are close to those found in a gas turbine. The experimental aspects of the Dean rig for HTHC testing are summarized in figure 24.

A horizontal, three-zone laboratory furnace with 4.5 cm ID alumina tube was specifically used for the Dean rig at ISU. The three temperature zones were set at 1070, 890 and 910°C to establish the hotter and cooler zones. The furnace conditions were such that the cooler and hotter zones were each about 10 cm in length. A measured thermal profile along the length of the furnace is also shown in figure 24. An alumina sample tray was kept in the cooler zone at 900°C and a 10 cm long alumina boat containing pure Na<sub>2</sub>SO<sub>4</sub> was kept in the hotter zone at ~ 1040°C. The equilibrium melting temperature of sodium sulfate is 884°C, so that the salt is indeed liquid in the hotter zone. Samples were then cooled to room temperature after every 20 hours of exposure and then re-sprayed with salt at 125°C. Samples were weighed after each 20 hour cycle before salt spraying. The weight gain after corrosion also includes salt replenishment after each cycle. No attempts were made to retain any corrosion product that may have spalled during cooling to room temperature or handling. The weight of the salt crucible was measured after each 20 hour cycle and it was found that ~ 0.025 g of salt vaporized during each 20 hour cycle. Experiments were also carried out to determine the amount of salt that condensed on the samples in the 900°C zone, but the weight change was too small to be of any significance, *i.e.*, <0.1 mg/cm<sup>2</sup> after five 20-hour cycles. The HTHC experiments were carried out for 100 hours of total exposure. An additional set of HTHC tests were conducted in which all the specimens were pre-oxidized in a box furnace at 1100°C for 80 hours and then furnace cooled to room temperature. These pre-oxidized specimens were also tested for HTHC resistance.

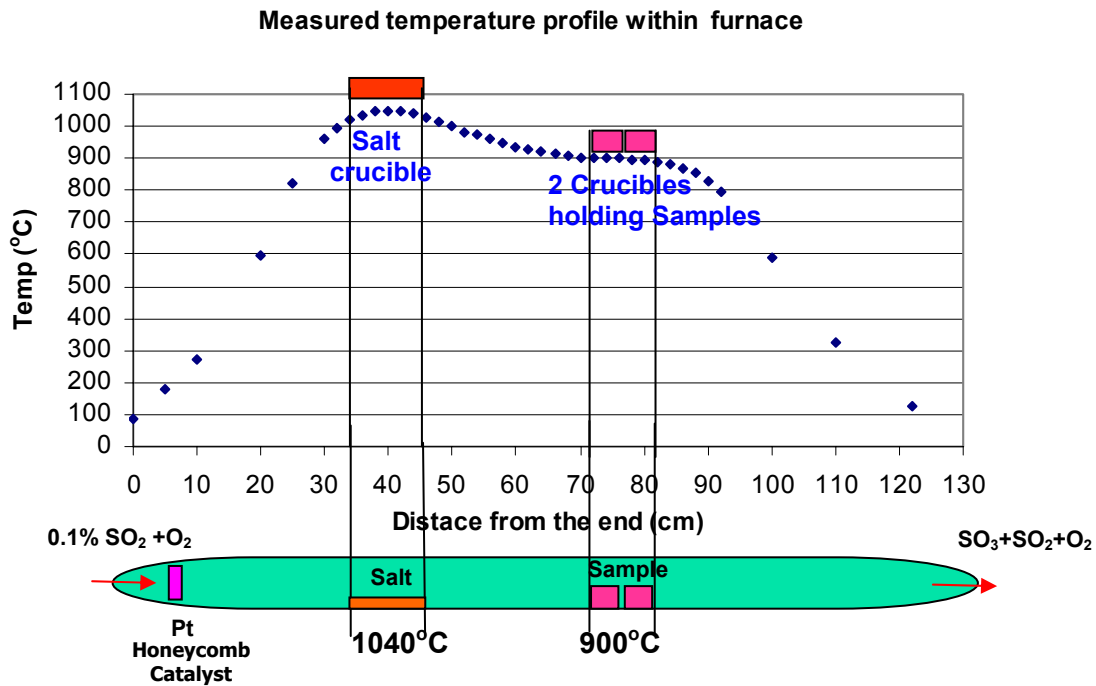


**Figure 24.** Temperature profile and positions of salt and sample crucibles for HTHC in the three-zone furnace. The three zones were set at 1070, 890 and 910°C.

### 3.3 Low Temperature (Type II) Hot Corrosion Dean-rig Testing

The same experimental procedures were followed for LTHC testing, with the settings of the three furnace zones now giving a 10 cm long hotter zone and a 5 cm long cooler zone. The hotter zone was above 900°C (so that the sodium sulfate was molten) and the cooler zone was at 705°C. The 5 cm cooler zone for LTHC testing could only accommodate one alumina sample tray. The sample positions were also changed for LTHC in comparison to the positions for HTHC. The measured thermal profile along the furnace length for LTHC was similar in shape to the one shown for HTHC testing (figure 25). An additional set of LTHC tests were conducted in which all the specimens were pre-oxidized in a box furnace at 1100°C for 80 hours and then furnace cooled to room temperature. The LTHC experiments were carried out for 100 hours of total exposure.

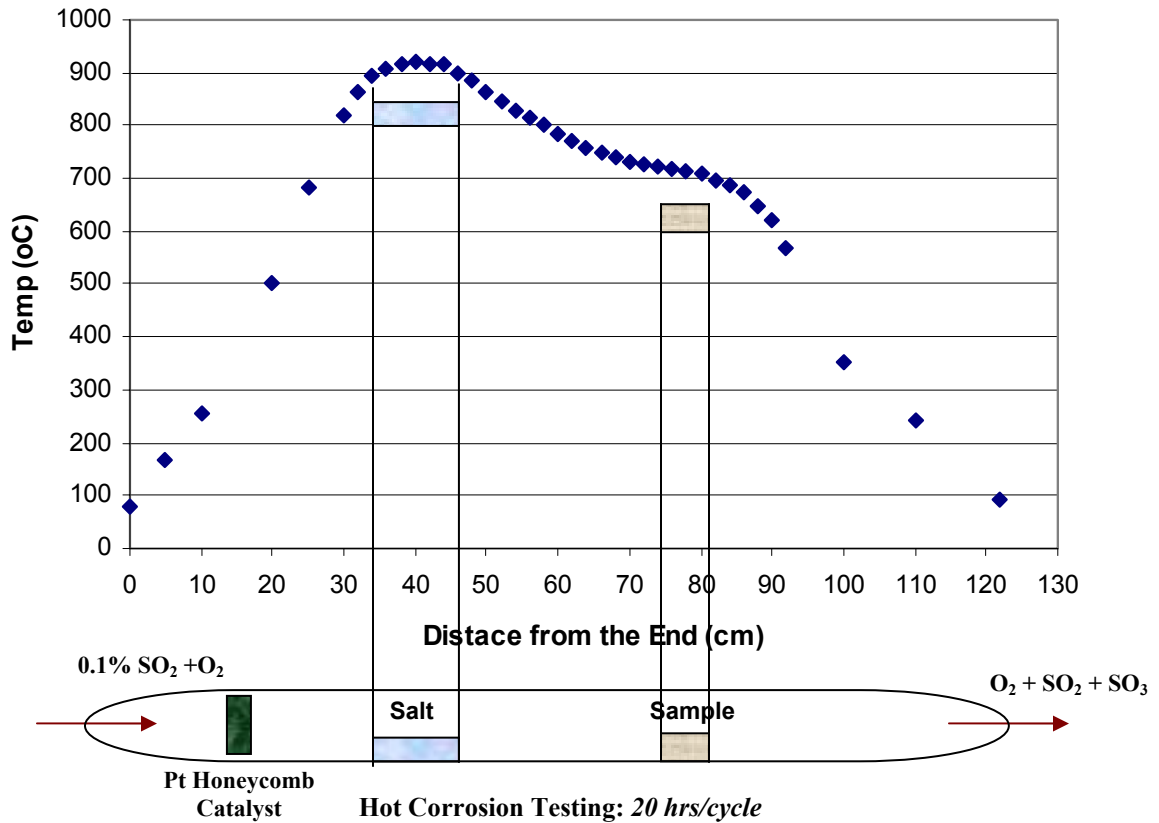


**Figure 25.** Schematic of experimental set-up and measured temperature profile within the furnace for the hot corrosion testing at 705°C.

### 3.4 Isothermal and Cyclic Oxidation Testing

Isothermal oxidation tests were carried out at 1150°C in still air for 100 hours using a horizontal furnace. All test samples were air-cooled to room temperature at the completion of testing. Cyclic oxidation tests were carried out at 1150°C in still air using vertical furnace. Each cycle consisted of one hour at 1150°C followed by 30 minutes at ~75°C. Sample weight change was measured using an analytical balance after every 2 cycles for the first 20 cycles and then intermittently thereafter. No attempt was made to retain any scale that may have spalled during cooling to room temperature or handling. As a consequence, weight loss kinetics were observed in some cases.

### 3.5 Characterization and Analysis

Digital macro images of the test samples were taken after each 20-hour cycle of hot corrosion and oxidation. After the completion of a requisite number of 20-hour cycles, the corroded and oxidized specimens were sectioned, mounted, and prepared for microscopic examination using standard metallographic techniques. Use of water or water-based products was avoided for the hot-corroded test specimens during sectioning and sample preparation procedures in order to avoid affecting the corrosion product or the salt build-up on the surface. XRD, SEM and EDS were used for characterizing the corroded and oxidized samples. An electron probe micro-analyzer (EPMA) with wavelength dispersive spectrometry (WDS) was also used for analyzing alloy and corrosion/oxidation product phases.

Each corroded pin sample was sectioned at two positions for characterization of the hot corrosion attack. One section was taken 4-5 mm from the bottom and the other 3-4 mm from the top of a given sample. A Hitachi S-2460N VP SEM/EDS was used in the back-scattered electron (BSE) imaging mode for the characterization and analysis. All images were taken at 20 keV. Both the extent of attack and the maximum depth of penetration were measured from SEM images. The extents of attack were categorized as follows: if depth of penetration over a given length (*i.e.*, arc) of the coating/substrate was between 0-25  $\mu\text{m}$  it was designated as low corrosion; if it was between 25-60  $\mu\text{m}$  it was medium corrosion; and if it was more than 60  $\mu\text{m}$  it was high corrosion. The three different extents of attack are summarized schematically in figure 26. After defining arc lengths for the different extents of attack, the arc angles from the centre of the image were determined. These angles were then added for low, medium and high extents of corrosion. The same procedure was conducted for both cross-sections and an average was taken for each extent of attack to arrive at a percentage. The maximum depth of penetration into the coating/substrate was also recorded from any of the two cross-sections using SEM images taken at magnifications of 100 and 1000. Cross-sectional X-ray dot maps were collected from corroded areas of the specimens to gain insights on the elemental distribution and the phases present in the corrosion products. X-ray point counts were also obtained from corroded areas to confirm the dot map results. In this report only X-ray dot maps results are presented.

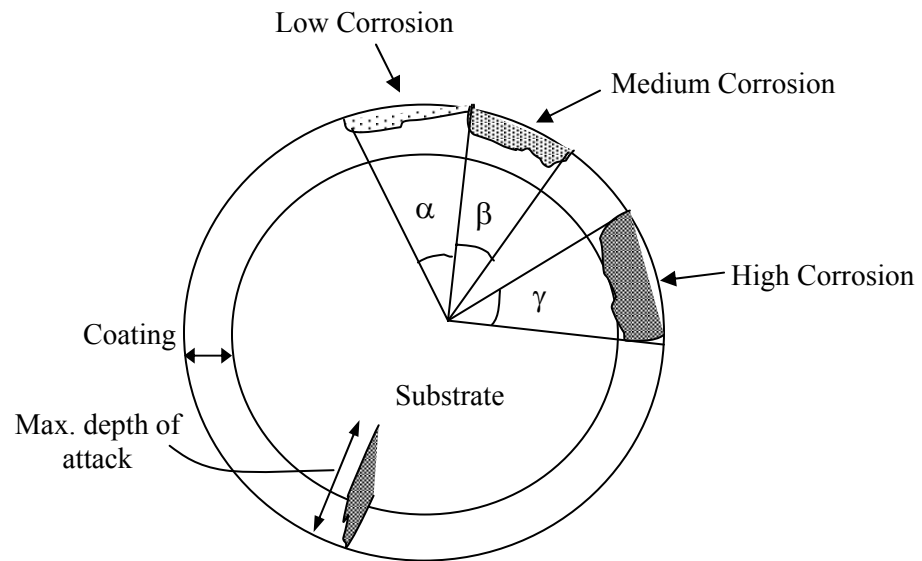


**Figure 26.** A schematic cross-section of corroded specimen showing extents of different extents of attack, which subtend an angle for measurement.

## 4. HOT CORROSION BEHAVIOR OF COMMERCIAL METALLIC COATINGS

### 4.1 Comparative Study of Low- and High-Temperature Hot Corrosion Resistance of Various Aluminide Coatings

This study compares and ranks the HTHC (900°C) and LTHC (705°C) HC resistance of various candidate metallic coatings for the marine gas turbine engine components. The metallic coatings used in this study were different types of Pt-modified  $\beta$ -NiAl and  $\gamma$ + $\beta$ -CoCrAlY coatings on Ni-based superalloy substrates. The baseline overlay CoCrAlY and diffusion  $\beta$  coatings were applied on substrates of the MAR-M 247 (superalloy 247) and IN 792 (superalloy 792). The nominal compositions of these alloys (in wt. %) are given in Table 2.

**Table 2.** Nominal composition (wt. %) of superalloy substrates used in this study.

Alloy	Ni	Cr	Co	Ti	W	Al	Nb	Mo	C	Zr	B	Ta	Hf
Superalloy 792	60	13	9	4.2	4	3.2	2	2	0.2	0.1	0.02	-	-
Superalloy 247	59	8	10	1	10	5.5	-	0.7	0.15	-	-	3	1.5

The CoCrAlY coating was deposited via physical vapor deposition (PVD) to an actual vane airfoil made of superalloy 792. The composition of this coating was fairly uniform; however, the coating thickness varied along the length of the airfoil. Specifically, the coating on the upper portion of the airfoil was much thinner than the bottom (*i.e.*, 15  $\mu\text{m}$  compared to 56  $\mu\text{m}$ ). The bottom-thick and upper-thin portions shall be identified CoCrAlY 1 and CoCrAlY 2, respectively.

In the case of the aluminide coatings, the superalloy 247 and 792 substrates were in the form of pins, 3.1 mm in diameter, 80 mm long and domed at one end. The Ni-rich aluminide 1 and Ni-rich aluminide 2 coatings were standard Pt-modified  $\beta$ -NiAl diffusion

coatings. Al-Pt-rich aluminide and Ni-rich aluminide 3 were also Pt-modified  $\beta$ -NiAl coatings, but deposited using a proprietary commercial process. The Ni-rich aluminide coatings 1 and 2 on superalloys 247 and 792 were both quite smoother (*i.e.*, similar in appearance to a  $\sim 6 \mu\text{m}$  finish) while the Al-Pt-rich aluminide and Ni-rich aluminide 3 coatings were comparatively rough (*i.e.*, similar in appearance to a 400 grit finish). The average chemical composition of each as-received coating was measured via energy dispersive spectroscopy (EDS) analysis and the results are summarized in Table 2. The measured thickness of each coating is also given in this table. The domed end of each pin was coated while 5-10 mm of the other end was uncoated. The coated portions of the pins were sectioned into  $\sim 12$  mm pieces for hot corrosion testing. The CoCrAlY-coated vane airfoils were 30 mm long and were sectioned into 5 mm wide samples. To avoid direct exposure to the corrosive environment, uncoated ends of the pin test samples were covered with alumina cement. For the same reason, the uncoated cut sides of the CoCrAlY-coated samples were covered with alumina cement prior to testing.

**Table 3.** Coating composition of the tested coupons.

<b>Alloy</b>	<b>Coating</b>	<b>Measured Average Composition (at. %)</b>
superalloy 792	Al-Pt-rich aluminide (60-65 $\mu\text{m}$ )	44Al-10Pt-4Cr-4Co-Bal Ni
superalloy 247	Ni-rich aluminide 1 (60-65 $\mu\text{m}$ )	36Al-7Pt-4Cr-6Co-Bal Ni
superalloy 792	Ni-rich aluminide 2 (60-65 $\mu\text{m}$ )	35Al-9Pt-6Cr-5Co-Bal Ni
superalloy 247	Ni-rich aluminide 3 (60-65 $\mu\text{m}$ )	37Al-7Pt-4Cr-5Co-Bal Ni
superalloy 792	CoCrAlY 1(Thick $\sim 56 \mu\text{m}$ )	Co-27Cr-18Al-7Ni-0.1Y
superalloy 792	CoCrAlY 2 (Thin $\sim 15 \mu\text{m}$ )	Co-27Cr-18Al-7Ni-0.1Y

#### 4.1.1 High Temperature Hot Corrosion Results (900 °C)

The various coated samples were tested at 900°C (HTHC) for 100, 200 and 500 hours, with a cool-down and salt application after every 20 hours. Digital macro and SEM images of Al-Pt-rich aluminide, Ni-rich aluminides 1 and 2 and CoCrAlY coatings 1 and 2

after 500 hours of total exposure are shown in figures 27-30. The test specimens exposed for shorter times (100h, 200h) were also attacked in similar manners, but to a lesser extent. For the sake of clarity whilst maintaining representative analysis, only the 500 h SEM images are shown and only semi-quantitative results of the extents of attack after 200 h HTHC will be compared. In general, a considerable amount of corrosion product was found in each coating type. The results of the semi-quantitative analyses of the extents of corrosion are summarized in the form of histograms in figures 31 and 32 for 200 and 500 hours of exposure, respectively. Ni-rich aluminide 1 was better after 100h, but more attack was noted after longer times (200 and 500 hours) when compared to Ni-rich aluminide 2.

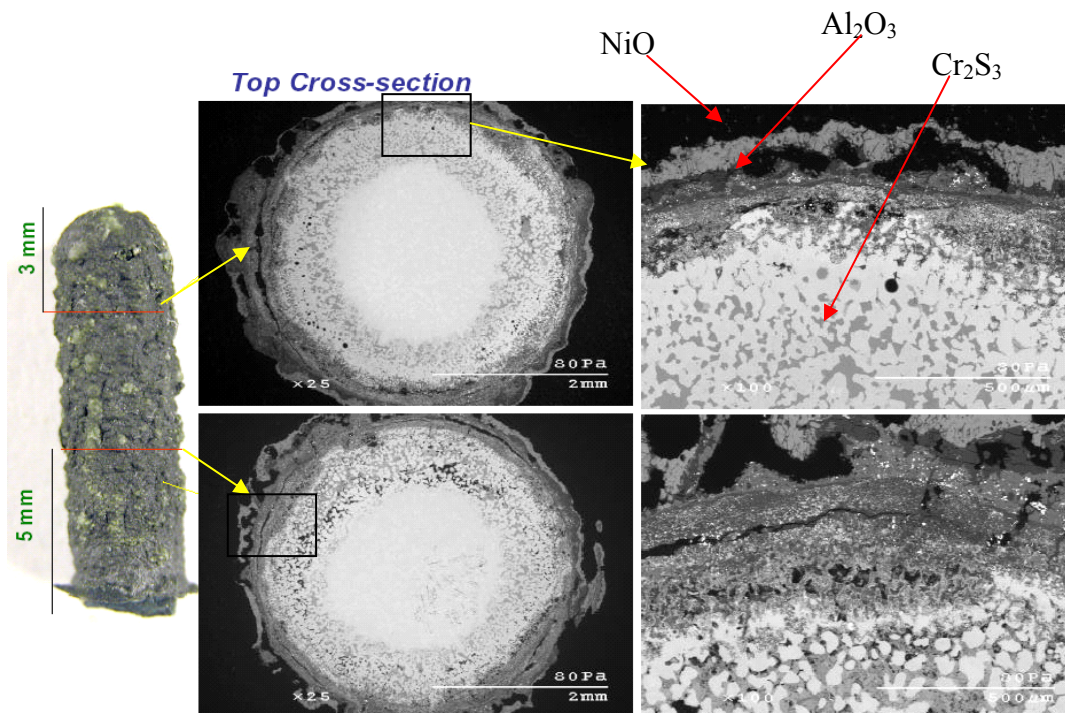


**Figure 27.** Cross-sectional SEM images of Ni-rich aluminide 1 after 500 hours of HTHC testing at 900°C.

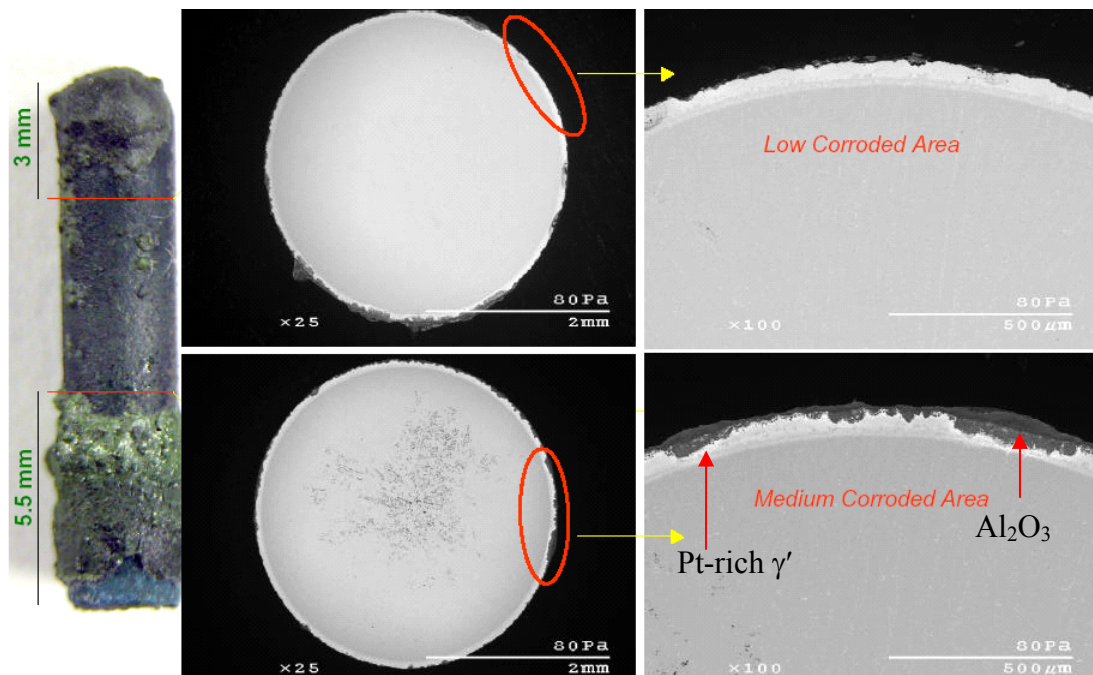


**Figure 28.** Cross-sectional SEM images of Al-Pt-rich aluminide after 500 hours of HTHC testing at 900°C.

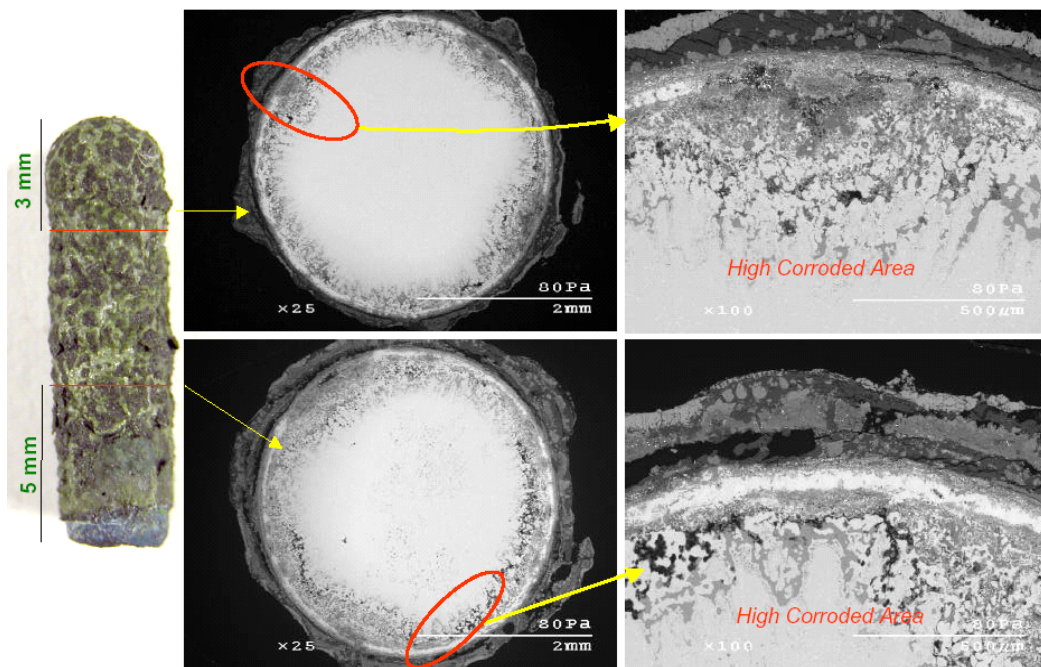


**Figure 29.** Cross-sectional SEM images of Ni-rich aluminide 2 after 500 hours of HTHC testing at 900°C.

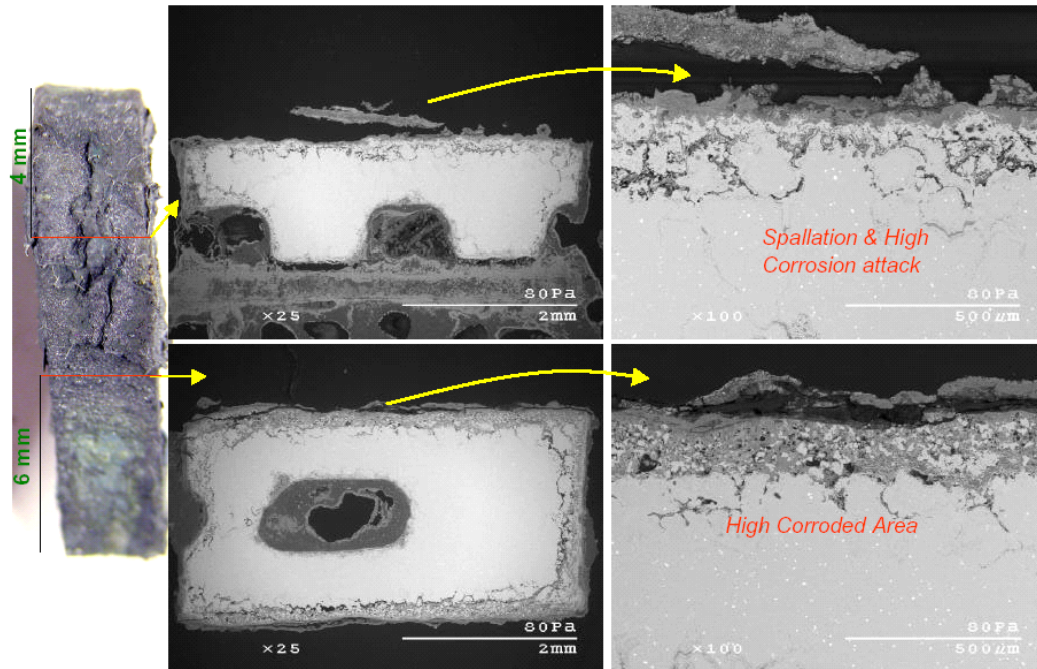


**Figure 30.** Cross-sectional SEM images of CoCrAlY's 1 and 2 after 500 hours of HTHC testing at 900°C.

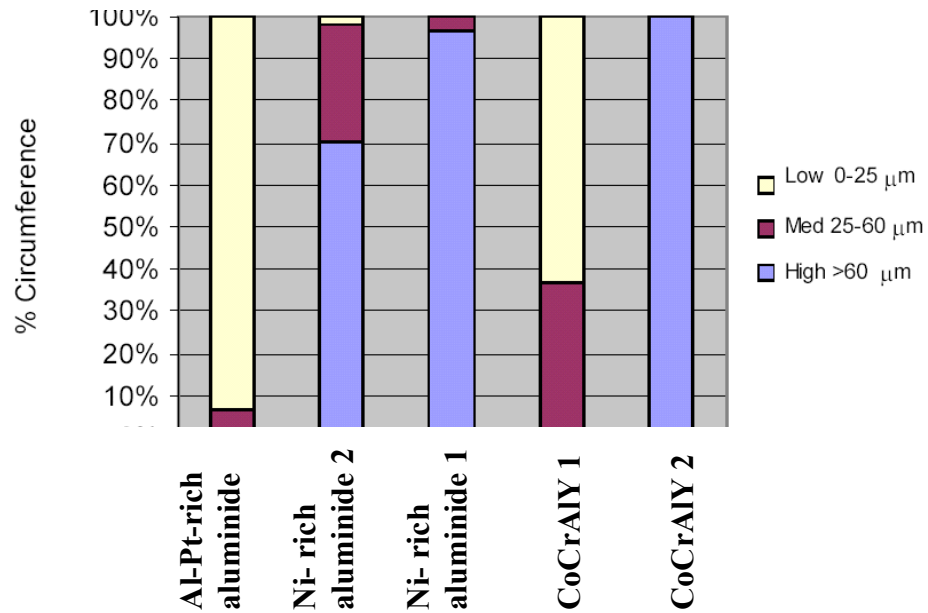


**Figure 31.** Extents of attack at 900°C (HTHC) along specimen circumference of untreated samples after 200 hours of exposure.

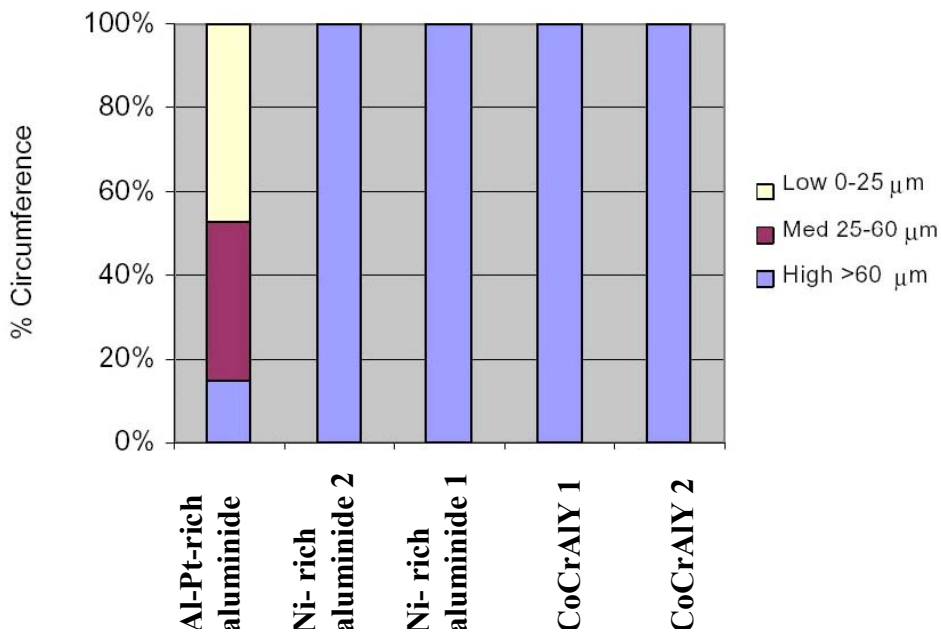


**Figure 32.** Extents of attack at 900°C (HTHC) along specimen circumference of untreated samples after 500 hours of exposure.

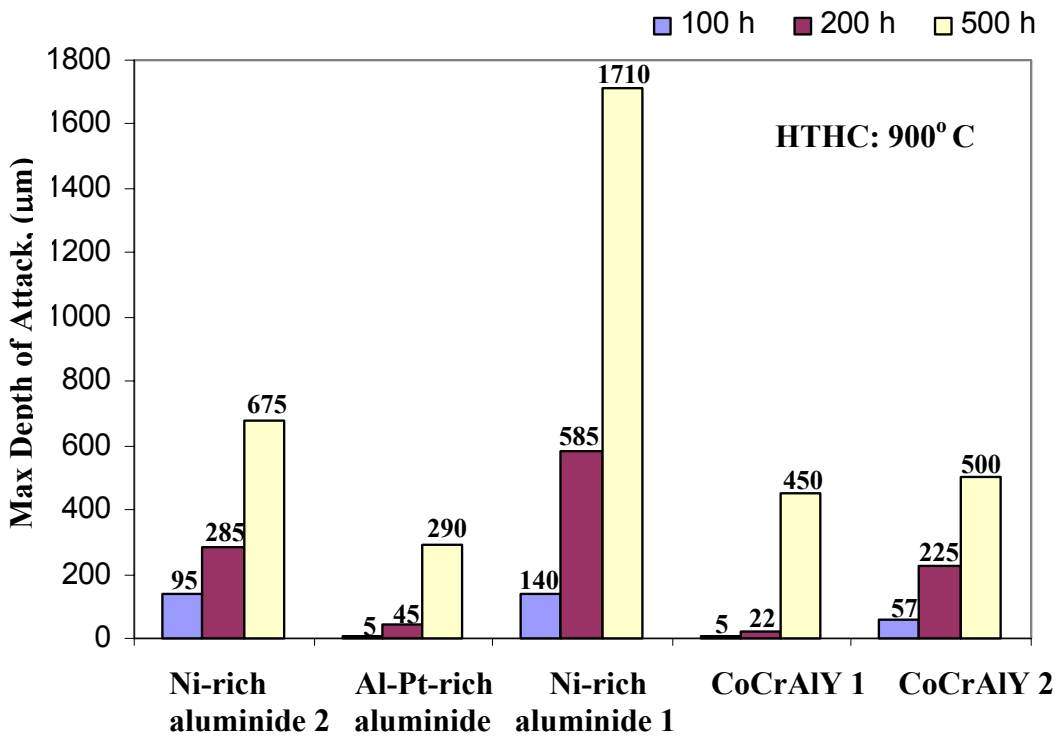


**Figure 33.** Maximum depth of attack on coating and substrate during HTHC (900°C) testing.

The Al-Pt-rich aluminide and CoCrAlY 1 coated samples showed superior resistance after 100 hours of testing; whereas the CoCrAlY 2 coating was extensively attacked and the Ni-rich aluminides 1 and 2 showed varying levels of all three extents of attack (low, medium and high). With regards to Ni-rich aluminides 1 and 2, the 100 and 200 h results, together with maximum depth of attack measurements (figure 33), suggest that the superalloy 792 substrate confers greater corrosion resistance to this coating than the superalloy 247 substrate. This is at least partly attributable to compositions being different on the different substrates. Specifically, it is believed that the higher HTHC resistance of the Ni-rich aluminide 2 on superalloy 792 substrate for longer times can be partly ascribed to the higher chromium content (13 wt.%) in superalloy 792 compared to superalloy 247 (8 wt.%). Also superalloy 247 has a higher content of the refractory elements W and Ta, which promote topologically closed packed (TCP) phase formation. Such phase formation is detrimental to the oxidation and hot corrosion resistance of the alloy [102]. It is further noted that superalloy 792 would be intrinsically more resistant to HTHC due to its higher Cr content compared to 247. After 500 hours of exposure Ni-rich aluminides 1 and 2 and CoCrAlY's 1 and 2 were heavily attacked. Only the Al-Pt-rich aluminide exhibited regions of remaining coating, with approximately 50% of the cross-sectional circumference undergoing low (0-25  $\mu\text{m}$ ) attack. The present results clearly show that the Al-Pt-rich aluminide coating (on superalloy 792) was the best amongst the coatings tested. The CoCrAlY 1 coating (on superalloy 792) was susceptible to HTHC attack after longer hours of exposure. The results in figure 33 compare maximum depth of penetration into the coatings after 100, 200 and 500 hours of exposure. These results clearly indicate that Ni-rich aluminide 1 shows deeper penetration into the alloy compared to the Ni-rich aluminide 2 coating; although, both systems were heavily attacked after 500 hours of exposure. These results further confirm that Al-Pt-rich aluminide was the best coating to resist HTHC amongst the coatings tested. To summarize, the order of performance from best to worst coating after 500 hours of testing is as follows: Al-Pt-rich aluminide > CoCrAlY 1 > Ni-rich aluminide 2 > Ni-rich aluminide 1 > CoCrAlY 2.

Ni-rich aluminides 1 and 2 had a lower initial Al content compared to Al-Pt-rich aluminide. Aluminide coatings also deplete in Al during HTHC testing due to formation

of an  $\text{Al}_2\text{O}_3$  scale and coating/substrate interdiffusion. The Al depletion eventually causes the  $\beta$  coating to transform into  $\gamma'$ - $\text{Ni}_3\text{Al}$ . Al-Pt-rich aluminide has a comparatively high Pt (10 at %) content. Higher Pt content helps to form a more planar, adherent and protective  $\text{Al}_2\text{O}_3$  scale. Pint *et al.* [102] indicated that higher Al content within  $\beta$ -NiAl shows better scale adhesion and oxidation resistance. In order to study the effect of Al content in  $\beta$ -NiAl, an additional set of HTHC experiments was carried out on Ni-47Al (at%)-10Pt (at %) and Ni-37Al (at %)-10Pt (at %) bulk alloys. Ni-47Al-10Pt and Ni-37Al-10Pt are similar in composition to the Al-Pt-rich aluminide and the Ni-rich aluminides 1 and 2, respectively.

Mass loss due to HTHC was more from the Ni-37Al-10Pt alloy compared to the Ni-47Al-10Pt. Cross-sectional SEM images of the alloys shown in figure 34 confirm that Ni-47Al-10Pt formed more protective  $\text{Al}_2\text{O}_3$  scale. The coated samples were highly corroded after 500 hours of testing and hence the samples exposed for 100 hours were selected for more detailed elemental analysis (X-ray dot maps and point counts). X-ray dot map of the hot-corroded coating of Al-Pt-rich aluminide after 100 h exposures at  $900^\circ\text{C}$  are shown in figure 35. The dot maps indicate the formation of a relatively thick, non-planar and internally oxidized zone containing oxides rich in Al and Cr, presumably  $\text{Al}_2\text{O}_3$  and  $\text{Cr}_2\text{O}_3$ . Cr- and Ni-rich sulfide precipitates inferred to be  $\text{Cr}_2\text{S}_3$  and  $\text{Ni}_3\text{S}_2$  formed beneath this oxide-containing zone. Pt-rich  $\gamma'$ - $\text{Ni}_3\text{Al}$  was observed within the inner zone of the coating layer below the corroded area. The transformation from  $\beta$ -NiAl to Pt-enriched  $\gamma'$ - $\text{Ni}_3\text{Al}$  was more in the Ni-rich aluminide coatings 1 and 2 compared to the Al-Pt-rich aluminide coating. Also, higher percentages of spinel ( $\text{NiAl}_2\text{O}_4$ ) and NiO oxides were observed within the oxide layer found on the Ni-rich aluminides 1 and 2 than on the Al-Pt-rich aluminide. These results were supported by the EDS point counts.

#### 4.1.2 Comparison Between Dean Rig and Burner Rig testing

Burner rig tests are often purported to better simulate the actual operating conditions in gas turbine engines; however, such a test requires a long running time and tend to be quite costly. The HTHC resistance of test pins was compared between Dean rig results obtained in this study and burner rig test results obtained by Shifler [103]. Cross-sectional SEM images after 100 hours of Dean rig testing and 1000 hours of burner rig testing are

compared in figure 36. HTHC attack seems to be similar in both types of tests, showing formation of a scale consisting of NiO and spinel ( $\text{NiAl}_2\text{O}_4$ ) oxides at the outside and  $\text{Al}_2\text{O}_3$  at the inside. Sulfide precipitates rich in Cr and Ni were also observed in the subsurface regions of the coatings. Cross-sectional SEM images of Al-Pt-rich aluminide after burner rig testing showed comparable results and better performance than Ni-rich aluminide 2. The best to worst performance after 100 hours of Dean rig testing was Al-Pt-rich aluminide > Ni-rich aluminide 1 > Ni-rich aluminide 2. Similar performance was observed for 1000 hours of burner rig testing. Equally as noteworthy is the fact that 100 hours of Dean rig testing and 1000 hours of burner rig testing were insufficient to accurately rank the long-term performance of the coatings. HTHC testing after 200 and 500 hours of exposure in the Dean rig provided the necessary information to rank such performance.

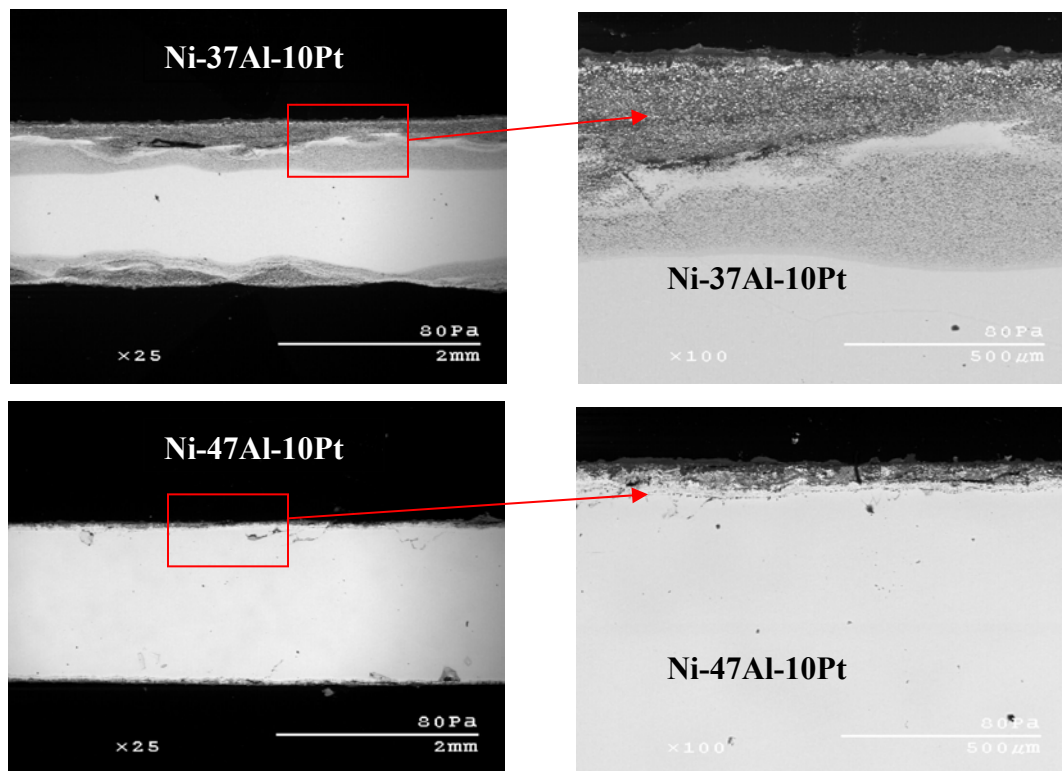


**Figure 34.** SEM images of Ni-37Al (at%)-10Pt (at %) and Ni-47Al (at%)-10Pt (at %) bulk alloys showing effect Al addition on HTHC resistance in  $\beta$ -NiAl coatings.

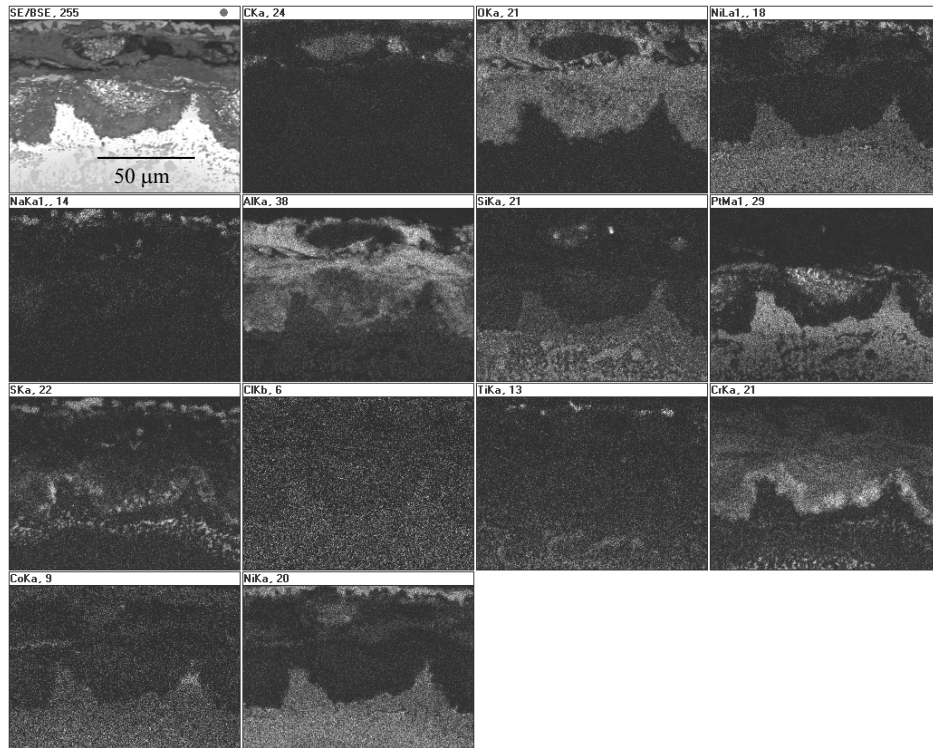


**Figure 35.** X-ray dot maps for Al-Pt-rich aluminide after 200 hours of exposure at 900°C for HTHC testing showing elemental distribution in coating at 1000x.

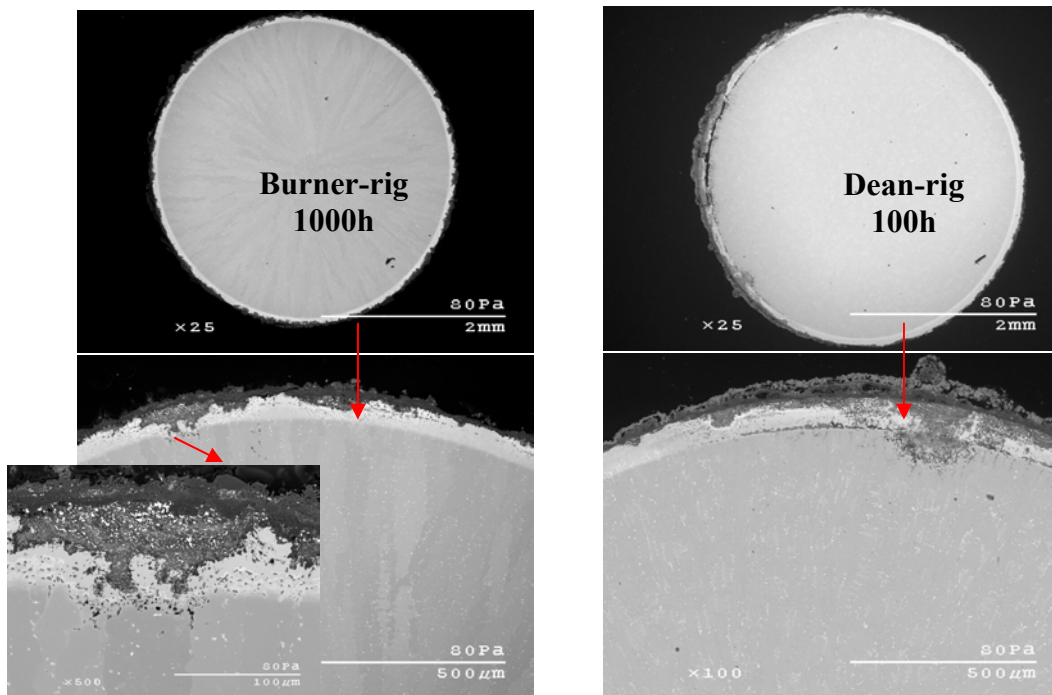


**Figure 36.** Comparison between hot corroded (900°C) Ni-rich aluminide after burner rig (1000h) and Dean rig (100h) testing.

#### 4.1.3 Low Temperature Hot Corrosion Results (705 °C and 750 °C)

Samples with and without pre-oxidation were tested for 100 and 200 hours at 705 and 750°C in 20 hour cycles, as described in the experimental section. Since the melting point of Na<sub>2</sub>SO<sub>4</sub> is 884°C, the samples were covered primarily with solid salt deposit during LTHC testing, as indicated by the digital images in figures 37-40. All of the coatings showed localized hot corrosion attack just after 100 hours of exposure. SEM images of the pre-oxidized samples after 200 hours of LTHC exposure are shown in figures 37-41. LTHC attack was highly localized compared to that observed after HTHC testing. Accordingly, the variable of where the sample cross-section is taken becomes very critical for analysis. Semi-quantitative analysis performed on the untreated and pre-oxidized samples are shown in figures 42, 43. The LTHC resistance increased when the samples were pre-oxidized, as observed from the 100 and 200 hours test results. Coatings on the superalloy 792 substrate showed excellent LTHC resistance when pre-oxidized as compared to coatings on the superalloy 247 substrate. This is believed to be due to the fact that superalloy 792 contains higher Cr content and lower TCP forming elements, *i.e.*, W and Ta.

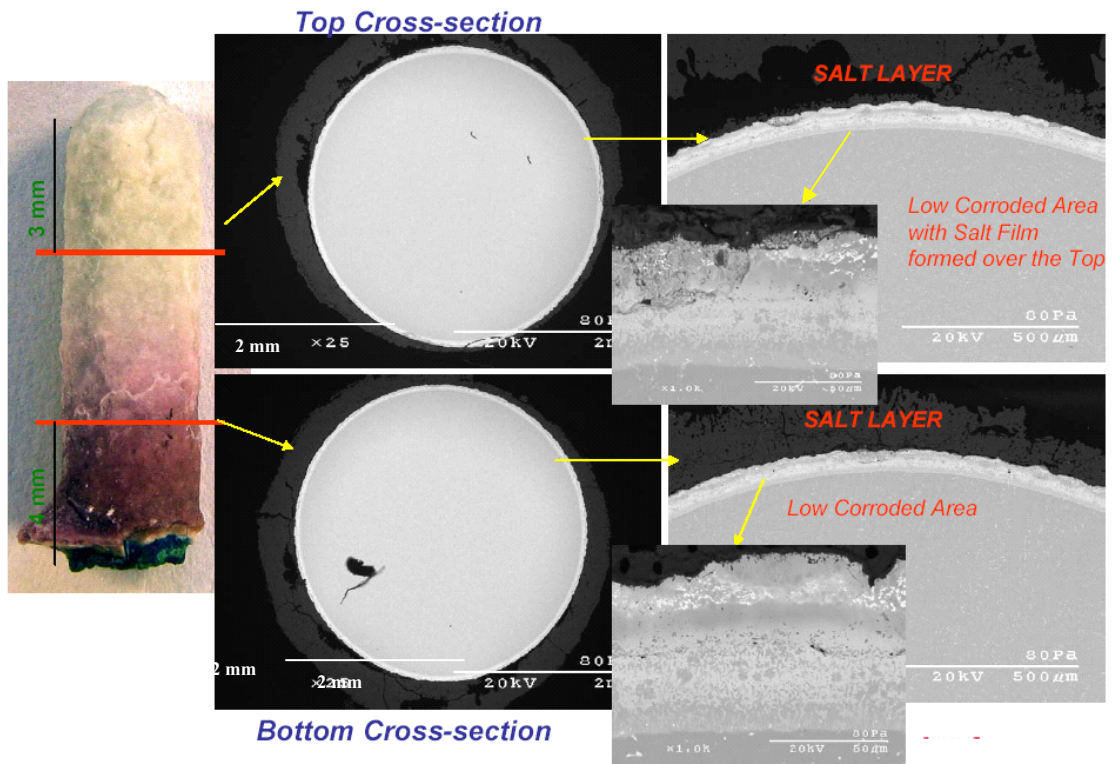


Figure 37. SEM images of pre-oxidized Al-Pt-rich aluminide after 200 hours at 705°C.

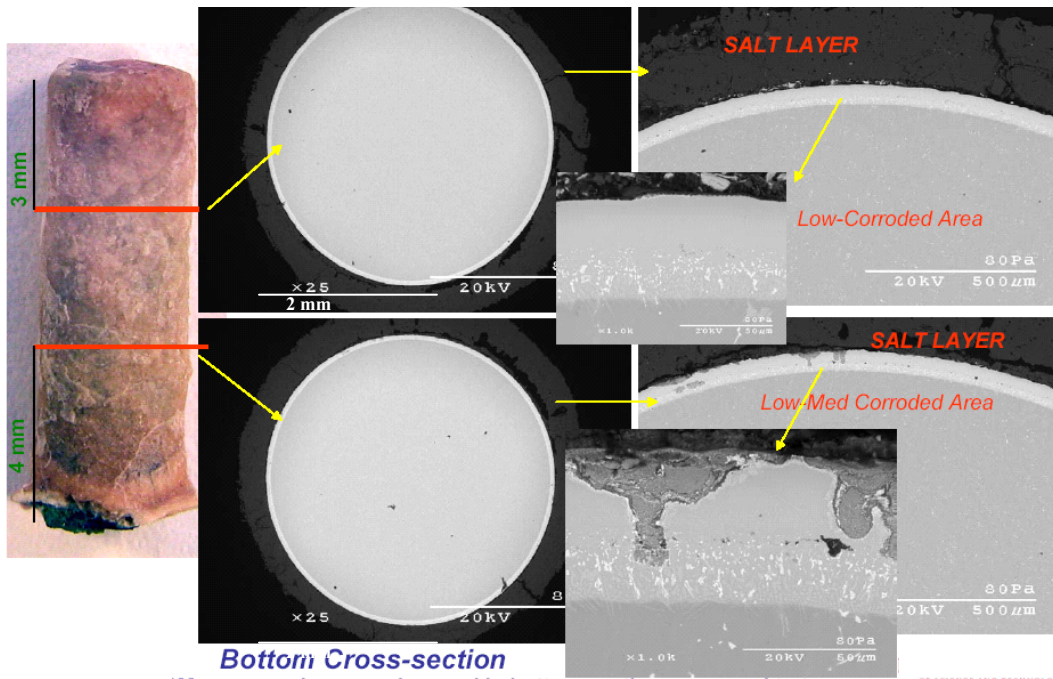


Figure 38. SEM images of pre-oxidized Ni-rich aluminide 2 after 200 hours at 705°C.

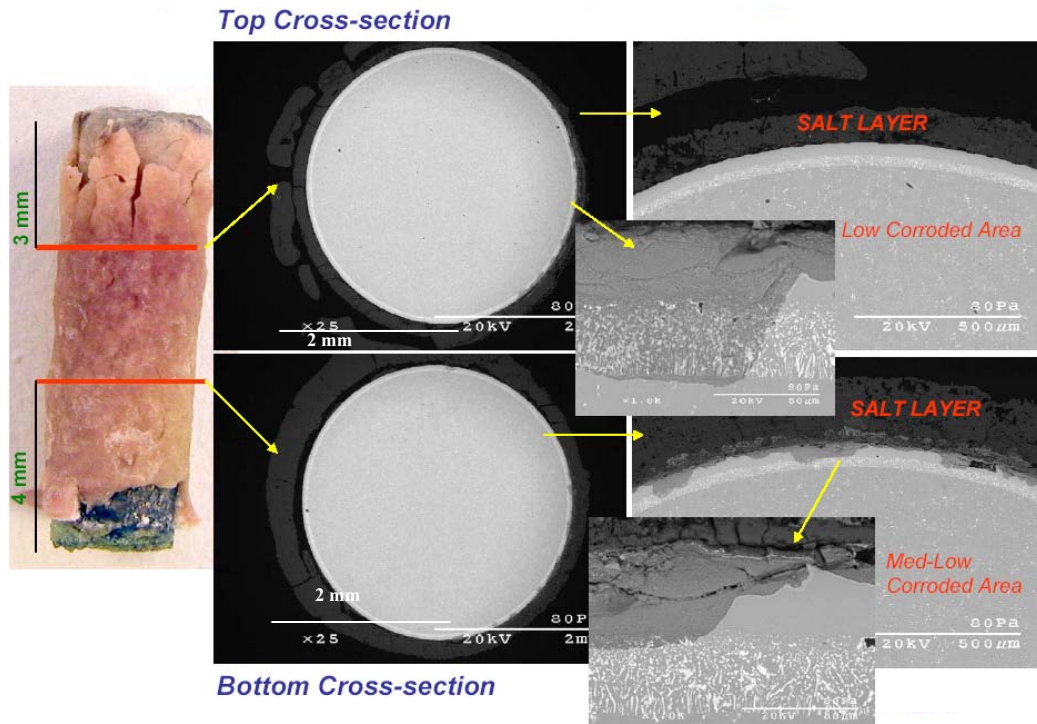


Figure 39. SEM images of pre-oxidized Ni-rich aluminide 1 after 200 hours at 705°C.

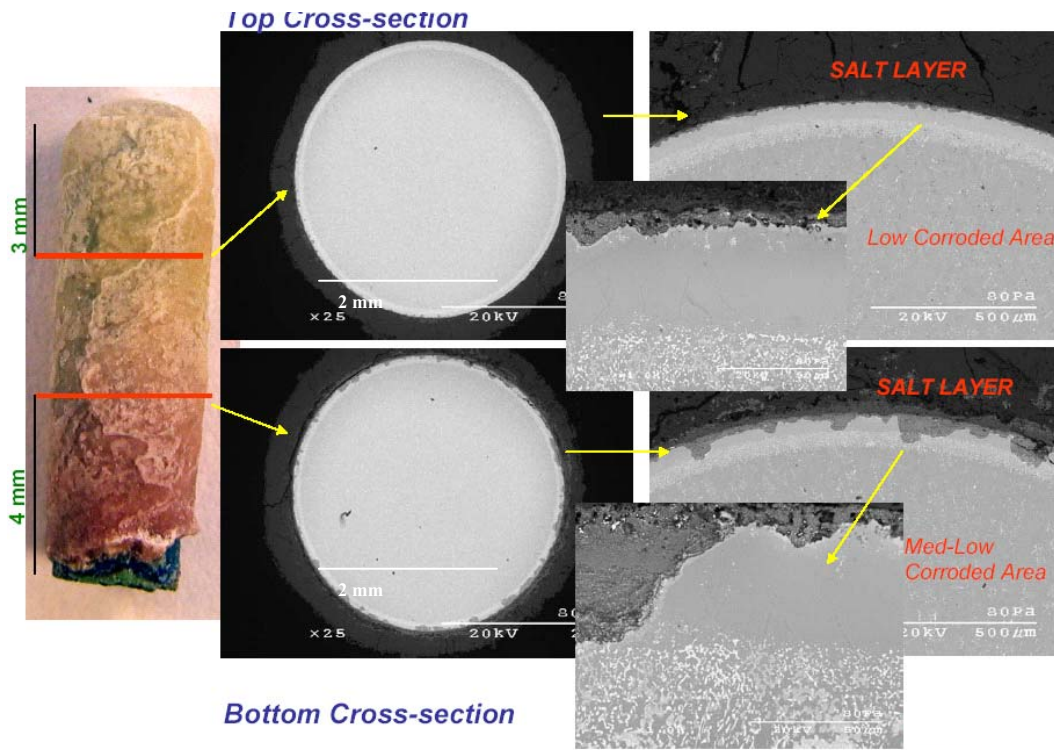
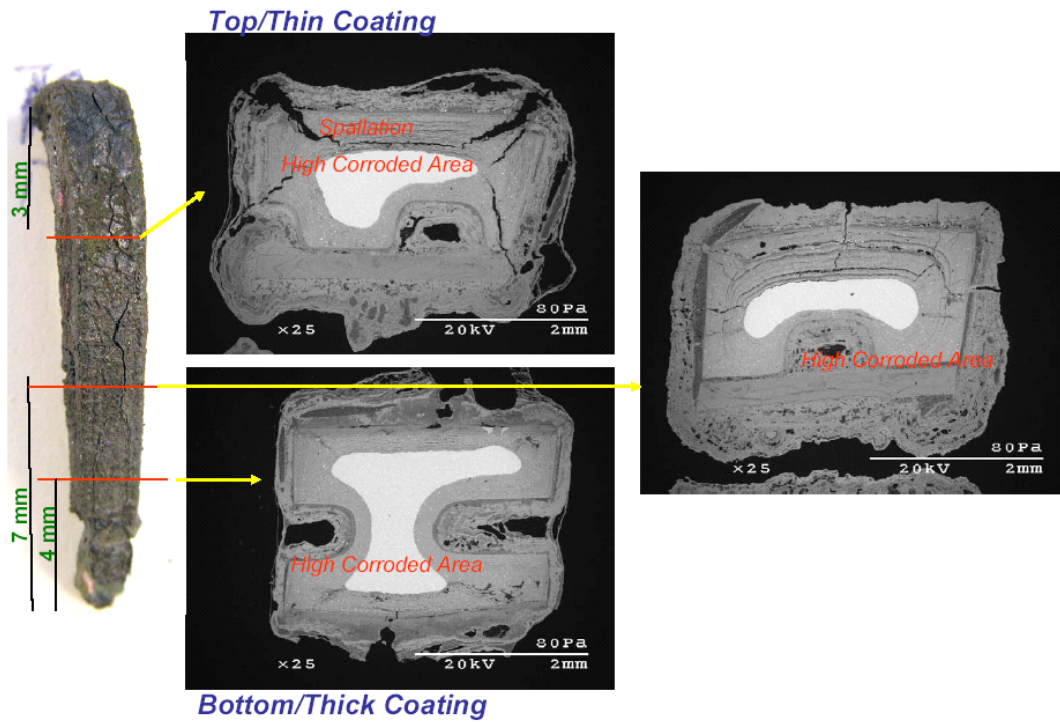
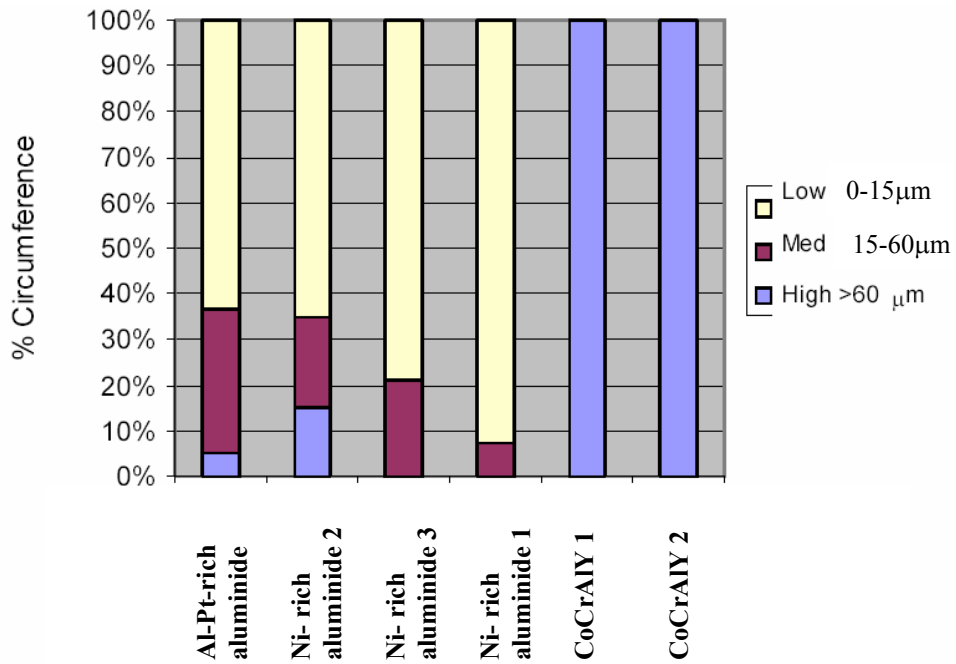


Figure 40. SEM images of pre-oxidized Ni-rich aluminide 3 after 200 hours at 705°C.



**Figure 41.** SEM images of pre-oxidized CoCrAlY's 1 and 2 after 200 hours at 705°C.



**Figure 42.** Extents of attack at 705°C (LTHC) of untreated samples after 200 h of exposure

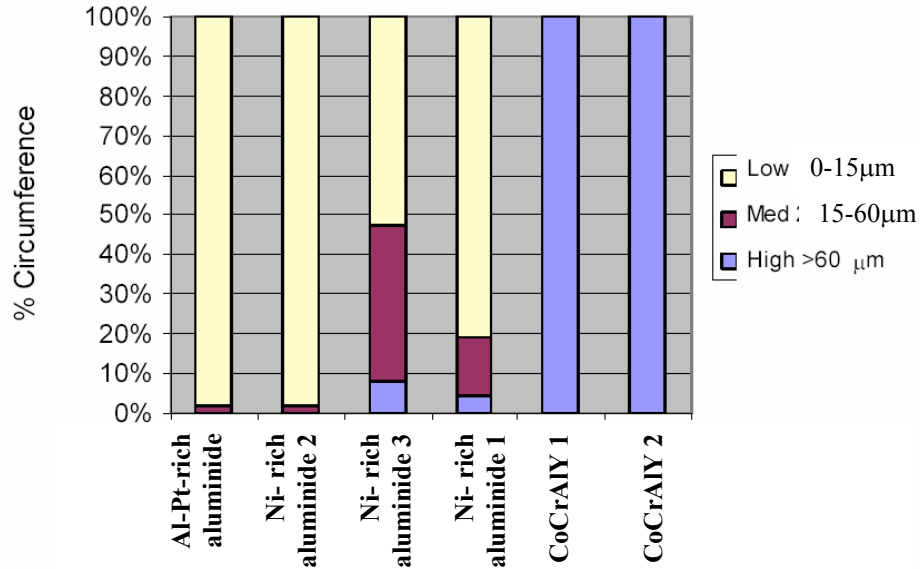


**Figure 43.** Extents of attack at 705°C (LTHC) of pre-oxidized samples after 200 hours of exposure.

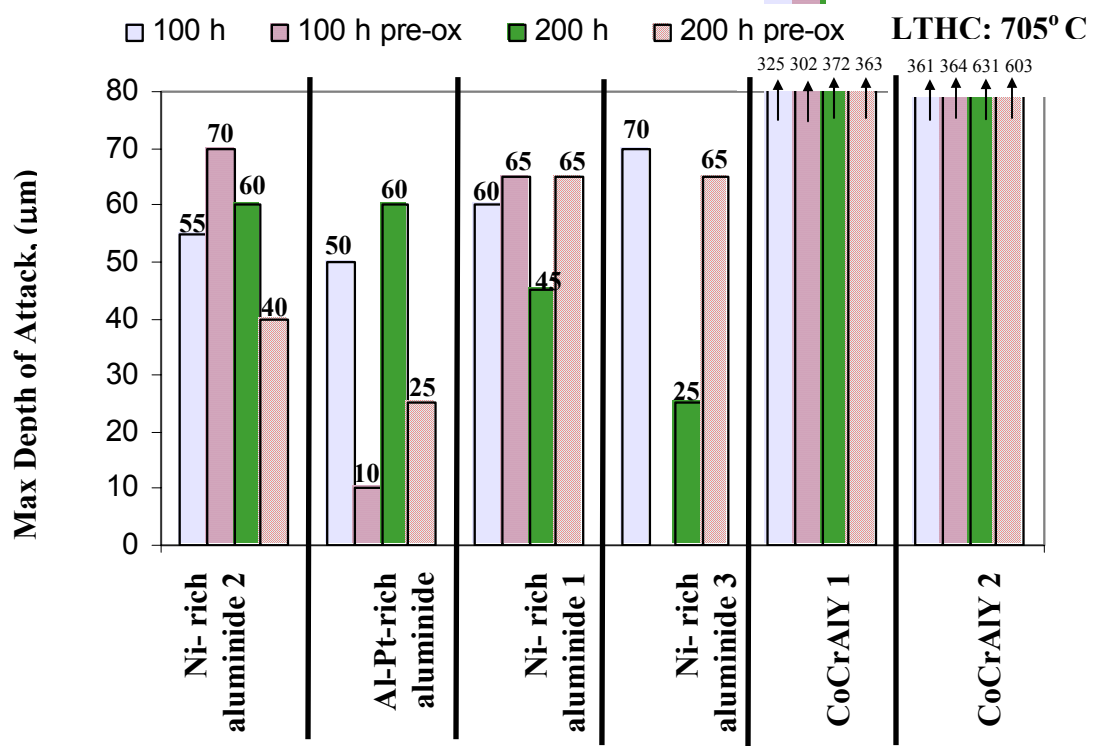


**Figure 44.** Maximum depth of attack on coating and substrate during LTHC (705°C) testing.

Histograms showing maximum depths of attack (figure 44) indicate that all of the coatings tested were comparable. However, these histograms further show that there is less attack of the pre-oxidized Al-Pt-rich aluminide, which was the most resistant coating to LTHC testing. Pre-oxidation of the Al-Pt-rich aluminide was most beneficial due to the relatively high Al and Pt contents in this coating, which in turn, promoted the formation of a planar, adherent and protective  $\text{Al}_2\text{O}_3$ . The CoCrAlY coatings were completely attacked (*i.e.*, corrosion penetration through the coatings) just after 100 hours of testing, thus showing the worst corrosion resistance. The poor performance of CoCrAlY coatings in LTHC conditions is often attributed to the formation of eutectic  $\text{Na}_2\text{SO}_4$ - $\text{CoSO}_4$  liquid ( $T_{\text{melt}} = 565^\circ\text{C}$ ) liquid resulting from the sulfidation of cobalt oxides present on the surface of the coating [49-52].  $\text{CoSO}_4$  (s) could form on Co-based coatings under LTHC hot corrosion conditions by the reaction (4).

The Gibbs free energy of formation ( $\Delta G^\circ_f$ ) for this reaction was used to calculate the  $\text{P}_{\text{SO}_3}$  versus temperature stability diagram for the Co-S-O system, figure 45. The stability diagram demarcates the regions of solid CoO and solid  $\text{CoSO}_4$  stability. The equilibrium partial pressures of  $\text{SO}_3$  gas for the experimental conditions were also calculated and the results are also plotted on the stability diagram in figure 45. As indicated in this diagram, solid  $\text{CoSO}_4$  should be the stable phase at the  $\text{P}_{\text{SO}_3}$  and temperature used in this study.  $\text{Na}_2\text{SO}_4$  (s) in conjunction with sufficient  $\text{P}_{\text{SO}_3}$  can stabilize and form eutectic  $\text{Na}_2\text{SO}_4$ - $\text{CoSO}_4$  liquid at a reaction temperature of  $705^\circ\text{C}$ . Indeed, Luthra [49] found that cobalt-based alloys undergo LTHC attack at low  $\text{SO}_3$  pressures in  $\text{O}_2 + 0.15\%$  ( $\text{SO}_2 + \text{SO}_3$ ) mixtures. The conditions used by Luthra were very close to those used in the current experiments. In contrast to the Co-based coatings, salt was generally in a solid state on the Pt-modified  $\beta$ -NiAl even after 200h of exposure, but there could have been localized liquid formation resulting in LTHC hot corrosion attack. There are at least two possible mechanisms by which Pt-modified  $\beta$ -NiAl undergoes LTHC hot corrosion attack, which are described here. According to Rapp and Goto [46], a negative solubility gradient is required for metal oxide fluxing in the melt. Therefore, one of the more likely mechanism for LTHC of Ni based alloys is sulfidation [49, 104, 105]. Experiments carried out to investigate the

role of  $\text{SO}_3$  and  $\text{SO}_2$  on LTHC showed that a binary Ni-47Al (at %) alloy was heavily attacked only when salt was present in the atmosphere (figure 46). EDS analysis performed on the extensively corroded aluminide-coated samples showed regions of voluminous  $\text{Al}_2\text{O}_3$  formation. Reaction to form such a product suggests the presence of a liquid salt. Sodium pyrosulfate melts at  $365^\circ\text{C}$ , and this pyrosulfate could have formed from the reaction between solid  $\text{Na}_2\text{SO}_4$  and gaseous  $\text{SO}_3$  as shown in reaction (13).

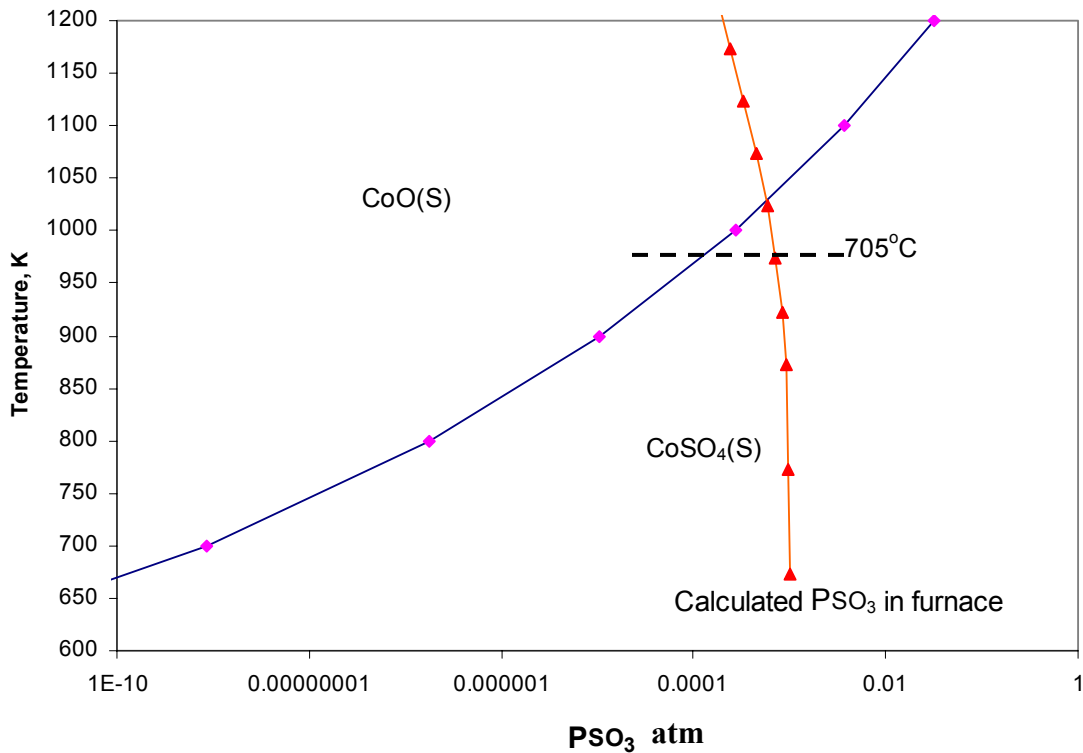


**Figure 45.** Stability diagram of (a)  $\text{CoO(S)}$  and  $\text{CoSO}_4(\text{S})$ .

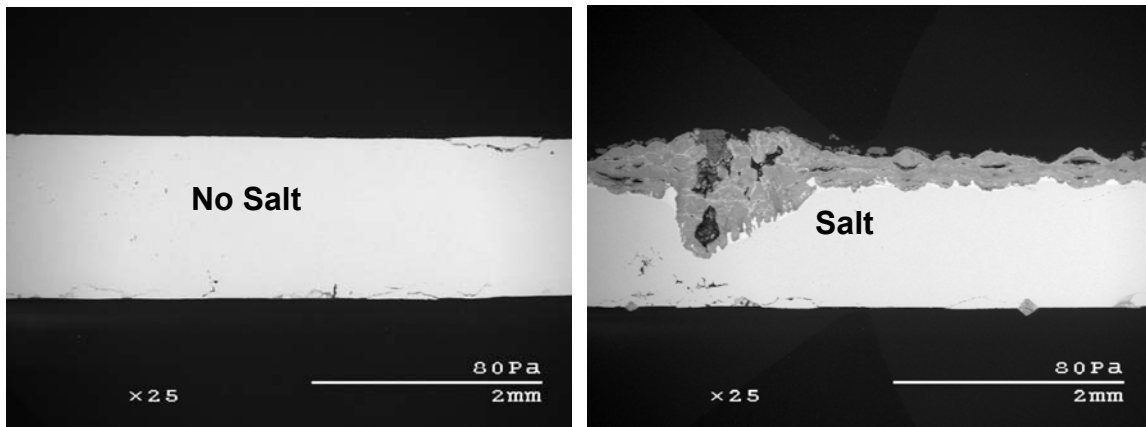


**Figure 46.** Cross-sectional SEM images of Ni-47Al bulk alloy with and without salt addition at 705°C.

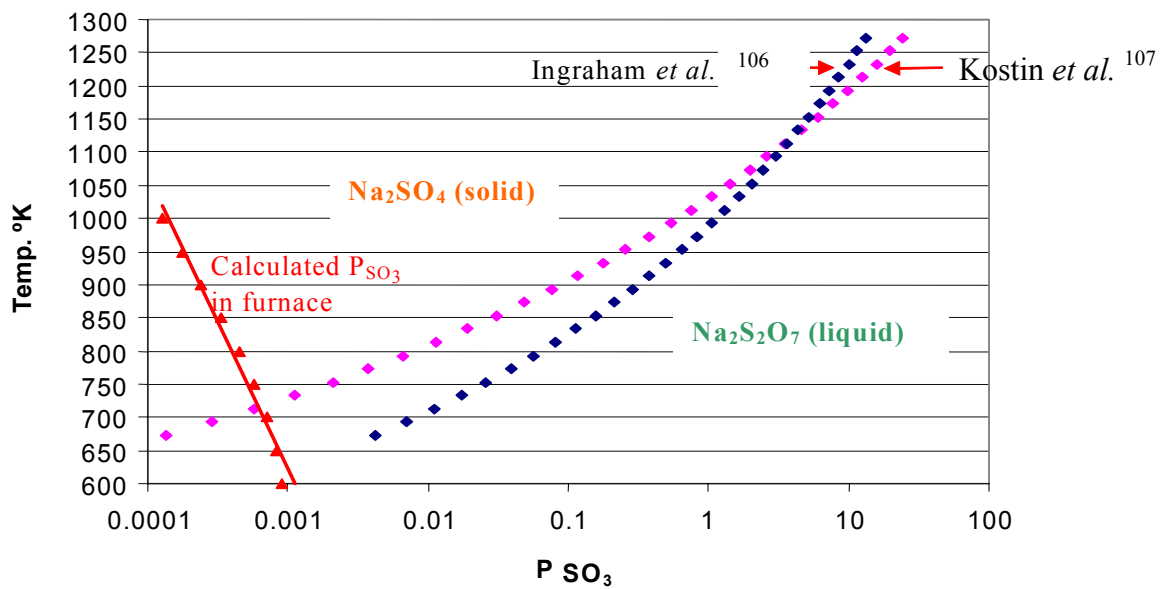


**Figure 47.** Stability diagram of solid  $Na_2SO_4$  and liquid  $Na_2S_2O_7$ . The temperature dependence of the equilibrium  $P_{SO_3}$  for the test conditions used is also given. This shows that the  $Na_2SO_4$  in contact with the test environment should be solid at the test temperatures of 750°C and 705°C.

Kostin *et al.* [106] and Ingraham *et al.* [107] determined the Gibbs free energy of formation ( $\Delta G_f^\circ$ ) for the above reaction. Their  $\Delta G_f^\circ$  values were used to calculate the stability diagram for the Na-S-O system as a function of  $P_{SO_3}$  and temperature, figure 47. The

stability diagram demarcates the regions of solid  $\text{Na}_2\text{SO}_4$  and liquid  $\text{Na}_2\text{S}_2\text{O}_7$  stability. The equilibrium partial pressures of  $\text{SO}_3$  gas for the experimental conditions used were also calculated and the results are also plotted on the stability diagram in figure 47.

In agreement with the SEM images, the stability diagram in figure 45 suggests that the  $\text{Na}_2\text{SO}_4$  in contact with the test atmosphere should be solid at  $750^\circ\text{C}$  (1023 K) and  $705^\circ\text{C}$  (978 K). However, there could be local formation of liquid pyrosulfate if the  $\text{P}_{\text{SO}_3}$  at the salt/coating interface increased above the  $\text{P}_{\text{SO}_3}$  in the test atmosphere. This could occur by the following reaction:



where  $\text{Al}$  is the aluminum from the coating and/or the Al-containing oxide scale on the coating. While the above reaction is thermodynamically possible, the main drawback to such a mode of local liquid pyrosulfate formation is that the  $\text{P}_{\text{SO}_3}$  would have to increase to almost 1 atm (see figure 44), which is significant. Sufficient data are not available to further analyze the possibilities and modes for liquid salt formation.

The other possible mechanism involves the formation of eutectic  $\text{Na}_2\text{SO}_4$ - $\text{NiSO}_4$  liquid ( $T_{\text{melt}} = 671^\circ\text{C}$ ). The oxide scale in Pt-modified  $\beta$ -NiAl may not solely consist of  $\text{Al}_2\text{O}_3$ , as other oxides such as NiO and/or  $\text{NiAl}_2\text{O}_4$  can be at the surface as a consequence of the initial stages of oxidation.  $\text{NiSO}_4(\text{s})$  could form from NiO under LTHC conditions by the following reaction (5).

The  $\Delta G_f^\circ$  value of this reaction was used to calculate the  $\text{P}_{\text{SO}_3}$  versus temperature stability diagram for the Ni-S-O system, figure 48. This diagram suggests that solid NiO should have been stable under LTHC conditions used in this study; however, solid  $\text{NiSO}_4$  could form if the  $\text{P}_{\text{SO}_3}$  at the salt/oxide interface is increased by only  $\sim 2.5 \times 10^{-4}$  atm above the  $\text{P}_{\text{SO}_3}$  in the test atmosphere. Such an increase may be possible at the salt/oxide interface owing to an initial oxidation stage and the development of a  $\text{P}_{\text{SO}_3}$  gradient across the salt deposit. It should be noted, however, that the above assessment does not consider the effect of  $\text{Na}_2\text{SO}_4$  on the phase stabilities. A study by Lillerud and Kofstad [54] suggests that the chemical activity of  $\text{NiSO}_4$  is increased in the presence of  $\text{Na}_2\text{SO}_4$ , thus allowing for  $\text{NiSO}_4 +$

$\text{Na}_2\text{SO}_4$  liquid formation at lower  $\text{P}_{\text{SO}_3}$  values than what are indicated in the Ni-S-O stability diagram.

Experiments were also carried out on bulk  $\beta$ -NiAl alloys to investigate the  $\text{Na}_2\text{SO}_4 + \text{NiSO}_4$  formation in the LTHC conditions. XRD analysis showed that  $\text{Na}_2\text{SO}_4$ ,  $\text{NiSO}_4$  and  $\text{NiO}$  were indeed formed on the surface of Ni-36Al (at %) and Ni-36Al (at%)-15Pt (at%) alloys after 50 h exposure to the LTHC conditions (figure 49). In addition, XRD also showed the presence of  $\text{Na}_2\text{Ni}(\text{SO}_4)_2$  (*i.e.*,  $\text{Na}_2\text{SO}_4 + \text{NiSO}_4$ ) on the surface of a Ni-36Al-15Pt alloy .

LTHC hot corrosion of Pt-modified  $\beta$ -NiAl was highly localized and was in the form of pits. This is possibly due to localized breakdown of  $\text{Al}_2\text{O}_3$ -rich scale.  $\text{Al}_2\text{O}_3$  is an acidic oxide in nature and quite a high  $\text{P}_{\text{SO}_3}$  is required for formation of  $\text{Al}_2(\text{SO}_4)_3$ . Luthra [50] constructed an Al-S-O stability diagram and suggested that in  $\text{O}_2 + 2\% (\text{SO}_2 + \text{SO}_3)$  mixtures  $\text{Al}_2\text{O}_3$  (s) would be stable at  $750^\circ\text{C}$ . Hence under the less severe LTHC conditions (*i.e.*  $\text{O}_2 + 0.1\% (\text{SO}_2 + \text{SO}_3)$ ) used in this study  $\text{Al}_2\text{O}_3$  should be stable and it is only during localized scale breakdown by some thermo-mechanical mechanism that more aggressive hot corrosion attack can occur. It should also be noted that the alumina formed in the temperature range conducive to LTHC attack tends not to consist of highly protective  $\alpha$ - $\text{Al}_2\text{O}_3$ , but rather of less protective  $\gamma$ - $\text{Al}_2\text{O}_3$  or  $\theta$ - $\text{Al}_2\text{O}_3$ . EDS analysis performed in the corroded area showed that the reaction products in the pits are comprised of a sulfate mixture and voluminous  $\text{Al}_2\text{O}_3$ . The external regions of the corrosion products mainly consist of  $\text{NiO}$ .

The LTHC experiments were also carried out at  $750^\circ\text{C}$ . Similar to  $705^\circ\text{C}$  testing, a solid salt film apparently formed at  $750^\circ\text{C}$ . LTHC attack at  $750^\circ\text{C}$  was also localized, similar to that observed at  $705^\circ\text{C}$ . Ni-rich aluminide 3 showed more LTHC attack at  $750^\circ\text{C}$  compared to the other coatings. It is recalled that Ni-rich aluminide 3 has low Al and Pt contents compared to Al-Pt-rich aluminide; hence, the former may not have as good HTHC resistance.

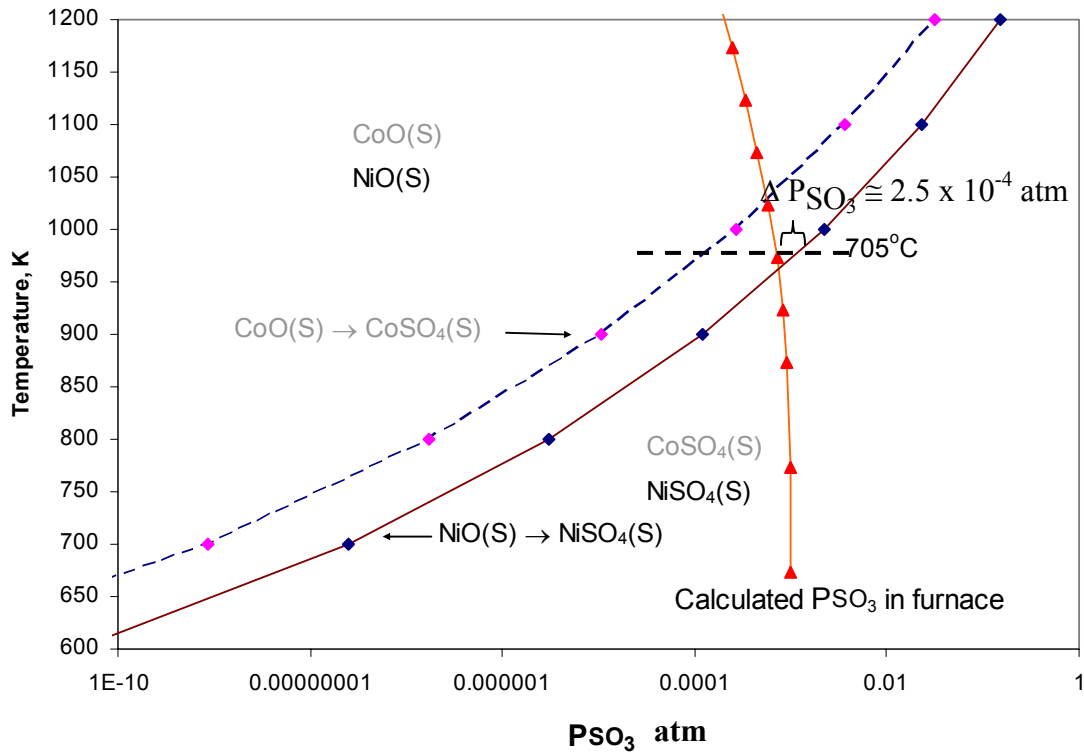


**Figure 48.** Stability diagram of (a)  $\text{CoO(S)}$  and  $\text{CoSO}_4(\text{S})$  and  $\text{NiO(S)}$  and  $\text{NiSO}_4(\text{S})$ .

The temperature dependence of the equilibrium  $\text{P}_{\text{SO}_3}$  for the test conditions used is also given.

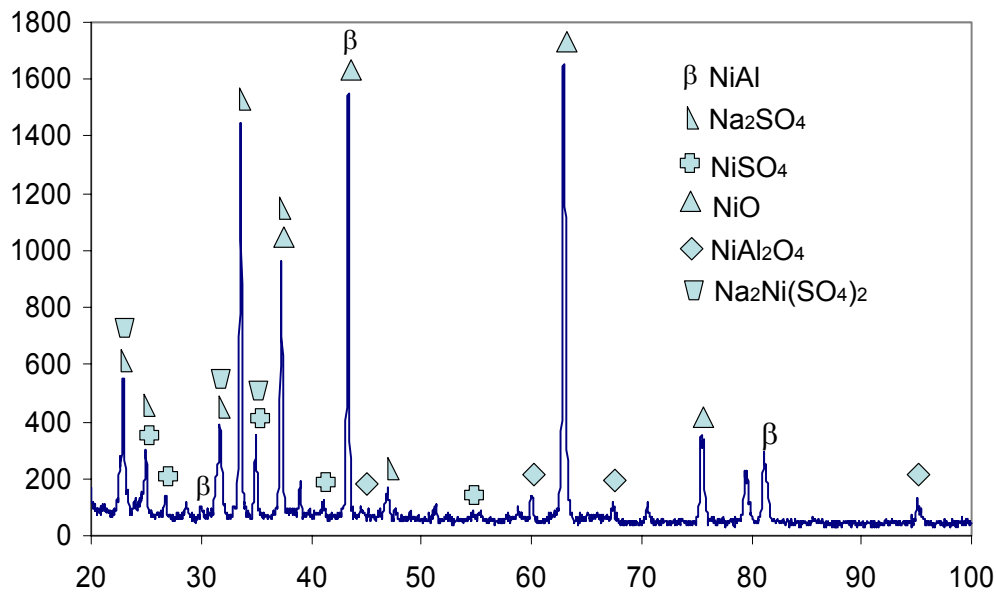


**Figure 49.** XRD pattern of Ni-36Al (at%)-15Pt (at%) after 50 h of LTHC at  $705^\circ\text{C}$ .

The LTHC behavior of the Ni-rich aluminide 3 is currently being further assessed by microstructural analyses. The Ni-rich aluminide coatings 1 and 2 were smoother than the Al-Pt-rich aluminide and Ni-rich aluminide 3 coatings, and the former coatings showed very good LTHC resistance when compared to its HTHC resistance. Extents of attack are similar to those at 705°C, except for Ni-rich aluminide 3, which showed much poorer resistance at 750°C. The overall performance of coatings considering both HTHC and LTHC resistance from best to worst is as follows: Al-Pt-rich aluminide > Ni-rich aluminide 2 > Ni-rich aluminide 1 > Ni-rich aluminide 3 > CoCrAlY 1 > CoCrAlY 2.

#### 4.1.4 Summary of Hot Corrosion Results

##### High temperature hot corrosion (HTHC)

- Under HTHC testing conditions it was found that Al-Pt-rich aluminide was the best coating, with overall ranking of coatings in the following order (from best to worst): Al-Pt-rich aluminide > CoCrAlY 1 > Ni-rich aluminide 2 > Ni-rich aluminide 1 > CoCrAlY 2. The improved performance in Al-Pt-rich aluminide is attributable to the presence of higher Al and Pt content in this coating promoting the formation of a more protective alumina scale. It is inferred that this protection is a result of the alumina scale being homogeneous and having little to no transient oxides rich in Ni and/or Co.
- Ni-rich aluminide 1 was good for shorter times (< 100 h) against HTHC – possibly due to the high smoothness of this coating – but underwent deep attack through to the substrate after longer exposures.
- The diffusion aluminide coatings (Ni-rich aluminides 1 and 2) exhibited better HTHC resistance when on the superalloy 792 substrate than on the superalloy 247 substrate after longer exposures (200 and 500 h). The improved performance in the superalloy 792 substrate is due to the presence of higher Cr content and lower amount of refractory elements, which, in turn, affect the “quality” (i.e. homogeneity, adherence and continuity) of the alumina scale.
- The reliability of Dean rig testing was confirmed by comparing the HTHC results with burner rig testing; however, Dean rig testing is more aggressive than burner rig testing.
- The CoCrAlY coating was good for HTHC when it was thick.

- More sulfidation was observed in the bottom portion of the pin test samples compared to the top.

Low temperature hot corrosion (LTHC)

- Under LTHC testing conditions (705 and 750°C) the corrosion resistance of the Al-Pt-rich aluminide coating was comparable to the other coatings, but the former does exhibit very good resistance to LTHC compared to the others when it is pre-oxidized.
- Pre-oxidation of the coatings on the superalloy 792 substrate improved LTHC resistance considerably; however, this was apparently not the case for the coatings on the superalloy 247 substrate.
- Thick solid salt films developed on the samples in LTHC, which could have limited general attack of the coupons. LTHC attack of the CoCrAlY coatings is attributed to the formation of eutectic  $\text{Na}_2\text{SO}_4\text{-CoSO}_4$  ( $T_{\text{melt}} = 565^\circ\text{C}$ ) liquid; while the LTHC attack in diffusion Pt-modified  $\beta$  coatings was possibly due to the eutectic  $\text{Na}_2\text{SO}_4\text{-NiSO}_4$  ( $T_{\text{melt}} = 671^\circ\text{C}$ ).
- The overall ranking of the coatings against LTHC from best to worst is as follows:

Al-Pt-rich aluminide > Ni-rich aluminide 2 > Ni-rich aluminide 1 > Ni-rich aluminide  
3 > CoCrAlY 1 > CoCrAlY 2.

#### **4.2 Structural and Compositional Effects on the Hot Corrosion Resistance of Al- Pt-rich $\beta$ Aluminides and Their Performance Compared with a Standard CoCrAlY Coatings**

The Al-Pt-rich  $\beta$  aluminide described in the previous section is similar to a diffusion type coating which was produced by a proprietary electrophoretic deposition process developed at Rolls-Royce Corporation, USA. It was found in the previous section that such a coating can offer a viable alternative to current state-of-the-art Pt-modified  $\beta$  diffusion coating and CoCrAlY overlay coating for the marine gas turbine engine components. One of the beneficial effects of such a coating is that the deposition technique allows for a uniformly high Al content (*i.e.* greater than ~45 at.%) throughout the coating, which may be beneficial

in improving hot corrosion and oxidation resistance. However, a potential issue is the fact that the Pt content in the electrophoretically deposited Pt-modified  $\beta$  coating (*i.e.* Al-Pt-rich aluminide) is not uniform throughout. Furthermore, a high percentage of porosity may be present in the certain regions of the coated blade surface, depending on the deposition conditions.

The effects of coating composition and structure on the hot-corrosion behavior of a developmental-Al-Pt-rich aluminide (Pt-modified  $\beta$ ) coating were assessed and compared to a commercial CoCrAlY ( $\gamma+\beta$ ) coating. The primary objective of this research was to understand the effect of Pt and porosity on the Type II HC resistance of Pt-modified  $\beta$  coating and compare their HC resistance with the CoCrAlY thick and thin coatings. This study compares and ranks both types of hot corrosion resistance of various Pt-modified  $\beta$  and a CoCrAlY coating.

The as-received aluminide-coated airfoils were 30 mm long and were sectioned into 6-7 mm wide samples. The airfoil (*i.e.*, substrate) was Superalloy 792 alloy, which has the following nominal composition (in at. %):

59.6Ni-14.6Cr-8.9Co-6.9Al-5.1Ti-1.3W-1.3Nb-1.2Mo-1C-0.1B-0.06Zr.

The chemical-composition range of each as-received and pre-oxidized coating was measured via energy dispersive analysis (EDS) and the results are summarized in Table 4. The approximate regions in which the coating compositions were measured are shown in figure 50. The measured thickness and phase constitution of each as-deposited coating is also given in Table 4.

**Table 4.** Measured compositional range, thicknesses, and phase constitution of as-deposited coatings.

Coating Type	Phase constitution	Thickness	As-deposited Measured Composition (at%)
Al-Pt-rich aluminide	$\beta$ -NiAl	(~45-50 $\mu$ m)	Ni-(42-47)Al-(7-9)Pt- 5Co-4Cr; Al (47-49) near the surface
Al-Pt-rich aluminide: Medium Porosity	$\beta$ -NiAl	(~45-55 $\mu$ m)	Ni-(42-47)Al-(7-9)Pt- 5Co-4Cr; Al (46-49) near the surface
Al-Pt-rich aluminide: Low-Pt	$\beta$ -NiAl	(~45-52 $\mu$ m)	Ni-(46-49)Al-(2-3)Pt-5Co-4Cr; Al (49-52) near the surface
CoCrAlY (Thick &Thin)	$\gamma$ -Ni+ $\beta$ -NiAl	Thick: ~90-130 $\mu$ m Thin: ~30-50 $\mu$ m	Top: Co-25Cr-17Al-3Ni-0.4Y Bottom: Co-24Cr-15Al-12Ni-0.4Y

All Al-Pt-rich aluminide  $\beta$  coatings are Pt-modified and were deposited by proprietary electrophoretic process at Rolls-Royce Corporation. The CoCrAlY coating was deposited via physical vapor deposition (PVD). The composition and thickness of the Al-Pt-rich aluminide coatings were fairly uniform; while the CoCrAlY coating thickness varied along the airfoil length. Specifically, the CoCrAlY coating on the convex upper portion of the airfoil was much thinner than the bottom. Accordingly, the coatings were identified as CoCrAlY-thick and CoCrAlY-thin (figure 50). The Al-Pt-rich aluminide medium-porosity coating was different from the denser Al-Pt-rich aluminide-baseline coating in that the former contained surface and intermediate zones of rather uniformly distributed  $\sim 4$ -8  $\mu$ m diameter pores.

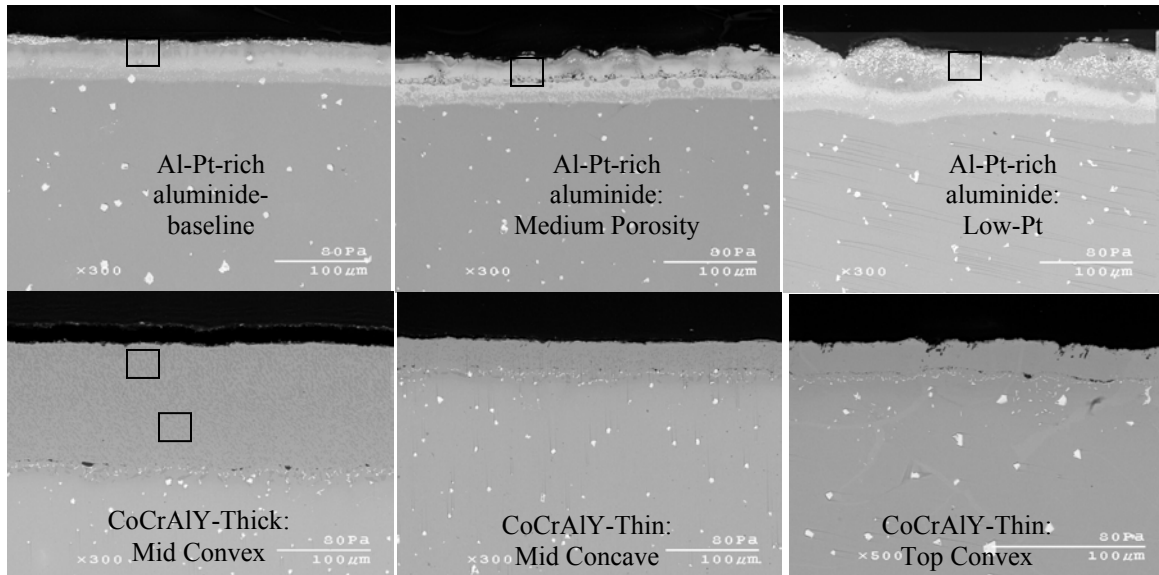


**Figure 50.** SEM micrographs of as-deposited Al-Pt-rich aluminide and CoCrAlY coatings on Superalloy 792 substrate. SEM images also show the region where the range of composition was measured.

#### 4.2.1 Low Temperature Hot Corrosion (705 °C) Results

Figure 51 shows cross-sectional SEM images of the Al-Pt-rich aluminide and CoCrAlY coatings after 100 h of exposure. In general, all coatings underwent a considerable amount of corrosion. It was generally found that an increase in porosity and decrease in Pt content of Al-Pt-rich aluminide coating resulted in comparatively higher attack. The Al-Pt-rich aluminide coatings were attacked throughout the cross-section and were penetrated deep inside (*i.e.*  $\sim 30 \mu\text{m}$ ) the coating in a few localized regions, particularly for the Al-Pt-rich aluminide medium-porosity and low-Pt coatings. Even so, it was found that all the Al-Pt-rich aluminide coatings exhibited improved LTHC hot corrosion performance compared to CoCrAlY coatings. The CoCrAlY-thin coating was completely attacked and even spalled, as shown in figure 51; whereas, in case of CoCrAlY-thick coating, HC attack was still within the coating. However, in this latter case the extent of attack was still greater than what the Al-Pt-rich aluminide coatings had undergone. Specifically, greater than  $\sim 50 \mu\text{m}$  of the CoCrAlY-thick coating was attacked. The corroded regions of the Al-Pt-rich aluminide coatings were analyzed using EDS and, based on compositional analysis, it was deduced that

the outermost layer consisted primarily of NiO followed by an inner layer of Ni+Al-rich oxide and then internal Al-rich oxidation. A much thicker NiO was seen in the convex section of the airfoil for the Al-Pt-rich aluminide low-Pt coating (figure 51). The oxide scale formed on the CoCrAlY coating consisted primarily of external CoO and internal Al+Cr-rich oxide.

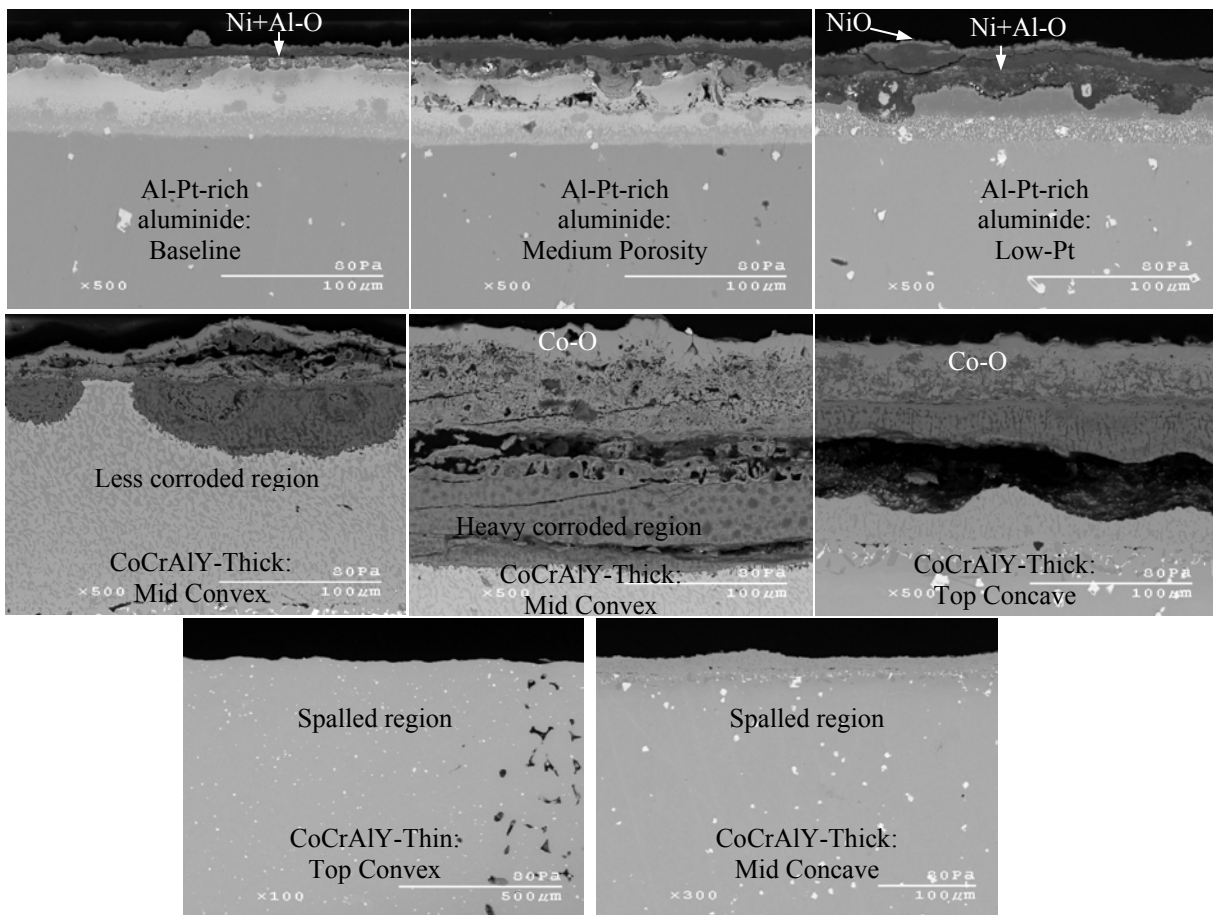


**Figure 51.** Cross-sectional SEM images after 100 h LTHC of the Al-Pt-rich aluminide and CoCrAlY coatings.

The results of semi-quantitative analyses of the extents of attack are summarized in the form of histograms in figure 52. Compared to the Al-Pt-rich aluminide-baseline, the Al-Pt-rich aluminide low-Pt and medium-porosity coatings exhibited a higher percentage of high corrosion ( $> 15 \mu\text{m}$ ). The CoCrAlY-thin coating was completely attacked, such that only high corrosion was measured. The CoCrAlY-thick also exhibited a significant proportion (*i.e.*, 79%) of high corrosion. Maximum depth of penetration was also highest for the CoCrAlY coatings ( $\sim 80 \mu\text{m}$ ), thus confirming that the Al-Pt-rich aluminide coatings exhibited better LTHC performance than the CoCrAlY coatings (figure 53).

LTHC testing was carried out for an extended period of exposure of 200 h and resulting cross-sectional SEM images are shown in figure 54. In general, all of the samples underwent more LTHC attack compared to 100 h of testing. For instance, the Al-Pt-rich aluminide medium-porosity and low-Pt coatings showed considerable LTHC attack after 200 h of exposure, to the extent that attack penetrated inside the substrate in few localized regions. The Al-Pt-rich aluminide-baseline coating underwent a much lesser extent of attack (see figure 54). The CoCrAlY coatings exhibited rather poor LTHC resistance compared to Al-Pt-rich aluminide coatings, with the former forming a very thick external CoO scale in most of the attacked region.

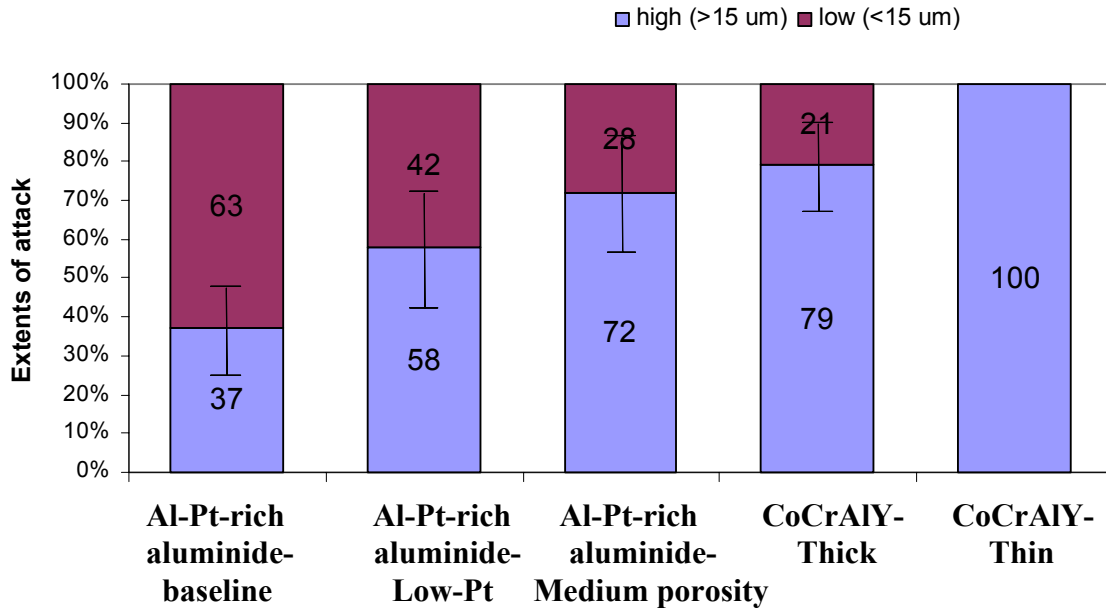


**Figure 52.** Extents of attack after 100 h LTCH of the various Al-Pt-rich aluminide and CoCrAlY coatings.

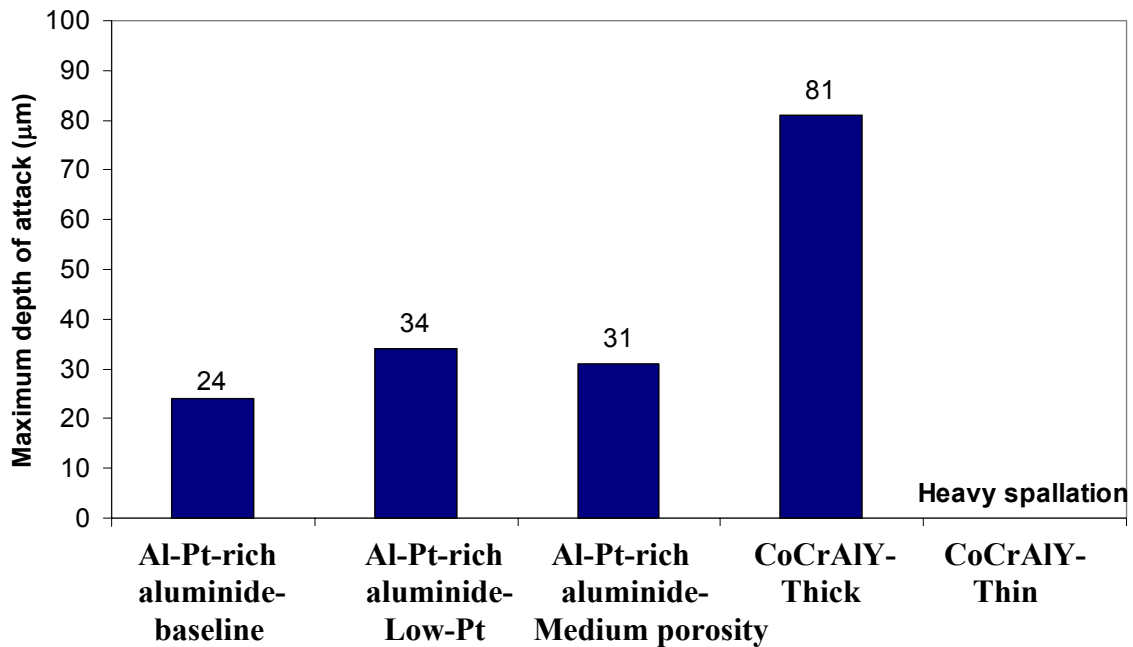


**Figure 53.** Maximum depth of attack after 100 h LTCH of the various Al-Pt-rich aluminide and CoCrAlY coatings.

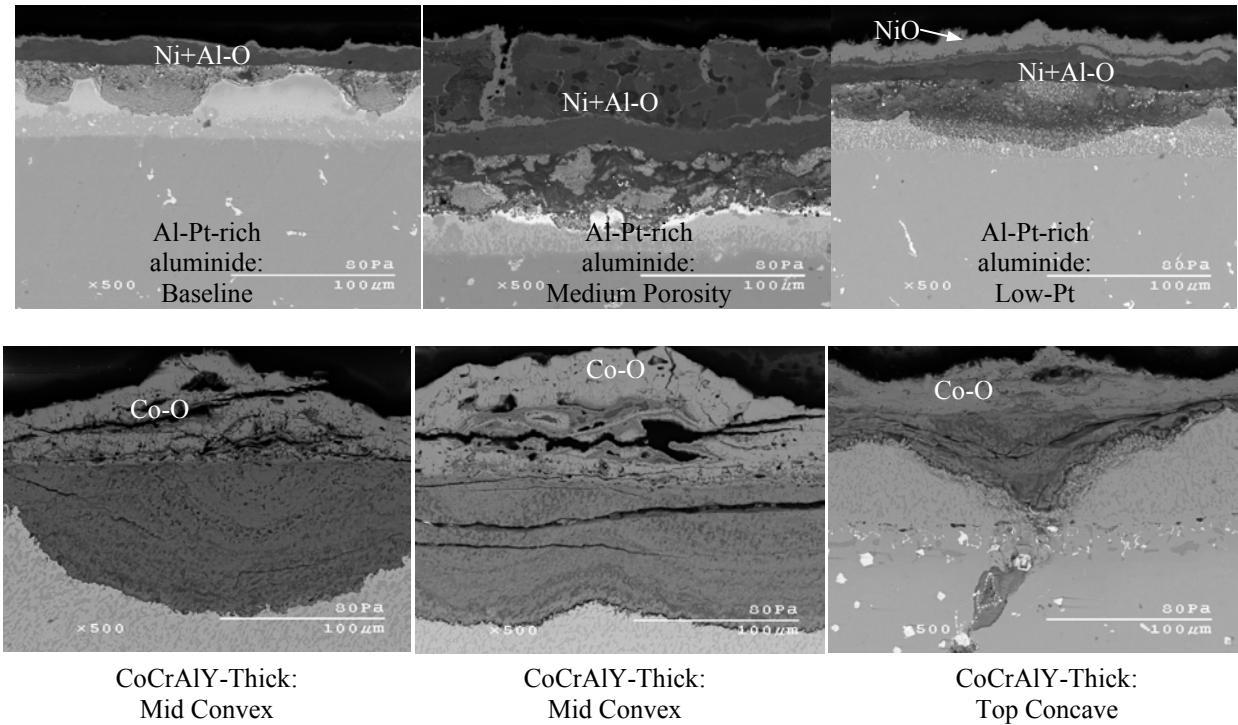


**Figure 54.** Cross-sectional SEM images after 200 h LTHC of the Al-Pt-rich aluminide and CoCrAlY coatings.

The extents of attack and maximum depth of penetration measurements are summarized in figure 55 and 56, respectively. The amount of high corrosion was above 90% for the Al-Pt-rich aluminide medium-porosity and low-Pt coatings, while it was just 65% for the Al-Pt-rich aluminide-baseline coating. Maximum depth of penetration was also comparatively high for the Al-Pt-rich aluminide medium-porosity and low-Pt coatings, particularly for the Al-Pt-rich aluminide medium-porosity coating (figure 56). The CoCrAlY-thin coating showed only high corrosion and since this coating had completely spalled in most regions, maximum depth of penetration could not be measured. The extents of attack were quite high and depth of penetration was in fact highest for the CoCrAlY-thick coating, indicating that the Al-Pt-rich aluminide coatings have greater LTHC resistance than the CoCrAlY coatings. The overall ranking of the various coatings under LTHC conditions from best to worst is as follows: Al-Pt-rich aluminide-baseline > Al-Pt-rich aluminide low-Pt > Al-Pt-rich aluminide medium-porosity > CoCrAlY-thick > CoCrAlY-thin.

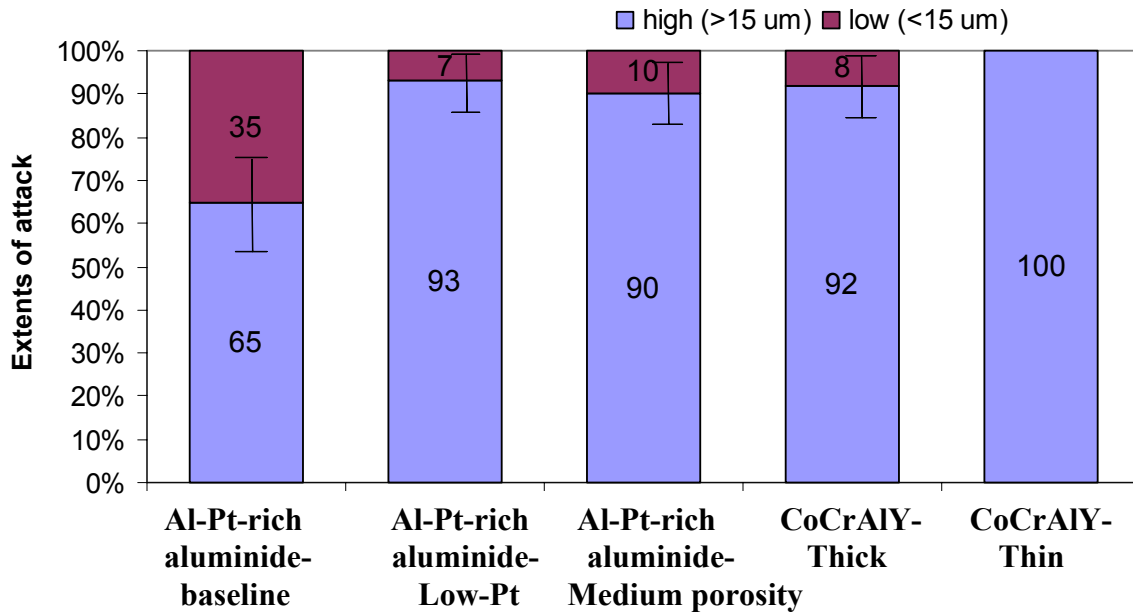


**Figure 55.** Extents of attack after 200 h LTHC of the various Al-Pt-rich aluminide and CoCrAlY coatings.

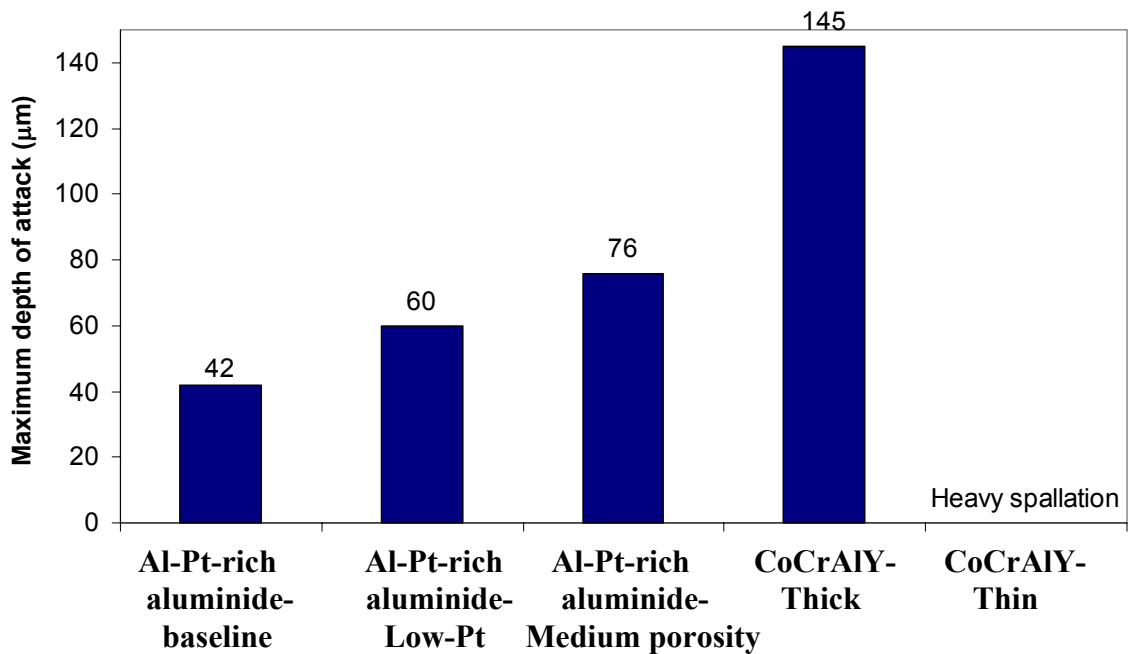
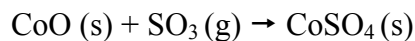


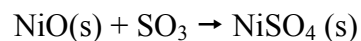
**Figure 56.** Maximum depth of attack after 200 h LTHC of the Al-Pt-rich aluminide and CoCrAlY coatings.

The rather poor HC resistance of Al-Pt-rich aluminide medium-porosity coating is believed to be partly attributable to the cracks and porosity in the coating providing easy access pathways for the molten deposit. In the case of the other coatings, the nature of the TGO scale is believed to be the important variable. The formation of a thermally-grown  $\text{Al}_2\text{O}_3$  scale plays an important role in limiting environmental degradation of various high temperature alloys and coatings. In general, an ideal alumina scale should be dense, relatively inert, adherent, and slow-growing to protect underlying metal surface. Addition of Pt is well known in increasing the scale adhesion on  $\beta$ -NiAl alloys and coatings, thereby improving oxidation and HC resistance [18, 19, 20, 66, 67]. Hence, the higher Pt in the Al-Pt-rich aluminide-baseline coating may have promoted the formation of more protective and adherent TGO scale compared, for instance, to the low-Pt AEP coating. This Al-rich TGO scale provided some degree of resistance to the salt deposit, to the extent that the LTHC hot corrosion resistance of the Al-Pt-rich aluminide-baseline coating was the best of all the coatings tested.

The poor performance of CoCrAlY coatings in LTHC conditions is often attributed to the formation of eutectic  $\text{Na}_2\text{SO}_4$ - $\text{CoSO}_4$  liquid ( $T_{\text{melt}} = 565^\circ\text{C}$ ) [49-52].  $\text{CoSO}_4$  (s) could form on Co-based coatings under LTHC conditions by the reaction,



where the CoO may be present as a consequence of the initial stages of coating or alloy oxidation. Similarly, LTHC in Al-Pt-rich aluminide coatings is attributable to the formation of eutectic  $\text{Na}_2\text{SO}_4$ - $\text{NiSO}_4$  liquid ( $T_{\text{melt}} = 565^\circ\text{C}$ ). The  $\text{NiSO}_4$  (s) could form under LTHC conditions by the reaction [39, 54],



EDS analysis of the hot-corroded samples clearly indicated formation of thick NiO and CoO scales on the Al-Pt-rich aluminide and CoCrAlY coatings, respectively (figure 51 and 54). The CoCrAlY coatings were found to be more susceptible to LTHC than Pt-modified  $\beta$ -NiAl coatings. The main inferred reasons for this behavior are described here.  $\text{CoSO}_4$  is more stable than  $\text{NiSO}_4$  with respect to CoO and NiO, respectively. As a consequence,  $\text{CoSO}_4$  can form at a lower  $\text{P}_{\text{SO}_3}$  than  $\text{NiSO}_4$ . In addition, the eutectic mixture of  $\text{Na}_2\text{SO}_4 + \text{CoSO}_4$  has a much lower melting temperature ( $565^\circ\text{C}$ ) than that of  $\text{Na}_2\text{SO}_4 + \text{NiSO}_4$  ( $T_{\text{melt}} = 671^\circ\text{C}$ ).

Hence, the CoCrAlY coating is likely to be more susceptible to LTHC attack than the Al-Pt-rich aluminide (Pt-modified  $\beta$ ) coatings at lower temperatures. Luthra and Shores [49] also showed that CoO is a better catalyst for the  $\text{SO}_2 + \frac{1}{2} \text{O}_2 \rightarrow \text{SO}_3$  reaction than NiO, and this would further exacerbate matters by increasing the  $\text{P}^{\text{SO}_3}$  at the CoO surface in comparison to the NiO surface.

#### 4.2.2 High Temperature Hot Corrosion (900 °C) Results

HTHC testing was carried out for 200 h of exposure and cross-sectional SEM images of the Al-Pt-rich aluminide (baseline and low-Pt) and CoCrAlY coatings are shown in figure 57. The Al-Pt-rich aluminide-baseline coating exhibited improved hot corrosion resistance compared to the Al-Pt-rich aluminide low-Pt coating. HTHC attack was observed only in a localized region for the Al-Pt-rich aluminide baseline, while attack was seen throughout the cross-section for the Al-Pt-rich aluminide low-Pt coating (figure 57). The CoCrAlY-thin coating underwent HTHC attack, but to a lower extent and attack was in fact comparable to the Al-Pt-rich aluminide-baseline coating. The CoCrAlY-thick coating exhibited excellent HTHC resistance with no discernable HTHC attack seen throughout the cross-section. The corrosion products on the Al-Pt-rich aluminide coatings were analyzed via EDS, which indicated formation of an NiO outer scale followed by inner Ni+Al-rich oxide scale and internal sulfide and Al-rich oxide. In case of the Al-Pt-rich aluminide low-Pt coating, a very thick NiO scale above an Ni+Al-rich oxide layer was observed, and HTHC attack penetrated deep inside the coating (figure 57). The order of performance under HTHC conditions of the various coatings from best to worst is as follows: CoCrAlY-thick > Al-Pt-rich aluminide-baseline  $\approx$  CoCrAlY-thin > Al-Pt-rich aluminide low-Pt. The results obtained thus far are in good agreement with hot corrosion results shown in the previous section, which also showed that the CoCrAlY coatings have rather poor LTHC but have excellent HTHC resistance.

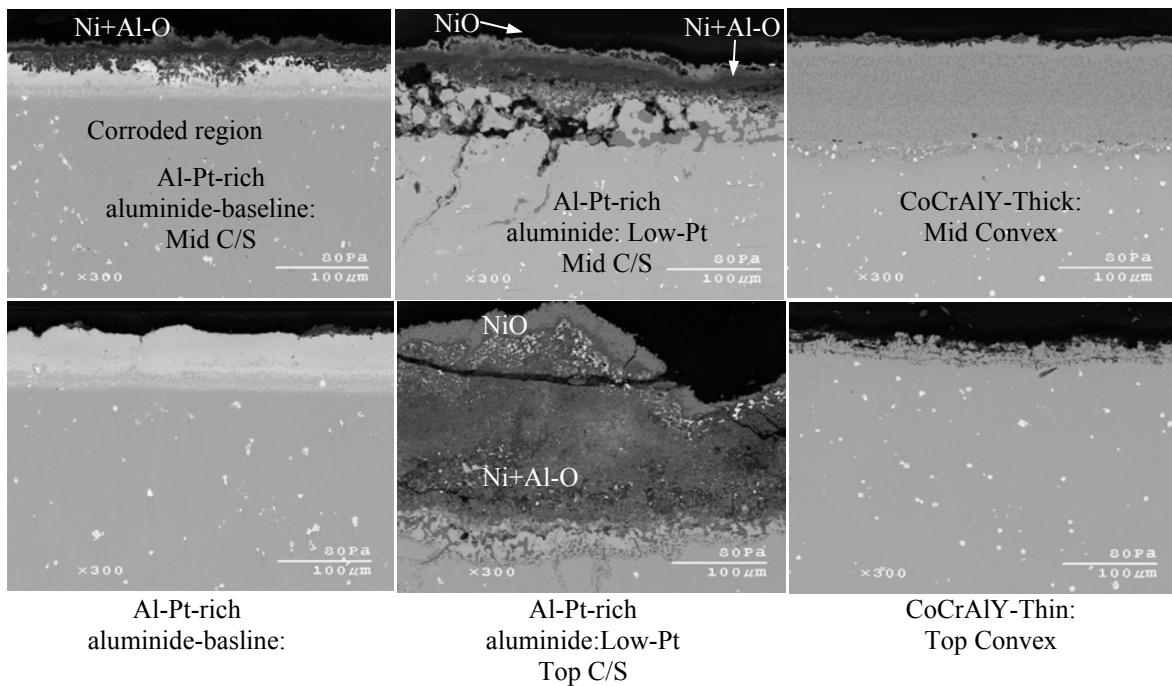


**Figure 57.** SEM images after 200 h Type I HC of the various Al-Pt-rich aluminide and CoCrAlY coatings.

#### 4.2.3 Summary and Conclusions

1. The overall ranking under LTHC conditions of the various coatings from best to worst is as follows: Al-Pt-rich aluminide-baseline > Al-Pt-rich aluminide low-Pt > Al-Pt-rich aluminide-medium porosity > CoCrAlY-thick > CoCrAlY-thin.
2. The order of performance under HTHC conditions of the various coatings from best to worst is as follows: CoCrAlY-thick > Al-Pt-rich aluminide-baseline  $\approx$  CoCrAlY-thin > Al-Pt-rich aluminide low-Pt.
3. The presence of porosity and reduction in Pt content considerably decreased the longer-term hot-corrosion resistance (LTHC and HTHC) of the Al-Pt-rich aluminide [Al-rich  $\beta$ -(NiPt)Al] coating.
4. The CoCrAlY coatings exhibited rather poor LTHC performance when compared with the Al-Pt-rich aluminide coatings, but under HTHC conditions the CoCrAlY coatings exhibit excellent hot corrosion resistance.

5. LTHC attack of the CoCrAlY coatings is attributed to the formation of eutectic  $\text{Na}_2\text{SO}_4\text{-CoSO}_4$  ( $T_{\text{melt}} = 565^\circ\text{C}$ ) liquid; while the LTHC attack in Al-Pt-rich aluminide coatings (Pt-modified  $\beta$ ) was possibly due to the eutectic  $\text{Na}_2\text{SO}_4\text{-NiSO}_4$  ( $T_{\text{melt}} = 671^\circ\text{C}$ ).

#### 4.3 Effects of Pt on the LTHC Behavior of Co-and Ni-Based Coatings

The benefits of Pt addition to  $\beta$ -NiAl coatings are well known, but there is very limited literature showing effect of Pt addition on Co-based aluminides. The primary purpose of this study was to compare and rank the resistance of the selected Co-based aluminide coatings (CoCrAlY and Pt-modified CoAl) and Pt-modified  $\beta$ -NiAl coating to LTHC. The nominal compositions of these alloys are as follows (in wt. %):

Superalloy 509: 56.7Co-21.5Cr-10Ni-7W-3.5Ta-0.6C-0.5Zr-0.2Ta.

Superalloy 247: 59Ni-10Co-10W-8Cr-5.5Al-3Ta-1Ti-1.5Hf-0.7Mo

The average chemical composition of each coating was measured via energy dispersive spectroscopy (EDS) analysis and the results are summarized in Table 5.

**Table 5.** Coating composition and thicknesses of the tested coupons

Alloy	Coating Type and Thickness	Measured Average Composition (at%)
Superalloy 509	CoCrAlY-Convex (65-75 $\mu\text{m}$ )	51Co-25Cr-21Al-2Si-0.7Y
Superalloy 509	Pt-modified CoAl (65-75 $\mu\text{m}$ )	50Al-23Co-9Pt-8Cr-5Ni-2Si-2W-1Fe
Superalloy 792	Pt-modified $\beta$ -NiAl (60-65 $\mu\text{m}$ )	35Al-9Pt-6Cr-5Co-Bal Ni

SEM images of pre-oxidized Pt-modified CoAl, CoCrAlY (mid-chord section) and Pt-modified  $\beta$ -NiAl coatings after 200 hours LTHC hot corrosion are shown in figures 58, 59, and 60, respectively. In general, the Co-based coatings underwent a considerable amount of

corrosion. The specimens exposed for shorter times (40h, 100h) were attacked in similar manners, but to a lesser extent. The Pt-modified CoAl coating was extensively attacked, with the coating being completely penetrated by 200 hours of exposure at all three cross-sections. The CoCrAlY coating was also heavily attacked, but it was also only partially attacked in some regions, indicating slightly better resistance compared to Pt-modified CoAl. The Pt-modified  $\beta$ -NiAl coating exhibited the greatest resistance to LTHC hot corrosion. Hot corrosion attack of the Pt-modified  $\beta$ -NiAl was highly localized compared to the Co-based aluminide coatings. As a consequence, the variable of where the sample cross-section is taken becomes very critical for analysis of the Pt-modified  $\beta$ -NiAl coating cross-sections. From 100 h test results it was also found that the Pt-modified CoAl coating was attacked to a greater extent than the CoCrAlY coating. A similar trend of the CoCrAlY coating showing better resistance than the Pt-modified CoAl was observed for the bottom-chord sections. The two types of Co-based coatings were completely attacked in the vicinity of the leading top edge of the airfoil after just 100h of exposure. The Pt-modified  $\beta$ -NiAl exhibited a very small fraction of localized attack after 100 hours of exposure.

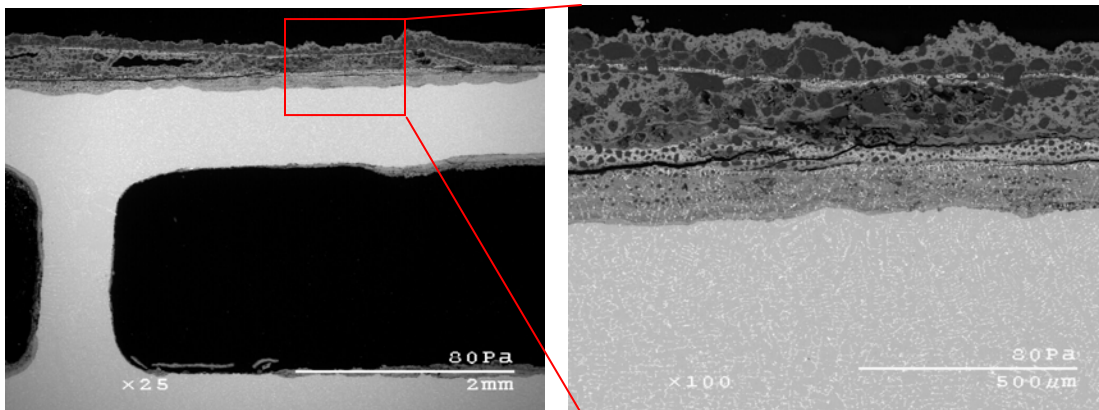


**Figure 58.** SEM images of Pt-modified CoAl (mid-chord) after 200 hours of LTHC testing at 705°C.

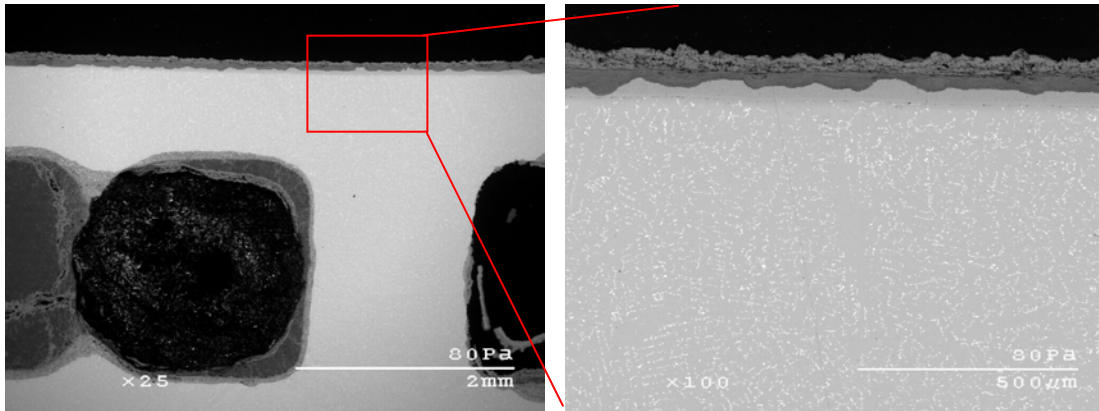


**Figure 59.** SEM images of CoCrAlY (mid-chord) after 200 hours of LTHC testing at 705°C.

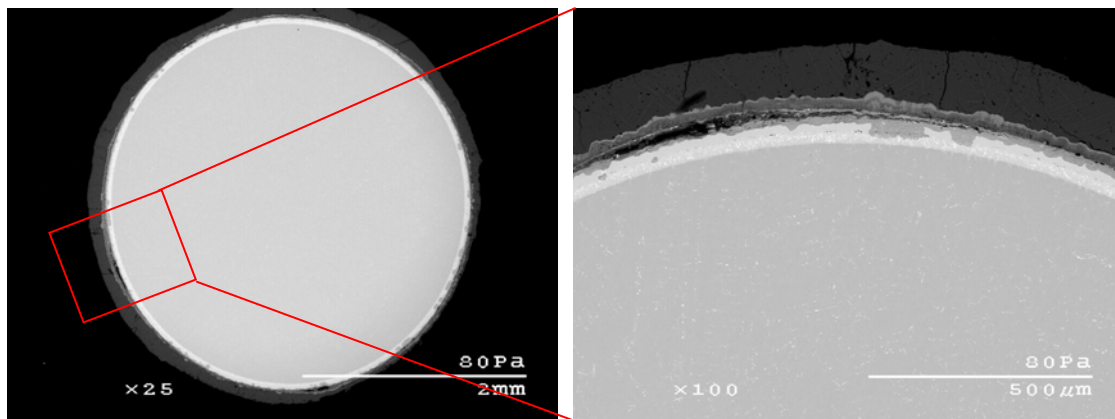


**Figure 60.** SEM images of Pt-modified  $\beta$ -NiAl after 200 hours of LTHC testing at 705°C.

Shorter-term LTHC hot corrosion experiments were also carried out on the Co-based coatings that were not given any pre-oxidation treatment. These experiments showed a similar trend in performance, with the CoCrAlY coating being generally better than the Pt-modified CoAl coating. The overall ranking of coating performance from best to worst was as follows: Pt-modified  $\beta$ -NiAl > CoCrAlY > Pt-modified CoAl.

EDS analysis of the coating cross-sections was used to deduce the phases present in the corroded areas. Pt-rich phases were intermittently distributed in Pt-modified CoAl coating. The oxide scale that formed on the CoCrAlY coating was primarily CoO with a small fraction of  $\text{Cr}_2\text{O}_3$ ; while mixed non-protective scale of  $\text{CoO} + \text{Al}_2\text{O}_3 + \text{Cr}_2\text{O}_3$  formed on the Pt-modified CoAl coating. It is believed the inferior performance of the Pt-modified CoAl coating compared to the CoCrAlY coating can be partly ascribed to the more

heterogeneous phase constitution of the TGO scale formed on the former. This is in accordance with Luthra [51] who found that the simultaneous presence of various oxides can drastically reduce LTHC hot corrosion resistance. It should also be noted that Pt-modified CoAl was more brittle than the CoCrAlY coating, which may have also contributed to the inferior performance of the former. Interestingly, examination of the macro-images taken after each 20 hour cycle indicated that the salt deposit on the Pt-modified CoAl coating was completely molten just after 40 hours of exposure; while the salt on the CoCrAlY coating was apparently only semi-molten up to 60 hours. Grisik *et al.* [108] demonstrated that the presence of excess platinum on the surface of a CoCrAlY coating can increase corrosion rates relative to a platinum free CoCrAlY coating. These results suggest that a relatively high amount of platinum is not beneficial in improving LTHC hot corrosion resistance in Co-based coatings.

CoCrAlY is found to be more susceptible to LTHC hot corrosion than Pt-modified  $\beta$ -NiAl. The main reasons for this behavior are described here.  $\text{CoSO}_4$  is more stable than  $\text{NiSO}_4$  with respect to CoO and NiO, respectively (figure 46). As a consequence,  $\text{CoSO}_4$  can form at a lower  $P_{\text{SO}_3}$  than  $\text{NiSO}_4$ . In addition, the eutectic mixture of  $\text{Na}_2\text{SO}_4 + \text{CoSO}_4$  has much lower melting temperature ( $565^\circ\text{C}$ ) than that of  $\text{Na}_2\text{SO}_4 + \text{NiSO}_4$  ( $T_{\text{melt}} = 671^\circ\text{C}$ ); hence CoCrAlY coating is likely to be more susceptible to LTHC attack than Pt-modified  $\beta$ -NiAl at lower temperatures. Luthra and Shores [49] also showed that CoO is a better catalyst for the  $\text{SO}_2 + \frac{1}{2} \text{O}_2 \rightarrow \text{SO}_3$  reaction than NiO and this will further increase  $P_{\text{SO}_3}$  at the CoO surface than at the NiO surface.

The effect of platinum in improving HTHC and oxidation resistance of  $\beta$ -NiAl is quite well known [67, 68, 72, 73]. In order to study the effect of Pt in  $\beta$ -NiAl for the LTHC hot corrosion resistance, an additional set of experiments were carried out using cast  $\beta$ -NiAl bulk alloys Ni-47Al (at%) and Ni-47Al (at%)-15Pt (at%) at  $705^\circ\text{C}$ . SEM images of these alloys are shown in figure 61, which show voluminous attack on the binary Ni-47Al alloy, presumably due to liquid salt formation. By contrast, platinum addition up to 15 at% proved quite beneficial in  $\beta$ -NiAl, with the results indicating that only solid salt was on the surface. The Ni-47Al-15Pt alloy exhibited excellent LTHC hot corrosion resistance.

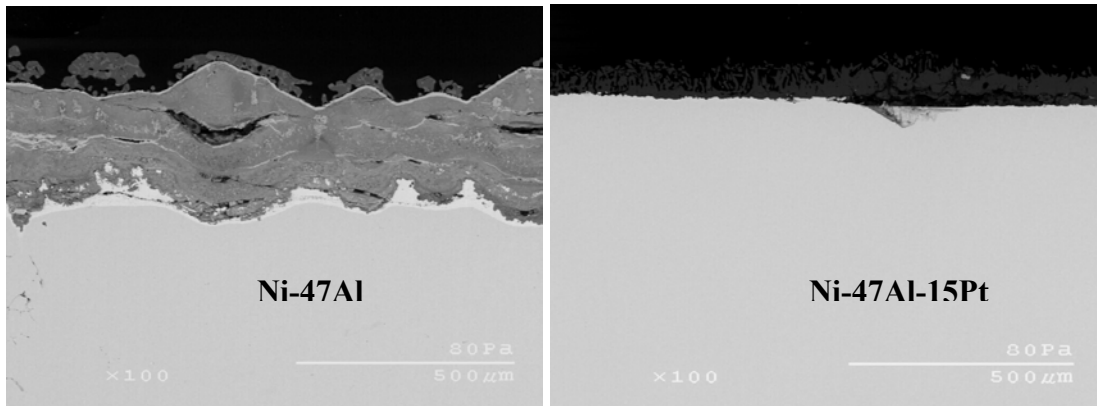


**Figure 61.** SEM images of Ni-47(at%)Al and Ni-47(at%)Al-15(at%)Pt after 100 hours of LTHC Hot Corrosion testing at 705°C.

### Summary and Conclusions

Under LTHC hot corrosion testing conditions it was found that Co-based coatings underwent extensive attack. The overall ranking was in the following order (from best to worst):

Pt-modified  $\beta$ -NiAl > CoCrAlY > Pt-modified CoAl.

- A highly mixed ( $\text{CoO} + \text{Al}_2\text{O}_3 + \text{Cr}_2\text{O}_3$ ) TGO scale formed on Pt-modified CoAl, while primarily CoO formed on CoCrAlY during exposure to the LTHC conditions. The tendency for the latter to form a simpler scale is believed to contribute to its better corrosion resistance. Pt-modified CoAl was more brittle than the CoCrAlY coating, which may have further contributed to the inferior performance of the former.
- Pt-modified CoAl was more brittle than the CoCrAlY coating, which may have contributed to the inferior performance of the former.
- The LTHC hot corrosion attack in Co-based aluminide coatings is attributed to the formation of eutectic  $\text{Na}_2\text{SO}_4\text{-CoSO}_4$  ( $T_{\text{melt}} = 565^\circ\text{C}$ ) liquid. The localized attack in Pt-modified  $\beta$ -NiAl was possibly due to the eutectic  $\text{Na}_2\text{SO}_4\text{-NiSO}_4$  ( $T_{\text{melt}} = 671^\circ\text{C}$ ).
- Platinum addition to Al-rich  $\beta$ -NiAl alloys improves LTHC hot corrosion resistance.

## 5. HOT CORROSION AND OXIDATION BEHAVIOR OF NOVEL $\gamma'$ -Ni<sub>3</sub>Al + $\gamma$ -Ni ALLOYS

### 5.1 Optimization of the High Temperature Hot Corrosion and Oxidation Resistance of Pt+(Cr+Si)+Hf-Modified $\gamma'$ -Ni<sub>3</sub>Al + $\gamma$ -Ni Alloys Containing 22 at.% Al

#### 5.1.1. Introduction

The present study was conducted to assess the HTHC (Type I hot corrosion-900°C) resistance of novel Pt+Hf-modified  $\gamma'+\gamma$  alloy compositions that exhibit excellent oxidation resistance. In addition, this work was carried out to understand the effects of alloying additions such as Cr and Si on the HTHC and oxidation (isothermal and cyclic oxidation-1150°C) resistance of Pt+Hf-modified  $\gamma'+\gamma$  alloys. A targeted significant outcome of this study was the establishment of an optimum coating composition that is highly resistant to both hot corrosion and oxidation.

#### 5.1.2. Experimental

A set of Ni-Al-Pt alloys were prepared by Ar-arc melting with appropriate proportions of high-purity constituent elements. The starting compositions are indicated in the Ni-Al-Pt phase diagram [8] in figure 62. The alloys comprised a  $\gamma'$ -Ni<sub>3</sub>Al+ $\gamma$ -Ni phase constitution and it is seen that the aluminum content was kept constant at 22 at.%, while the platinum content was varied from 0-30 at.%. (Note that all compositions will be reported in atomic percent unless stated otherwise.) With the aim of further improving HTHC resistance of these alloys, 5-20% of Cr was added. Silicon (up to 5 at.%) was also added in some alloys to understand its effect on hot corrosion and oxidation resistance. All of the alloys contained 1wt% Hf, which helps in the formation of an adherent thermally grown oxide (TGO) scale [8]. Table 6 presents the nominal compositions of the alloys (all in at.%) that were prepared for this study. The alloys were drop-cast into the form of rods, 50 mm long and 10 mm in diameter. The as-cast rods were heat treated in flowing argon gas at 1200°C for 6 hours followed by 48 hours at 1150°C to ensure homogenization and equilibration. The heat-treated rods were then sectioned into ~ 1.5 mm thick coupon samples and polished to a 1200-

grit finish. Test samples were ultrasonically cleaned in acetone before hot corrosion and oxidation testing. The HTHC experiments were carried out for 100 hours of total exposure. An additional set of HTHC tests were conducted in which all the specimens were pre-oxidized in a box furnace at 1100°C for 80 hours and then furnace cooled to room temperature.

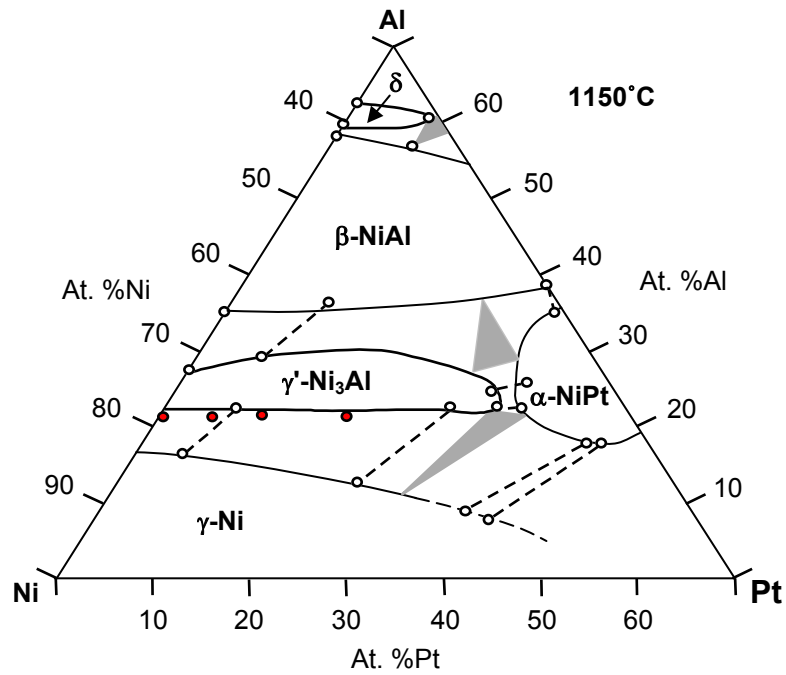


**Fig. 62.** Ni-Al-Pt phase diagram at 1150°C [8] and base compositions studied.

**Table 6.** Nominal composition (at %) of the alloys prepared for HTHC and oxidation testing.

Alloy	Composition (at %)					
	Ni	Al	Pt	Cr	Si	Hf
1	Bal	22	-	-	-	0.4
2	Bal	22	-	5	-	0.4
3	Bal	22	-	5	2.5	0.4
4	Bal	22	5	-	-	0.4
5	Bal	22	5	5	-	0.4
6	Bal	22	5	10	-	0.4
7	Bal	22	5	20	-	0.4
8	Bal	22	5	5	2.5	0.4
9	Bal	22	5	5	5	0.4
10	Bal	22	10	-	-	0.4
11	Bal	22	10	5	-	0.4
12	Bal	22	10	10	-	0.4
13	Bal	22	10	20	-	0.4
14	Bal	22	10	-	5	0.4
15	Bal	22	20	-	-	0.4
16	Bal	22	20	5	-	0.4
17	Bal	22	20	10	-	0.4
18	Bal	22	20	20	-	0.4
19	Bal	22	20	-	5	0.4
20	Bal	22	20	-	10	0.4
21	Bal	22	20	5	5	0.4
22	Bal	22	30	-	-	0.4
23	Bal	27	-	20	-	-
24	Bal	50	15	-	-	-
25	Bal	47	10	-	-	-
26	Bal	37	10	-	-	-

### 5.1.3. Results and Discussion

#### 5.1.3.1. Improving the HTHC Resistance of $\gamma'+\gamma$ Alloys by Alloying Additions and with a Pre-oxidation Treatment

A set of  $\gamma'+\gamma$  alloys with increasing Pt content from 0-30 at.% were tested for HTHC resistance and the mass gains after 100 hours of exposure are shown in figure 63. These alloys were tested with and without the pre-oxidation treatment. Addition of up to 10 at.% Pt to the base binary alloy (Ni-22Al-0.4Hf) significantly improved hot-corrosion resistance (*i.e.*, decreased weight gain due to reaction), but further Pt addition caused the resistance to decrease. Corresponding cross-sectional SEM images of binary and Pt+Hf-modified  $\gamma'+\gamma$  alloys after 100 hours of testing are shown in figure 64. These images confirm that up to 10 at.% Pt addition helped considerably to improve hot corrosion resistance of the alloys, but higher amounts of Pt addition (*i.e.* Ni-22Al-20/30Pt-0.4Hf) showed extensive internal attack. It is relevant to note that previous studies reported that Pt addition to  $\gamma'+\gamma$  superalloys was beneficial to hot corrosion and oxidation resistance [94-97]; however, the level of Pt and Al in those studies was < 3 at.% and 12-14 at.%, respectively, and hence comparatively low.

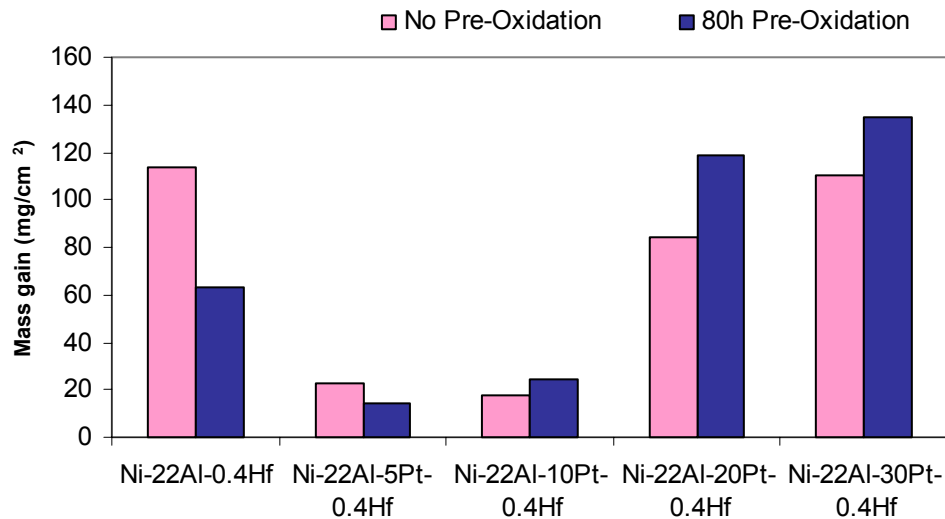


**Figure 63.** Mass gain of  $\gamma'+\gamma$  alloys after a total of 100 hours (5 x 20 h cycles) HTHC at 900°C.

Electron probe microanalysis (EPMA) was used to analyze the corrosion products and phases formed during the testing. The results are summarized in figure 65. In general, the outermost region of the scale products consisted of porous NiO and this was followed by inner layers or zones rich in  $\text{NiAl}_2\text{O}_4$  and  $\text{Al}_2\text{O}_3$ . A Pt-enriched  $\gamma'$  layer typically formed in a given alloy subsurface in contact with the scale. Internal precipitates of  $\text{Ni}_3\text{S}_2$  were commonly detected within a given alloy, beneath the Pt-enrich  $\gamma'$  layer. The extent of  $\text{Ni}_3\text{S}_2$  formation clearly increased with increasing Pt content in the alloy. As shown in figure 65, the  $\text{Ni}_3\text{S}_2$  formation was observed in the Ni-22Al-30Pt-0.4Hf alloy just after 20h of exposure.

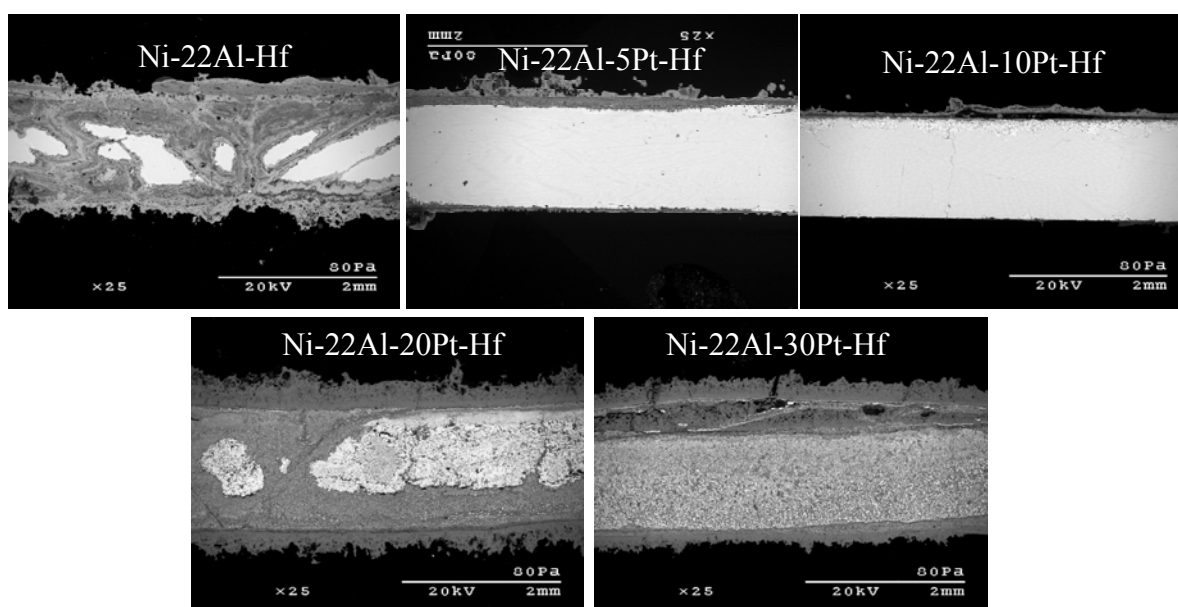


**Figure 64.** Corresponding (figure 63) cross-sectional SEM images of the  $\gamma' + \gamma$  alloys (w/ no pre-oxidation).

It is relevant to note that Izumi and Gleeson [109] have shown that a Pt-free Ni-20Al-Hf alloy indeed forms a non protective  $\text{NiO} + \text{NiAl}_2\text{O}_4$  scale after isothermal oxidation. In figure 64 it is seen that the Pt-free Ni-22Al-Hf alloy underwent intergranular hot corrosion attack; while, the mode of attack was predominantly through the grain boundaries (i.e., intergranular) in the Pt-containing  $\gamma' + \gamma$  alloys. This change in the mode of attack is clearly when comparing from the Pt-free Ni-22Al-0.4Hf alloy to the “high-Pt” Ni-22Al-30Pt-0.4Hf alloy. It is further seen in figure 64 that a relatively low amount of Pt ( $< 10\%$ ) addition markedly improved the hot corrosion resistance of the Ni-22Al-0.4Hf alloy. The beneficial

role of Pt in improving hot corrosion resistance in  $\beta$ -NiAl is well known and its effect in improving oxidation resistance of  $\gamma' + \gamma$  alloys has been studied in detail by Gleeson *et al.* [1, 109] and Pint [92]. Pt addition to Ni-22Al-Hf alloy apparently suppressed NiO formation and promoted more protective alumina scale formation during the HTHC exposure [109]. However, above 10% Pt addition considerably decreased the hot corrosion resistance in  $\gamma' + \gamma$  alloys (figures 63 and 64). Associated with this decreased resistance was a significant amount of  $\text{Ni}_3\text{S}_2$  formation. Thus, the poor performance of “high-Pt”  $\gamma' + \gamma$  alloys (*i.e.* Ni-22Al-20/30Pt-0.4Hf) against HTHC is inferred to be attributed to the liquid  $\text{Ni}_3\text{S}_2$  formation ( $T_m = 787^\circ\text{C}$ ).

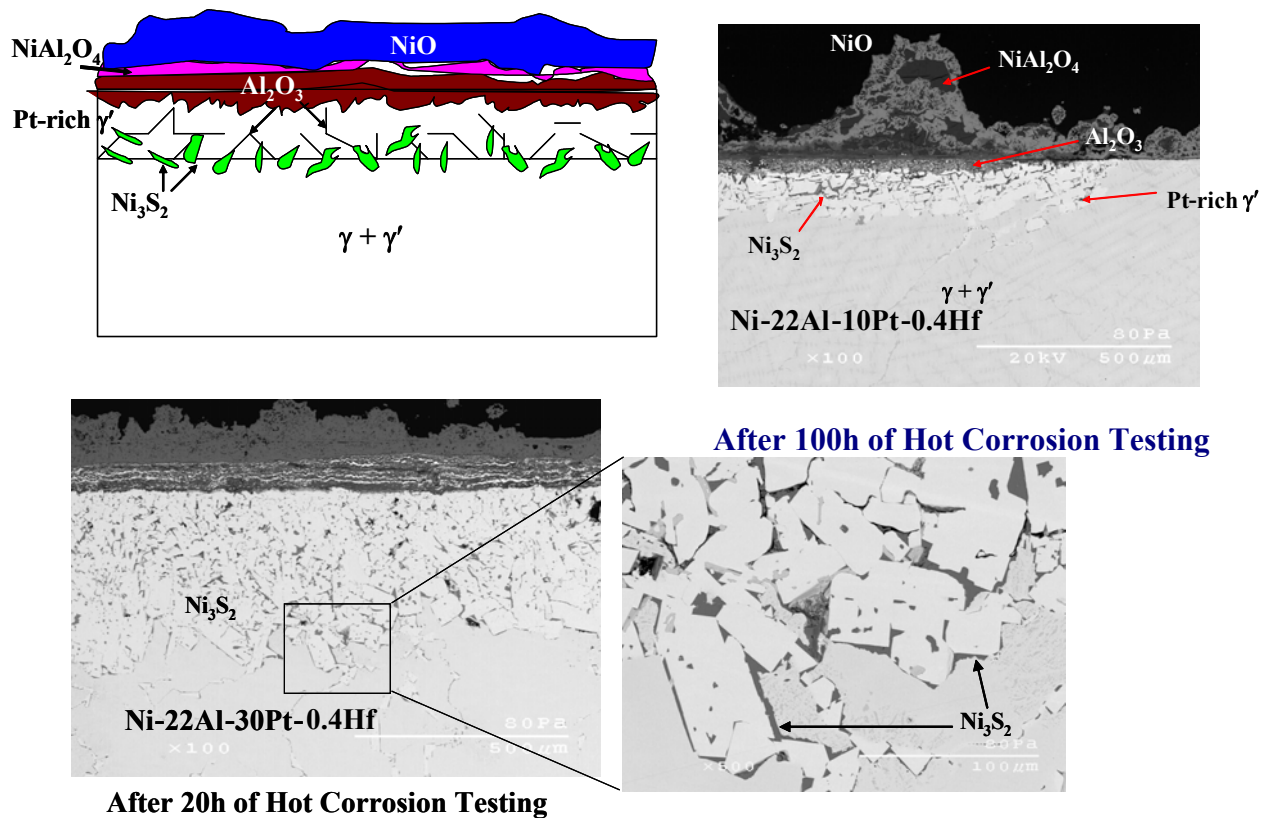
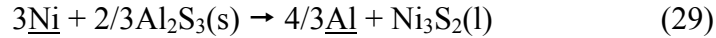


**Figure 65.** Summary of cross-sectional characterization results of the Ni-Al-Pt-Hf  $\gamma' + \gamma$  alloys after hot corrosion at  $900^\circ\text{C}$ .

An Ellingham diagram comparing the stabilities of  $\text{Ni}_3\text{S}_2$  and  $\text{Al}_2\text{S}_3$  is shown in figure 66 [110]. This diagram shows that  $\text{Al}_2\text{S}_3$  is thermodynamically more stable than

$\text{Ni}_3\text{S}_2$  at  $900^\circ\text{C}$  under standard-state conditions in which Al and Ni are in their pure elemental form (*i.e.*, not alloyed and with a chemical activity of unity). However, Copland [111] found in a recent study that Pt addition to  $\gamma'$ - $\text{Ni}_3\text{Al}$  decreases the chemical activity of Al ( $a_{\text{Al}}$ ), but increases the activity of Ni ( $a_{\text{Ni}}$ ) (figures 67 and 68). Thus, increasing Pt eventually favors the formation of  $\text{Ni}_3\text{S}_2$  in preference to  $\text{Al}_2\text{S}_3$ , as given by the following displacement reaction:



where the understroke represents a constituent in the alloy phase. An increase  $a_{\text{Ni}}$  due to Pt addition may also favor direct  $\text{Ni}_3\text{S}_2$  formation by the following reaction,



The higher  $a_{\text{Ni}}$  is, the lower  $a_{\text{S}}$  in the alloy can be for reaction (30). The formation of a liquid would greatly accelerate and enhance the rate of which is consistent with, what is shown in figure 64.

To analyze the displacement reaction (29) further, the law of mass action for this reaction

gives, 
$$K = \frac{a_{\text{Al}}^{4/3}}{a_{\text{Ni}}^3}.$$

Under standard state conditions,  $a_{\text{Al}} = a_{\text{Ni}} = 1$  and therefore, law of mass action constant,

$K = 1$ ; while,  $K_{\text{eq}}$  at  $927^\circ\text{C}$  is calculated to be, 
$$K_{\text{eq}} = \exp\left(\frac{-\Delta G_f^\circ}{RT}\right) = 1.2 \times 10^{-10}.$$
 Therefore,

under standard state conditions reaction (30) is not possible as  $K > K_{\text{eq}}$ . The constant  $K$  can be calculated using the activity measurements made by Copland [111] and the results are summarized in Table 7. Reactions (29) and (30) are thus favored with Pt addition in  $\gamma'$  alloys as  $K < K_{\text{eq}}$ . Moreover, an increase in Pt addition (from 2 to 25%) progressively decreases  $K$ , thereby increasing the driving force for the formation of liquid  $\text{Ni}_3\text{S}_2$  (Table 7). Furthermore, Gulvanitskaya *et al.* studied the Pt-Ni-S system and proposed that a eutectic mixture of  $\text{Ni}_3\text{S}_2$  and Ni-Pt solid solution has a melting region between  $734\text{-}775^\circ\text{C}$  [112]. It is clear that the

formation of liquid exacerbated the extent HTHC degradation of Ni-22Al-20/30Pt-0.4Hf  $\gamma' + \gamma$  alloys.

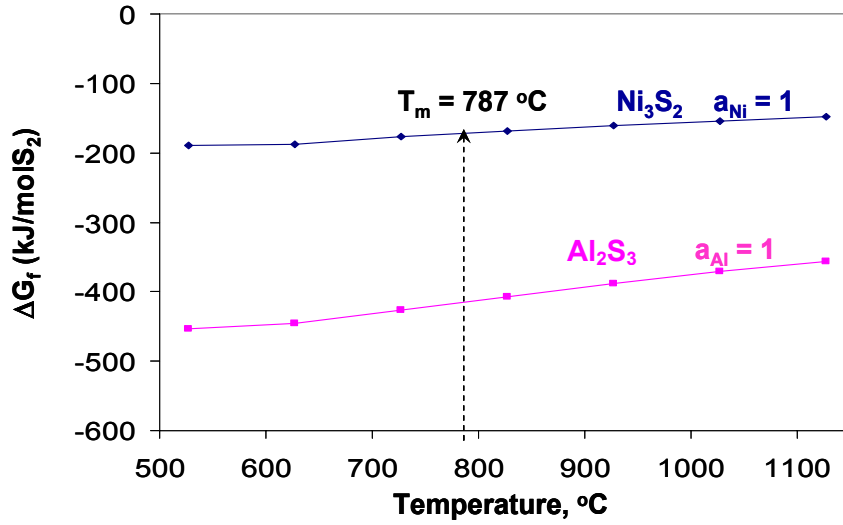


Figure 66. Ellingham diagram for Ni<sub>3</sub>S<sub>2</sub> and Al<sub>2</sub>S<sub>3</sub> formation [110].

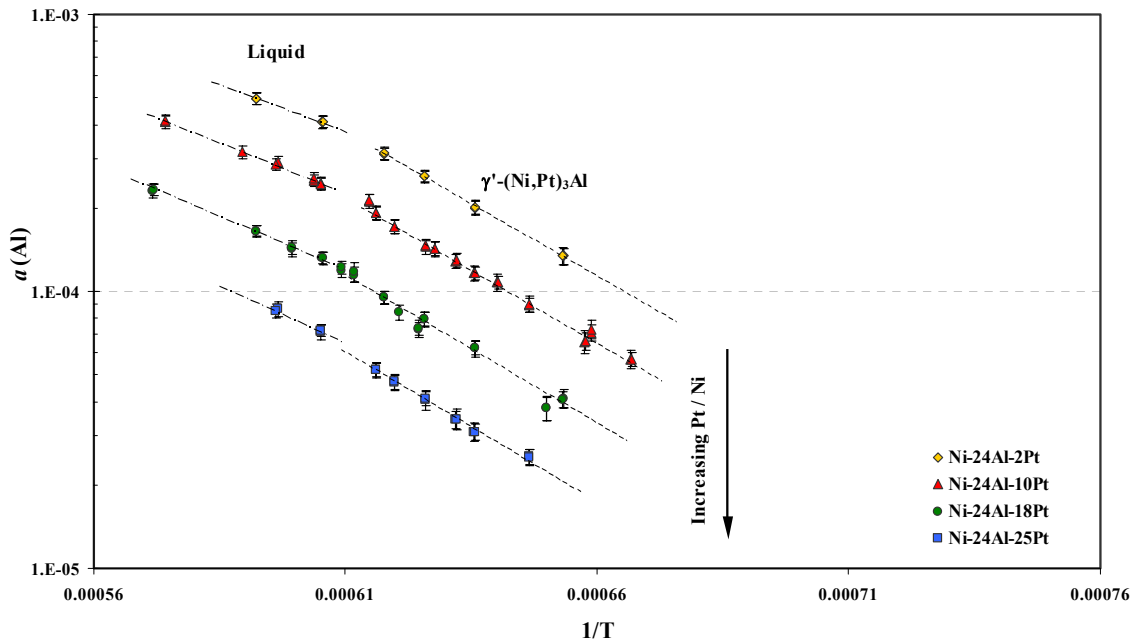
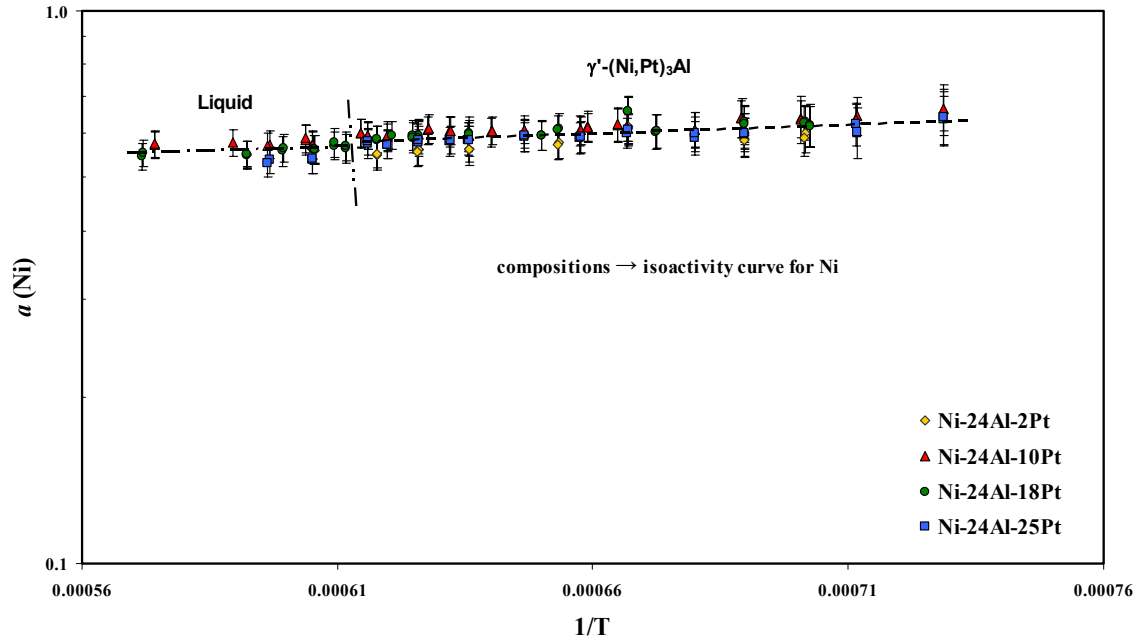


Figure 67. Measured  $a_{Al}$  in  $\gamma'-(Ni,Pt)_3Al$  alloys and liquid [111].



**Figure 68.** Measured  $a_{\text{Ni}}$  in  $\gamma'$ -(Ni,Pt)<sub>3</sub>Al alloys and liquid [111].

**Table 7.** Law of mass reaction constant  $K$  for various  $\gamma'$ -(Ni,Pt)<sub>3</sub>Al alloys calculated using the activity measurements made by Copland [111].

Alloy	$K = a_{\text{Al}}^{4/3} / a_{\text{Ni}}^3$
Ni-24Al-2Pt	$9.6 \times 10^{-24}$
Ni-24Al-10Pt	$8.2 \times 10^{-25}$
Ni-24Al-18Pt	$3.2 \times 10^{-26}$
Ni-24Al-25Pt	$5.9 \times 10^{-27}$

It is well known that Cr and Si additions improve hot corrosion resistance in aluminide coatings and superalloys [68-71]; hence, the effects of Cr and Si additions on the HTHC resistance of Pt+Hf-modified (*i.e.*, 5, 10, and 20%)  $\gamma'$ + $\gamma$  alloys were investigated.

The mass gains of Cr-modified,  $\gamma' + \gamma$  alloys (with 20% Pt) after 100 h HTHC testing are shown in figure 69. These alloys were tested with and without any pre-oxidation treatment. Addition of a relatively low amount of Cr (up to 10%) improved hot corrosion resistance but the improvement increased significantly when a high amount of Cr (20%) was added. Similarly, Si addition (5%) was also found to be beneficial in improving HTHC resistance even without a pre-oxidation treatment. Cross-sectional SEM images shown in figure 70 of pre-oxidized Ni-22Al-20Pt-Cr/Si-0.4Hf alloys after 100h of HTHC confirmed the beneficial effect of Cr and Si additions to the HTHC resistance of an Ni-22Al-20Pt-Hf  $\gamma' + \gamma$  alloy.

It was observed that the “low-Pt” (*i.e.* Ni-22Al-5/10Pt-Hf) containing  $\gamma' + \gamma$  alloys exhibited much improved HTHC resistance than the “high-Pt” (*i.e.* Ni-22Al-20/30Pt-Hf)  $\gamma' + \gamma$  alloys. Hence, to further improve the performance of the best-performing alloys, Cr and Si additions were made to the “low-Pt” containing  $\gamma' + \gamma$  alloys. The mass gains of Cr/Si-modified, “low-Pt” (*i.e.*, 10%)  $\gamma' + \gamma$  alloys after 100 h HTHC testing are shown figure 71. Alloys with as low as 10 and 20% Cr are shown to exhibit excellent HTHC resistance. The final weight gain of the Ni-22Al-10Pt-10Cr-0.4Hf alloy is greatly reduced by a pre-oxidation treatment, whereas, there was apparently no benefit in pre-oxidizing the Ni-22Al-10Pt-20Cr-0.4Hf alloy. Cross-sectional SEM images of pre-oxidized Ni-22Al-10Pt-Cr/Si-0.4Hf alloys after 100h HTHC testing are shown in figure 72. It is seen that Ni-22Al-10Pt-10Cr-0.4Hf and Ni-22Al-10Pt-20Cr-0.4Hf are exceptionally resistant to HTHC. A lower amount of chromium was not beneficial to HTHC resistance, as the Ni-22Al-10Pt-5Cr-0.4Hf showed a considerable amount of spallation even after pre-oxidation treatment. The results for the low-Pt (up to the 10%)  $\gamma' + \gamma$  alloys suggest that the Cr content should be either equal to or greater than Pt content for improved hot-corrosion resistance. It should be noted that the  $\gamma' + \gamma$  phase constitution is retained for the alloys with Cr addition up to 10%. Addition of 20% Cr in Ni-22Al-10/20Pt-Hf alloys resulted in a more complex phase assemblage with the formation of  $\beta$ -NiAl and  $\alpha$ -Cr in addition to the  $\gamma'$  and  $\gamma$  phases. It is seen that the addition of 5% Si to the base Ni-22Al-10Pt-0.4Hf  $\gamma' + \gamma$  alloy is also quite beneficial for improving HTHC resistance, while retaining the  $\gamma' + \gamma$  phase constitution.

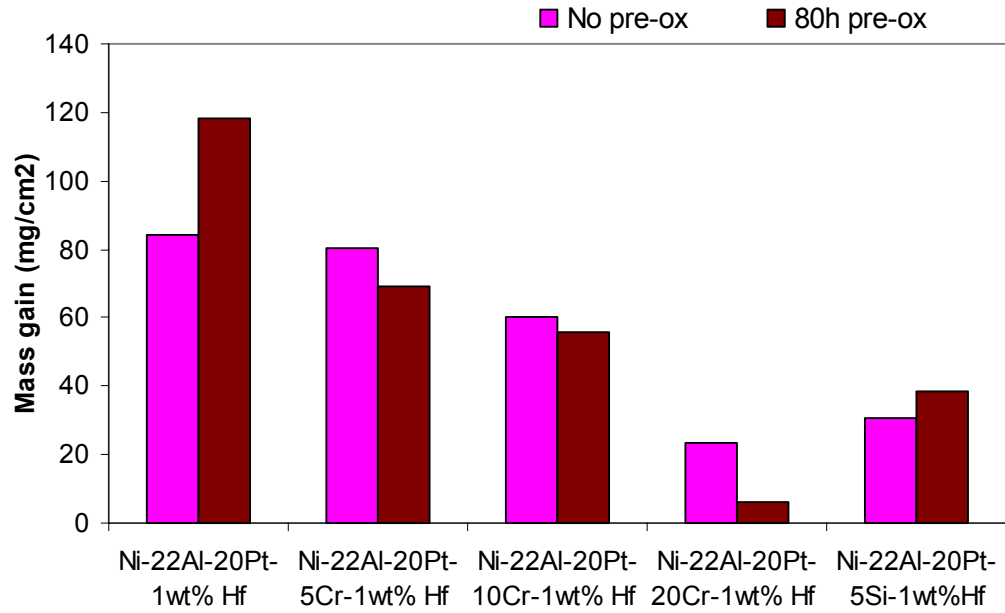


**Figure 69.** Effect of Cr addition on the 900°C hot-corrosion resistance of  $\gamma' + \gamma$  alloys containing 22 at.% Al and 20 at.% Pt.

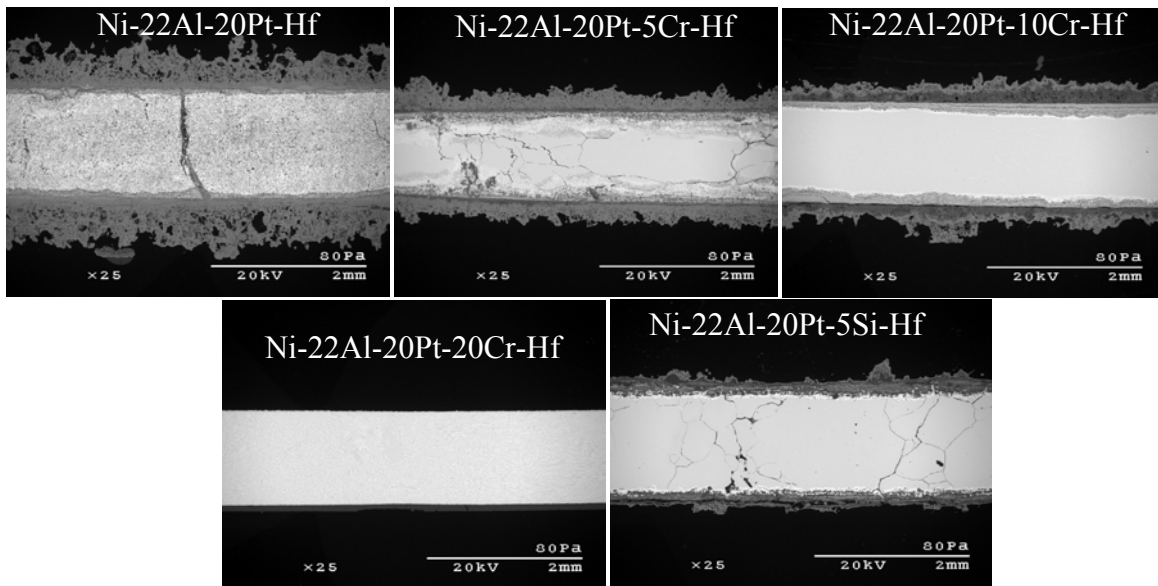


**Figure 70.** Corresponding (figure 69) cross-sectional SEM images of the  $\gamma' + \gamma$  alloys (w/ pre-oxidation).

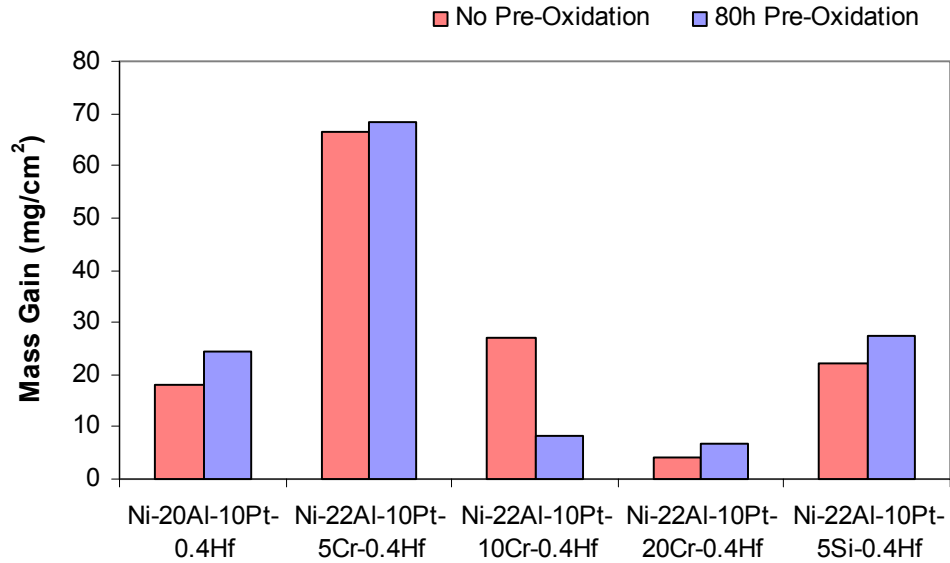


**Figure 71.** Effect of Cr or Si addition on the 900°C hot-corrosion resistance of  $\gamma'$  +  $\gamma$  alloys containing 22 % Al and 10 % Pt.

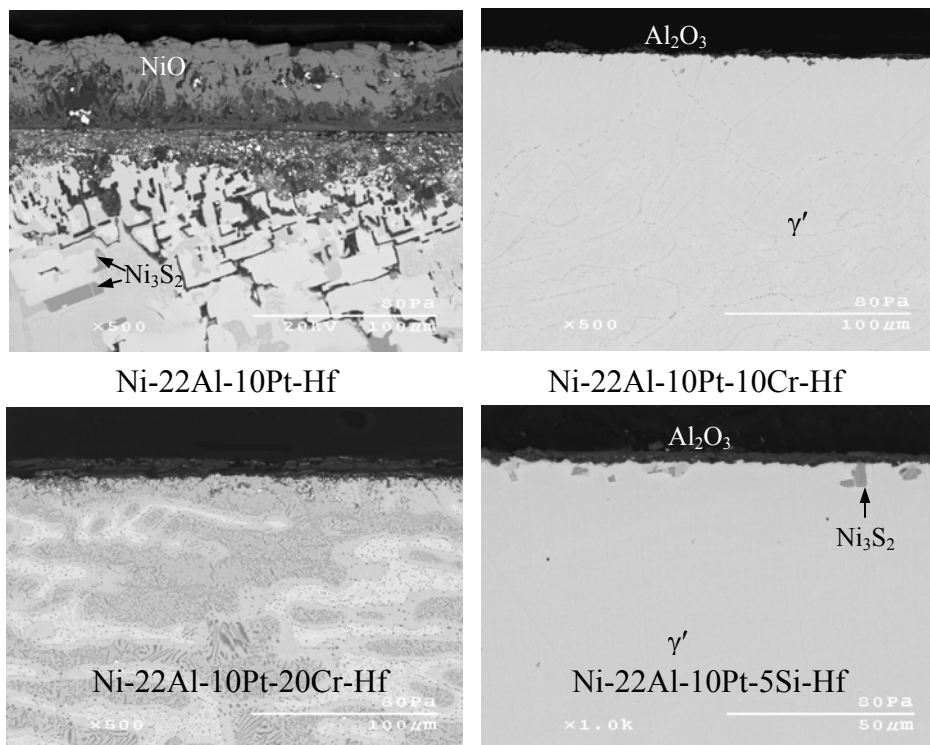


**Figure 72.** Cross-sectional SEM images showing beneficial effect of Cr or Si addition (w/ pre-oxidation) on the HC resistance of  $\gamma'$  +  $\gamma$  alloys containing 22 % Al and 10% Pt.

The mass gains of the various Ni-22Al-5Pt-XCr-Hf alloys with and without pre-oxidation treatment after 100 hours of hot-corrosion exposure at 900°C are shown in figure 73. The pre-oxidized versions of the Cr-modified Ni-22Al-5Pt-Hf alloys exhibited excellent HTHC resistance and addition of as low as 5% Cr is seen to have excellent HTHC resistance. Addition of Si to the Ni-22Al-5Pt-0.4Hf alloy was also beneficial in improving HTHC resistance (figure 73). Interestingly, however, no significant benefit was gained by adding both Si (2.5%) and Cr (5%).

The weight gains of Pt-modified  $\beta$ -NiAl and  $\gamma+\beta$ -NiCrAl alloys after HTHC testing are compared in figure 74 to the better-performing Pt+Cr+Hf-modified  $\gamma'+\gamma$  alloys. The cross-sectional SEM images in figure 75 reveal that the  $\gamma'+\gamma$  alloys with Pt and/or Cr additions have comparable and even significantly better HTHC resistance than conventional  $\beta$  (Ni-37/47Al-10Pt) and  $\gamma+\beta$  (Ni-27Al-20Cr) alloy compositions. The various low-Pt+Cr/Si-modified versions formed an exclusive and protective Al<sub>2</sub>O<sub>3</sub> scale. This scale was established during pre-oxidation exposure and then it persisted during HTHC testing (figure 72 and 75). Some Cr-modified pre-oxidized versions of “low-Pt”  $\gamma'+\gamma$  alloys (*i.e.* Ni-22-5Pt-5/10Cr-Hf and Ni-22Al-10Pt-10Cr-Hf) showed very little or no Al depletion after HTHC testing, indicating their excellent hot corrosion resistance. The Pt-modified  $\beta$  alloy composition Ni-37Al-15Pt exhibited rather poor HTHC.

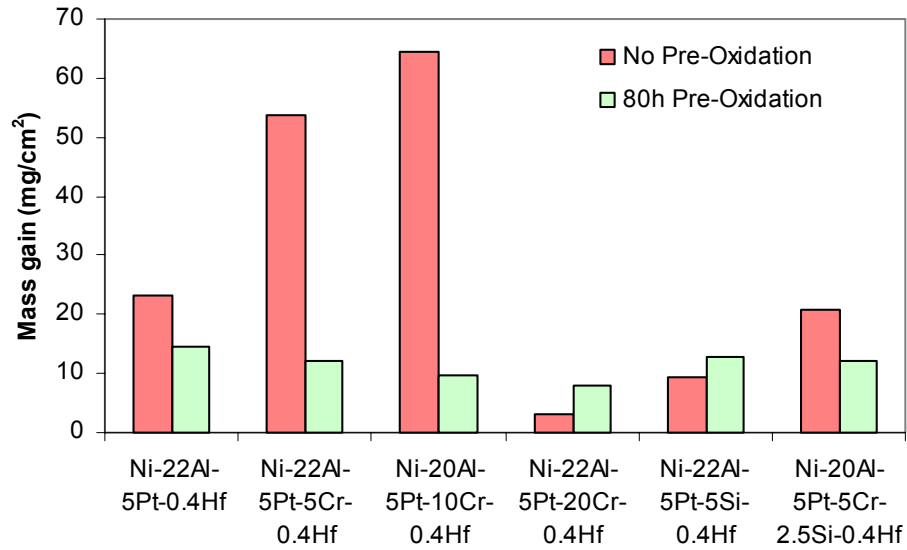


**Figure 73.** Effect of Cr, Si or Cr+Si addition on the 900°C hot-corrosion resistance of  $\gamma'+\gamma$  alloys containing 22 % Al and 5% Pt.

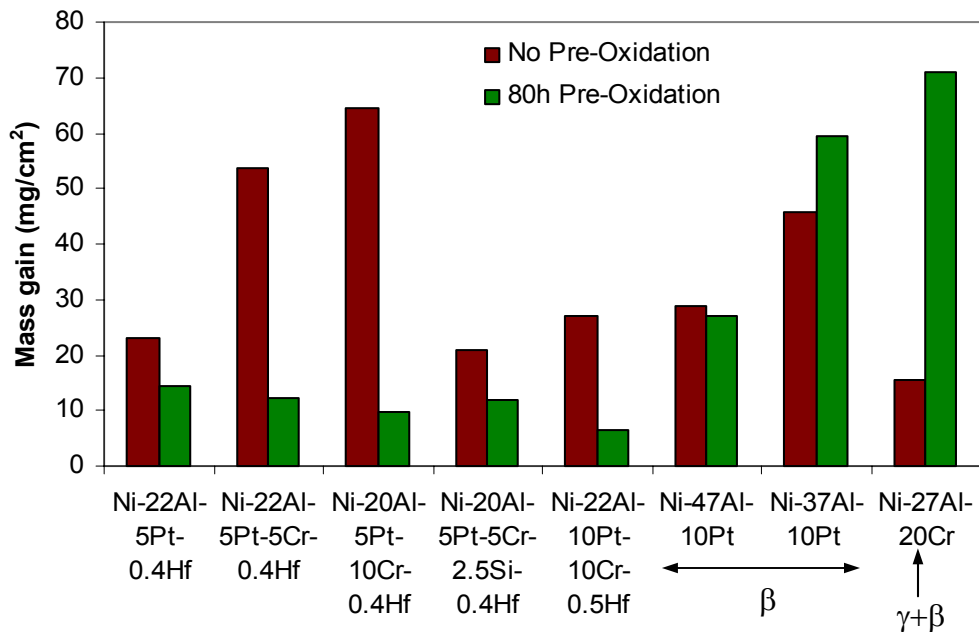


**Figure 74.** Comparison of the HTHC of various  $\gamma'+\gamma$ ,  $\beta$ , and  $\gamma+\beta$  alloys after a total of 100 hours of HTHC at 900°C.

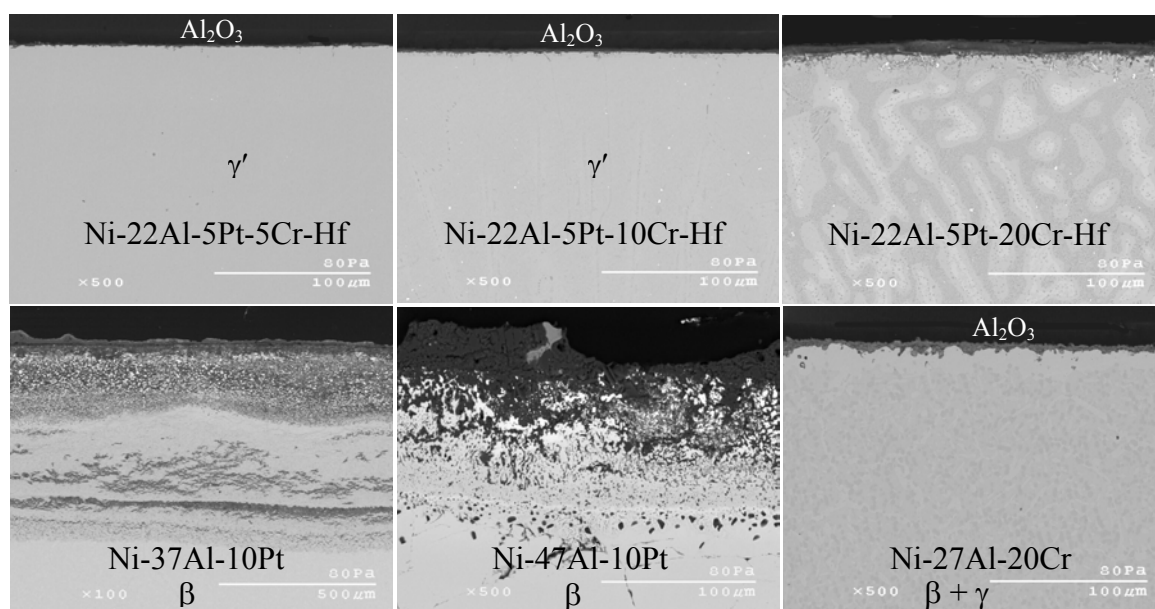


**Figure 75.** Cross-sectional SEM images of pre-oxidized Ni-22Al-5Pt-Cr-Hf  $\gamma' + \gamma$  alloys, Ni-37/47Al-10Pt  $\beta$  alloys, and non pre-oxidized Ni-27Al-20Cr  $\gamma + \beta$  alloy after 100h of HTHC.

### 5.1.3.2 Effects of Alloying Additions on the Oxidation Behavior of Modified $\gamma' + \gamma$ Alloys

#### 5.1.3.2A Isothermal Oxidation (1150°C)

The beneficial effect of Pt addition on the oxidation resistance in Hf-modified  $\gamma' + \gamma$  alloys is indicated in figure 76. Addition of 5Cr and 5Cr+2.5Si to a Ni-22Al-0.4Hf base alloy considerably improved oxidation resistance from the standpoint of weight gain; however, these additions did promote some scale spallation. By contrast, the scale was extremely adherent on the Pt+Hf-modified  $\gamma' + \gamma$  alloy. XRD analysis performed on these alloys confirmed the formation of an  $\alpha$ -Al<sub>2</sub>O<sub>3</sub> scale on the Cr(+Si)+Hf- and Pt+Hf-modified  $\gamma' + \gamma$  alloys; while, the scale formed on the binary Ni-22Al-Hf alloy was adherent but consisted of NiO, NiAl<sub>2</sub>O<sub>4</sub>, and Al<sub>2</sub>O<sub>3</sub>.

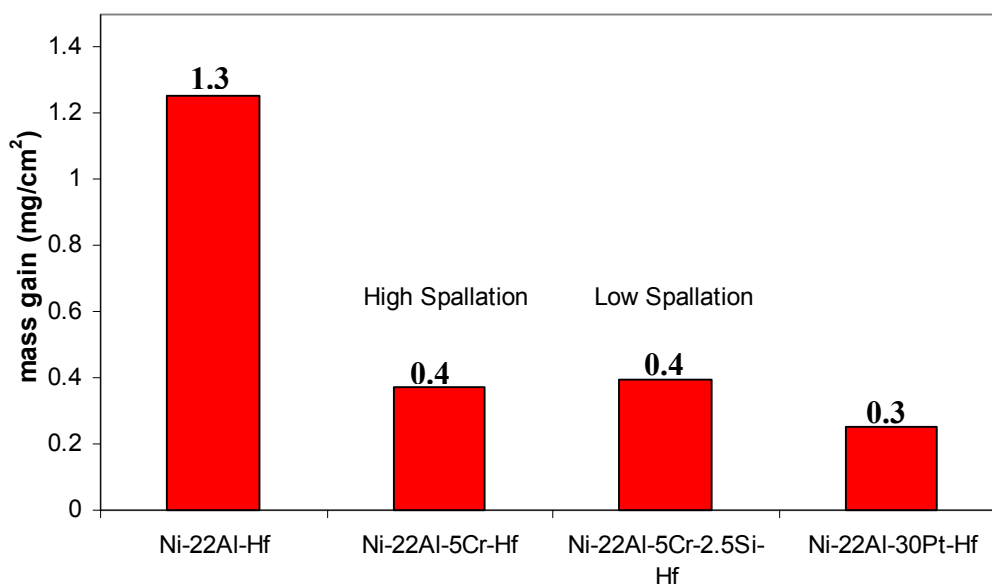


**Figure 76.** Comparison of the effect of Cr, Si, and Pt addition on the 1150°C oxidation resistance of  $\gamma' + \gamma$  alloys exposed to air for 100 hours and containing a fixed Al content of 22% Al.

The effects of Cr and Si addition were studied on the Ni-22Al-20Pt-0.4Hf base alloy and mass gains after 100h of isothermal oxidation are shown in figure 77. It was observed that a higher amount of Cr addition *i.e.*, 20%, resulted in a higher mass gain; while, 5%Si addition was quite beneficial in improving oxidation resistance of the base alloy. Addition of 5% Cr to the Ni-22Al-20Pt-Hf alloy was not detrimental to the oxidation resistance; whereas, 10% Cr addition resulted in localized scale spallation. Representative cross-sectional SEM images in figure 78 show that an Al-depletion zone was not present when up to 10% Cr is added to the Ni-22Al-20Pt-Hf base alloy. It was observed from the HTHC experiments that the Ni-22Al-20Pt-20Cr-Hf alloy had excellent HTHC resistance; however, this alloy exhibited rather poor oxidation resistance. The cross-sectional SEM images shown in figure 78 indicate that the higher mass gain for the Ni-22Al-20Pt-20Cr-Hf alloy was indeed due to the growth of a thick Al-rich outer scale and internal HfO<sub>2</sub>. Figure 78 also indicates that the  $\alpha$ -Al<sub>2</sub>O<sub>3</sub> scale that formed on the Ni-22Al-20Pt-5Si alloy was thin, planar, and adherent.

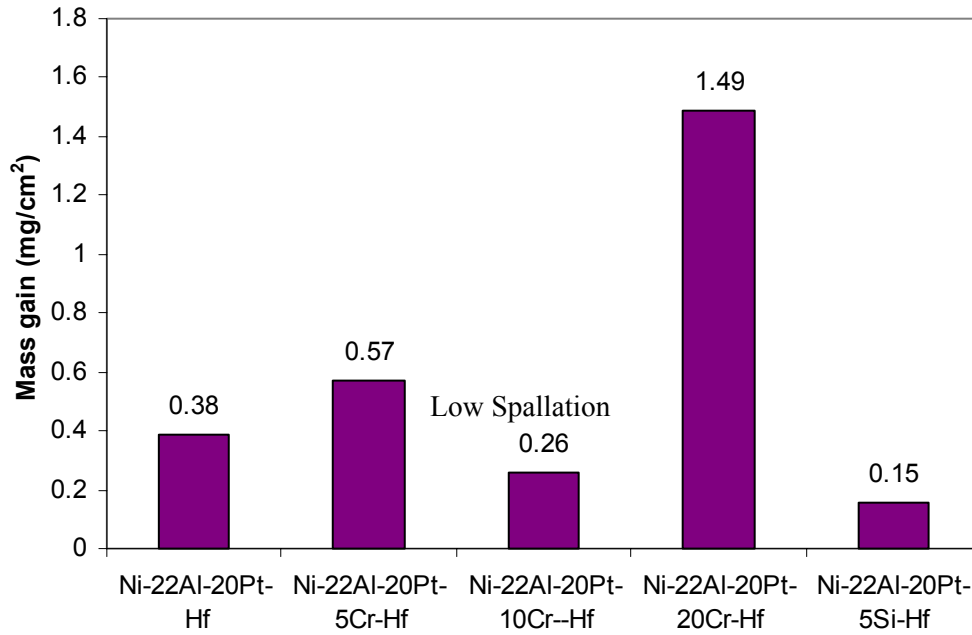


**Figure 77.** Comparison of the effect of Cr and Si addition on the 1150°C oxidation resistance of  $\gamma+\gamma'$  alloys exposed to air for 100 hours and containing a fixed Al content of 22% Al and Pt content of 20%.

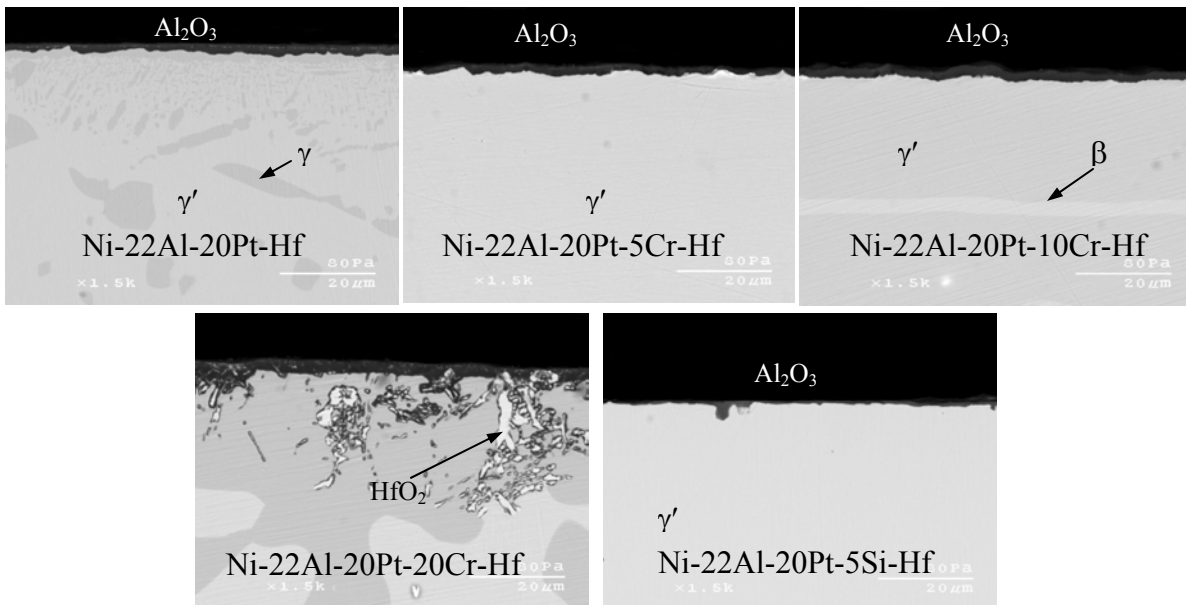


**Figure 78.** Corresponding (figure 77) SEM images of Ni-22Al-20Pt-Cr/Si-0.4Hf alloys after 100h of isothermal oxidation at 1150°C.

It was found in the previous section that Cr or Si addition was also beneficial in improving HTHC resistance of a base Ni-22Al-10Pt-Hf alloy. In fact, certain versions of the Cr/Si-modified Ni-22Al-10Pt-Hf alloy had excellent HTHC resistance. The weight gains of various Ni-22Al-10Pt-Cr/Si-Hf alloys after 100 hours isothermal oxidation at 1150°C in air are shown in figure 79. Scale spallation was observed with 5% Cr addition, but it was quite adherent with 10% Cr addition. The Ni-22Al-10Pt-20Cr-Hf alloy, having the highest Cr content tested, exhibited high mass gain and poor overall oxidation resistance. It was observed that 5% Si addition considerably improved oxidation resistance, resulting in the lowest apparent weight gain.

SEM imaging of Ni-22Al-10Pt-Hf revealed a subsurface Al-depletion zone of  $\gamma$  below the scale (figure 80). Chromium addition (up to 10%) considerably decreased the presence of this zone in Ni-22Al-10Pt-Cr-Hf alloys and the zone was completely absent in the Si-containing alloy, which formed a very thin and adherent  $\text{Al}_2\text{O}_3$  scale. The Ni-22Al-10Pt-10Cr-Hf alloy also exhibited excellent HTHC resistance; however, it should be noted that at 1150°C this alloy contained  $\beta$  precipitates, as shown in figure 80.

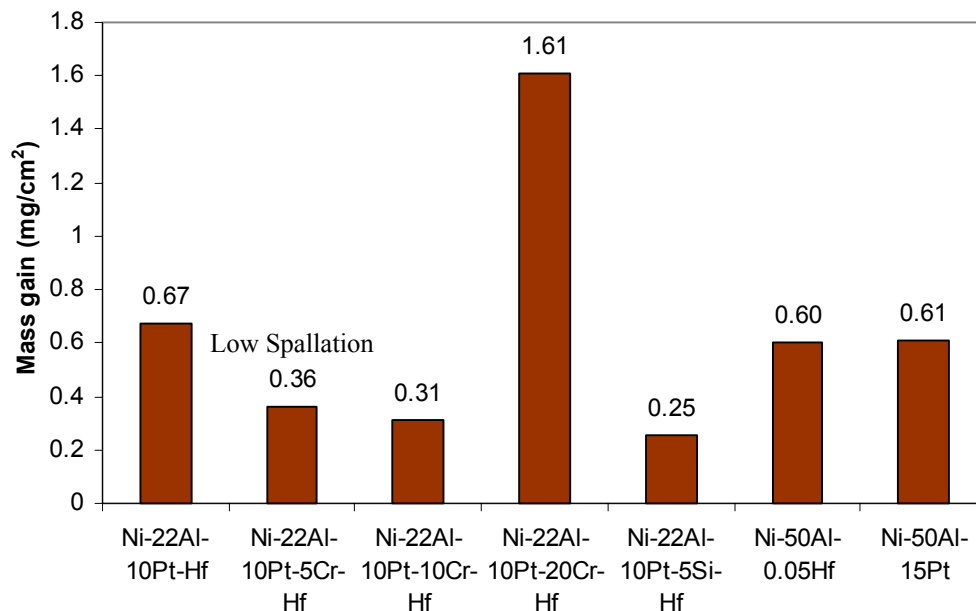


**Figure 79.** Comparison of the effect of Cr and Si addition on the 1150°C oxidation resistance of  $\gamma+\gamma'$  alloys exposed to air for 100 hours and containing a fixed Al and Pt content of 22% and 10% respectively.

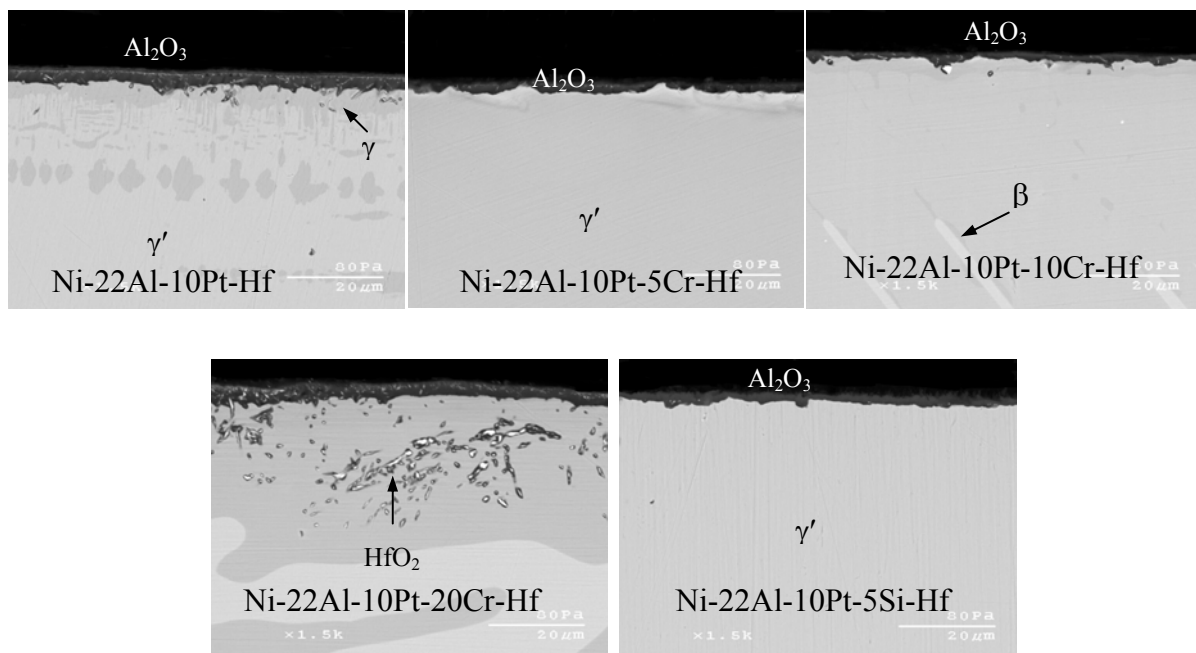


**Figure 80.** Corresponding cross-sectional SEM images (figure 79) of Ni-22Al-10Pt-Cr/Si alloys after 100h of isothermal oxidation at 1150°C.

HTHC results also indicated that certain compositions of the Cr+Si-modified Ni-22Al-5Pt-Hf alloys have excellent HTHC resistance; hence, isothermal oxidation testing of these alloys was carried out in air at 1150°C. Resulting weight gains and corresponding cross-sectional SEM images of selected alloys are shown in figures 81 and 82, respectively. The weight gains of selected Pt-and Hf-modified  $\beta$  alloys are also included in figure 81 for comparison. None of the modified versions of Ni-22Al-5Pt-Hf alloys showed spallation after testing.

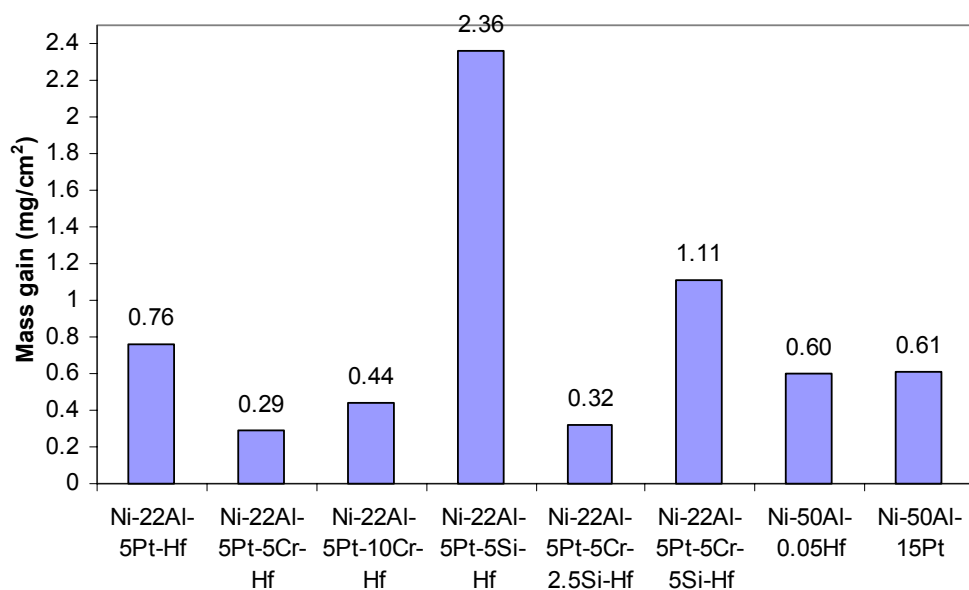


**Figure 81.** Comparison of the effect of Cr, Si and Cr+Si addition on the 1150°C oxidation resistance of  $\gamma+\gamma'$  alloys exposed to air for 100 hours and containing a fixed Al content of 22% Al and Pt content of 5%.

Addition of Cr (up to 10%) was quite beneficial in improving oxidation resistance, resulting in lower weight gains than the Ni-22Al-5Pt-Hf alloy; while 5% Si addition resulted in a higher weight gain after 100h of exposure. The Cr-modified versions of Ni-22Al-5Pt-Hf alloy showed much lower weight gains than the Pt- and Hf-modified  $\beta$  alloys (*i.e.* Ni-50Al-15Pt and Ni-50Al-0.05Hf), indicating improved performance over the  $\beta$  alloys. The combined effect of 5Cr+2.5Si addition was also studied using the Ni-22Al-5Pt-Hf alloy and it was found that a relatively low amount of Si addition (2.5%) was beneficial in improving oxidation resistance, while a higher amount of Si addition (5%) was deleterious and resulted in stabilizing the  $\beta$  phase. The Ni-22Al-5Pt-Hf alloy formed a continuous scale consisting of an outermost layer of NiAl<sub>2</sub>O<sub>4</sub>; whereas, chromium addition to Ni-22Al-5Pt-Hf suppressed NiAl<sub>2</sub>O<sub>4</sub> formation and promoted the exclusive formation of an  $\alpha$ -Al<sub>2</sub>O<sub>3</sub> layer (figure 82). An Al-depletion zone of  $\gamma$  phase (>20  $\mu$ m) was observed in the subsurface region of the Ni-22Al-5Pt-Hf alloy. This zone was not observed in the Ni-22Al-5Pt-5Cr-Hf and Ni-22Al-5Pt-5Cr-2.5Si-Hf alloys, which also exhibited excellent oxidation resistance (*i.e.*, the lowest

weight gains). SEM images of these alloys indicated formation of thin  $\alpha$ -Al<sub>2</sub>O<sub>3</sub> scales; while, 10% Cr addition resulted in higher percentage of HfO<sub>2</sub> formation within the scale and the alloy subsurface (figure 82).

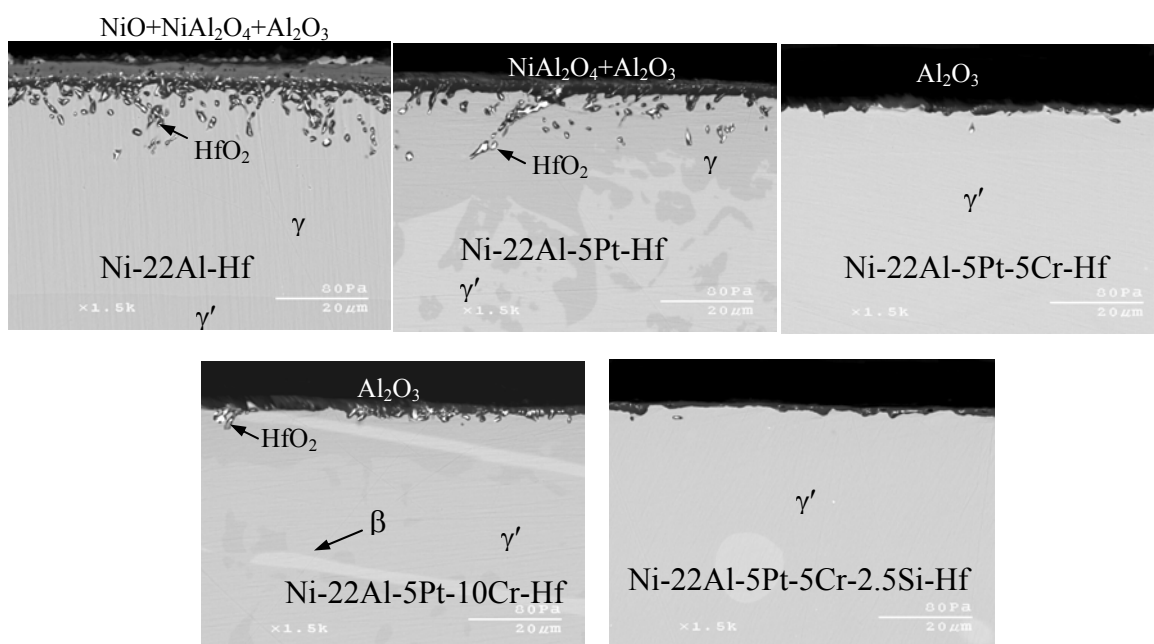


**Figure 82.** Corresponding (figure 81) cross-sectional SEM images of Ni-22Al-5Pt-Cr/Si alloys after 100h of isothermal oxidation at 1150°C.

### 5.1.3.2B Cyclic Oxidation (1150°C)

The results presented thus far show that Cr addition to “low Pt” Ni-22Al-5/10Pt-Hf alloys is highly beneficial to both HTHC and isothermal oxidation resistance. The cyclic oxidation kinetics of Pt(+Cr)+Hf-modified  $\gamma'$ + $\gamma$  alloys are shown in figure 83. The cyclic oxidation behavior of the established, oxidation-resistant Ni-22Al-30Pt-Hf [8] and a Pt-modified  $\beta$ -NiAl (Ni-50Al-15Pt) alloys [109] is also included in this figure for comparison. It is seen that the Pt+Hf-modified  $\gamma'$ + $\gamma$  alloys showed positive weight-change kinetics with no indication of spallation throughout the 500 one-hour thermal cycles. Further, the amount of weight gain decreased with increasing Pt content from 0 to 30%. The Ni-22Al-5Pt-Hf alloy exhibited good oxidation resistance that was comparable to the Pt-modified  $\beta$ -NiAl. The Pt+Cr+Hf-modified  $\gamma'$ + $\gamma$  alloys, in particular Ni-22Al-5Pt-5Cr-Hf and Ni-22Al-10Pt-10Cr-

Hf, exhibited excellent oxidation resistance throughout the 500 cycles of testing. In fact, the Ni-22Al-5Pt-5Cr-Hf alloy showed the lowest weight gain of  $0.39 \text{ mg/cm}^2$ , with no visible scale spallation after 500 cycles. The Ni-22Al-10Pt-10Cr-Hf alloy showed a little spallation, but overall had excellent oxidation resistance. Addition of higher Cr (10%) to Ni-22Al-5Pt-Hf increased the weight gain, but it was still comparable to the Pt-modified  $\beta$ . XRD analysis showed  $\alpha$ - $\text{Al}_2\text{O}_3$  scale formation on all alloys except for Ni-22Al-Hf and Ni-22Al-5Pt-Hf. The former of these alloys showed NiO,  $\text{NiAl}_2\text{O}_4$ , and  $\text{Al}_2\text{O}_3$  formation, while the latter showed  $\text{NiAl}_2\text{O}_4$  and  $\text{Al}_2\text{O}_3$  (figure 84), indicating that Pt addition suppressed NiO formation. Further, addition of 5% Cr to Ni-22Al-5Pt-Hf alloy also suppressed  $\text{NiAl}_2\text{O}_4$  formation and resulted in the formation of an exclusive of an  $\text{Al}_2\text{O}_3$  scale, as seen from the surface morphologies (figure 84) of these alloys after cyclic oxidation testing. Figure 85 shows corresponding cross-sectional SEM images of the set of Ni-22Al-Pt-Cr-Hf alloys. An Al-depleted subsurface zone of  $\gamma$ -Ni was observed in the Ni-22Al-5Pt-Hf alloy, which had also formed a duplex scale structure comprised from outside-to-inside of  $\text{NiAl}_2\text{O}_4$  and  $\text{Al}_2\text{O}_3$ . The Ni-22Al-5Pt-5Cr-Hf and Ni-22Al-10Pt-10Cr-Hf alloys formed a very thin, continuous, and adherent  $\text{Al}_2\text{O}_3$  scale. A very thin subsurface zone of  $\gamma$ -Ni was observed in the Ni-22Al-10Pt-10Cr-Hf alloy. The Ni-22Al-5Pt-10Cr-Hf alloy formed a relatively thick  $\text{Al}_2\text{O}_3$  scale and a high percentage of  $\text{HfO}_2$ , which led to a higher weight gain compared to other Pt+Hf+Cr-modified versions.

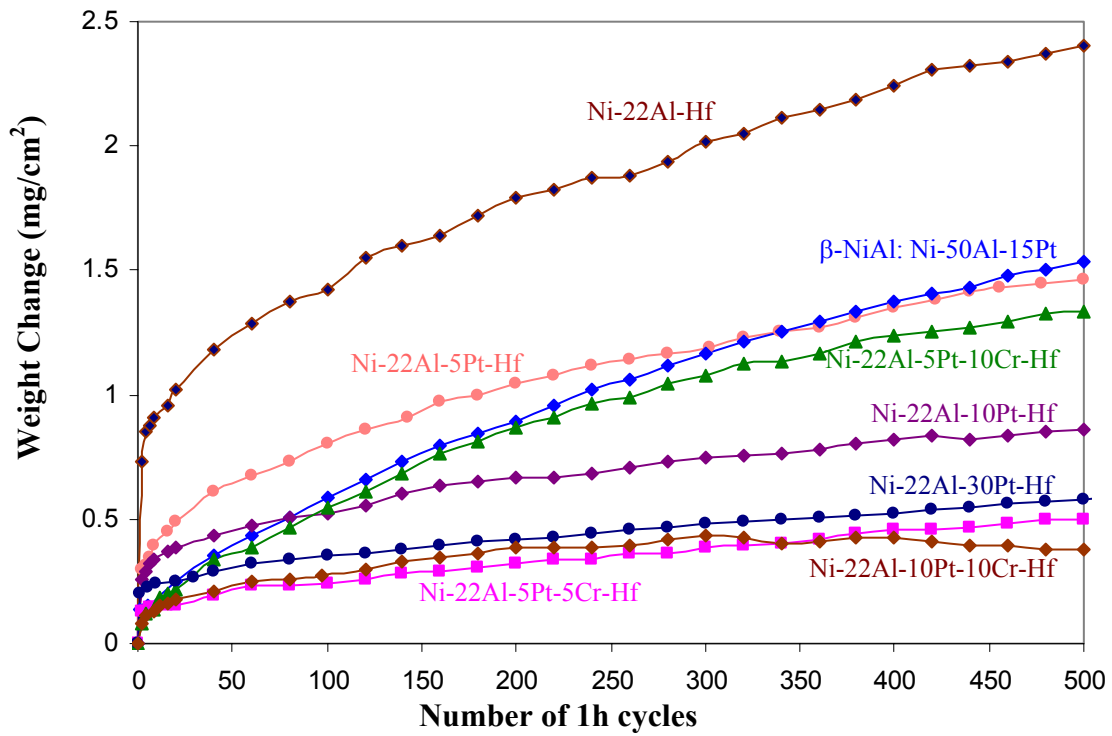


**Figure 83.** Cyclic oxidation kinetics at 1150°C in air.

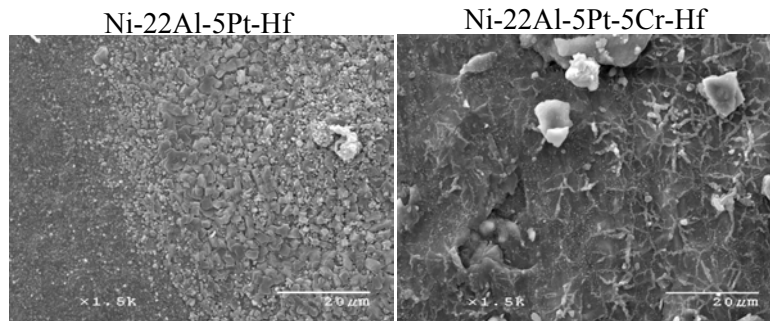


**Figure 84.** Surface morphologies of Ni-22Al-5Pt-Hf with and without Cr addition.

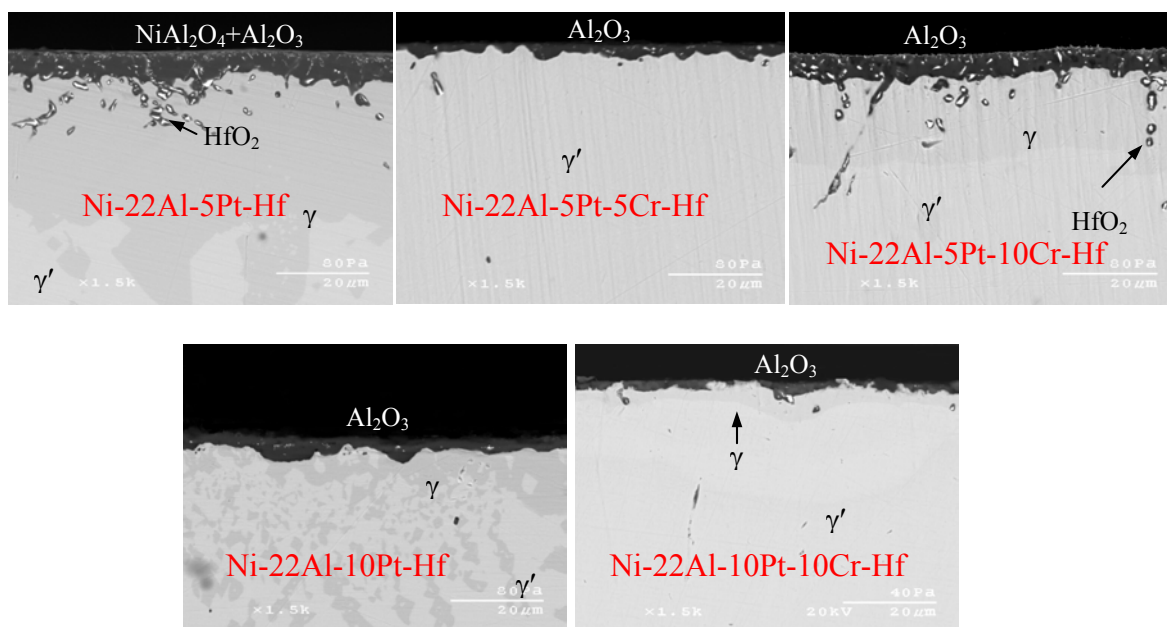


**Figure 85.** Corresponding (figure 83) cross-sectional images of the Ni-22Al-Pt-Cr-Hf alloys after 500 one-hour cycles at 1150°C in air.

It was observed that Cr addition of up to 10% in low-Pt containing  $\gamma' + \gamma$  alloys (e.g. Ni-22Al-5Pt-5Cr-0.4Hf and Ni-22Al-10Pt-10Cr-0.4Hf) was beneficial in improving cyclic oxidation and hot corrosion resistance with a pre-oxidation treatment. It was also found that the untreated alloy with up to 20% Cr addition of in Pt+Hf-modified  $\gamma' + \gamma$  alloys was highly beneficial in improving HTHC resistance. Cyclic oxidation weight-change kinetics of Pt+Cr+Hf-modified alloys having higher Cr content (20%) are shown in figure 86. It was found that the higher percentage of Cr addition in these alloys resulted in higher weight gains after 500 cycles. Cross-sectional SEM images of high-Cr-containing alloys showed the presence of a thick Al-rich outer scale and internal HfO<sub>2</sub> formation after cyclic oxidation (figure 87).

Cyclic oxidation weight-gain kinetics of the Pt+Si+Hf-modified  $\gamma' + \gamma$  alloys (Ni-22Al-XPt-5Si) are shown in figure 88. The addition of 5Si to the Ni-22Al-10Pt-Hf alloy considerably reduced the short-term oxidation kinetics and, in turn, reduced the overall weight gain. A similar trend was seen for 5Si addition to the Ni-22Al-20Pt-Hf alloy. For the various modified  $\gamma' + \gamma$  alloys tested, the lowest weight gain of 0.36mg/cm<sup>2</sup> was observed for

Ni-22Al-20Pt-5Si-Hf. It should be noted that a similar beneficial effect was not observed in Ni-22Al-5Pt-5Si-Hf alloy, suggesting that Si addition is beneficial only if the alloy is able to form a protective alumina scale. Indeed, Ni-22Al-10/20Pt-Hf alloys were alumina formers but Ni-22Al-5Pt-Hf alloy formed spinel and alumina after oxidation testing.

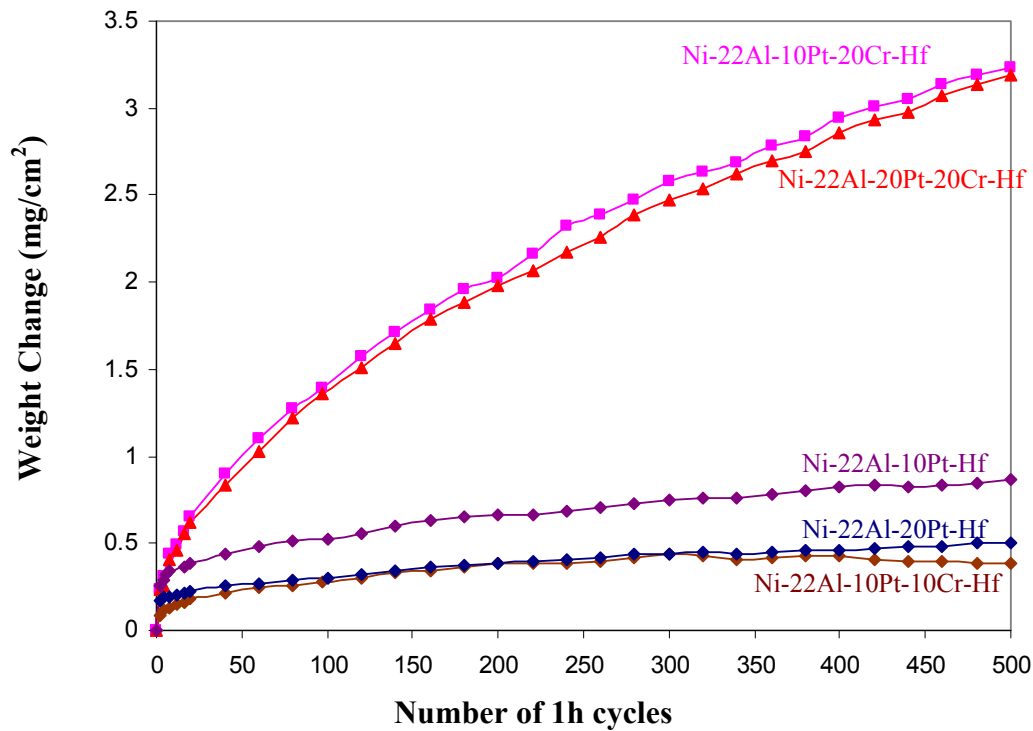


**Figure 86.** Effect of Cr addition in Ni-22Al-10/20Pt-Hf on cyclic oxidation kinetics at 1150°C in air.

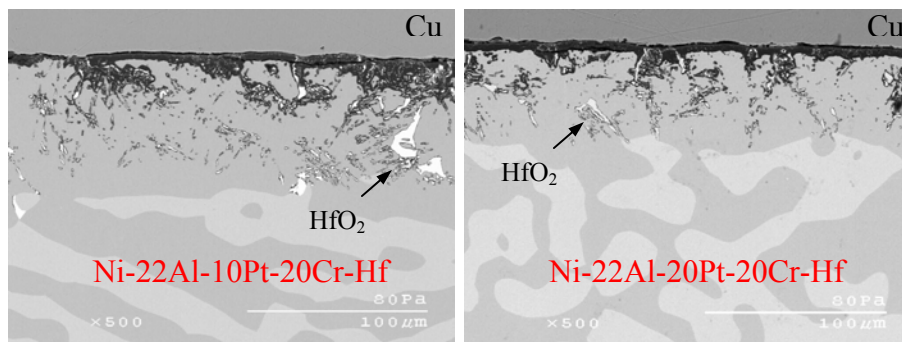


**Figure 87.** Corresponding (figure 86) cross-sectional images of the Ni-22Al-10/20Pt-20Cr-Hf alloys after 500 one-hour cycles at 1150°C in air.

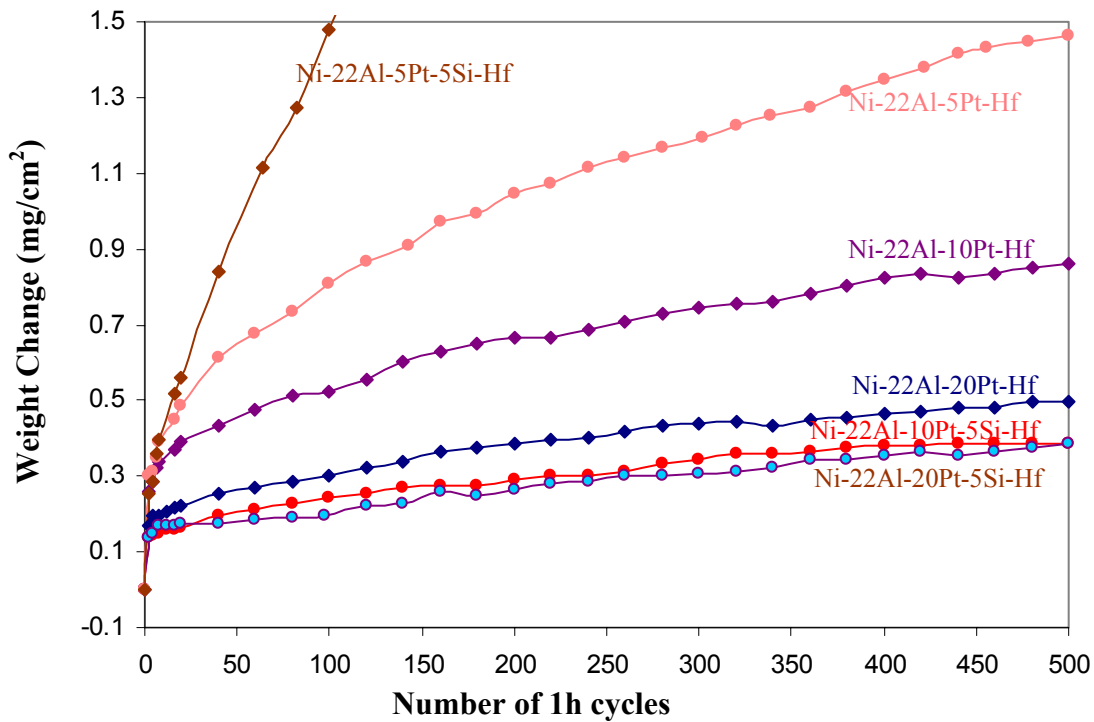


**Figure 88.** Effect of Si on cyclic oxidation kinetics at 1150°C in air.

The combined effect of Cr+Si addition on cyclic oxidation behaviour was studied in “low-Pt” (5%)  $\gamma'+\gamma$  alloys. As summarized in figure 89, the Ni-22Al-5Pt-5Cr-2.5Si-Hf alloy exhibited excellent cyclic oxidation resistance. It is recalled that the Ni-22Al-5Pt-5Cr-Hf and Ni-22Al-5Pt-5Cr-2.5Si-Hf alloys also exhibited excellent HTHC resistance with pre-oxidation treatment. Addition of Cr without Pt in  $\gamma'+\gamma$  alloys showed spallation after just 60 cycles, suggesting that Pt improves scale adhesion on the  $\gamma'+\gamma$  alloys (figure 89). The effect of 5Cr+2.5Si addition without Pt addition was also studied and spallation was observed, but to a lower extent than for the Ni-22Al-5Cr-0.4Hf alloy. XRD analysis of these Pt-free  $\gamma'+\gamma$  alloys (*i.e.* Ni-22Al-5Cr-2.5Si-Hf and Ni-22Al-5Cr-Hf) indicated formation of  $\text{Al}_2\text{O}_3$ , but the scale formed was not adherent compared to Pt(+Cr)+Hf-modified  $\gamma'+\gamma$  alloys. Corresponding surface and cross-sectional SEM images of the modified  $\gamma'+\gamma$  alloys are shown in figure 90. The Pt+Si+Hf- modified  $\gamma'+\gamma$  alloys formed a very thin but continuous  $\alpha\text{-Al}_2\text{O}_3$  scale. The scales on these alloys did not show any evidence of  $\text{HfO}_2$  formation, which may be related to

the reduced initial-stage oxidation kinetics of these alloys. The Ni-22Al-5Pt-5Cr-2.5Si-Hf alloy also formed a thin and continuous  $\alpha$ -Al<sub>2</sub>O<sub>3</sub> scale.

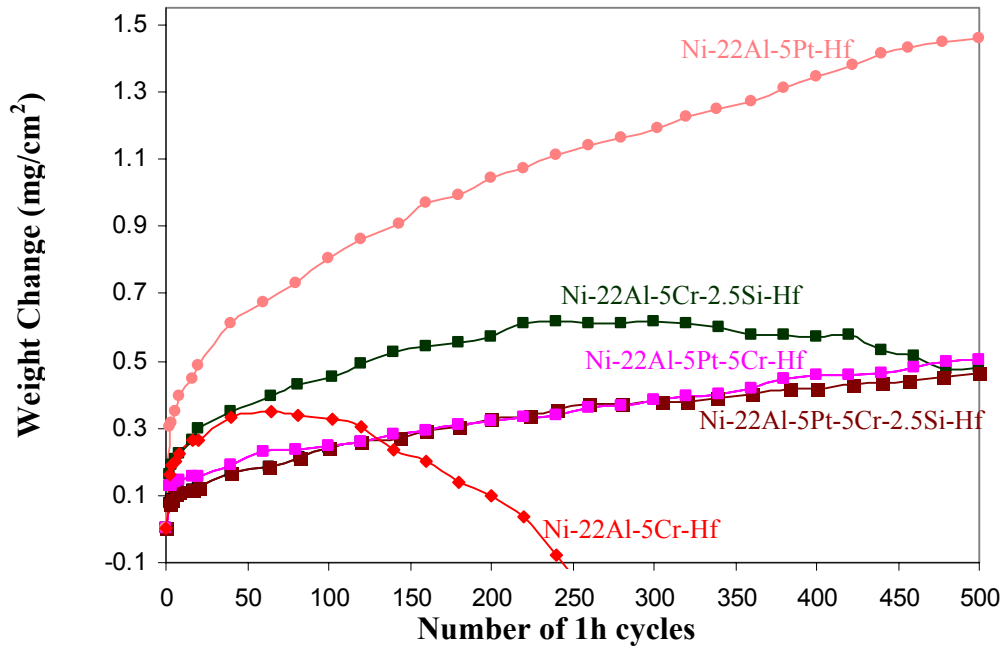


**Figure 89.** Effect of Cr and Cr+Si on cyclic oxidation kinetics at 1150°C in air.

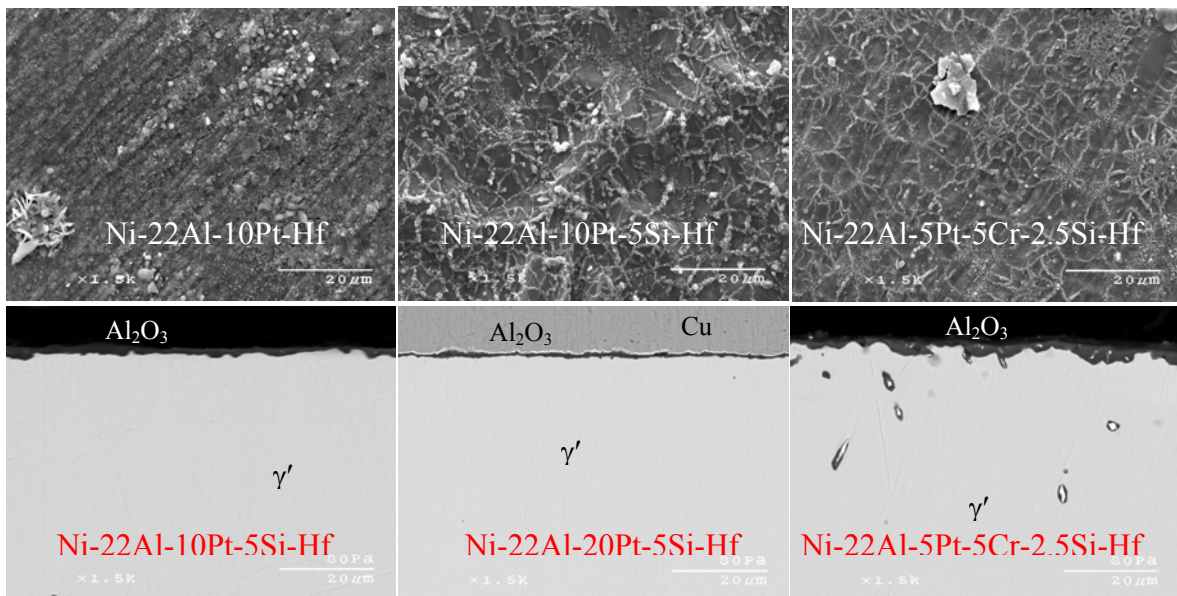


**Figure 90.** Corresponding surface and cross-sectional SEM images of the modified  $\gamma'$  +  $\gamma$  alloys after 500 one-hour oxidation cycles at 1150°C in air.

Figure 91 summarizes the steady-state parabolic rate constants  $k_p$ , of these modified  $\gamma'$ -based alloys, as determined from regression of the cyclic data plotted as mass gain vs.  $t^{1/2}$  and disregarding the first 100 cycles. In accordance with the observed to kinetics behaviors,  $k_p$  values decreased with systematic additions of Cr and/or Si to the Pt+Hf-modified  $\gamma'+\gamma$  alloys. Moreover and as shown in figure 91, the  $k_p$  values for some modified versions of Pt+(Cr+Si)+Hf-modified and Pt+Si+Hf-modified  $\gamma'$ -based alloys are significantly lower than those of the Pt-modified  $\beta$  and Hf-modified  $\beta$  alloys.

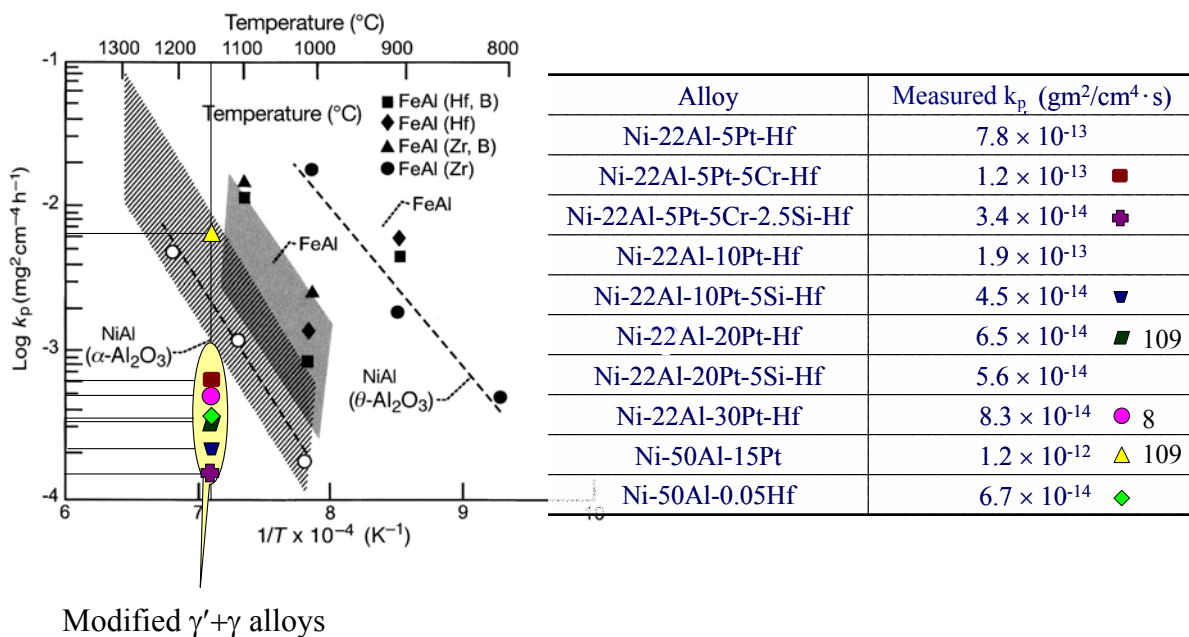


**Figure 91.** State-steady parabolic rate constants  $k_p$ , determined by regression of the cyclic oxidation kinetics.

It was observed that Cr addition of up to 10% to “low-Pt” containing  $\gamma'+\gamma$  alloys without pre-oxidation treatment did not improve hot corrosion resistance; however, certain modified versions of Cr-modified “low-Pt”  $\gamma'+\gamma$  alloys (*i.e.* Ni-22Al-5Pt-5Cr-Hf and Ni-22Al-10Pt-10Cr-Hf) showed excellent hot corrosion resistance with a pre-oxidation treatment. These modified versions of alloys also exhibited excellent isothermal and cyclic oxidation resistance, suggesting that the scale formed after pre-oxidation treatment improved the HTHC resistance. Similarly, some versions of Pt+Si+Hf-modified  $\gamma'+\gamma$  alloys (*i.e.* Ni-

22Al-10Pt-5Si-Hf and Ni-22Al-20Pt-5Si-Hf) also exhibited excellent HTHC and oxidation resistance. XRD analysis performed on these representative Pt+(Cr/Si)+Hf-modified  $\gamma'+\gamma$  alloys after oxidation testing, as well as after a pre-oxidation treatment, indicated the formation of an  $\alpha$ -Al<sub>2</sub>O<sub>3</sub> scale. SEM/EDS analysis also confirmed the formation of a continuous and adherent alumina scale. Figure 92 shows cross-sectional SEM images of representative Pt+(Cr/Si)+Hf-modified Ni-22Al-5Pt-5Cr-Hf and Ni-22Al-10Pt-5Si-Hf  $\gamma'+\gamma$  alloys after pre-oxidation treatment. It should be noted that the TGO scale formed after the isothermal oxidation (figure 80 and 82) is quite similar to the one formed after the pre-oxidation treatment. Therefore, improved hot-corrosion performance in modified  $\gamma'+\gamma$  alloys with pre-oxidation treatment is inferred to be due to the formation of a protective alumina scale.

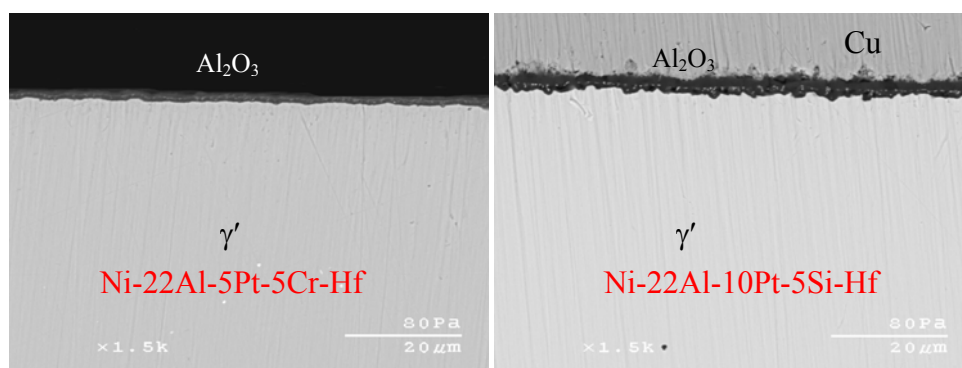


**Figure 92.** Cross-sectional SEM images of Ni-22Al-5Pt-5Cr-Hf and Ni-22Al-10Pt-5Si-Hf alloys after the pre-oxidation treatment at 1100°C for 80h in air.

The beneficial effect of Pt, Cr, and Si additions in improving hot corrosion (w/ pre-oxidation) and oxidation resistance in the  $\gamma'+\gamma$  alloys shall now be discussed. The beneficial effects of Pt in promoting exclusive Al<sub>2</sub>O<sub>3</sub> formation on  $\gamma'$  alloys have been elucidated by Gleeson and colleagues [8, 83, 113]. According to these authors, the so-called Pt-effect can be ascribed to a number of contributing factors. First and foremost, Pt has strong preference for occupying Ni sites in the ordered L1<sub>2</sub> crystal structure  $\gamma'$ -Ni<sub>3</sub>Al [114]. As a consequence, a given crystallographic of  $\gamma'$  containing both Al and Ni shows an increase in the Al:Ni atom fraction with increasing Pt addition. Such an effective Al enrichment at the  $\gamma'$  surface kinetically favors the formation of Al<sub>2</sub>O<sub>3</sub> relative to NiO. An important aspect of this

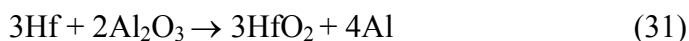
inference is the non-reacting nature of Pt to oxidation. Another contributing factor is that the Pt-containing  $\gamma'$ -based alloys show subsurface Pt enrichment during the very early stages of oxidation [83, 113]. This enrichment reduces Ni availability for oxidation and can increase the Al supply to the evolving scale owing to the negative chemical interaction between Al and Pt. With regard to the latter, Pt decreases the chemical activity of Al [111], so that a subsurface Pt enrichment would confer an increased subsurface gradient in the Al activity and, hence, an increased Al flux from the alloy to the evolving scale. This effect would also contribute to kinetically enhancing  $\text{Al}_2\text{O}_3$  formation. It is apparent from the present results that the Pt effect is most pronounced when the Pt content is increased from 0% to 10%, with minor benefit when going from 10% to 20% Pt. It should be noted that 5% Pt addition to Ni-22Al-0.4Hf alloy could establish exclusive  $\text{Al}_2\text{O}_3$  formation. A further addition of 5% Cr to the Ni-22Al-5Pt-0.4Hf alloy eventually resulted in exclusive  $\text{Al}_2\text{O}_3$  formation.

The role of Cr in promoting  $\text{Al}_2\text{O}_3$  scale formation during oxidation is not entirely understood. One of the possible hypotheses for this behavior is referred to as the third-element or gettering effect [17]. According to this hypothesis, the critical concentration for protective alumina-scale formation is decreased by Cr addition, the oxide of which (*i.e.*  $\text{Cr}_2\text{O}_3$ ) is of intermediate thermodynamic stability to  $\text{Al}_2\text{O}_3$  and NiO. The oxide of ternary addition, *i.e.*  $\text{Cr}_2\text{O}_3$  develops during the transient oxidation, thereby reducing the  $\text{PO}_2$  at the alloy/scale interface to a value that is significantly lower than if there were no ternary additions. The lowered  $\text{PO}_2$  at the alloy/oxide interface consequently enables in establishing continuous  $\text{Al}_2\text{O}_3$ -scale. Although gettering effect is well-established, not all ternary additions of intermediate thermodynamic stability have the beneficial effects. SEM/EDS analyses could not confirm  $\text{Cr}_2\text{O}_3$ -scale formation in the Cr-modified  $\gamma'+\gamma$ -based alloys. However, recent results have shown Cr-enrichment in the oxide scale during early stages of oxidation these  $\gamma'+\gamma$ -based alloys [115].

The combined beneficial effect Cr and Pt in the present case shall be discussed here. It was found that Ni-22Al-Hf alloy forms NiO,  $\text{NiAl}_2\text{O}_4$ , and  $\text{Al}_2\text{O}_3$  after 100h of oxidation and addition of 5% of Cr to this alloy promoted exclusive alumina formation. Even so the Ni-22Al-5Cr-Hf alloy underwent scale spallation, suggesting that Cr addition helps in promoting alumina-scale but it was not helpful in improving scale adhesion. A combination of 5%Cr

and 5%Pt to the Ni-22Al-0.4Hf alloy not only promoted exclusive Al<sub>2</sub>O<sub>3</sub> scale but it also did not indicate any scale spallation even after 500 cycles (figures 84 and 85). Hence, some versions of Pt+Cr+Hf-modified  $\gamma'+\gamma$  alloys (*i.e.* Ni-22Al-5Pt-5Cr-Hf and Ni-22Al-10Pt-10Cr-Hf) exhibited excellent cyclic oxidation resistance and HTHC resistance with a pre-oxidation treatment.

A further important aspect of Cr addition is its influence on the oxidation of Hf. Specifically, it was found that the extent of internal HfO<sub>2</sub> formation decreased with addition of 5%Cr in the Ni-22Al-5Pt-Hf alloy, to the extent that a lower percentage of internal HfO<sub>2</sub> was found in the alloy. This is because addition of 5% Cr resulted in a protective Al<sub>2</sub>O<sub>3</sub> scale and suppressed NiAl<sub>2</sub>O<sub>4</sub> formation. Interestingly, a higher amount of Cr addition (*i.e.* Ni-22Al-5Pt-10Cr-Hf) resulted in higher weight gain after cyclic oxidation. A cross-sectional SEM image of this alloy indicates that the higher weight gain in this alloy is primarily due to thick alumina scale and HfO<sub>2</sub> formation internally and within the scale (figures 82 and 85). For the Hf to oxidize beneath an Al<sub>2</sub>O<sub>3</sub> scale in local equilibrium with the alloy, it is necessary for the following displacement reaction to proceed:



where the underlined elements are in the alloy solution at a chemical activity less than unity. This reaction can only proceed to the right if the activity of Hf is sufficiently high, such that the equilibrium constant for (31),  $K_{\text{eq}}$ , is higher than activity quotient,  $K = (a_{\text{Al}})^4/(a_{\text{Hf}})^3$ . Given that, under standard state conditions, HfO<sub>2</sub> is thermodynamically more stable than Al<sub>2</sub>O<sub>3</sub> [110] and the value of  $a_{\text{Hf}}$  in Ni-22Al-5Pt-10Cr-Hf would have to be significantly higher than  $a_{\text{Hf}}$  in the Ni-22Al-5Pt-5Cr-Hf alloy. Moreover, extent of  $a_{\text{Hf}}$  increase is directly related to increase in Cr content (10 and 20at.%), as indicated by the observed trend in extent of HfO<sub>2</sub> formation (figure 85 and 87).

Addition of Cr may have resulted in increasing  $a_{\text{Hf}}$  in the alloy in turn promoting HfO<sub>2</sub> formation. In order to understand the effect of Cr addition on the  $a_{\text{Hf}}$  an interdiffusion experiment using a couples of Ni-22Al-5Pt-0.5Hf and Ni-22Al-5Pt-5/10Cr-0.5Hf alloys was carried out. Thus, the Hf content in all couples was kept constant at 0.5%. As shown in figure 94, it was found that Hf diffused from Cr-containing (Ni-22Al-5Pt-5Cr-Hf) to non-Cr

containing side (Ni-22Al-5Pt-0.5Hf) indicating that Cr indeed increases  $a_{\text{Hf}}$ , since the diffusion direction is always down an activity gradient. A similar trend was observed in the case of Ni-22Al-5Pt-10Cr-Hf alloy but a comparatively higher percentage of Hf was depleted in Ni-22Al-5Pt-10Cr-Hf than the Ni-22Al-5Pt-5Cr-Hf alloy and a higher percentage of Hf diffused into the Ni-22Al-5Pt-Hf side. Although Cr addition increases  $a_{\text{Hf}}$ , the Ni-22Al-5Pt-5Cr-Hf alloy formed less  $\text{HfO}_2$  compared to Ni-22Al-5Pt-Hf alloy. As explained earlier, this is due to the formation of protective  $\text{Al}_2\text{O}_3$  scale. The establishment of a protective  $\text{Al}_2\text{O}_3$  scale during early stages of oxidation resulted in decreasing  $\text{HfO}_2$  formation internally and within the scale. In contrast, in the Ni-22Al-5Pt-10Cr-Hf alloy the  $a_{\text{Hf}}$  was quite high which resulted in the higher percentage of  $\text{HfO}_2$  formation during oxidation.

Although Cr addition is beneficial in improving HTHC (w/ pre-oxidation) and oxidation resistance, it is also important to understand its effect on the phase evolution in these alloys (figure 93). The lower amounts of Cr addition in a resulted primarily  $\gamma'$  phase constitution. The higher of amount of Cr addition resulted in  $\beta$ -phase formation and only a relatively low percentage ( $< 10\%$ ) of Cr addition was able maintain primarily  $\gamma' + \gamma$  phases. The Ni-22Al-5Pt-20Cr-Hf alloy exhibited excellent HTHC resistance but such a higher amount of Cr addition resulted in complex alloy phase structure of  $\gamma' + \gamma + \beta + \alpha$ , as shown in figure 93.

The beneficial effects of Si addition are deemed to be different from that of Cr and Pt in  $\gamma' + \gamma$  alloys. Addition of Si can cause the solubility for oxygen to decrease, thus decreasing the critical concentration required for the external protective oxide formation. Clemens *et al.* [84] gave a similar explanation for the beneficial effect of 2wt.% Si additions in promoting alumina scale formation on NiCrAlY-based alloys. It was also observed that Si addition increase volume fraction of  $\gamma'$  ( $f_{\gamma'}$ ), which may have been further contributing factor in improving oxidation kinetics of the Ni-22Al-10/20Pt-5Si-0.4Hf  $\gamma' + \gamma$  alloys.

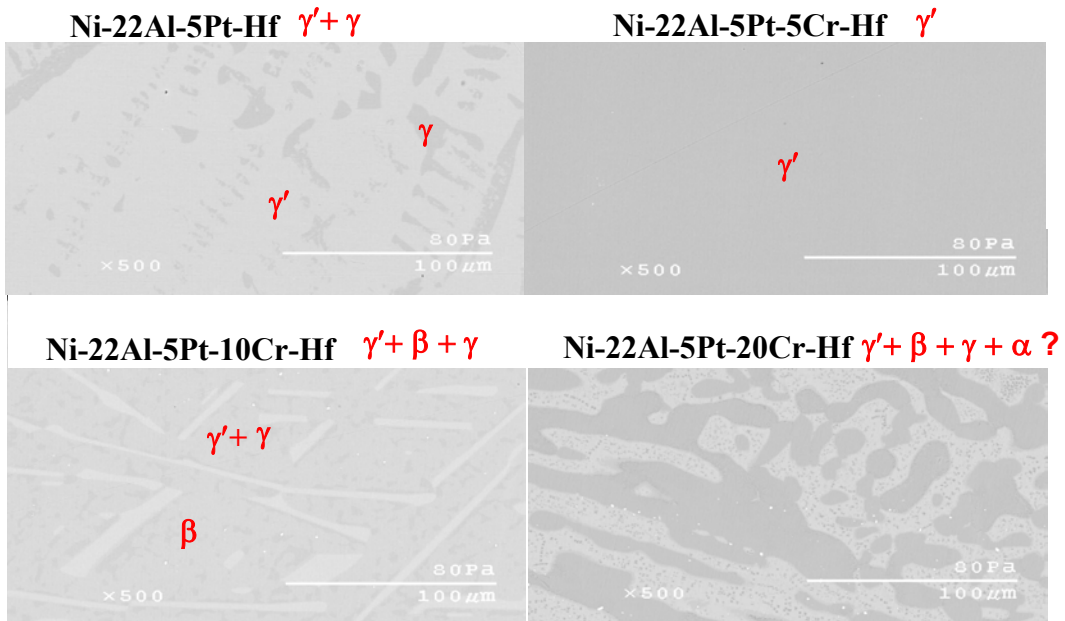


**Figure 93.** Phase evolution in Ni-22Al-5Pt-Hf alloy with Cr additions.

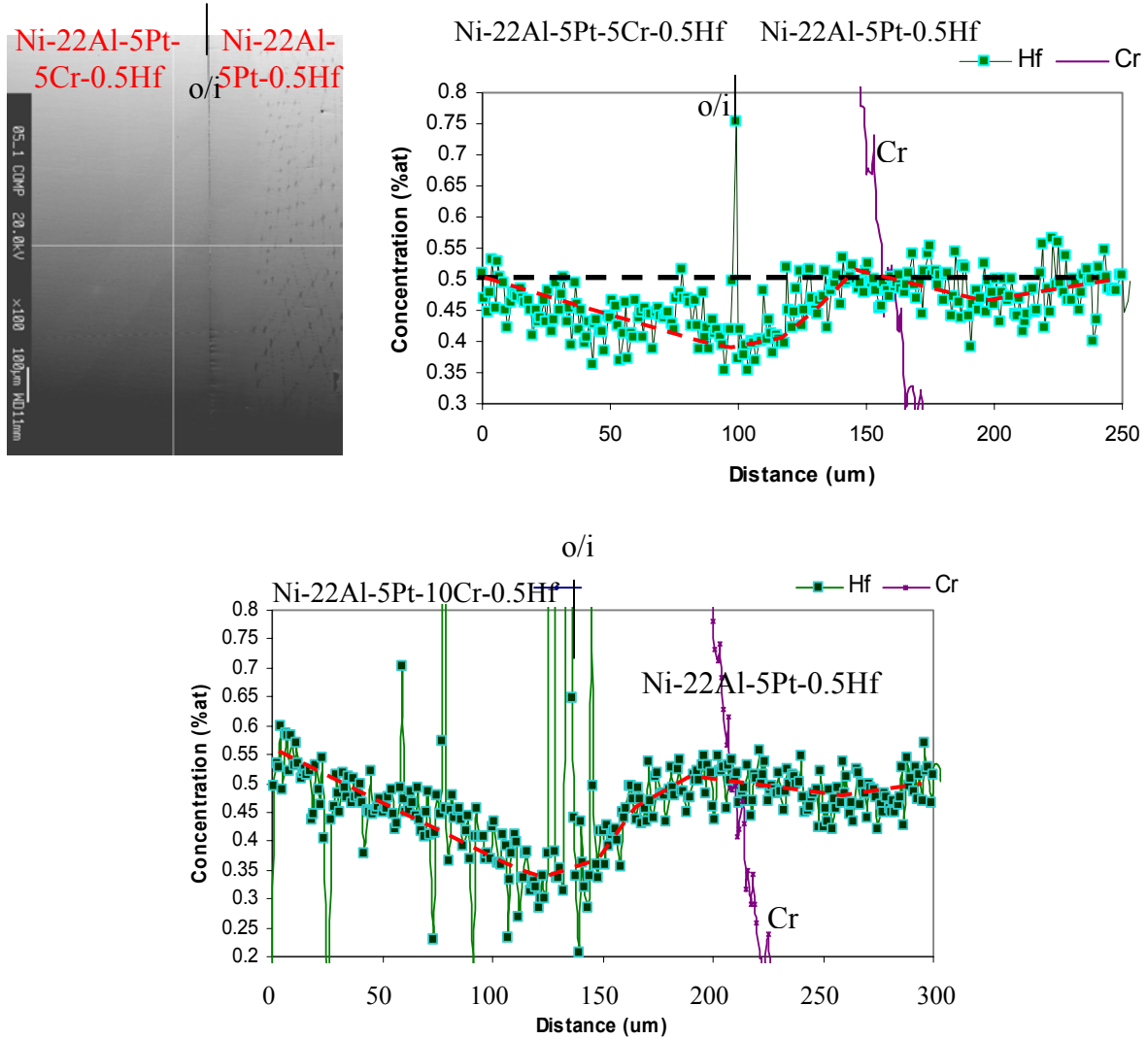


**Figure 94.** Interdiffusion behavior between Ni-22Al-5Pt-Hf and Ni-22Al-5Pt-5/10Cr-Hf alloys.

### 5.1.3.3. Optimizing the HTHC and Oxidation Resistance of $\gamma'+\gamma$ Alloys

The thermogravimetric hot corrosion and cyclic oxidation data can be converted into a single attack parameter (K) to rank the hot corrosion and cyclic oxidation resistance. The higher the K value the poorer the resistance. Hot corrosion of an alloy resulted in quite

high weight gain and comparatively there was insignificant spallation; hence spallation was not taken into consideration while calculating the hot corrosion attack parameters ( $K_{h-c}$ ). In the case of hot corrosion attack parameters the weight gains used for each alloy were those from the pre-oxidized samples. The equation used to calculate  $K_{h-c}$  was:

$$K_{h-c} = \left( \frac{\Delta W}{A} \right)^2 / t$$

The attack parameter results for hot corrosion are summarized in figure 95. Based on the hot corrosion attack parameters, alloys were ranked as follows:

$K_{h-c} < 0.2$ : Excellent;

$0.5 > K_{h-c} > 0.2$ : Fair;

$K_{h-c} > 0.5$ : Poor.

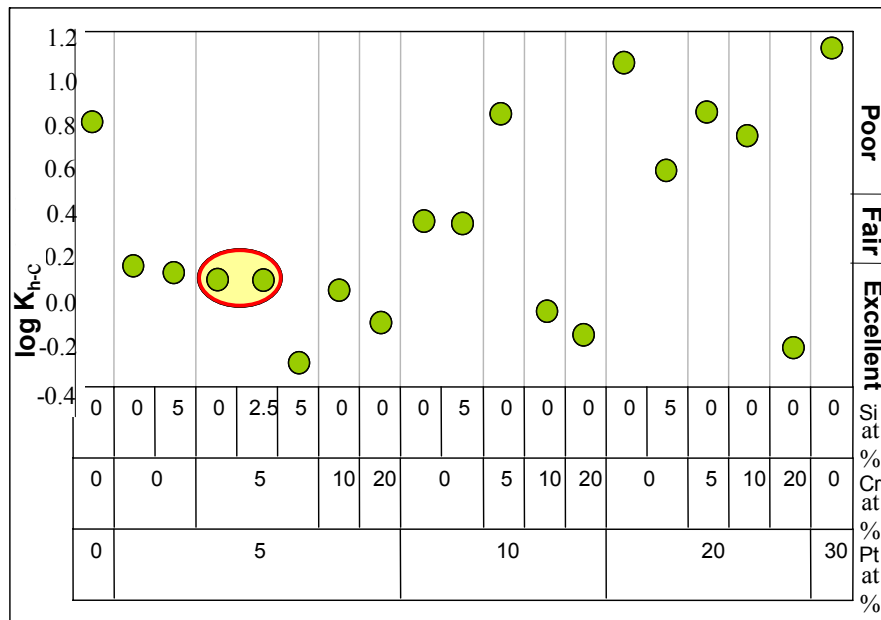


**Figure 95.** Calculated attack parameters for the 900°C hot-corrosion of  $\gamma' + \gamma$  alloys containing 22% Al.

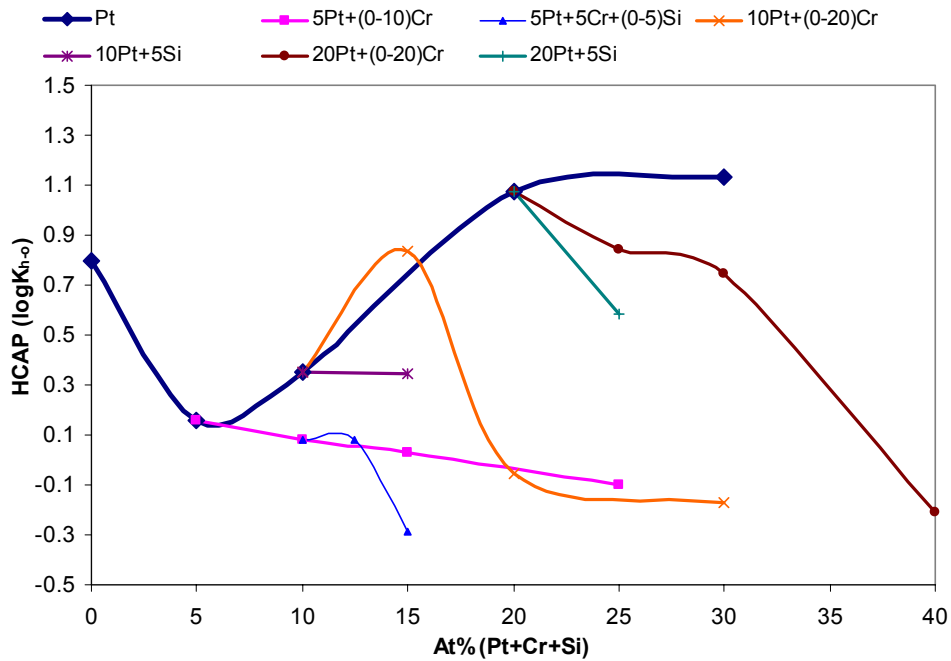


**Figure 95.** Continued.

Barret [116] used a statistical approach to calculate oxidation attack parameters ( $K_o$ ). The cyclic weight-change measurements that were obtained in this study were used for calculating the oxidation attack parameter using following equation:

$$\frac{\Delta W}{A} = k_1^{1/2} t^{1/2} + k_2 t \pm S.E.E$$

Where  $k_1^{1/2}$ , and  $k_2$  are constants analogous to the scale growth and scale spalling constants; while S.E.E. is standard error of estimate on the  $\Delta W/A$  estimates. If the data fits have  $R^2 > 0.90$ , then the attack parameter  $K_o$  is defined as:

$$K_o = (k_1^{1/2} + 10|k_2|)$$

The results from the  $K_o$  determinations are summarized in figure 96. Based on the oxidation attack parameters, alloys were ranked as follows:

- $K_o < -1.5$  : Excellent;
- $-1.2 > K_o > -1.5$  : Fair;
- $K_o > -1.2$  : Poor.

Assessing the statistical analyses of hot corrosion (figure 95) and oxidation attack (figure 96) parameters, it is inferred that the optimized coating composition is Ni-22Al-5Pt-5Cr-(0-2.5)Si-0.4Hf.

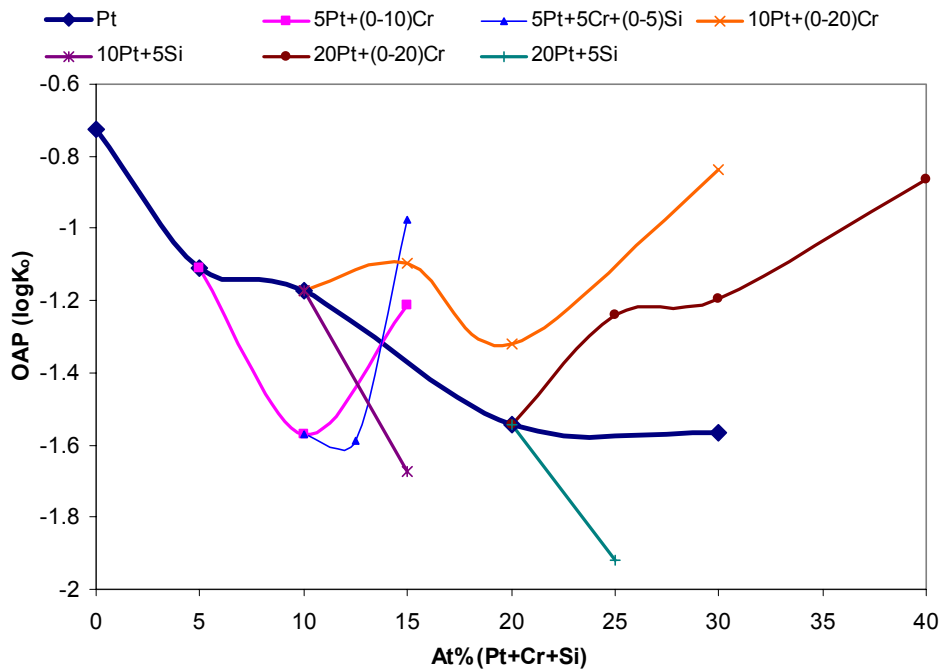
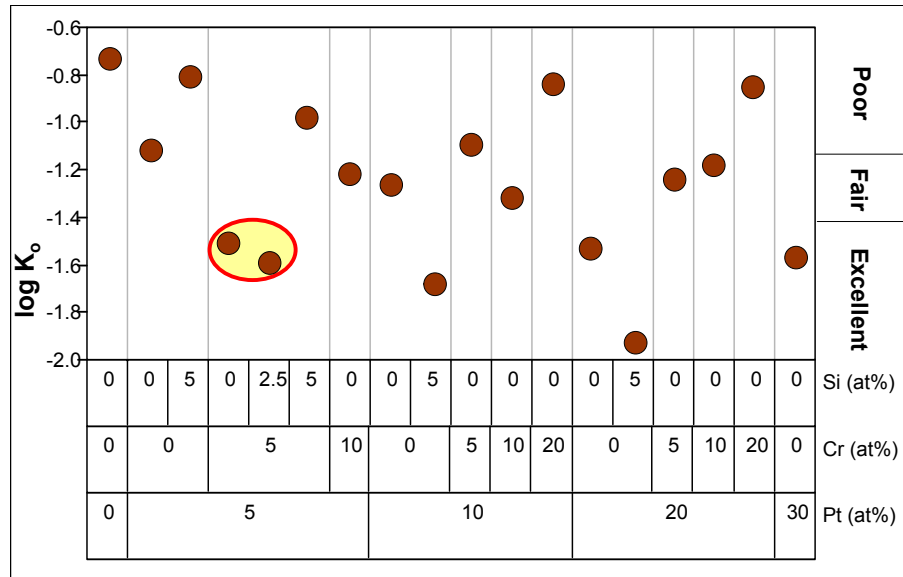


**Figure 96.** Calculated attack parameters for the 1150°C cyclic oxidation of  $\gamma'$  +  $\gamma$  alloys containing 22 at.% Al.

#### 5.1.4 Summary and Conclusions

1. The establishment of an adherent, intact and homogeneous  $\alpha$ -Al<sub>2</sub>O<sub>3</sub> scale is critical in providing high temperature protection from hot corrosion and oxidation. The novel Pt+Hf-modified  $\gamma'$ + $\gamma$  alloys have excellent oxidation resistance; however, addition of only “low Pt” (up to 10%) to  $\gamma'$ + $\gamma$  alloys improved HTHC resistance and addition of Pt >10% exhibited rather poor HTHC resistance. This is because Pt decreases  $a_{Al}$  and increases  $a_{Ni}$  to the extent that Ni<sub>3</sub>S<sub>2</sub>, which is liquid above about 787°C, forms in preference to Al<sub>2</sub>S<sub>3</sub> with increasing Pt content.
2. The formation of a protective  $\alpha$ -Al<sub>2</sub>O<sub>3</sub> scale on “low Pt” Ni-22Al-(5-10)Pt-0.4Hf  $\gamma'$ + $\gamma$  alloys is achieved by Cr addition up to 10%. Pre-oxidation treatment applied to the Pt+Cr+Hf-modified  $\gamma'$ + $\gamma$  alloys resulted in the formation of continuous and adherent  $\alpha$ -Al<sub>2</sub>O<sub>3</sub> scale. In the case of “low Pt” (up to 10%)  $\gamma'$ + $\gamma$  alloys, the present results suggest that addition of Cr should be either equal to or greater than Pt content for optimum HTHC and oxidation resistance. The Pt+Cr+Hf-modified  $\gamma'$ + $\gamma$  alloy (Ni-22Al-5Pt-5Cr-Hf) also exhibited excellent cyclic oxidation resistance.
3. Pre-oxidation of Pt+Cr+(Si)+Hf-modified  $\gamma'$ + $\gamma$  alloys (*i.e.* Ni-22Al-5Pt-5Cr-Hf, Ni-22Al-5Pt-5Cr-2.5Si-Hf, Ni-22Al-5Pt-10Cr-Hf, and Ni-22Al-10Pt-10Cr-Hf) and Pt+Si+Hf-modified  $\gamma'$ + $\gamma$  alloy (Ni-22Al-10Pt-5Si) also resulted in the formation of a continuous and adherent Al<sub>2</sub>O<sub>3</sub> scale, which prevented these alloys from HTHC attack. These modified versions of  $\gamma'$ + $\gamma$  alloys also possessed improved HTHC and oxidation resistance than the Ni-50Al-15Pt  $\beta$  and  $\gamma$ + $\beta$ -NiCrAl alloy. The Pt+Si+Hf-modified  $\gamma'$ + $\gamma$  alloy (*i.e.* Ni-22Al-10/20Pt-5Si-Hf) showed lowest weight gain amongst the alloys tested under cyclic conditions.
4. Higher Cr-content (20%) alloys with varying Pt content (5-20%), *e.g.*, Ni-22Al-5Pt-20Cr-Hf, Ni-22Al-10Pt-20Cr-Hf, Ni-22Al-20Pt-20Cr-Hf gave the best performance of the alloys not given a pre-oxidation treatment. These particular alloys showed excellent HTHC resistance, better than Pt-modified  $\beta$  and MCrAl alloys, but their oxidation resistance is rather poor.

5. Statistical analyses of the oxidation and HTHC results from the various Ni-22Al-based alloys studied gave an optimized coating composition of (in at%) Ni-22Al-5Pt-5Cr-(0-2.5)Si-0.5Hf.

## **5.2 Effects of Alloying Additions on the LTHC Resistance of $\gamma'$ -Ni<sub>3</sub>Al + $\gamma$ -Ni- and $\beta$ -NiAl-Based Alloys**

### 5.2.1. Introduction

This section reports the LTHC behavior of Hf-modified  $\gamma'+\gamma$ -based alloys. The primary objective of this fundamental study is to understand the effect systematic additions of Pt, Cr, and Si on the LTHC resistance of  $\gamma'+\gamma$  alloys and to evaluate the LTHC resistance of modified  $\gamma'+\gamma$  alloys that exhibited optimum HTHC and oxidation resistance. The results presented in this and previous section will help in obtaining a coating composition that exhibits optimum resistance to both types of hot corrosion and oxidation. This study also assess the comparative resistance of  $\beta$ -(Ni, Pt)Al alloys. Also assessed are the effects of Pt, Al and other alloying additions such as Co and other refractory elements that are present in  $\beta$ -(Ni, Pt)Al diffusion coating.

### 5.2.2. Experimental

A set of  $\gamma'$ -Ni<sub>3</sub>Al+ $\gamma$ -Ni and  $\beta$ -NiAl alloys were prepared by Ar-arc melting with appropriate proportions of high purity constituent elements. Tables 3 and 8 summarize the alloys (all in at.%) that were prepared for this study. The set of model alloys in Table 8 that were comprised of  $\beta$ -NiAl phase constitution and had varying levels of Al and Pt content. The effect of Co addition was also studied on the Ni-37Al-6Pt and Ni-31Al-6Pt  $\beta$  compositions.

**Table 8.** Chemical composition (at. %) of the alloys prepared for LTHC testing.

Alloy	Composition (at. %)			
	Ni	Al	Pt	Co
1	Bal	50	5	-
2	Bal	50	15	-
3	Bal	36	-	-
4	Bal	36	5	-
5	Bal	36	15	-
6	Bal	31	6	-
7	Bal	37	6	-
8	Bal	31	6	6
9	Bal	37	6	6

The  $\beta$  diffusion coating was exposed at 1150°C for different oxidation times and EPMA analysis was performed on the coating to obtain  $\beta$  compositions. Model  $\beta$  alloys that represent  $\beta$  coating compositions after different oxidation times were then prepared. These alloys, which contain of Co and other alloying additions, were as follows:

1. Ni-47Al-5.8Pt-2.5Co-0.7Cr-0.1Mo (As deposited coating composition)
2. Ni-37Al-7.2Pt-3.9Co-2.9Cr-0.1Ta-0.1Mo  
(Coating composition after 1 h of oxidation @ 1150°C)
3. Ni-35Al-6.3Pt-4.2Co-4Cr-0.2Ta-0.1Mo-0.03W  
(Coating composition after 2 h of oxidation @ 1150°C)
4. Ni-33Al-5.4Pt-4.6Co-4.5Cr-0.4Ta-0.1Mo-0.05W  
(Coating composition after 3 h of oxidation @ 1150°C)
5. Ni-31Al-4.5Pt-5.3Co-5.2Cr-0.5Ta-0.1Mo-0.1W  
(Coating composition after 5 h of oxidation @ 1150°C)

The LTHC experiments were carried out for 100 hours of total exposure. An additional set of LTHC tests were conducted in which the specimens were pre-oxidized on a case-to-case basis in a box furnace at 1100°C for 80 hours and then furnace cooled to room temperature.

### 5.2.3. Results and Discussion

#### 5.2.3.1 Effect of Pt on the LTHC Resistance of Hf-Modified $\gamma'$ + $\gamma$ Alloys

Initial testing focused on a set of Hf-modified  $\gamma'$ + $\gamma$  alloys having a fixed Al content of 22% and increasing Pt content from 0-30%. Sample weight gains after 100 h of exposure are shown in figure 97. Addition of up to 30% of Pt to the base Ni-22Al-0.4Hf alloy improved hot corrosion resistance. The improvement was progressive with increasing Pt content when no pre-oxidation was given. It was also found that pre-oxidation of these alloys resulted in lower weight gains. Corresponding cross-sectional SEM images of various untreated alloys after 100 h of LTHC are shown in figure 98. In general, all of the alloys underwent uniform LTHC attack throughout the cross-section. The base Ni-22Al-Hf alloy was extensively attacked after 100 h of exposure and 5% Pt addition considerably improved the LTHC resistance. The extent of attack decreased with increase in the Pt content for up to 30%. The improved performance with Pt addition in  $\gamma'$ + $\gamma$  alloys is believed to be due to the formation of more protective Al-rich TGO scale, even at the lower temperature of LTHC testing (*i.e.*, 705°C).

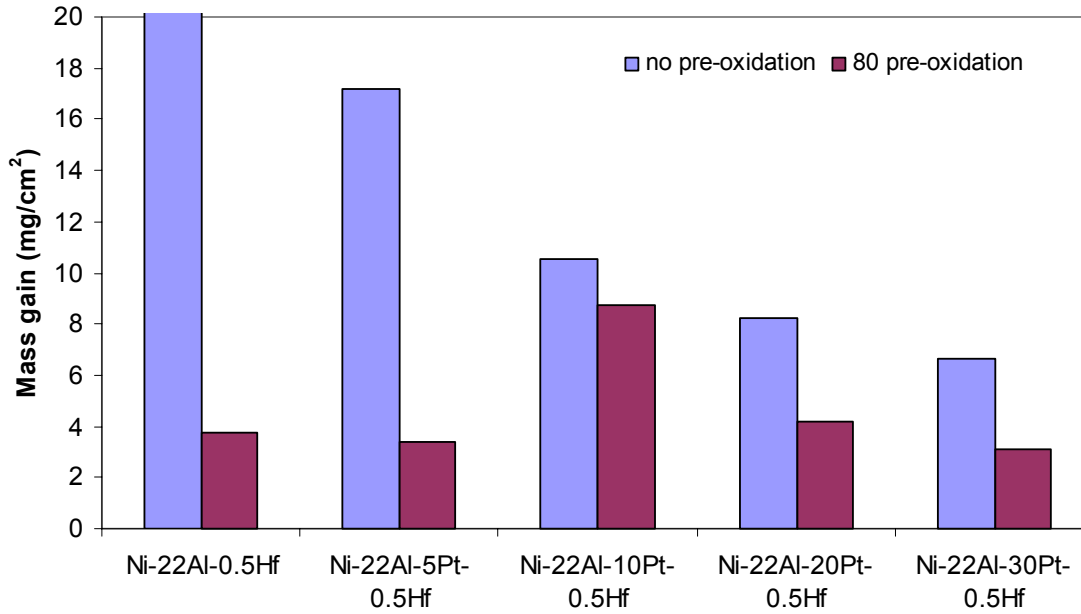


**Figure 97.** Weight gains of  $\gamma' + \gamma$  alloys after 100 h (5 x 20 h cycles) LTHC at 705°C.

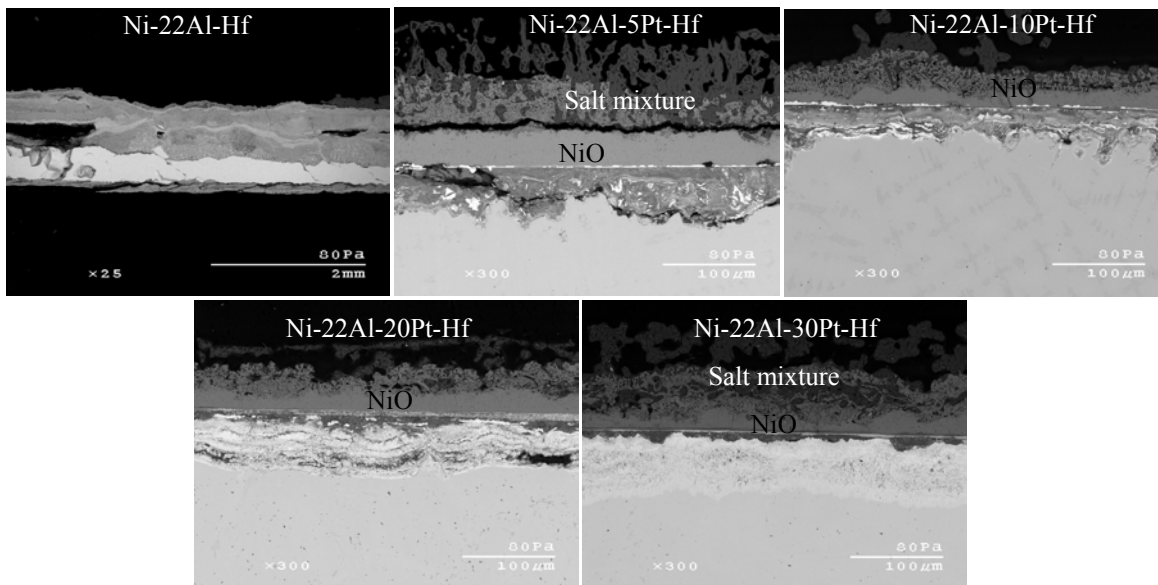


**Figure 98.** Cross-sectional SEM images of untreated  $\gamma' + \gamma$  alloys after 100 h LTHC at 705°C.

The LTHC of  $\gamma' + \gamma$  Ni-based alloys is attributed to the formation of eutectic  $\text{Na}_2\text{SO}_4$ - $\text{NiSO}_4$  liquid ( $T_{\text{melt}} = 671^\circ\text{C}$ ) [14, 15]. The  $\text{NiSO}_4$  (s) can form under LTHC conditions by the

reaction (1), where the NiO may be present as a consequence of the initial stages of coating or alloy oxidation. EDS analyses of the hot-corroded samples clearly indicated formation of thick NiO scale below the salt mixture (figure 98).

In contrast to the LTHC results, Pt addition above 10% considerably decreased the HTHC hot corrosion resistance of  $\gamma'+\gamma$  alloys due to the formation of  $\text{Ni}_3\text{S}_2$  liquid at  $900^\circ\text{C}$  as discussed in the previous section. A similar detrimental effect of Pt addition was not seen under the LTHC conditions since liquid  $\text{Ni}_3\text{S}_2$  formation occurs above temperature of LTHC testing (*i.e.*  $700^\circ\text{C}$ ). However, Pt addition may have had some detrimental effect in the formation of  $\text{NiSO}_4$  under LTHC conditions, since addition of up to 30% Pt could not completely prevent LTHC after 100 h of exposure (figure 97).

The formation of a thermally-grown  $\text{Al}_2\text{O}_3$  scale plays an important role in limiting environmental degradation of various high temperature alloys and coatings. In general, an ideal alumina scale should be dense, relatively inert, adherent, and slow-growing to protect underlying metal surface. A recent oxidation study by Izumi and Gleeson [108] on a (in at%) Ni-20Al-20Pt-Hf  $\gamma'+\gamma$  bulk alloy showed that this alloy is an excellent alumina former. XRD analysis performed on the pre-oxidized  $\gamma'+\gamma$  bulk alloys used in this study also confirmed the formation of an  $\alpha$ - $\text{Al}_2\text{O}_3$  scale. The improved performance of the Pt+Hf-modified  $\gamma'+\gamma$  bulk alloys is therefore attributed to the presence of a protective  $\alpha$ - $\text{Al}_2\text{O}_3$  scale that forms during a pre-oxidation period (*i.e.*, air- $1100^\circ\text{C}$ -80h). The formation of Al-rich scale apparently provided a barrier to the inward transfer of salt and the outward migration of Ni.

#### 5.2.3.2 Effect of Cr on the LTHC Resistance of Pt+Hf-Modified $\gamma'+\gamma$ Alloys

It was observed in the previous section that systematic additions of Cr were quite beneficial to improving HTHC and oxidation resistance of Pt+Hf-modified  $\gamma'+\gamma$  alloys; hence, Cr was added to Pt+Hf-modified  $\gamma'+\gamma$  alloys to study its effect on the LTHC resistance. Sample mass-gains after 100 h of LTHC are shown in figure 99 and it was seen that Cr addition to the untreated Ni-22Al-10/20Pt-0.4Hf  $\gamma'+\gamma$  alloys resulted in slightly lower yet still rather large weight gains. Notwithstanding, Cr addition to these  $\gamma'+\gamma$  alloys with pre-oxidation was highly beneficial in improving the LTHC resistance. Cross-sectional SEM images of the untreated  $\gamma'+\gamma$  alloys after 100h of LTHC are shown in figure 100. In general,

all of the alloys underwent LTHC attack and the mode of attack was uniform throughout the cross-section. Systematic Cr additions to the Ni-22Al-10/20Pt-Hf alloys slightly improved LTHC resistance but could not completely prevent the LTHC attack after 100 h of exposure. EDS analysis of the attacked region showed a mixed salt outer layer followed by thick NiO layer and internal Al-rich oxide.

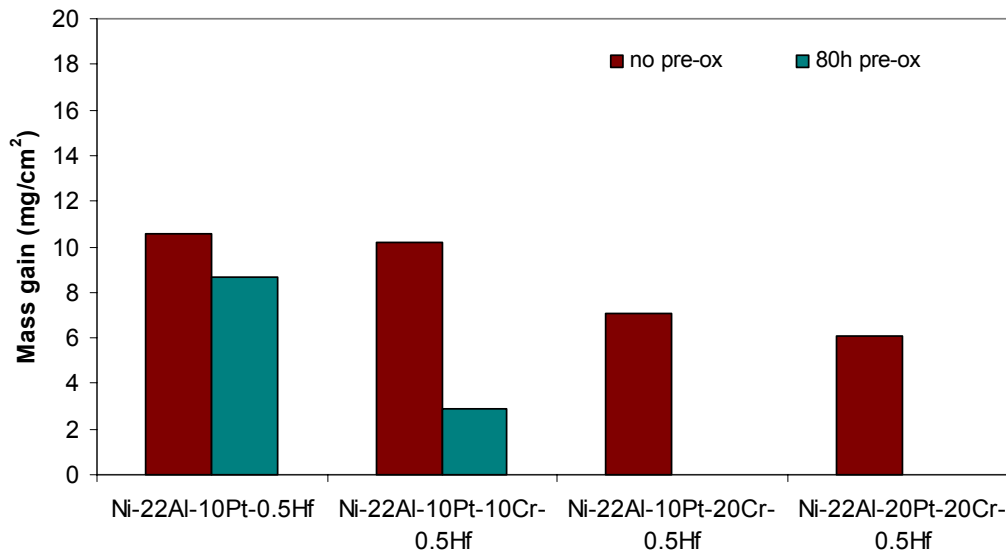


**Figure 99.** Weight gains of  $\gamma' + \gamma$  alloys after 100 h (5 x 20 h cycles) LTHC at 705°C.

A similar beneficial effect of Cr addition was also seen in the Ni-22Al-5Pt-0.4Hf  $\gamma' + \gamma$  alloy, except for the fact that Cr addition resulted in comparatively lower weight gain even without the pre-oxidation treatment (figure 101). However, the Cr-modified alloys still showed relatively high weight gains, suggesting that Cr addition could not completely prevent LTHC of the untreated alloys. The pre-oxidized versions of these alloys showed extremely low weight gains, indicating no LTHC attack after 100 h of exposure. Cross-sectional SEM images of the Cr-modified Ni-22Al-5Pt-Hf containing alloy with and without pre-oxidation are shown figure 102. It was observed that Cr additions to the ternary Ni-22Al-5Pt-Hf alloy considerably reduced the extent of attack but these modified versions alloys still underwent uniform LTHC attack when not given a pre-oxidation treatment. SEM images of the pre-oxidized Cr-modified Ni-22Al-5Pt-Hf alloys confirmed that LTHC attack was completely prevented with no discernable attack observed after 100 h of exposure.

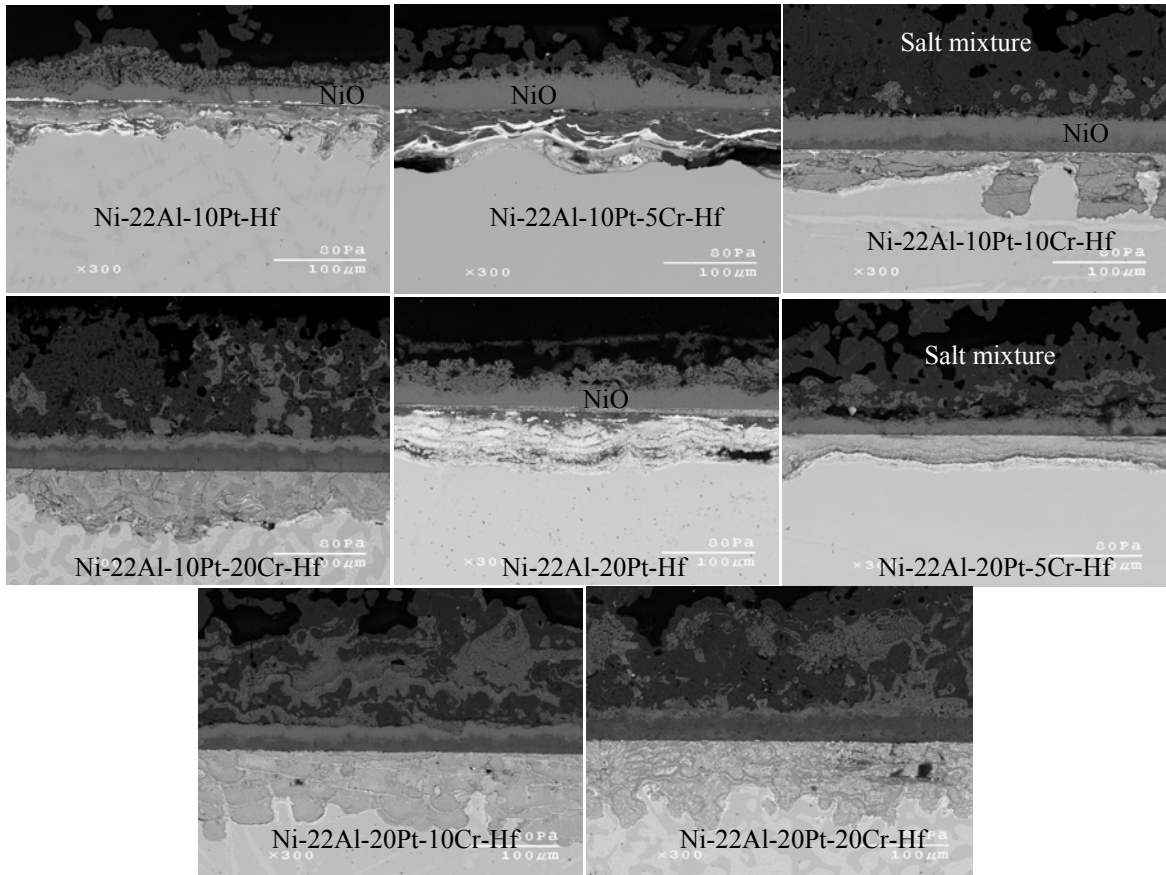


**Figure 100.** Cross-sectional SEM images of untreated  $\gamma' + \gamma$  alloys after 100 h LTBC at 705°C.

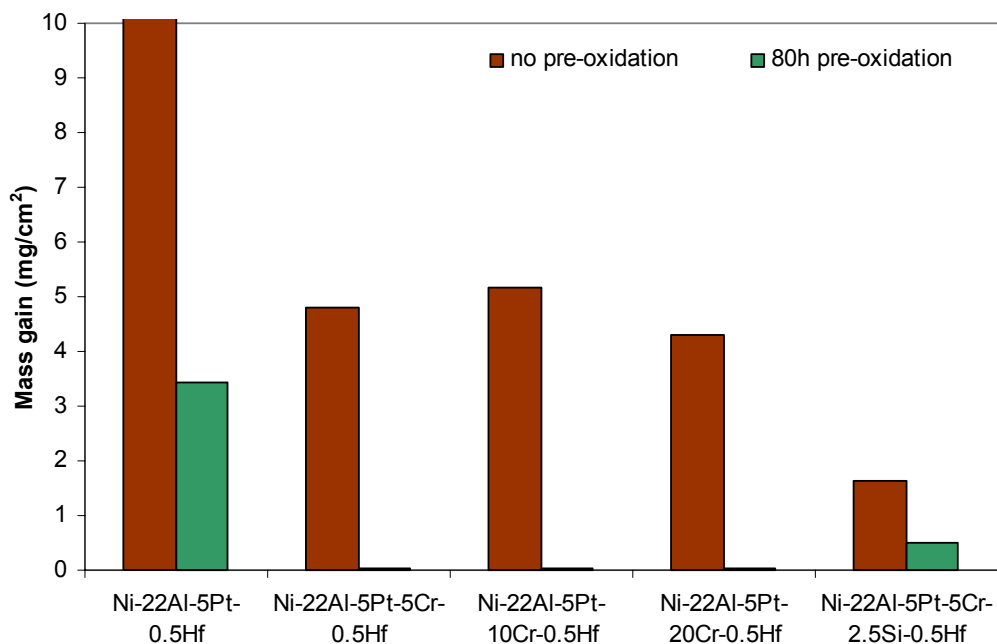


**Figure 101.** Weight gains of  $\gamma'+\gamma$  alloys after 100 h (5 x 20 h cycles) LTTC at 705°C.

EDS analysis performed on these pre-oxidized  $\gamma'+\gamma$  alloys confirmed the presence of solid  $\text{Na}_2\text{SO}_4$  salt, suggesting that there was no reaction between the salt and alloy. This improvement in the hot corrosion resistance is attributable to the presence of a protective reaction product barrier *i.e.* Al-rich TGO scale that was pre-formed during the pre-oxidation treatment at 1100°C for 80 h.

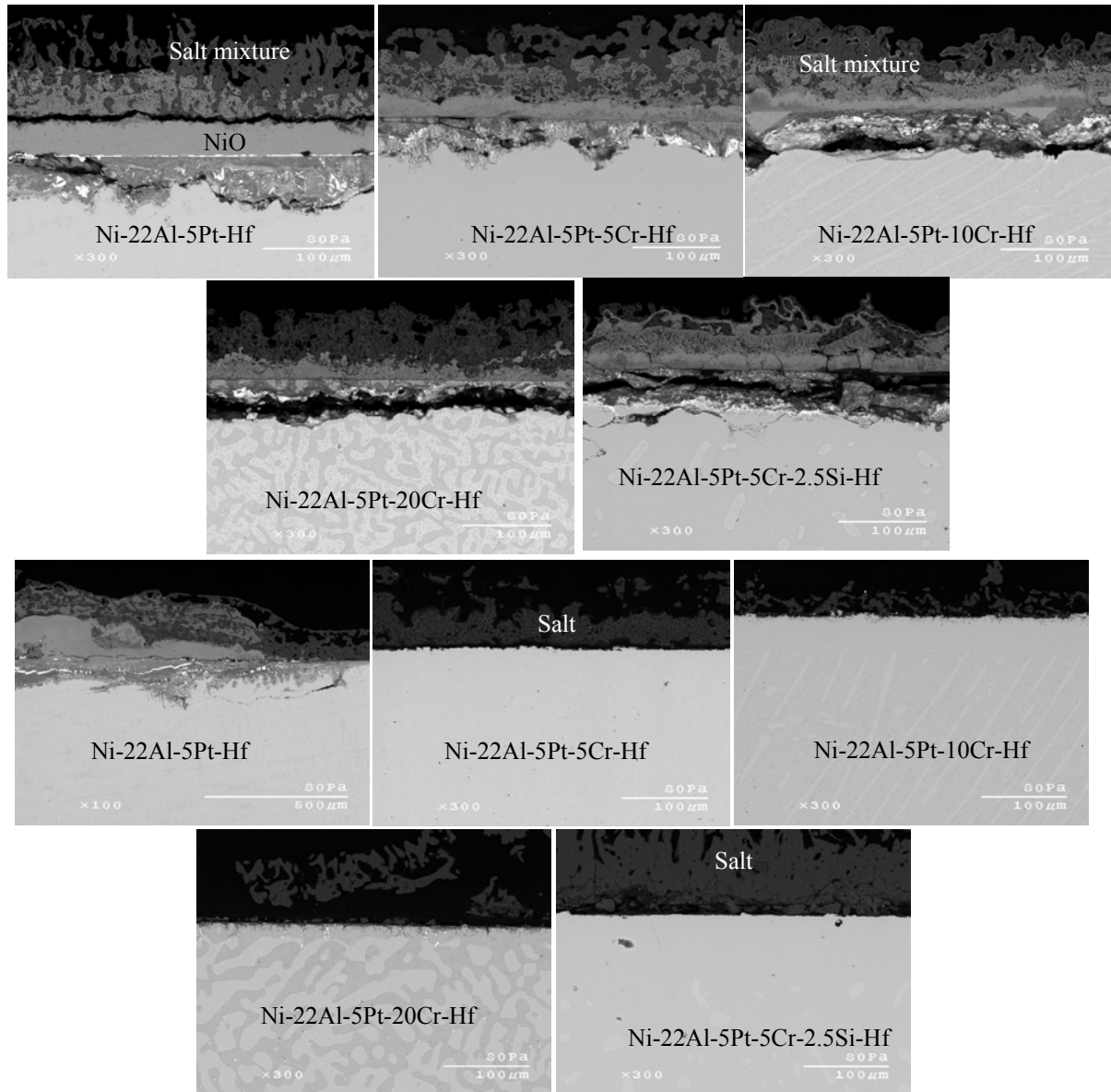


**Figure 102.** Cross-sectional SEM images of untreated and pre-oxidized Ni-22Al-5Pt-Cr-Hf  $\gamma' + \gamma$  alloys after 100 h LTHC at 705°C.

### 5.2.3.3 Effect of Si on the LTHC Resistance of Pt+Hf-Modified $\gamma' + \gamma$ Alloys

It is well known that along with Cr and Si addition also improves oxidation and hot corrosion resistance of aluminide coating and alloys [70]. It was found in the previous section that Si addition was beneficial in improving HTHC and oxidation resistance of Ni-

22Al-10/20Pt-Hf  $\gamma'+\gamma$  alloys. The effect of Si addition on the LTHC behavior of Pt+Hf-modified  $\gamma'+\gamma$  alloys was thus standard. Resulting sample weight gains of the untreated and pre-oxidized alloys after 100h LTHC are shown in figure 103. It is seen that Si addition was highly beneficial for the Ni-22Al-10/20Pt-Hf  $\gamma'+\gamma$  alloys even with no pre-oxidation treatment. Si addition to Ni-22Al-5Pt-Hf alloy was also beneficial, but to a lower extent. Cross-sectional SEM images of the Pt+Si+Hf-modified  $\gamma'+\gamma$  alloys confirmed the improvement in LTHC resistance with the Si additions. Interestingly, from the weight gain and SEM analysis (figure 104) it was found that Si addition to the Ni-22Al-10/20Pt-Hf  $\gamma'+\gamma$  alloys showed no discernable attack with no pre-oxidation treatment. None of the untreated  $\gamma'+\gamma$  alloys tested so far have shown such an improvement in the LTHC resistance. This is at least partly attributable to the formation protective or native oxide scale formation during the early stages of oxidation/corrosion.

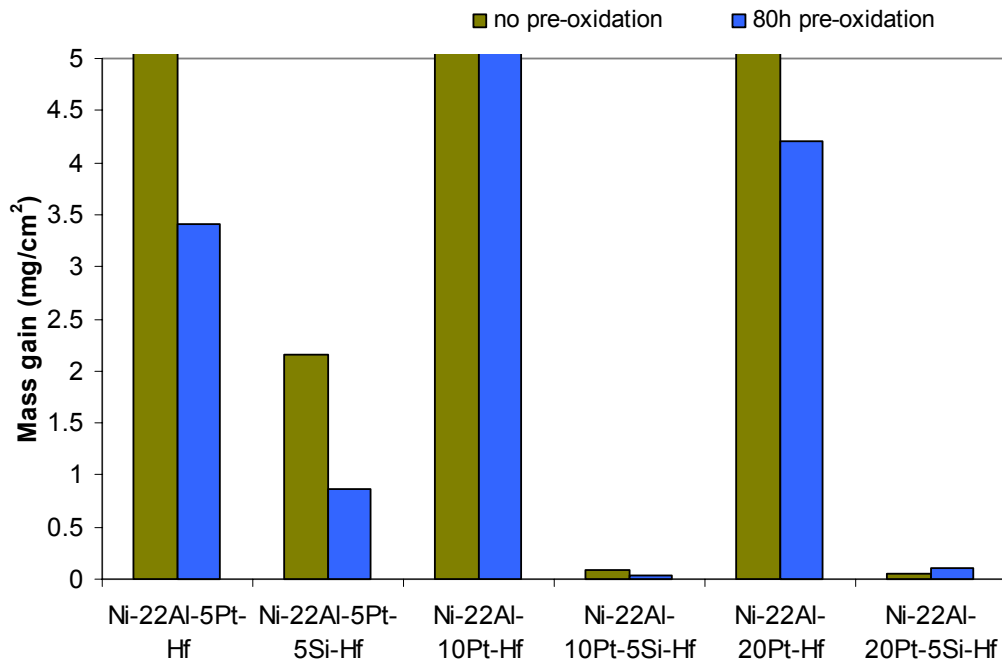


**Figure 103.** Weight gains of  $\gamma'+\gamma$  alloys after 100 h (5 x 20 h cycles) LTHC at 705°C.

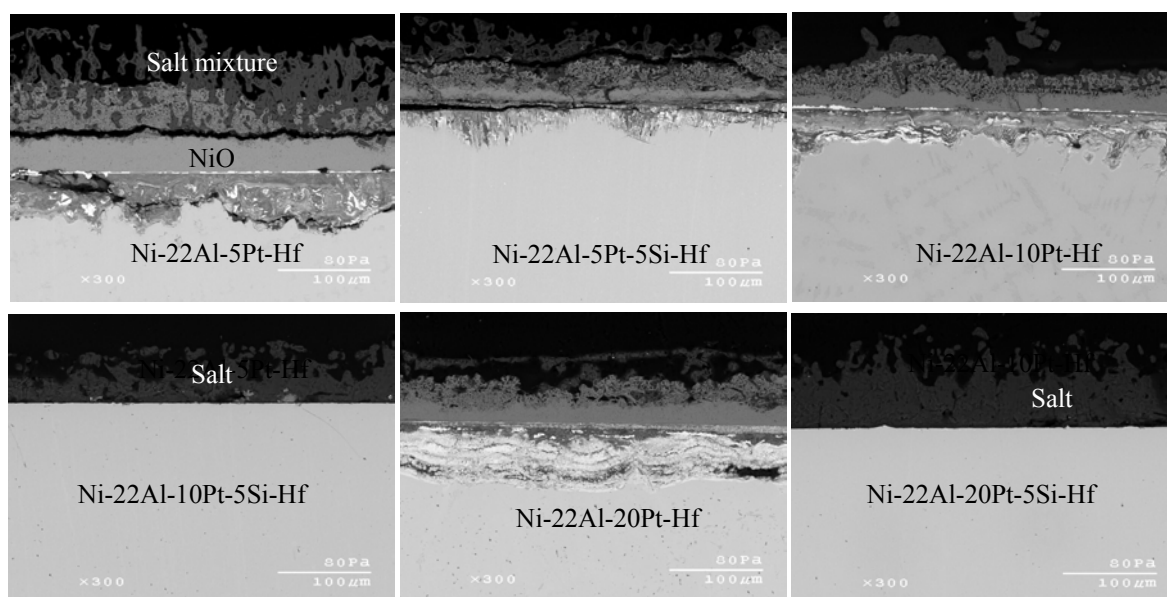


**Figure 104.** Cross-sectional SEM images of untreated Si+Pt-modified  $\gamma' + \gamma$  alloys after 100 h LTHC at 705°C.

#### 5.2.3.4 Effect of Al and Pt Content in $\beta$ -NiAl Alloys and their LTHC Resistance Compared with $\gamma' + \gamma$ Alloys

The effect of Pt addition to  $\beta$ -NiAl alloys having different levels of Al content were studied and sample weight gains of various untreated  $\beta$  alloys are shown in figure 105. By comparing weight gain and cross-sectional SEM images of untreated Pt+Hf modified  $\gamma' + \gamma$  to the Pt-modified  $\beta$  alloys it is seen that Pt-modified  $\beta$  alloys exhibit improved LTHC resistance (figure 106). The Pt+Hf modified  $\gamma' + \gamma$  alloys have a comparatively higher  $a_{Ni}$  than the Pt-modified  $\beta$  alloys because of the higher Ni content in the former. This favors formation of  $NiSO_4$  and, in turn, eutectic  $Na_2SO_4$ - $NiSO_4$  liquid ( $T_{melt} = 671^\circ C$ ) which results in extensive LTHC attack. Also, the lower temperature of the LTHC exposure is apparently insufficient for  $\gamma' + \gamma$  alloys to kinetically establish a protective and continuous  $Al_2O_3$  scale, which is necessary for prolonged hot corrosion resistance. Recently, Izumi and Gleeson also found that Pt-modified  $\beta$  alloy (Ni-50Al-15Al) exhibit superior oxidation resistance to

Pt+Hf-modified  $\gamma'+\gamma$  alloys when oxidation was at 1000°C [115]. The contrary was found to be true when the oxidation temperature was increased to 1150°C.

It is shown in figure 105 that untreated Pt-modified “Al-rich  $\beta$ ” alloys (*i.e.* Ni-50Al-5/15Pt) exhibited in lowest weight gains, indicating excellent hot corrosion resistance after 100 h of exposure. A lower amount of Pt addition was also extremely beneficial in improving hot corrosion resistance of the binary Ni-36Al  $\beta$  alloy. However, Pt addition was comparatively less beneficial in the “Ni-rich” Ni-31Al-6Pt  $\beta$  alloy. Corresponding cross-sectional SEM images shown in figure 106 confirmed that Pt-modified “Al-rich  $\beta$ ” alloys *i.e.* Ni-50Al-5/15Pt and Ni-36Al-5Pt underwent no discernable LTHC attack; while, the binary Ni-36Al and “Pt-modified Ni-rich  $\beta$ ” Ni-31Al-6Pt alloys underwent uniform LTHC attack.

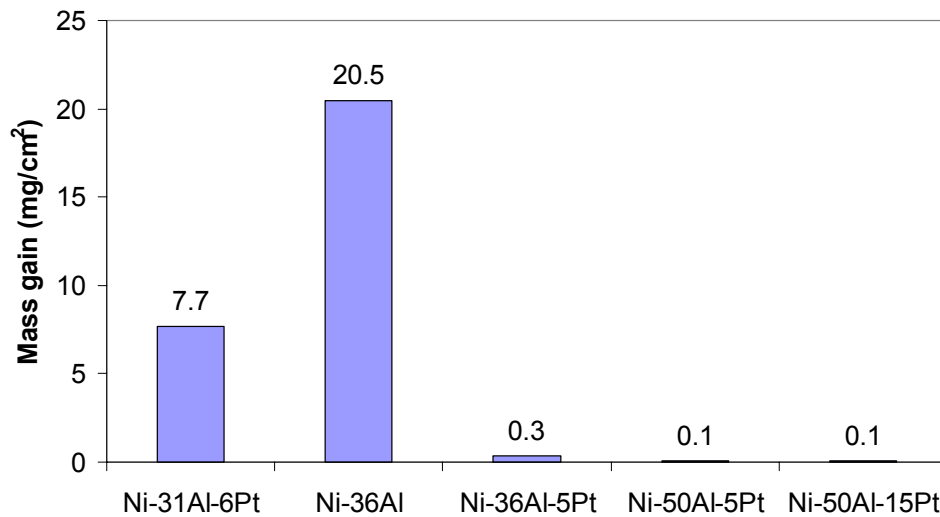


**Figure 105.** Weight gains of untreated  $\beta$  alloys after 100 h (5 x 20 h cycles) LTHC at 705°C.

The results obtained thus far clearly indicate that Pt additions to “Al-rich  $\beta$ ” confer excellent LTHC resistance; however, Pt addition to “Ni-rich  $\beta$ ” (*i.e.* Ni-31Al-6Pt) could not prevent LTHC attack. This may be attributable to rather poor TGO scale that may have formed in the Ni-31Al-6Pt alloy thus resulting in the LTHC attack.

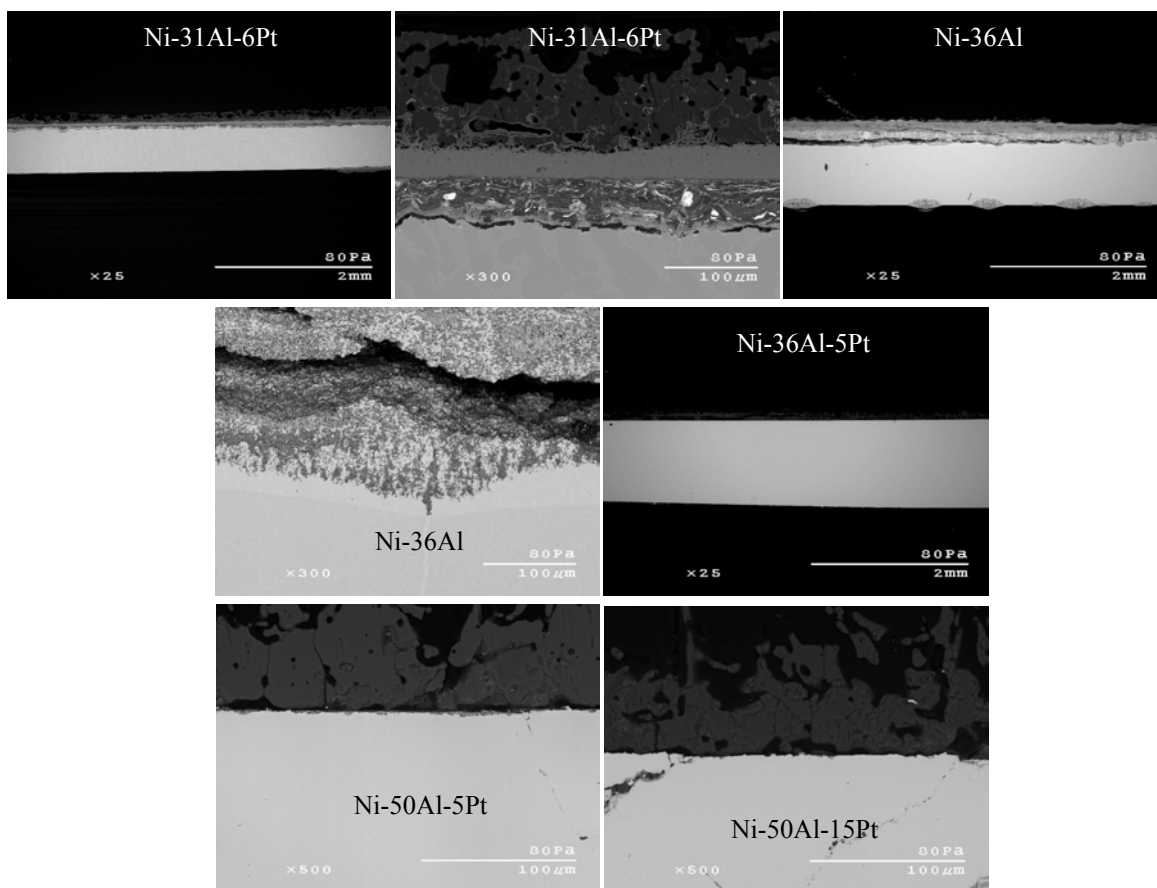


**Figure 106.** Cross-sectional SEM images of untreated  $\beta$  alloys after 100 h LTHC at 705°C.

#### 5.2.3.5 Effects of Co and Refractory Elements on the LTHC Resistance of $\beta$ -NiAl Alloys

It was shown in the previous sections that untreated Pt-modified  $\beta$  alloys have better LTHC resistance than the Pt+Hf-modified  $\gamma'+\gamma$  alloys. The Pt-modified  $\beta$  and Pt+Hf-modified  $\gamma'+\gamma$  coatings are often deposited by a diffusion process and elements present in superalloy substrate, such as Cr, Co, and other refractory elements (*i.e.* W, Mo, Ta), are also expected to be present within a coating. During high-temperature exposure Al content in the coating is expected to decrease with time due to interdiffusion between coating and substrate. To better understand the effects of these elements in particular Co and the refractories W, Mo, Ta, various Pt-modified  $\beta$  alloys of different Al contents were prepared. The alloy compositions were based on measured Pt-modified  $\beta$  coating after oxidation at 1150°C for

various times. The  $\beta$  coatings used in this study were received from General Electric Aircraft Engines. Sample weight gains of various Pt-modified  $\beta$  alloys after 100 h of LTHC are shown in figure 107. The Ni-31Al-6Pt alloy had a higher weight gain compared to Ni-37Al-6Pt, that Pt addition is more beneficial in higher Al  $\beta$  alloys. It was found that Co addition increased the weight gains in these alloys, with the detrimental effect of Co being most pronounced for “low-Al” Ni-31Al-6Pt-6Co alloy (*i.e.* decreased weight gain than Ni-37Al-6Pt-6Co).

Cross-sectional SEM images confirmed that Pt addition to Ni-37Al is more beneficial than to Ni-31Al alloy. Specifically, showing no discernable LTHC attack could be found in the Ni-37Al-6Pt alloy; while, the Ni-31Al-6Pt alloy underwent uniform LTHC attack throughout the cross-section. Addition of Co to  $\beta$  alloys of both Al levels (31 and 36 at%) resulted in LTHC attack; however, the extent of attack was higher in case of “low-Al” Ni-31Al-6Pt-6Co alloy (figure 108). Addition of Co plus other refractory elements to the ternary Ni-Al-Pt  $\beta$  alloys increased LTHC attack and a decrease in Al content further exacerbated the extents of attack (figure 107 and 108). This suggests that Co addition to  $\beta$  alloys plays a role in setting the stage for liquid-product formation and that this is at least partly attributable to the formation of  $\text{Na}_2\text{SO}_4\text{-CoSO}_4$  liquid ( $T_{\text{melt}} = 565^\circ\text{C}$ ) [49, 50]. The presence of other elements, in particular Co, may further exacerbate the LTHC resistance of  $\beta$  alloys and coatings by the formation of  $\text{CoSO}_4$ , which is even more stable than  $\text{NiSO}_4$  [49, 54]. Moreover, the  $\text{Na}_2\text{SO}_4\text{-CoSO}_4$  eutectic mixture has a much lower melting temperature ( $565^\circ\text{C}$ ) than that of the  $\text{Na}_2\text{SO}_4\text{-NiSO}_4$  mixture ( $T_{\text{melt}} = 671^\circ\text{C}$ ).  $\text{CoSO}_4$  is more stable than  $\text{NiSO}_4$  with respect to  $\text{CoO}$  and  $\text{NiO}$ , respectively. As a consequence,  $\text{CoSO}_4$  can form at a lower  $\text{PSO}_3$  than  $\text{NiSO}_4$ . Luthra and Shores also showed that  $\text{CoO}$  is a better catalyst for the  $\text{SO}_2 + \frac{1}{2} \text{O}_2 \rightarrow \text{SO}_3$  reaction than  $\text{NiO}$  and this will further increase  $\text{PSO}_3$  at the  $\text{CoO}$  surface than the  $\text{NiO}$  surface [49]. The formation of a low-melting-temperature  $\text{Na}_2\text{SO}_4\text{-NiSO}_4\text{-CoSO}_4$  eutectic is also a possibility; however, at this point there is not enough information available on the  $\text{Na}_2\text{SO}_4\text{-NiSO}_4\text{-CoSO}_4$  eutectic to fully analyze this possibility.

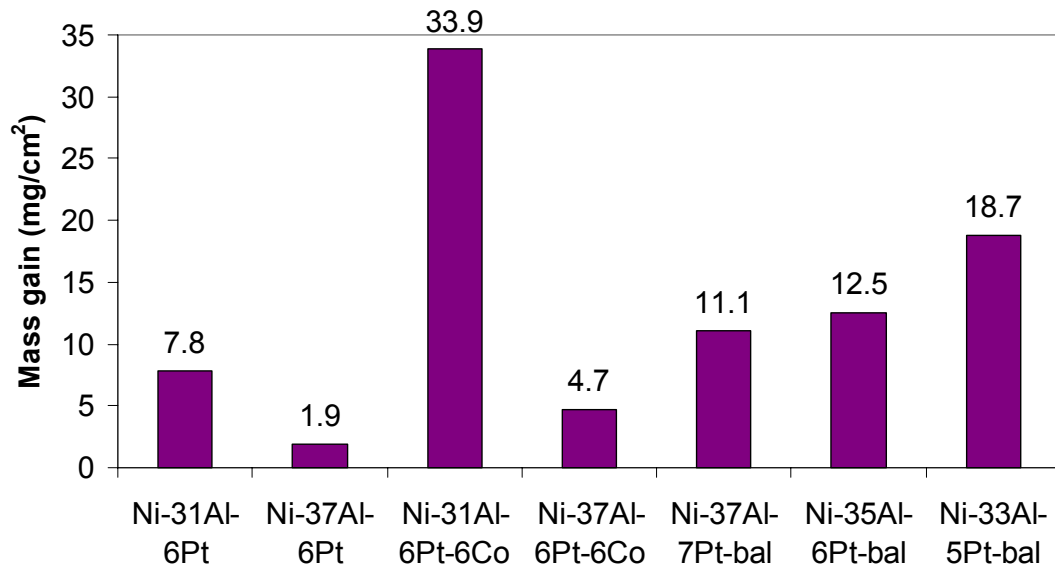


**Figure 107.** Weight gains of untreated  $\beta$  alloys after 100 h (5 x 20 h cycles) LTTC at 705°C.

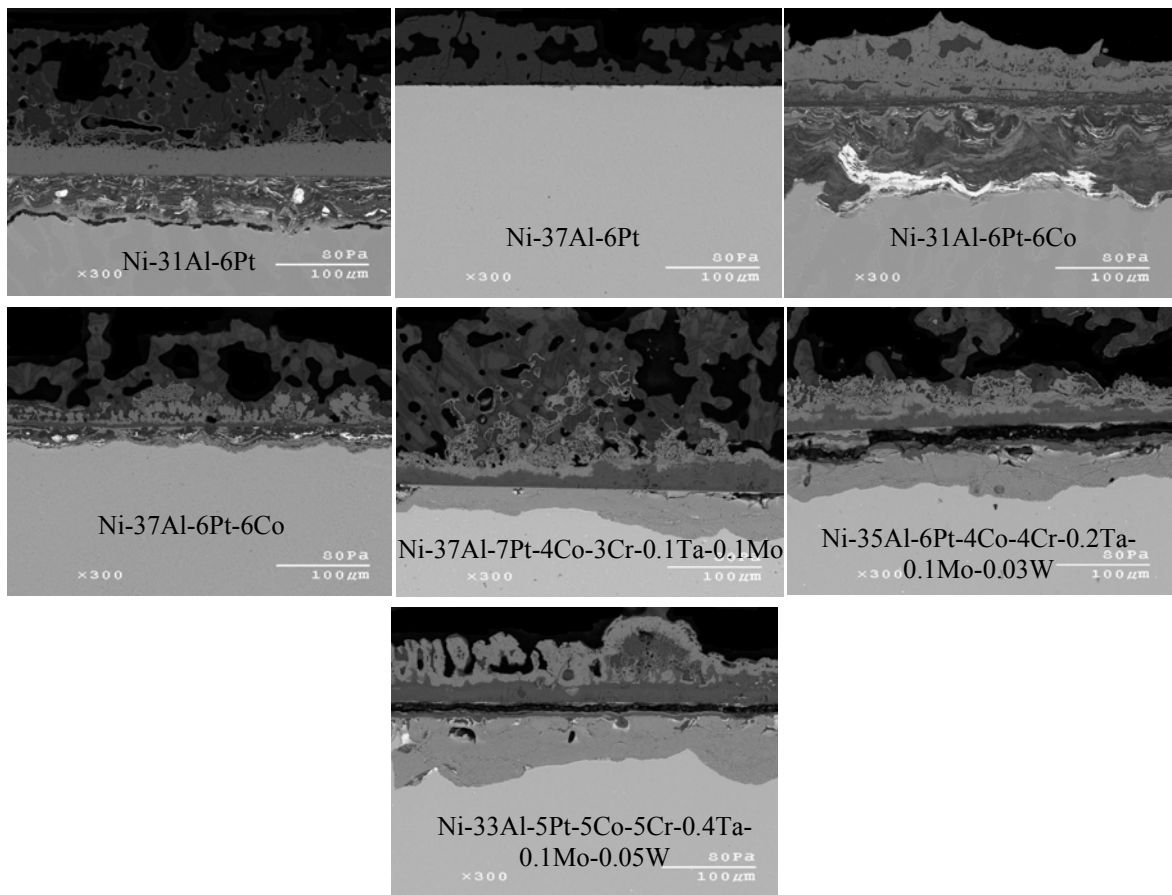


**Figure 108.** Cross-sectional SEM images of untreated  $\beta$  alloys after 100 h LTTC at 705°C.

The LTHC experiment was carried out on a model Pt-modified  $\beta$  alloys having 31Al-47Al (*i.e.* Ni-31Al-5Pt-5Co-5Cr-0.5Ta-0.1Mo-0.1W and Ni-47Al-6Pt-3Co-0.7Cr-0.5Ta-0.1Mo). These model alloys also contained Co and other refractory elements as observed in the diffusion aluminide coatings. Cross-sectional SEM images of both alloys are shown in figure 109 and it can be seen that higher Al content is highly beneficial in improving the LTHC resistance Pt-modified  $\beta$  containing Co and other refractory elements.

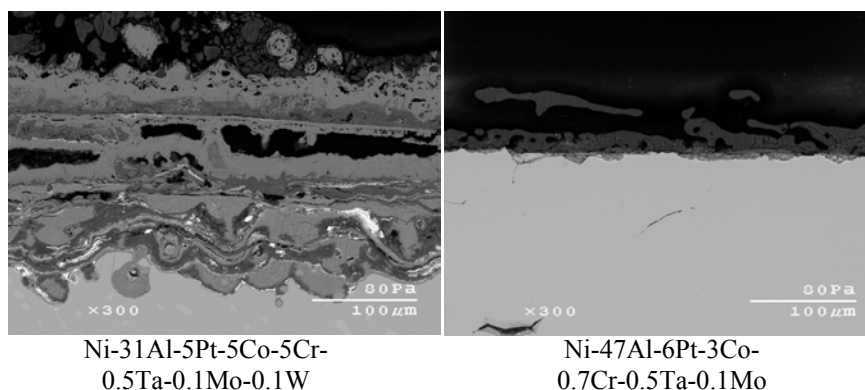


**Figure 109.** Cross-sectional SEM images of untreated  $\beta$  alloys after 100 h LTHC at 705°C.

### 5.2.3.6 Summary and Conclusions

1. Addition of Pt (up to 30%) improved LTHC resistance of  $\gamma'+\gamma$  alloys; however, it could not completely prevent LTHC after 100 h exposure. The LTHC in the  $\gamma'+\gamma$  alloys is due to the formation of  $\text{NiSO}_4+\text{Na}_2\text{SO}_4$  liquid at 705°C.
2. Chromium addition to Pt+Hf-modified  $\gamma'+\gamma$  alloys considerably improved LTHC resistance of  $\gamma'+\gamma$  alloys with a pre-oxidation treatment. The Ni-22Al-5Pt-5Cr-Hf  $\gamma'+\gamma$  alloy with an optimum HTHC and oxidation resistance also exhibited excellent LTHC resistance with a pre-oxidation treatment.
3. Addition of Si to high Pt-containing  $\gamma'+\gamma$  alloys resulted in excellent LTHC resistance even without pre-oxidation treatment. This is attributable to the relatively rapid establishment of a protective alumina-rich scale during early stages of oxidation/corrosion.

4. Most of the untreated  $\gamma'+\gamma$  alloys exhibited rather poor LTHC when compared with the Pt-modified  $\beta$  alloys. Addition of Pt is quite beneficial in improving LTHC resistance  $\beta$  alloys; while, a decrease in Al content and additions of Co and other refractory elements in  $\beta$  alloys significantly decreased LTHC performance due to increased stabilization of eutectic  $\text{Na}_2\text{SO}_4\text{-CoSO}_4$  ( $T_{\text{melt}} = 565^\circ\text{C}$ ) liquid.

### **5.3 Effects of Pre-oxidation on the Hot Corrosion Resistance of Pt+Cr+Hf-modified $\gamma'+\gamma$ Alloys**

#### **5.3.1 Introduction**

In order to maximize the lifetimes of gas turbine components, it is critical to control the microstructure, composition, and growth rate of the thermally grown oxide (TGO) that develops on the component surface. This can be at least partly achieved with an optimum pre-oxidation treatment that is arrived at by adjusting various critical pre-oxidation parameters such as oxidation atmosphere, time, temperature, and oxygen partial pressure [117-119]. It was shown in the previous sections that pre-oxidized Pt+Hf-modified  $\gamma'+\gamma$  alloys can exhibit superior HTHC (*i.e.*,  $900^\circ\text{C}$ ) resistance and comparable LTHC (*i.e.*,  $700^\circ\text{C}$ ) resistance compared to a Pt-modified  $\beta$  coating [120]. However, pre-oxidation treatment applied in that set of experiments was quite long and may not be practical from a cost standpoint for actual gas turbine engine components. Hence, the present work was conducted to obtain effective short-term pre-oxidation treatment for improving the hot corrosion resistance of Pt+Hf-modified  $\gamma'+\gamma$  alloys and, in particular, coatings. A bulk  $\gamma'+\gamma$  alloy having a composition similar to the Pt+Hf-modified  $\gamma'+\gamma$  coatings was selected for this particular study.

#### **5.3.2 Experimental**

The LTHC hot corrosion performances for the various pre-oxidation treatments were analyzed by assessing weight-change behavior and cross-sectional SEM micrographs of the corroded samples. A bulk alloy with a nominal composition (all in at.%) Ni-22Al-20Pt-5Cr-0.35Hf was prepared by Ar-arc melting with appropriate proportions of high purity

constituent elements. The alloy was primarily comprised of  $\gamma'$ -Ni<sub>3</sub>Al and its composition approaches that of the Pt+Hf-modified  $\gamma'+\gamma$  coatings that have been tested to date.

### Pre-oxidation Treatments

To understand the effects of various pre-oxidation treatments on LTHC hot corrosion behavior of Pt+Hf-modified  $\gamma'+\gamma$  alloys and coating, experiments were carried out on the cast  $\gamma'+\gamma$  alloy. This alloy was pre-oxidized in a horizontal furnace at 1100, 1080, and 700°C in air (*i.e.*,  $P_{O_2} \approx 0.2$  atm) and in Ar (*i.e.*,  $P_{O_2} \approx 10^{-6}$  atm) atmospheres for times of 1, 6, and 24h. For the Ar pre-oxidation, the furnace was initially purged with flowing Ar for about 2h. All samples were air cooled after each pre-oxidation treatment. The pre-oxidized alloy samples were analyzed using X-ray diffraction (XRD) for oxide phase identification.

### 5.3.3 Results and Discussion

#### 5.3.3.1 Effects of Pre-oxidation on the Ni-22Al-20Pt-5Cr-0.4Hf Alloy

An initial “standard” pre-oxidation treatment of the bulk  $\gamma'+\gamma$  alloy was carried out in both air and Ar at 1100°C for 24 hours, air-1100°C-24h \* and Ar-1100°C-24h, respectively. Both of these “standard” treatments resulted in the formation of a planar and adherent oxide scale with no visible spallation. Sample weight gains after 100h of LTHC hot corrosion testing of the alloy with and without a standard pre-oxidation are shown in figure 110 (Set A). Both pre-oxidized samples showed lower weight gains compared to the untreated sample, indicating that pre-oxidation at 1100°C improved LTHC hot corrosion resistance. As shown in figure 111, the cross-sectional SEM micrographs confirmed that pre-oxidation considerably improved hot corrosion resistance.

To further optimize the standard pre-oxidation treatment, the  $\gamma'+\gamma$  alloy was pre-oxidized for shorter times (*i.e.* for 1 and 6h) at lower temperatures (*i.e.* at 700 and 1080°C) in both air and Ar atmospheres. Figure 110 (Set B) shows weight gains after 100h of LTHC hot corrosion testing of alloy samples given a 6h pre-oxidation in air and Ar atmospheres (air/Ar-1080°C/700°C-6h). In general, it was observed that pre-oxidation at 700°C only slightly

---

\* Pre-oxidation treatment is denoted in the following manner: atmosphere-temperature-time

improved hot corrosion resistance when compared to the untreated sample; however, it exhibited rather poor hot corrosion resistance than the standard pre-oxidation treatments. Pre-oxidation at 1080°C showed much lower weight gains after hot corrosion testing, with air-1080°C-6h ( $\sim 1.1 \text{ mg/cm}^2$ ) being the lowest compared to the standard pre-oxidation treatments. Cross-sectional SEM micrographs after 100h of LTHC hot corrosion testing of the samples either untreated\*\* or pre-oxidized for 6h in air or Ar (air/Ar-1080°C/700°C-6h) are shown in figure 112. The untreated sample (figure 112a) underwent considerable attack to a maximum depth of about 60  $\mu\text{m}$ . Similarly, samples pre-oxidized at 700°C (figure 112b and 112c) underwent uniform LTHC attack, but to a lesser extent (*i.e.*  $\sim 35 \mu\text{m}$  for air-700°C-6h and  $\sim 45 \mu\text{m}$  for Ar-700°C-6h). Pre-oxidation at 1080°C considerably improved LTHC resistance. The sample pre-oxidized in Ar (Ar-1080°C-6h) underwent localized LTHC attack due to breakdown of TGO scale (figure 112d), while the air-1080°C-6h sample showed minimal LTHC attack (figure 112e). However, the weight gain of the air-1080°C-6h sample after hot-corrosion testing indicates that this sample very likely underwent some LTHC attack.

Sample weight gains after 100h of LTHC with 1h pre-oxidation in air or Ar atmospheres (air/Ar-1080°C/700°C-1h) are shown in figure 110 (Set C). The trend observed with 1h of pre-oxidation was quite similar to that observed with the 6h treatments. Pre-oxidation at 700°C for 1h (air/Ar-700°C-1h) was not beneficial in improving hot corrosion resistance. The lowest weight gain was observed for the air-1080°C-1h treatment, indicating that pre-oxidation at higher temperatures for a shorter period gives optimum resistance to LTHC hot corrosion. Figure 113 shows cross-sectional SEM micrographs after 100h of LTHC hot corrosion testing of the 1h pre-oxidation samples (air/Ar-1080°C/700°C-1h). The extent of attack for samples pre-oxidized at 700°C (*i.e.*  $\sim 45 \mu\text{m}$  for air-700°C-1h and Ar-700°C-1h, figure 113b and 113c) was less than the untreated sample\*\* ( $\sim 60 \mu\text{m}$ , figure 6a); however, the extent of improvement is not considered to be significant. As indicated above, pre-oxidation for 1h in Ar at 1080°C was not as beneficial as 6h at 1080°C; while, pre-

---

\*\* The untreated sample shown in figure 111 (a), 112 (a), and 113 (a) is the same but at different magnifications. This sample is included in each of these figures for the purpose of comparison.

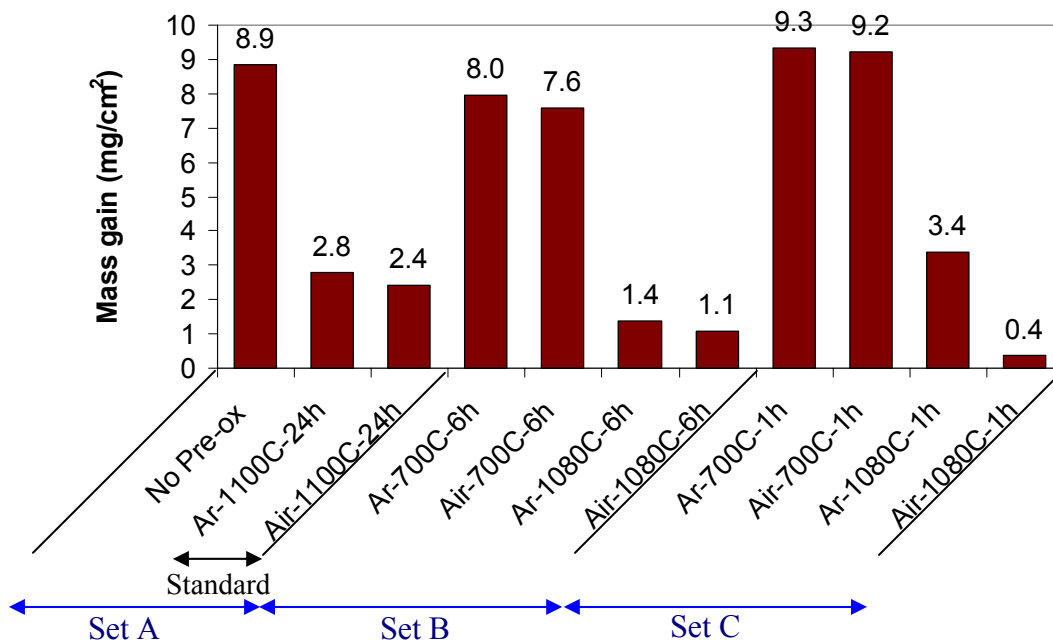
oxidation in air at 1080°C for either 1h or 6h resulted in excellent LTHC hot corrosion resistance.

It is noteworthy that the standard pre-oxidation at 1100°C for 24h in air resulted in a higher weight gain (2.4 mg/cm<sup>2</sup>) after hot corrosion testing compared to the treatment in air at 1080°C for shorter times *i.e.* 1h and 6h (0.4 and 1.1 mg/cm<sup>2</sup>). In order to determine if pre-oxidation for a shorter time is really more beneficial than for a longer time, an experiment was carried out using the air-1080°C-24h treatment conditions. Sample weight gain after 100h LTHC hot corrosion testing for the air-1080°C-24h treated alloy is compared with shorter-time pre-treatments (air-1080°C-1/6h) in figure 114. It is seen that pre-oxidation for shorter-times is more beneficial in improving LTHC hot corrosion resistance than pre-oxidation for a longer duration. Cross-sectional SEM micrographs showed that the samples exposed at 1080°C for a longer pre-oxidation time (24h) underwent localized LTHC attack, while the samples pre-oxidized for the shorter times (1h and 6h) showed only minimal LTHC attack (figure 115). This confirms our initial inference that pre-oxidation for shorter durations is more beneficial in improving LTHC hot corrosion than longer durations.

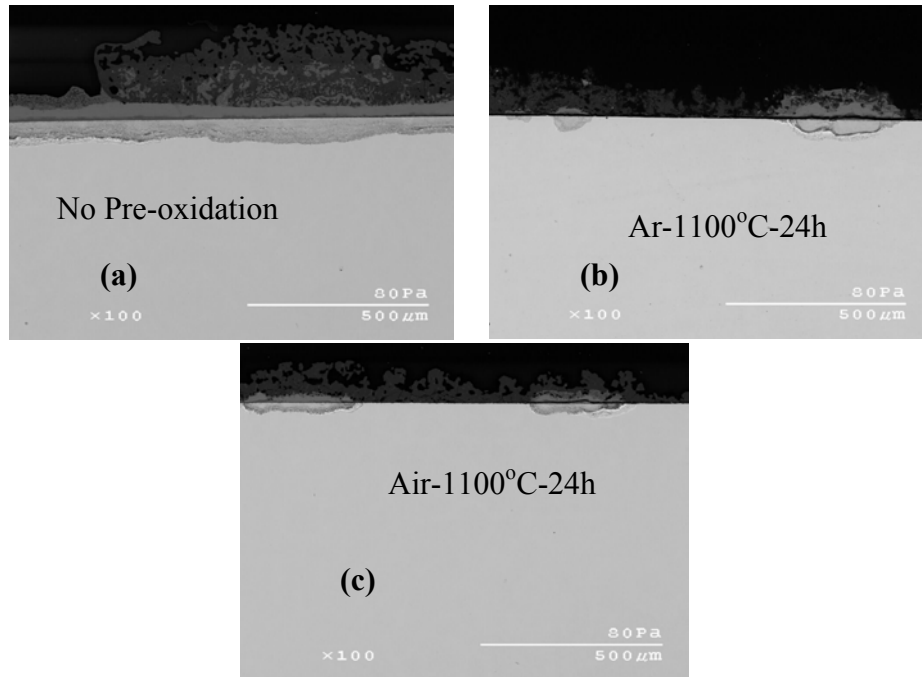
LTHC hot corrosion experiments performed on the  $\gamma'+\gamma$  alloy indicated that pre-oxidation at higher temperature for shorter times *i.e.* air-1080°C-1/6h exhibited superior LTHC resistance. Hence, an air-1080°C-6h pre-oxidation was given to various coatings in the next chapter. The formation of a thermally-grown Al<sub>2</sub>O<sub>3</sub> scale plays an important role in limiting environmental degradation of various high temperature alloys and coatings. In general, an ideal alumina scale should be dense, relatively inert, adherent, and slow-growing to protect underlying metal surface. A recent oxidation study by Izumi and Gleeson [109] on a (in at%) Ni-20Al-20Pt-Hf  $\gamma'+\gamma$  bulk alloy showed that this alloy is indeed an alumina former. However, it was observed in this study that pre-oxidation at a lower temperature (700°C) is less beneficial in improving LTHC hot corrosion resistance compared to pre-oxidation treatments at higher temperatures (1100°C and 1080°C). This is because the  $\gamma'+\gamma$  alloy could not establish a continuous and dense Al<sub>2</sub>O<sub>3</sub> scale at a temperature as low as 700°C. Indeed, Rybicki and Smialek [121] and later Grabke *et al.* [122-124] reported that  $\gamma$ -Al<sub>2</sub>O<sub>3</sub> and  $\theta$ -Al<sub>2</sub>O<sub>3</sub> form at temperatures < 950°C; however, the scale growth kinetics of these oxides are quite low (*i.e.*,  $k_p < 10^{-15}$  g<sup>2</sup>/cm<sup>2</sup>s) at 700°C. In accordance with this, SEM analysis performed on the  $\gamma'+\gamma$

alloy pre-oxidized at 700°C revealed that the scale was thin and non-uniform in thickness. The XRD analysis could not confirm the formation of metastable oxides since the oxide scale formed was quite thin. Notwithstanding, pre-oxidation at such a low temperature does still improve LTHC hot corrosion resistance compared to the untreated sample.

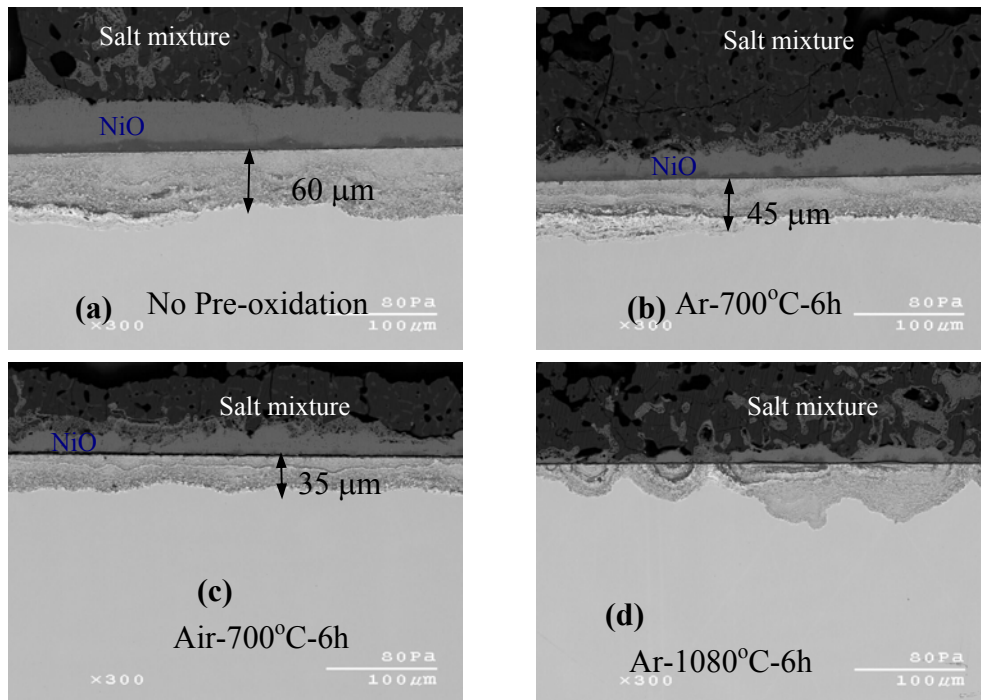
XRD analysis performed on samples after pre-oxidations at 1100°C and 1080°C indicated formation of  $\alpha$ -Al<sub>2</sub>O<sub>3</sub> scale. Grabke *et al.* [122-124] observed that the transformation of  $\theta$  to  $\alpha$ -Al<sub>2</sub>O<sub>3</sub> occurs between 950-1050°C. An  $\alpha$ -Al<sub>2</sub>O<sub>3</sub> scale is protective because of its high thermodynamic stability and slow growth rate compared to the metastable aluminas [123, 124]. A further aspect is the fact that an  $\alpha$ -Al<sub>2</sub>O<sub>3</sub> scale formed at higher temperature is comparatively thicker, denser and more continuous than the scale that may have formed at lower temperature. In fact, cross-sectional SEM analysis performed on the pre-oxidized samples for air-1080°C-6h confirmed the formation of thicker  $\alpha$ -Al<sub>2</sub>O<sub>3</sub> scale.



**Figure 110.** Weight gains after 100h LTHC hot corrosion of Ni-22Al-20Pt-5Cr-Hf with no pre-oxidation and with various (*i.e.* Set A: air/Ar-1100°C-24h; Set B: air/Ar-1080°C/700°C-6h; Set C: air/Ar-1080°C/700°C-1h) pre-oxidation treatments.



**Figure 111.** Cross-sectional SEM micrographs after 100h LTHC of Ni-22Al-20Pt-5Cr-Hf no pre-oxidation and with air/Ar-1100°C-24h (Set A) pre-oxidation treatments.



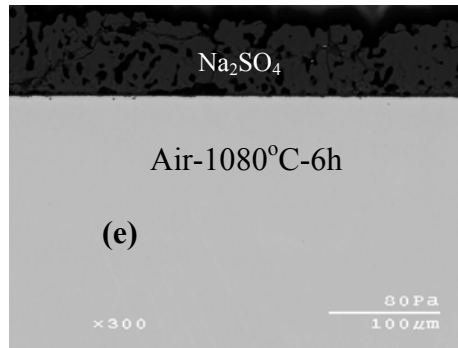


**Figure 112.** Cross-sectional SEM micrographs after 100h LTHC hot corrosion of Ni-22Al-20Pt-5Cr-Hf with air/Ar-1080°C/700°C-6h (Set B) pre-oxidation treatments.

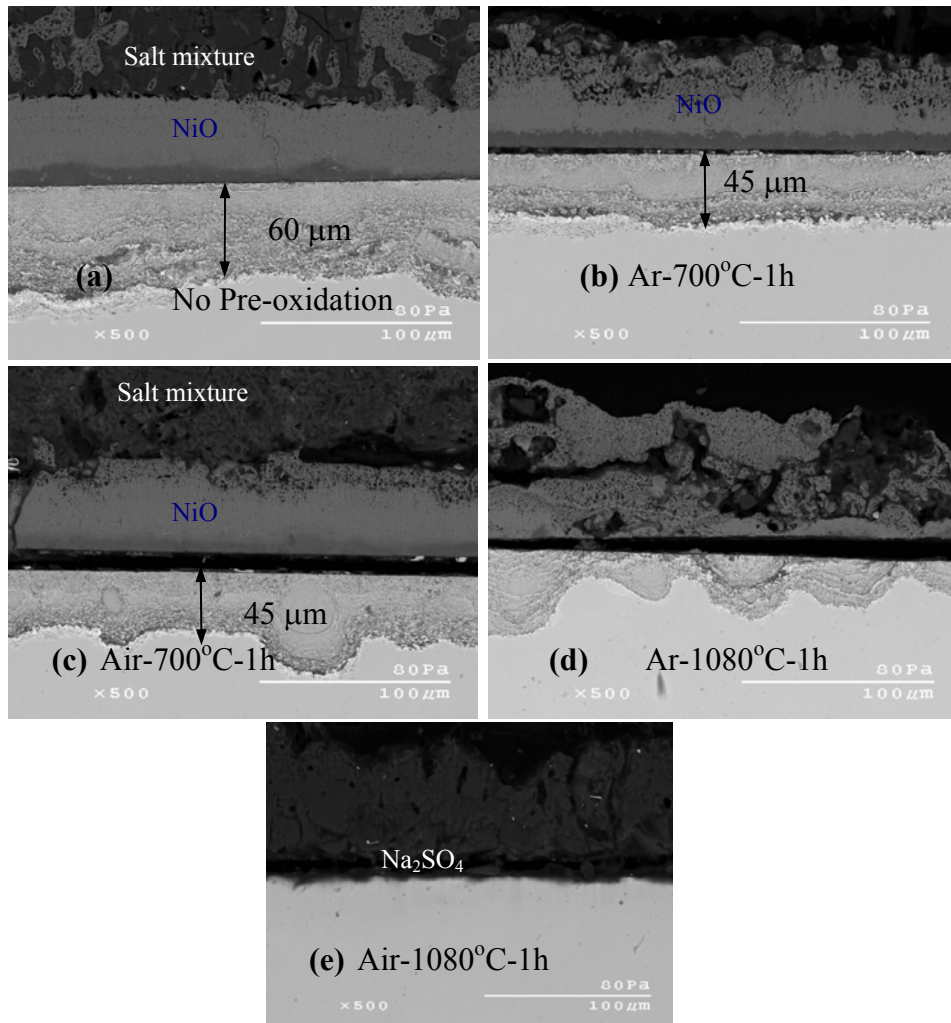


**Figure 113.** Cross-sectional SEM micrographs after 100h LTHC hot corrosion of Ni-22Al-20Pt-5Cr-Hf with air/Ar-1080°C/700°C-1h (Set C) pre-oxidation treatments.

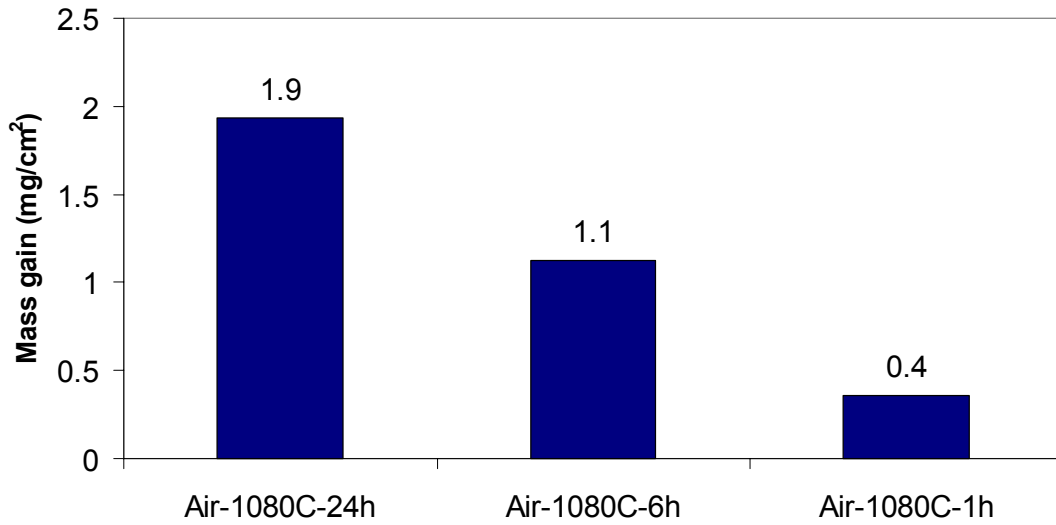


**Figure 114.** Weight gains after 100h LTHC hot corrosion of Ni-22Al-20Pt-5Cr-Hf with air-1080°C-24/6/1h pre-oxidation treatments.

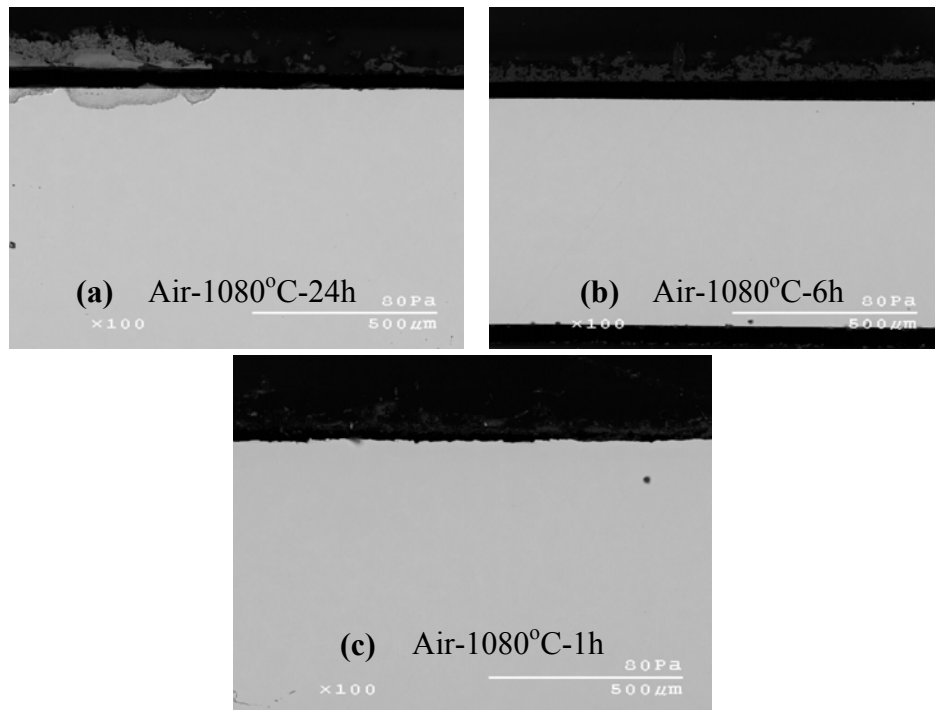


**Figure 115.** Cross-sectional SEM micrographs after 100h LTHC hot corrosion of Ni-22Al-20Pt-5Cr-Hf with air-1080°C-24/6/1h pre-oxidation treatments.

### 5.3.3.2. Effect of Pre-oxidation on the Ni-22Al-5Pt-5Cr-0.4Hf $\gamma'+\gamma$ Alloy

The results obtained thus far confirmed the beneficial role of pre-oxidation in the Cr-modified Ni-22Al-5Pt-Hf containing  $\gamma'+\gamma$  alloy. The pre-oxidation treatment used for this research was quite long and was at comparatively high temperature (*i.e.* 1100°C). It was observed from the previous section that pre-oxidation at 1080°C for shorter times also gave excellent LTHC resistance for the Ni-22Al-20Pt-5Cr-Hf  $\gamma'+\gamma$  alloy. A similar pre-oxidation treatment was then applied on the low-Pt Ni-22Al-5Pt-5Cr-Hf  $\gamma'+\gamma$  alloy and weight gain was compared with the longer period pre-oxidation at 1100°C and with the untreated sample as shown in figure 116. Sample weight gain with a shorter pre-oxidation time at 1080°C was quite similar with the longer pre-oxidation time at 1100°C and SEM images also showed no discernable LTHC attack in both the cases after 100h of exposure (figure 117). SEM image of the untreated alloy shown for comparison resulted in uniform LTHC attack.

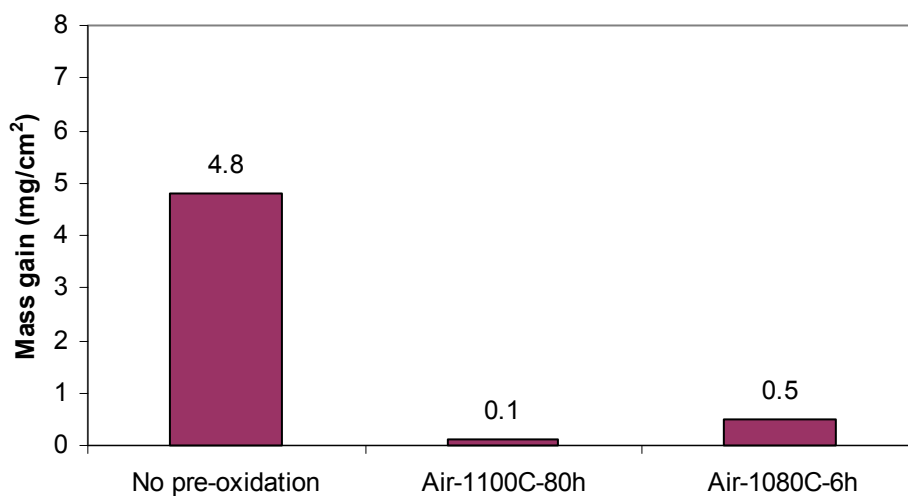


**Figure 116.** Weight gains of Ni-22Al-5Pt-5Cr-Hf  $\gamma'+\gamma$  alloy with different pre-oxidation treatment after 100 h (5 x 20 h cycles) LTHC at 705°C.

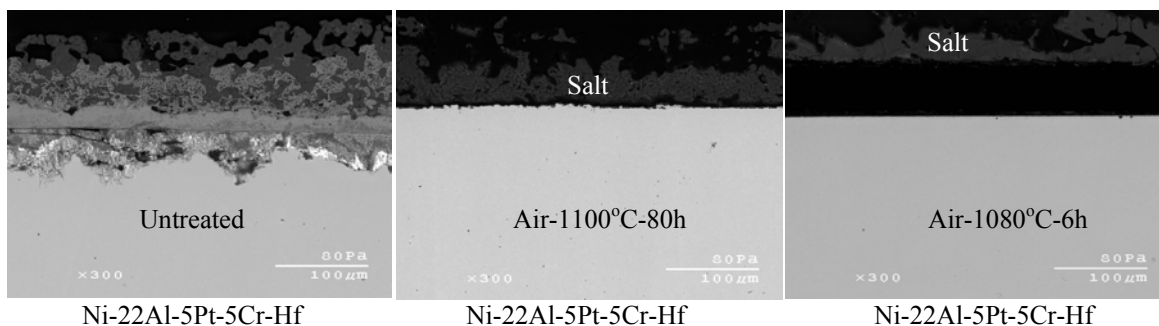


**Figure 117.** Cross-sectional SEM images of Ni-22Al-5Pt-5Cr-Hf  $\gamma' + \gamma$  alloy with different pre-oxidation treatment after 100 h LTHC at 705°C.

It was observed that Cr addition to the Pt+Hf-modified  $\gamma' + \gamma$  alloys without pre-oxidation treatment was not significant in improving hot corrosion resistance; however, all the Cr+Pt-modified  $\gamma' + \gamma$  alloys exhibited excellent hot corrosion resistance with a pre-oxidation treatment. XRD analysis performed on these Cr+Pt-modified  $\gamma' + \gamma$  alloys after a pre-oxidation treatment indicated the formation  $\alpha$ -Al<sub>2</sub>O<sub>3</sub> scale. Figure 118 shows surface and cross-sectional SEM images of a representative Cr+Pt-modified Ni-22Al-5Pt-5Cr-Hf  $\gamma' + \gamma$  alloy after a pre-oxidation treatment in air at 1100°C for 80 h. EDS analysis also confirmed the formation of continuous and adherent alumina scale. Therefore improved LTHC hot-corrosion performance in Cr+Pt-modified  $\gamma' + \gamma$  alloys with pre-oxidation treatment was due to the formation of protective alumina scale. An establishment of alumina-rich TGO scale during the pre-oxidation treatment due to Cr addition in the Pt+Hf-modified  $\gamma' + \gamma$  alloys can be described as the third-element or gettering effect as described in the earlier section.

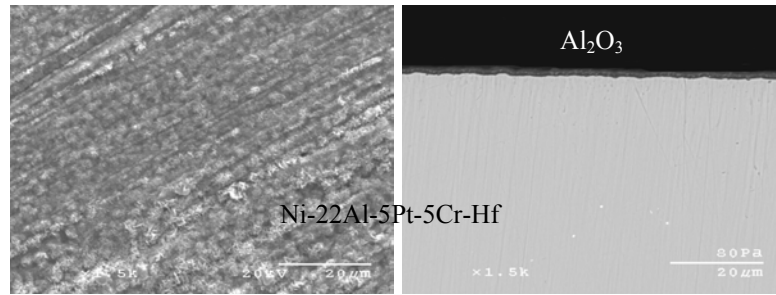


**Figure 118.** Surface and cross-sectional SEM images of Ni-22Al-5Pt-5Cr-Hf  $\gamma'+\gamma$  alloy after 80 h of pre-oxidation at 1100°C

#### 5.3.4. Summary and Conclusions

Pre-oxidation of a Ni-22Al-20Pt-5Cr-Hf  $\gamma'+\gamma$  alloy in air at 1080°C for relatively short times (6h and 1h) resulted in the greatest improvement in LTHC hot corrosion resistance. The hot corrosion performance of  $\gamma'+\gamma$  alloys and coatings with pre-oxidation (air-1080°C-1/6h) under LTHC conditions is believed to be attributable to the presence of a fairly homogeneous and continuous  $\alpha$ -Al<sub>2</sub>O<sub>3</sub> scale, which formed by pre-oxidation treatment.

## 6. HOT CORROSION EVALUATION OF DEVELOPMENTAL $\gamma'+\gamma$ COATING AND COMMERCIALY AVAILABLE METALLIC COATINGS

### 6.1 Introduction

The overall objective of this study was to compare and rank the hot-corrosion resistance of various commercial and developmental coatings applied to a Ni-based superalloy substrate. Both types of hot corrosion were investigated, but particular focus was directed at LTHC corrosion. The potential benefits of a pre-oxidation treatment to further improve the hot corrosion resistance of the coatings were also investigated. As a case of point, it was established in the previous section that a pre-oxidation treatment of  $\gamma'+\gamma$  alloys at higher temperatures for relatively short times results in a significant improvement in LTHC hot corrosion resistance. A similar pre-oxidation treatment was applied for this study. Finally, selected bulk  $\gamma'+\gamma$  alloys having optimum hot corrosion and oxidation resistance were tested with the coatings.

### 6.2 Experimental

Bulk  $\gamma'+\gamma$  alloys with a nominal compositions (in at%) Ni-22Al-5Pt-5Cr-1Si-0.35Hf and Ni-20Al-2.5Pt-2.5Ir-5Cr-0.35Hf were prepared by Ar-arc melting with appropriate proportions of high purity constituent elements. The alloys were primarily comprised of  $\gamma'$ -Ni<sub>3</sub>Al and were drop-cast into the form of rods, ~50 mm long and 10 mm in diameter. The as-cast rods were heat treated in flowing argon gas at 1200°C for 6 hours followed by 48 hours at 1150°C to ensure homogenization and equilibration. The heat-treated rods were then sectioned into ~1.5 mm thin coupon samples and polished to a 1200-grit finish. Test samples were ultrasonically cleaned in acetone before pre-oxidation or hot corrosion testing.

The as-received coated pins were ~8.8 mm in diameter and ~10 mm long. The substrate alloy used in this study was second-generation Ni-based superalloy, which has the following nominal composition (in at. %):

Ni-based superalloy: 63.6Ni-12.6Al-9.3Co-7.6Cr-2.2Ta-2.0W-1.3Ti-1Re-0.4Mo-0.03Hf.

The chemical-composition range for each as-received and pre-oxidized coating was measured via electron probe microanalysis (EPMA) and the results are summarized in Table 8. The approximate regions in which the coating compositions were measured are shown in figure 119. The measured thickness and phase constitution of each as-deposited coating is also given in Table 8.

**Table 8.** Measured compositional range, thicknesses, and phase constitution of as-deposited/pre-oxidized coatings.

Coating Type and Thickness	Phase constitution	As-deposited Measured Composition (at%)	Pre-oxidized Measured Composition (at%)
Pt-modified $\beta$ (~52-60 $\mu\text{m}$ )	$\beta$ -NiAl	Ni-(38-44)Al-(7-8)Pt-(4-5)Co-(2-3)Cr	Ni-(33-36)Al-(7-8)Pt-(5-6)Co-(3-4)Cr
Pt+Hf-modified $\gamma'+\gamma$ (~22-25 $\mu\text{m}$ )	$\gamma'$ -Ni <sub>3</sub> Al+ $\gamma$ -Ni	Ni-(16-17)Al-(23-25)Pt-(5-6)Co-(5-6)Cr-0.5Hf	NA
Ni-rich Pt-modified $\gamma+\gamma'$ (~20-25 $\mu\text{m}$ )	$\gamma$ -Ni+ $\gamma'$ -Ni <sub>3</sub> Al	Ni-(12-13)Al-(23-27)Pt-(6-7)Co-(5-6)Cr	Ni-(9-11)Al-(16-19)Pt-(7-9)Co-(5-6)Cr
Silica + Pt-modified $\gamma+\gamma'$ {~(40-45)+(20-25) $\mu\text{m}$ }	Ceramic top layer and $\gamma'$ -Ni <sub>3</sub> Al+ $\gamma$ -Ni	Outer layer: SiO <sub>2</sub> Inner layer: Ni-(17-19)Al-(18-21)Pt-(5-6)Co-(5-6)Cr	Outer layer: SiO <sub>2</sub> Inner layer: Ni-(14-16)Al-(13-14)Pt-(6-7)Co-(5-6)Cr
Ni-rich Pt+Si modified $\beta$ (~55-65 $\mu\text{m}$ )	$\beta$ -NiAl	Ni-(31-34)Al-(7-8)Pt-(5-6)Co-(3-4)Cr-(1-2)Si	Ni-(30-33)Al-(5-6)Pt-(5-6)Co-(3-4)Cr-(1-2)Si
Pt-free $\beta$ (~35-40 $\mu\text{m}$ )	$\beta$ -NiAl	Ni-(34-38)Al-(5-6)Co-(2-3)Cr	Ni-(30-32)Al-7Co-4Cr
Chromized (~10-15 $\mu\text{m}$ )	$\gamma$ -Ni	Ni-12Al-10Co-7Cr-2Ta-2W-1Ti	Ni-7Al-9Co-6Cr-1.5Ta-2W-1Ti
Aluminized $\beta$ (~55-60 $\mu\text{m}$ )	Top zone: Al-rich $\beta$ -NiAl Bottom zone: Ni-rich $\beta$ -NiAl	Top zone: Ni-(46-49)Al-(3-4)Co-1Cr Bottom zone: Ni-(38-42)Al-7Co-3Cr	Ni-(38-42)Al-(4-5)Co-(2-3)Cr

The Pt-modified  $\beta$  coating was deposited by Pt electroplating followed by Al chemical vapor deposition (CVD). The Pt+Hf-modified  $\gamma'+\gamma$  was deposited by Pt

electroplating followed a diffusion treatment and then a proprietary Al+Hf co-deposition pack cementation CVD process. The Ni-rich Pt-modified  $\gamma+\gamma'$  coating involved only a Pt electrodeposition followed by a diffusion treatment. The Silica + Pt-modified  $\gamma+\gamma'$  consists of two layers: outer ceramic layer of  $\text{SiO}_2$  and inner Pt-modified  $\gamma+\gamma'$  metallic layer. The metallic layer was deposited by Pt electroplating followed by a diffusion and proprietary process. The Ni-rich Pt+Si-modified  $\beta$  coating was deposited by Pt electroplating followed by a diffusion and proprietary process. The Pt-free  $\beta$  coating was deposited by an aluminizing CVD treatment. The Chromized coating was deposited by a proprietary process. The Aluminized  $\beta$  coatings consists of two zones having a different compositions of  $\beta$ . The outer zone consists of Al-rich  $\beta$ , while the inner zone is Ni-rich  $\beta$  and it was deposited by aluminizing CVD followed by proprietary BTSE process.

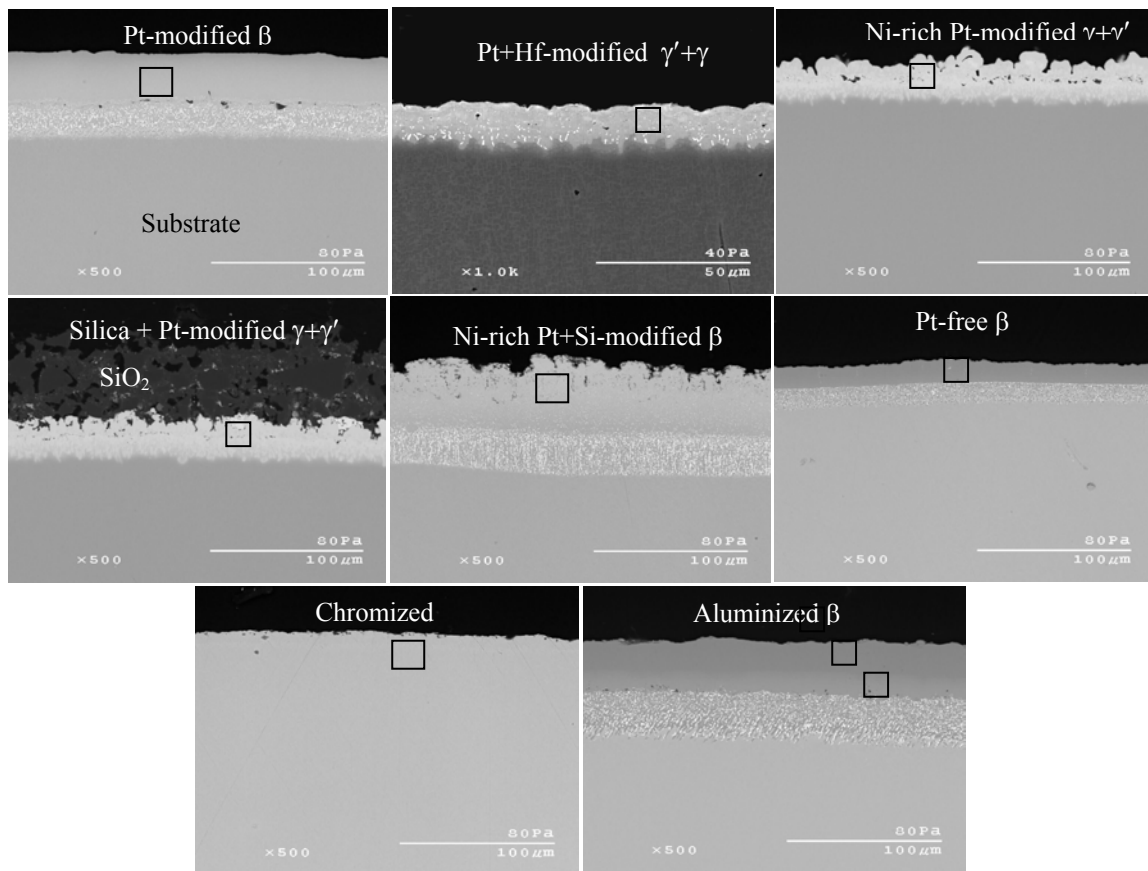


**Figure 119.** SEM micrographs of various as-deposited coatings on Ni-based substrate. SEM images show the region where the range of composition was measured.

### 6.3 Results and Discussion

#### 6.3.1. LTHC (700 °C) Testing with Pre-oxidation Treatment (Air-1080°C-6h)

Initial testing focused on the 100 h LTHC behavior of the various coatings and alloys having a pre-oxidation treatment. Sample weight gains of the coatings and alloys are shown in figure 120. The Ni-based superalloy and Ni-rich Pt-modified  $\gamma+\gamma'$  and Chromized coatings showed extremely high weight gains, indicating rather poor LTHC resistance. The Pt+Hf-modified  $\gamma'+\gamma$  and Silica + Pt-modified  $\gamma+\gamma'$  coatings and  $\gamma'+\gamma$  alloys (*i.e.* Ni-22Al-5Pt-5Cr-1Si-Hf and Ni-20Al-2.5Ir-2.5Pt-5Cr-Hf) showed the lowest weight gains. The Pt-modified  $\beta$  coating also showed a comparatively low weight gain after 100h of LTHC.

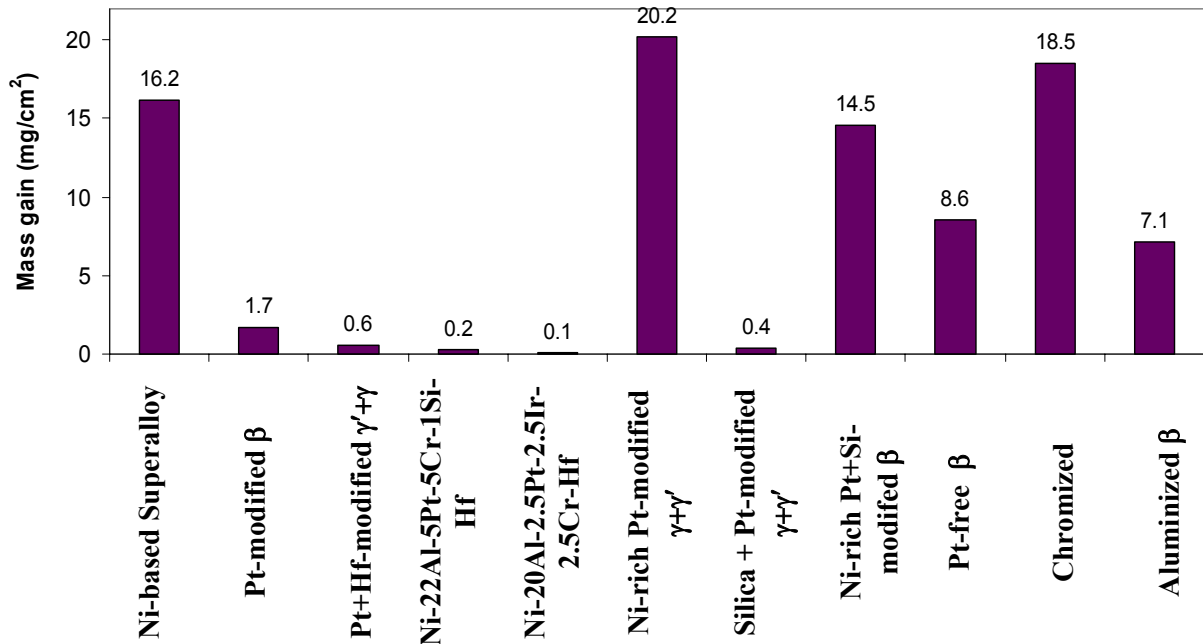


**Figure 120.** Weight gains after 100h LTHC of various coatings and alloys with a pre-oxidation treatment (air-1080°C-6h).

Corresponding cross-sectional SEM images of the various alloys and coatings after 100h of LTHC are shown in figure 121. It was seen that the mode of attack in Ni-based superalloy and the Ni-rich Pt-modified  $\gamma+\gamma'$  and Chromized coatings was uniform throughout the cross-section. The Ni-rich Pt+Si-modified  $\beta$  and Pt-free  $\beta$  coatings were also heavily

attacked and there were localized regions where attack penetrated into the substrate. The LTHC attack in Pt-modified  $\beta$  was seen only at a few localized regions, as indicated in figure 121, but overall it exhibited good hot corrosion resistance; while, the Pt+Hf-modified  $\gamma'+\gamma$  and Silica + Pt-modified  $\gamma+\gamma'$  coatings and  $\gamma'+\gamma$  bulk alloys showed no discernable LTHC attack after 100h of exposure. The corrosion products in the attacked regions of coatings were analyzed using EDS and, based on compositional analysis, it was deduced that the outermost layer primarily consisted of NiO followed by inner layers  $\text{NiAl}_2\text{O}_4$  and  $\text{Al}_2\text{O}_3$ . The coatings/alloys that were completely attacked (Ni-based superalloy, Ni-rich Pt-modified  $\gamma+\gamma'$ , Pt-free  $\beta$  and Chromized) formed a very thick NiO layer (figure 121), while those that were not visibly attacked (Pt+Hf-modified  $\gamma'+\gamma$ , Silica + Pt-modified  $\gamma+\gamma'$  coatings and  $\gamma'+\gamma$  bulk alloys) showed the presence of solid salt deposit and no evidence of Ni oxidation.

Semi-quantitative analyses results of the extents of attack are summarized in the form of histograms in figure 122. The Ni-based superalloy and Ni-rich Pt-modified  $\gamma+\gamma'$  and Chromized coatings exhibited only high corrosion ( $>45\mu\text{m}$ ); whereas, the Ni-rich Pt+Si-modified  $\beta$ , Pt-free  $\beta$  and Aluminized  $\beta$  coatings underwent varying extents of attack. The Pt-modified  $\beta$  coating had  $\sim 92\%$  low corrosion and only few regions of medium and high corrosion, reflecting generally good LTHC resistance. The coatings and alloys that exhibited excellent LTHC resistance on the basis of weight change, *i.e.*, Pt+Hf-modified  $\gamma'+\gamma$  and Silica + Pt-modified  $\gamma+\gamma'$  coatings and  $\gamma'+\gamma$  bulk alloys, showed 100% no/low corrosion. A similar trend was seen from the maximum depth of attack, except for the Pt-modified  $\beta$  coating, which had deep penetration of  $\sim 100\mu\text{m}$  into the substrate (figure 123).

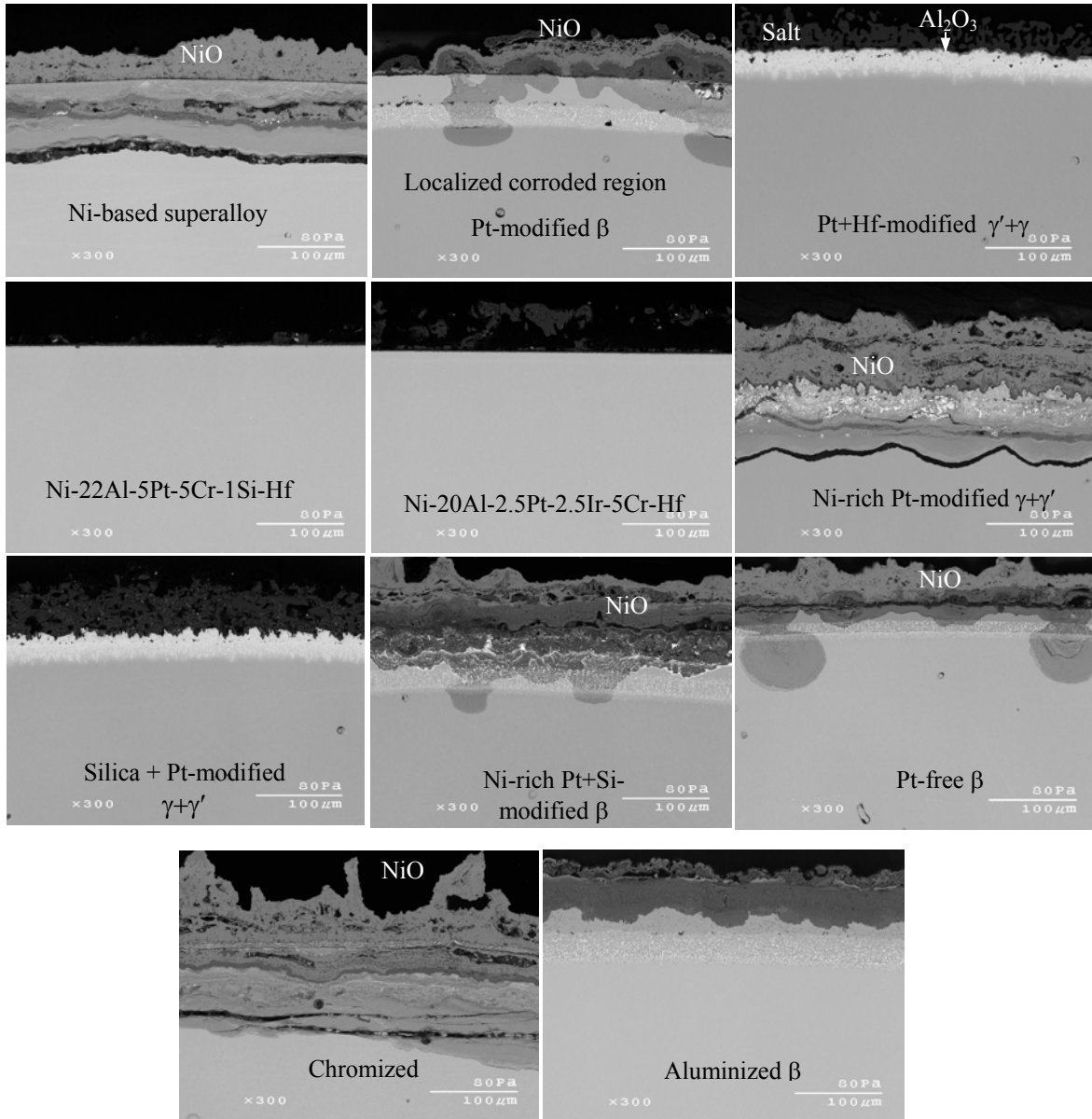


**Figure 121.** Cross-sectional SEM images after 100h LTHC of various coatings and alloys with a pre-oxidation treatment (air-1080°C-6h).

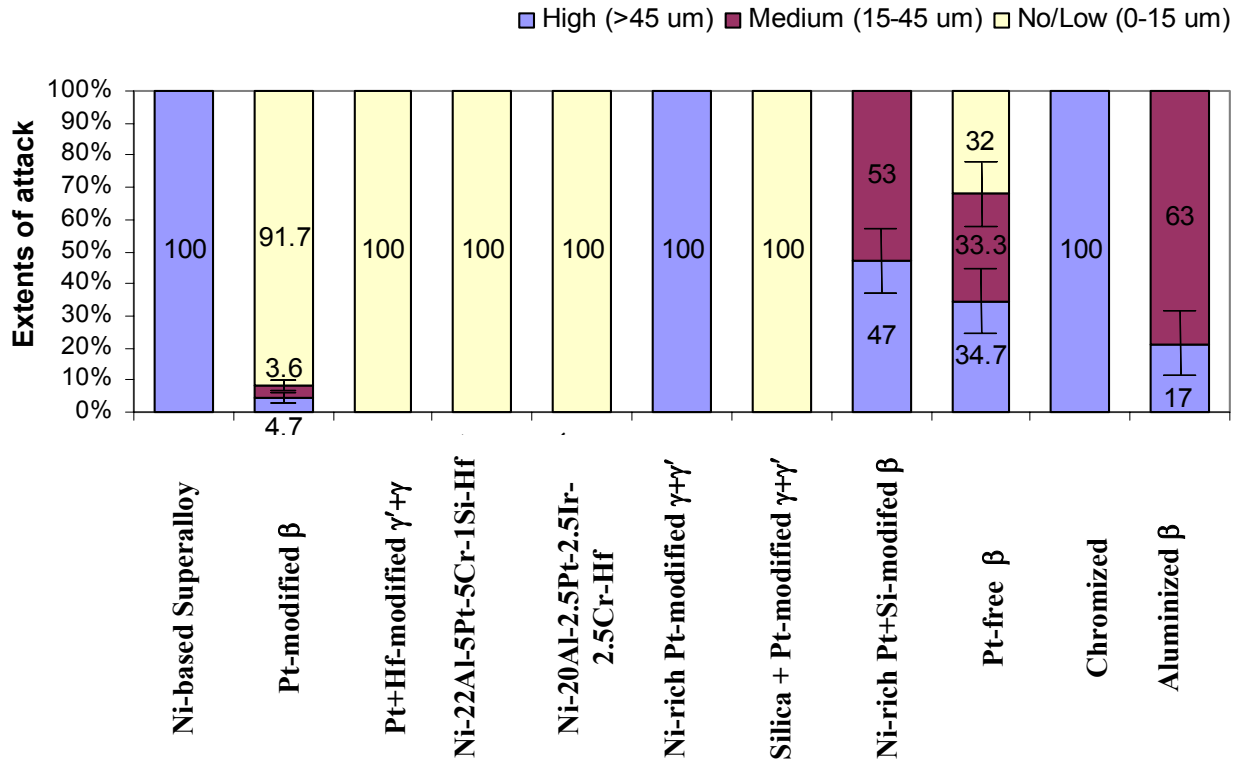


**Figure 122.** Extents of attack after 100h LTHC of various coatings and alloys with a pre-oxidation treatment (air-1080°C-6h).

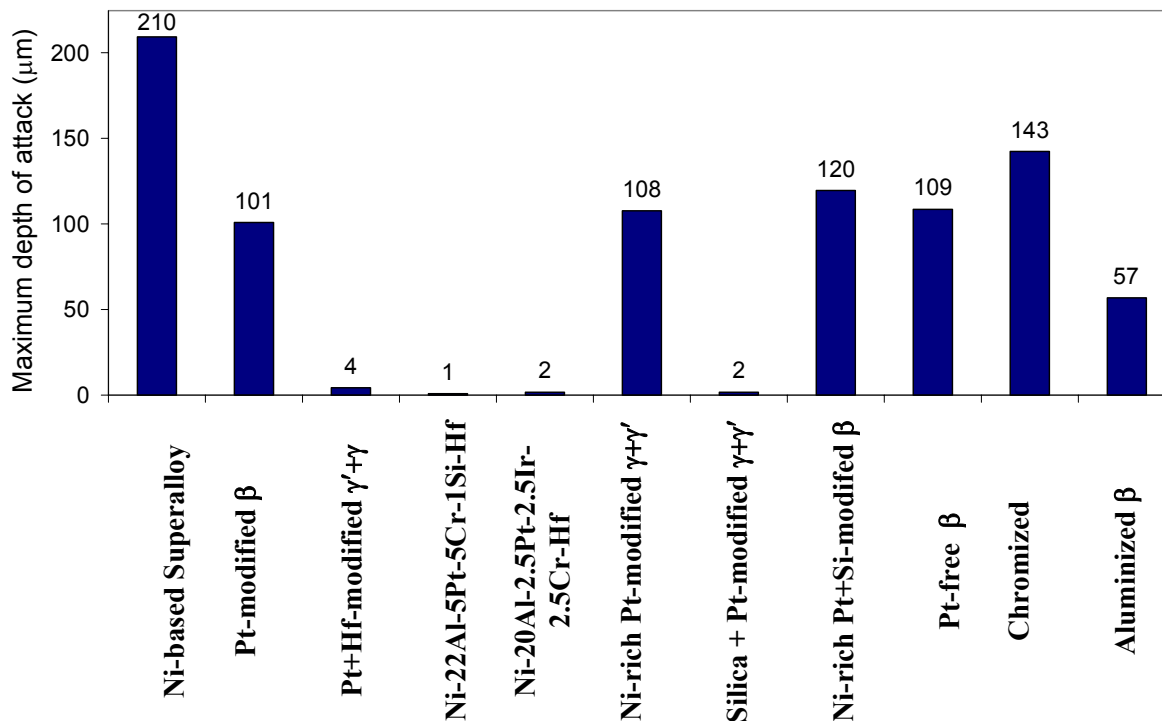


**Figure 123.** Maximum depth of attack after 100h LTHC of various coatings and alloys with a pre-oxidation treatment (air-1080°C-6h).

As described in the earlier section, the LTHC of Ni-based alloys and coatings is often attributed to the formation of eutectic  $\text{Na}_2\text{SO}_4\text{-NiSO}_4$  liquid ( $T_{\text{melt}} = 671^\circ\text{C}$ ) [39, 54]. The  $\text{NiSO}_4$  (s) can form under LTHC conditions, where the NiO may be present as a consequence of the initial stages of coating or alloy oxidation. EDS analyses of the hot-corroded samples clearly indicated formation of thick NiO scale below the salt mixture (figure 121). The elements such as Co and other refractory elements (*e.g.* Ta, W, and Re) are likely to be present in the diffusion aluminide coatings. The presence of these elements, in particular Co, may further exacerbate the LTHC resistance of aluminide coatings by the formation of  $\text{CoSO}_4$ , which is even more stable than  $\text{NiSO}_4$ . Moreover, the  $\text{Na}_2\text{SO}_4\text{-CoSO}_4$  eutectic mixture has a much lower melting temperature ( $565^\circ\text{C}$ ) than that of the  $\text{Na}_2\text{SO}_4\text{-NiSO}_4$  mixture ( $T_{\text{melt}} = 671^\circ\text{C}$ ). Indeed, it was reported in the previous section that the presence of Co and other refractory elements considerably decreases the LTHC resistance of Pt-modified

$\beta$ -NiAl alloys, particularly Ni-rich  $\beta$  alloys. A similar detrimental effect of Co and other refractory elements is expected in  $\gamma'+\gamma$  alloys and coatings.

The formation of a thermally-grown  $\text{Al}_2\text{O}_3$  scale plays an important role in limiting environmental degradation of various high temperature alloys and coatings. In general, an ideal alumina scale should be dense, relatively inert, adherent, and slow-growing to protect underlying metal surface. A recent oxidation study by Izumi and Gleeson [109] on a (in at%) Ni-20Al-20Pt-Hf  $\gamma'+\gamma$  bulk alloy showed that this alloy is an excellent alumina former. XRD analysis performed on the pre-oxidized  $\gamma'+\gamma$  bulk alloys used in this study also confirmed the formation of an  $\alpha$ - $\text{Al}_2\text{O}_3$  scale. The excellent performance of the Pt+Hf-modified  $\gamma'+\gamma$  coating and  $\gamma'+\gamma$  bulk alloys is therefore attributed to the presence of a protective  $\alpha$ - $\text{Al}_2\text{O}_3$  scale that forms during a relatively short-term pre-oxidation period (*i.e.*, air-1080°C-6h). This Al-rich scale apparently provided a barrier to the inward transfer of salt and the outward migration of Ni. By contrast, the excellent performance of the Silica+Pt-modified  $\gamma+\gamma'$  coating is believed to be attributable to both the outer  $\text{SiO}_2$  layer acting as barrier of sorts and the Al-rich scale that formed between this outer layer and  $\gamma'+\gamma$  coating.

The six best-performing coatings and alloys (w/ pre-oxidation: air-1080°C-6h) from the 100 h LTHC test were selected for extended testing to 200 h. The weight gains from this latter testing are shown in figure 124. In general, all the samples showed higher weight gains compared to 100 h of testing. Except for the Silica+Pt-modified  $\gamma+\gamma'$  coating, a similar trend was observed after 200 h of testing, with the Pt+Hf-modified  $\gamma'+\gamma$  coating and Ni-22Al-5Pt-5Cr-1Si-Hf  $\gamma'+\gamma$  alloy showing the lowest weight gain. The Silica+Pt-modified  $\gamma+\gamma'$  coating underwent considerable weight gain ( $\sim 30 \text{ mg/cm}^2$ ), indicating extensive attack with the extended period of exposure. The Pt-modified  $\beta$  coating showed comparatively lower weight gain, while the Ni-rich Pt-modified  $\gamma+\gamma'$  coating showed the highest weight gain after 200 h of exposure.

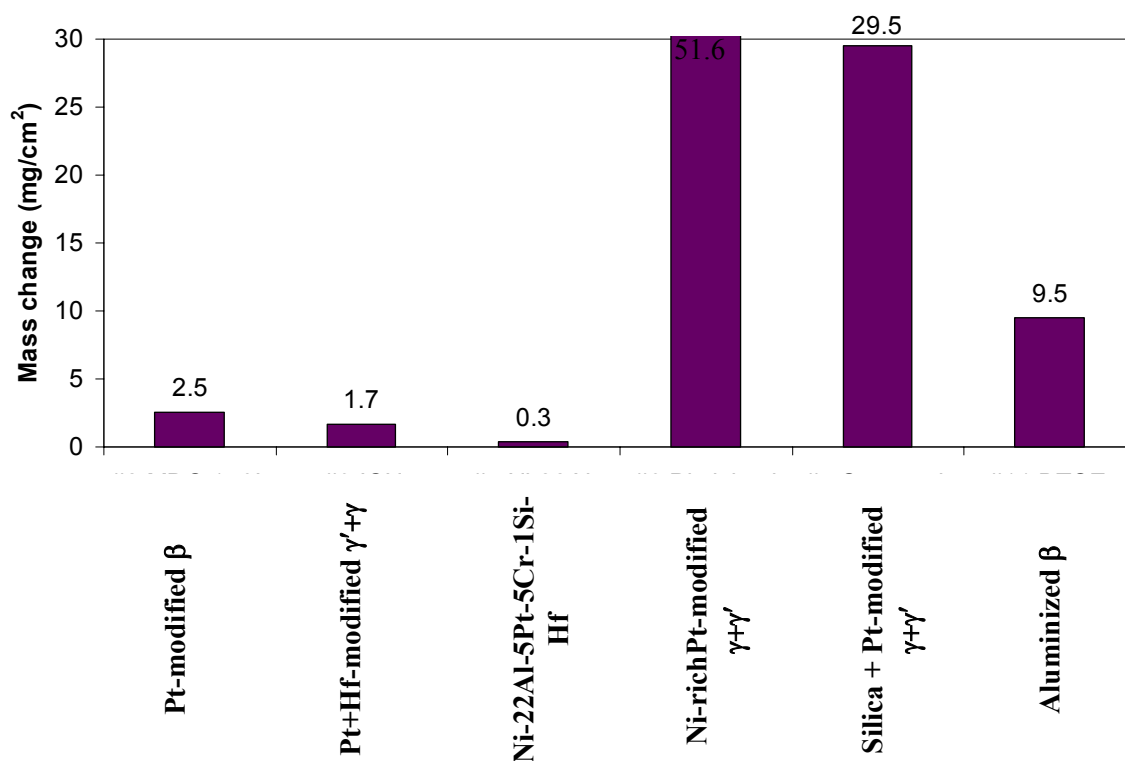


**Figure 124.** Weight gains after 200h LTHC of six selected coatings/alloy with a pre-oxidation treatment (air-1080°C-6h).

Cross-sectional SEM images of the selected coatings and alloys after 200 h of LTHC testing are shown in figure 125. The Pt+Hf-modified  $\gamma'+\gamma$  coating and Ni-22Al-5Pt-5Cr-1Si-Hf  $\gamma'+\gamma$  alloy showed no discernable attack throughout the cross-section. In general, the Pt-modified beta coating also showed excellent LTHC resistance; however, it did undergo localized breakdown in which hot corrosion attack penetrated into the substrate (figure 126). The Ni-rich Pt-modified  $\gamma+\gamma'$  coating was completely attacked, whereas Silica+Pt-modified  $\gamma+\gamma'$  was only partially attacked. A uniform LTHC attack was observed in the Aluminized  $\beta$  coating, but the depth of penetration was still within the coating thickness throughout the cross-section. EDS analysis of the attacked regions of the coatings clearly showed an outer NiO layer and internal Ni-rich oxide followed by Cr- and Al-rich oxides nearer to the substrate. The extents of attack and maximum depth of penetration were measured and are shown in the form of histograms in figures 126 and 127. These measurements confirmed the

extremely poor resistance of the Ni-rich Pt-modified  $\gamma+\gamma'$  coating, which showed high corrosion throughout the cross-section. The Silica+Pt-modified  $\gamma+\gamma'$  coating, which showed 100% low corrosion after 100 h of testing, exhibited varying levels of high, medium and low corrosion after 200 h of exposure. The Pt-modified  $\beta$  coating showed localized breakdown to give minor amounts of medium and high corrosion, but overall it showed a high percentage (~91%) of low corrosion. This coating also showed a comparatively high maximum depth of penetration (~141  $\mu\text{m}$ ) into the substrate after 200 h exposure (figure 126). Both the Pt+Hf-modified  $\gamma'+\gamma$  coating and the Ni-22Al-5Pt-5Cr-1Si-Hf  $\gamma'+\gamma$  alloy showed only low corrosion, due presumably to the formation of protective TGO scale after a pre-oxidation treatment. To summarize, the order of performance under LTHC conditions of various coatings/alloys (w/ pre-oxidation) from best to worst was as follows: Pt+Hf-modified  $\gamma'+\gamma$  coating  $\approx$   $\gamma'+\gamma$  alloys (Ni-22Al-5Pt-5Cr-1Si-Hf and Ni-20Al-2.5Pt-2.5Ir-5Cr-Hf) > Pt-modified  $\beta$  > Silica+Pt-modified  $\gamma+\gamma'$  > Aluminized  $\beta$  > Ni-rich Pt+Si-modified  $\beta$  > Pt-free  $\beta$  > Ni-rich Pt-modified  $\gamma+\gamma'$  > Chromized > Ni-based Superalloy.

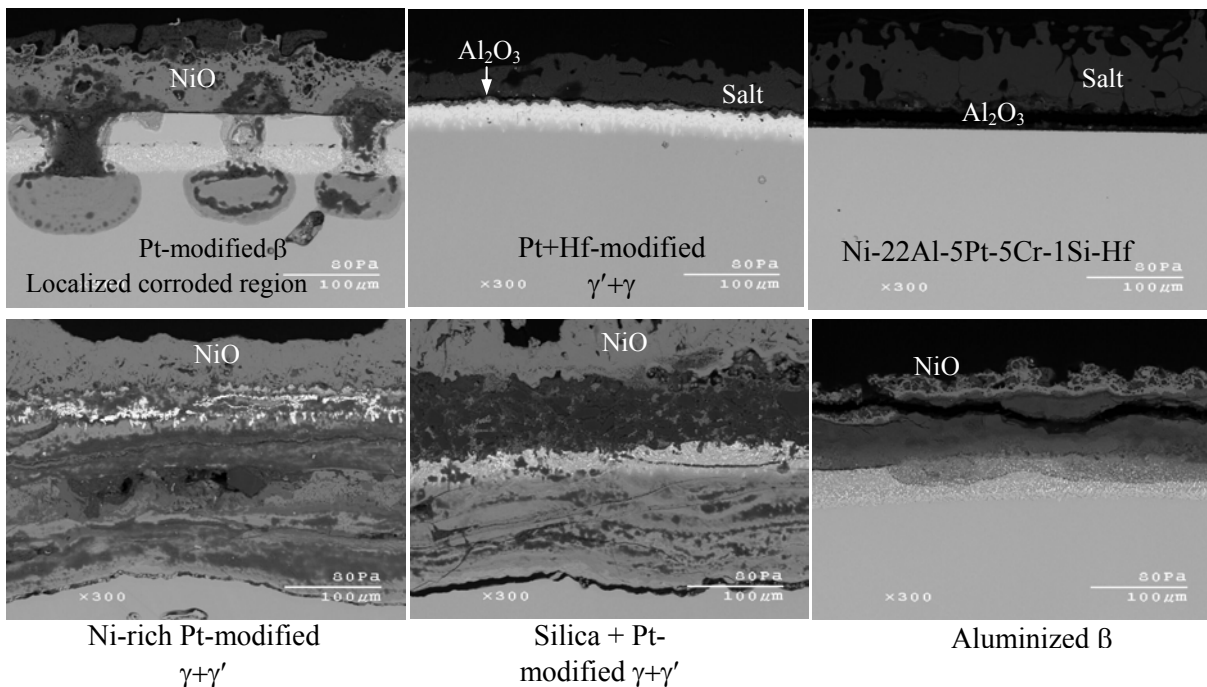


**Figure 125.** Cross-sectional SEM images after 200h LTHC of six selected coatings/alloy with a pre-oxidation treatment (air-1080°C-6h).

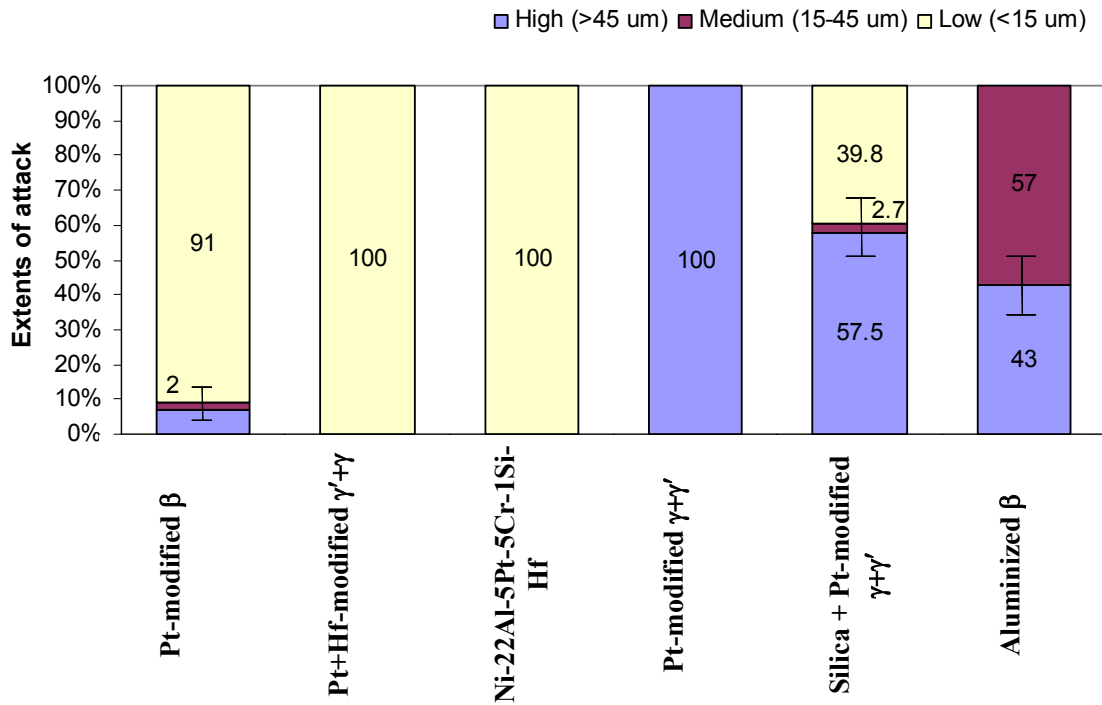


**Figure 126.** Extents of attack after 200h LTHC of six selected coatings/alloy with a pre-oxidation treatment (air-1080°C-6h).

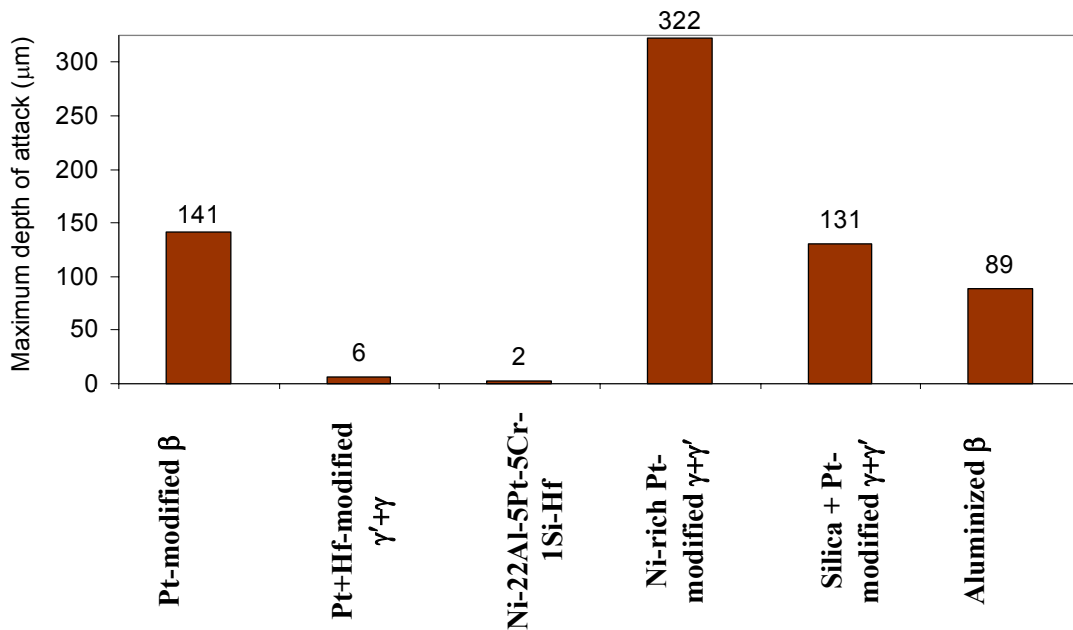


**Figure 127.** Maximum depth of attack after 200h LTHC of six selected coatings/alloy with a pre-oxidation treatment (air-1080°C-6h).

### 6.3.2 LTHC (705 °C) with No Pre-oxidation Treatment

The LTHC testing was also carried out on selected coatings and alloys that were not given a pre-oxidation treatment. The weight change behavior of the untreated samples after 100 h of testing is shown in figure 128. In contrast to LTHC testing with pre-oxidation, all the coatings resulted in quite higher weight gains *except* for the Pt-modified  $\beta$  coating, which showed a lower weight gain. Thus, the Pt-modified  $\beta$  coating showed better LTHC resistance when not pre-oxidized, whereas the Pt+Hf-modified  $\gamma'+\gamma$  coating, Ni-22Al-5Pt-5Cr-1Si-Hf alloy, and Silica+Pt-modified  $\gamma+\gamma'$  showed considerably higher weight gains than the pre-oxidation case. Cross-sectional SEM images of corroded regions of various alloys and coatings are shown in figure 129. It is seen that all of the coatings except Pt-modified  $\beta$  were completely attacked when no pre-oxidation treatment was given.

A semi-quantitative analysis of the extents of attack and maximum depth of attack were carried out and the results are summarized in figures 130 and 131. Several coatings and alloys, such as Ni-based superalloy, Pt+Hf-modified  $\gamma'+\gamma$  coating, Ni-rich Pt-modified  $\gamma+\gamma'$ , Silica+Pt-modified  $\gamma+\gamma'$ , and Chromized exhibited 100% high corrosion. The maximum depth of penetration was also quite deep inside the substrate in all these coatings/alloy. These results suggest that pre-oxidation is a very critical step in extending the service lives of gas turbine engine materials. This is particularly true for the Pt+Hf-modified  $\gamma'+\gamma$  coating. The coatings/alloys that exhibited varying levels of attack were Ni-22Al-5Pt-5Cr-1Si-Hf, Silica+Pt-modified  $\gamma+\gamma'$ , Pt-free  $\beta$ , and Aluminized  $\beta$ ; whereas, the Pt-modified  $\beta$  coating showed 100% low corrosion. The maximum depth of penetration was also lowest in Pt-modified beta and comparatively low for the Ni-22Al-5Pt-5Cr-1Si-Hf alloy (figure 131). The overall ranking of the untreated coatings and alloys from best to worst after 100h of LTHC testing is as follows: Pt-modified  $\beta$  > Ni-22Al-5Pt-5Cr-1Si-Hf  $\gamma'+\gamma$  alloy > Aluminized  $\beta$  > Pt-free  $\beta$  > Ni-rich Pt+Si-modified  $\beta$  > Chromized  $\approx$  Pt+Hf-modified  $\gamma'+\gamma$  coating  $\approx$  Silica+Pt-modified  $\gamma+\gamma'$  > Ni-based superalloy  $\approx$  Ni-rich Pt-modified  $\gamma+\gamma'$ .

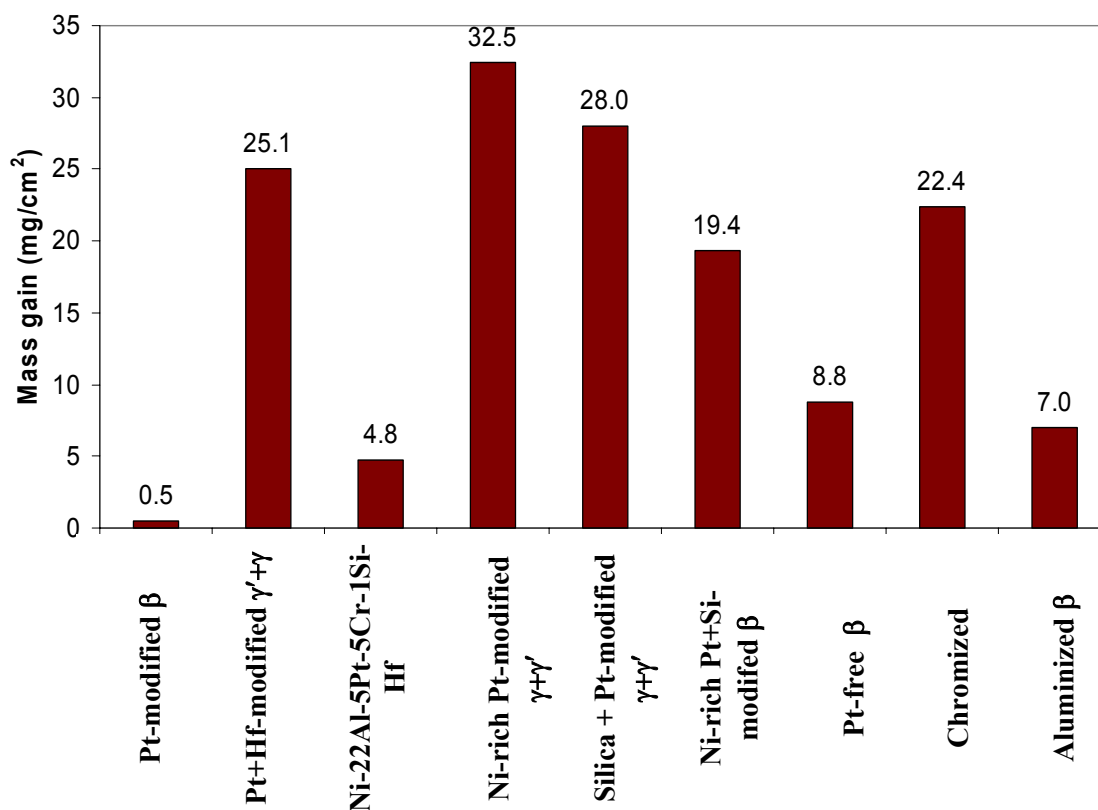


**Figure 128.** Weight gains after 100h LTHC of various coatings and alloys with no pre-oxidation treatment.

The results obtained clearly confirm the beneficial role of Pt addition in improving LTHC resistance in  $\beta$ -NiAl coatings. This was proven by the fact that Pt-modified beta, which is a Pt-modified  $\beta$  coating, exhibited much improved performance (w/ and w/o pre-oxidation) compared to the Pt-free  $\beta$  coating. The improved performance with Pt addition in  $\beta$  was probably due to the formation of more protective TGO scale, even at the lower temperature of LTHC testing (*i.e.*,  $\sim 700^\circ\text{C}$ ). It is noteworthy, however, that pre-oxidation of the Pt-modified  $\beta$  coating was in fact detrimental to its hot corrosion resistance. This is believed to be due to the higher temperature ( $1080^\circ\text{C}$ ) pre-oxidation at contriving to result in the Al depletion (from 38-44 at.% to 33-36 at.%) due to interdiffusion between coating and substrate (Table 8). Indeed, it was observed from the previous section that LTHC hot corrosion resistance of Pt-modified  $\beta$  alloys decreases with decrease in Al content.

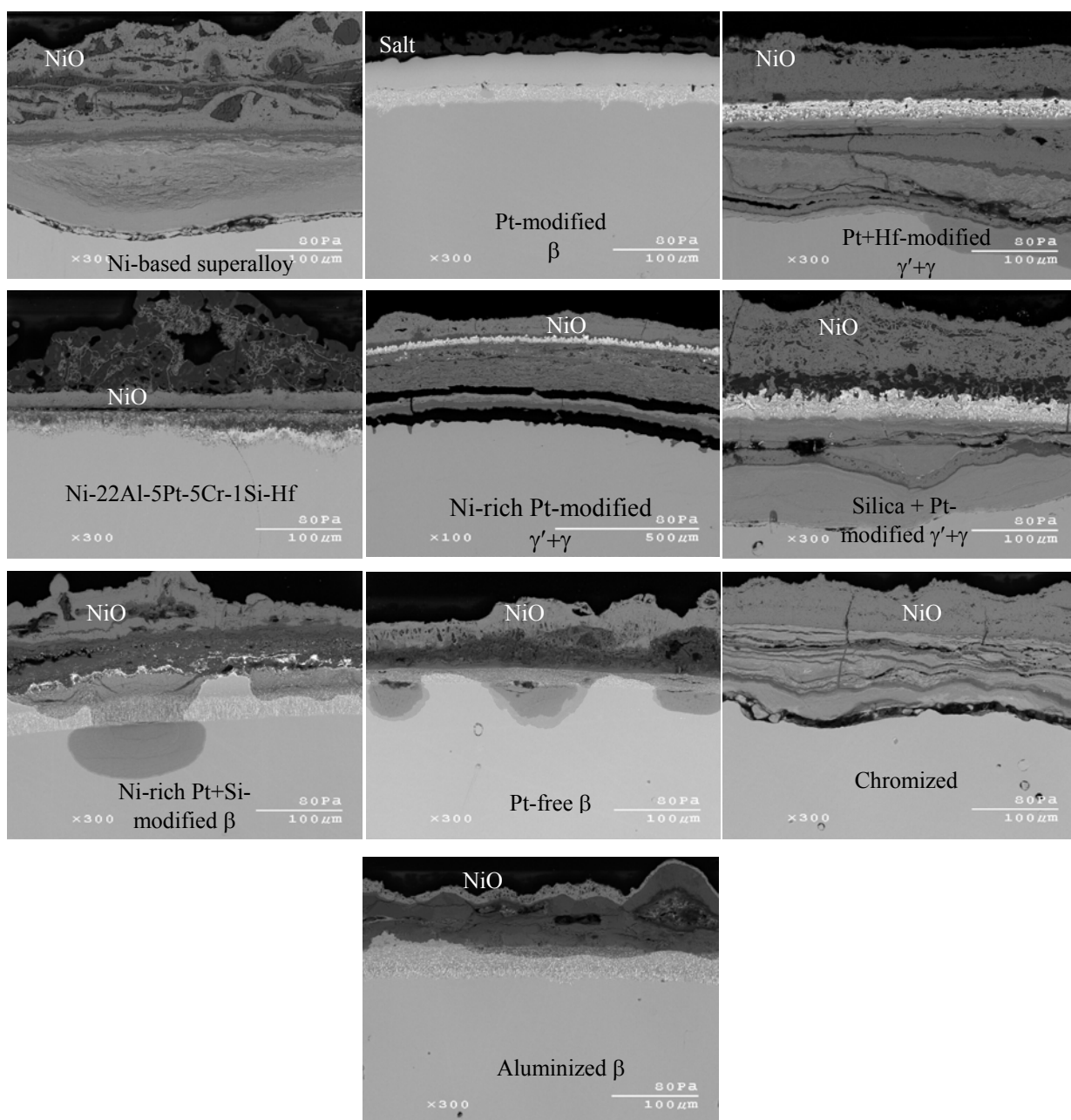


**Figure 129.** Cross-sectional SEM images after 100h LTHC of various coatings and alloys with no pre-oxidation treatment.

It was also observed that the untreated Pt+Hf-modified  $\gamma'+\gamma$  and Ni-rich Pt-modified  $\gamma'+\gamma'$  coatings had inferior LTHC resistance; however, both coatings exhibited improved hot corrosion behavior when given a pre-oxidation treatment. The Pt+Hf-modified  $\gamma'+\gamma$  coating

was particularly improved by a pre-oxidation treatment. The excellent performance of the Pt+Hf-modified  $\gamma'+\gamma$  coating is attributable to the presence of a highly protective  $\alpha$ - $\text{Al}_2\text{O}_3$  scale that forms during a relatively short-term pre-oxidation period (*i.e.*, air-1080°C-6h). The presence of Hf and the higher Al content in the Pt+Hf-modified  $\gamma'+\gamma$  coating resulted in a more protective scale compared to the scale that formed on the Ni-rich Pt-modified  $\gamma+\gamma'$  coating. It is inferred from these results that the low temperature of the LTHC test is insufficient for the  $\gamma'+\gamma$  coatings to kinetically establish a protective and continuous  $\text{Al}_2\text{O}_3$  scale, which is necessary for prolonged HC resistance. In fact, it is inferred that the  $\gamma'+\gamma$  coating requires a high-temperature (*i.e.*, greater than  $\sim 1050^\circ\text{C}$ ) pre-oxidation in order to acquire LTHC (and possibly HTHC) resistance.

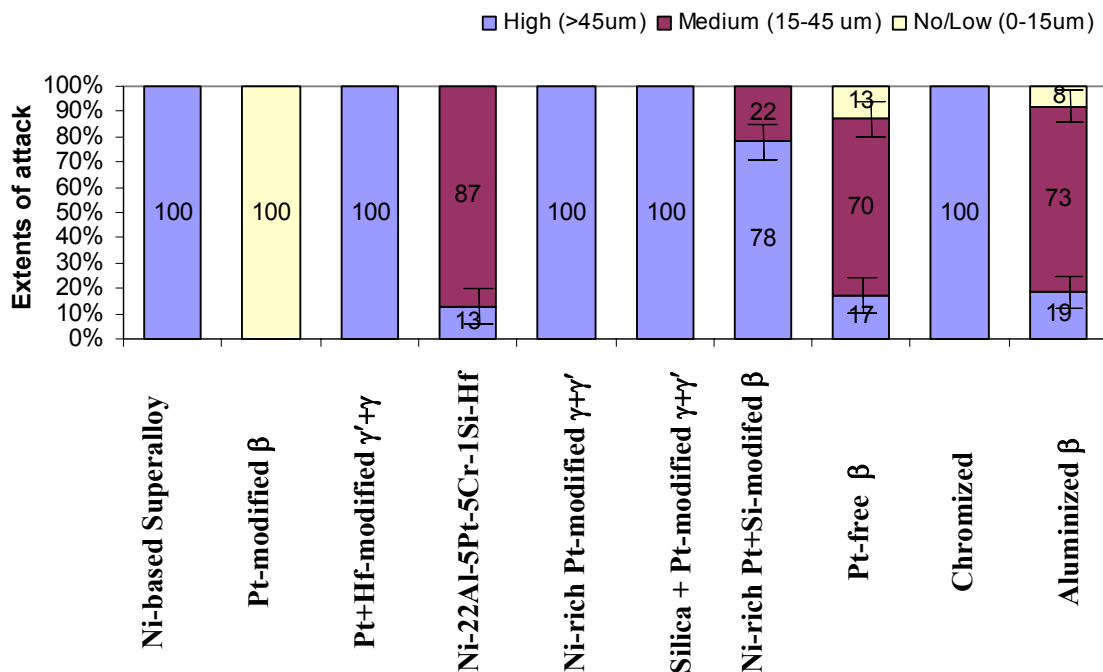


**Figure 130.** Extents of attack after 100h LTHC of various coatings and alloys with a pre-oxidation treatment.

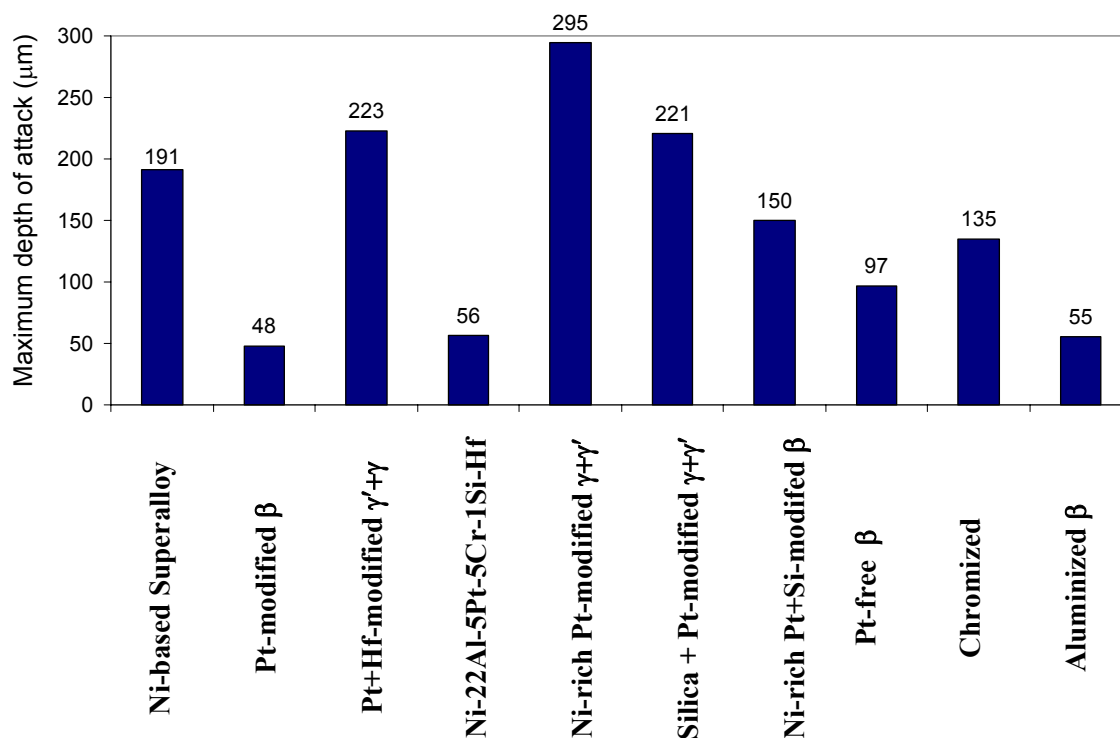


**Figure 131.** Maximum depth of attack after 100h LTHC of various coatings and alloys with no pre-oxidation treatment.

### 6.3.3 HTHC (900 °C) with Pre-oxidation Treatment (Air-1080°C-6h)

The weight change after 100 h of HTHC testing (w/ pre-oxidation) of all coatings and alloys is shown in figure 132. In general, most of the coatings resulted in higher weight gains except for the Silica+Pt-modified  $\gamma+\gamma'$ , Ni-rich Pt+Si-modified  $\beta$ , and Pt+Hf-modified  $\gamma'+\gamma$  coatings, which showed comparatively low weight gains. The  $\gamma'+\gamma$  alloys showed weight loss after each cycle and it was visually observed that a significant percentage of this weight loss was due to salt evaporation and not scale spallation. Figure 133 shows cross-sectional SEM images of coatings/alloys (w/ pre-oxidation) after 100 h of HTHC testing. The Ni-based superalloy and Pt-modified  $\beta$ , Pt-free  $\beta$ , Chromized and Aluminized  $\beta$  coatings were extensively attacked into the substrate. The Ni-rich Pt-modified  $\gamma+\gamma'$  coating exhibited localized regions of attack, as shown in figure 133. The HTHC attack in the Ni-rich Pt+Si-modified  $\beta$  coating was uniform but to a lower extent. EDS analysis of the corroded regions

of the coatings revealed formation of external NiO followed by inner layers or zones of Ni- and Al-rich oxide scale. An internal Al-rich oxide was also seen in the coating and sulfide precipitates were commonly detected beneath the Al-rich oxide. The Pt+Hf-modified  $\gamma'+\gamma$  and Silica+Pt-modified  $\gamma+\gamma'$  coatings and  $\gamma'+\gamma$  alloys showed no regions of aggressive HTHC attack.

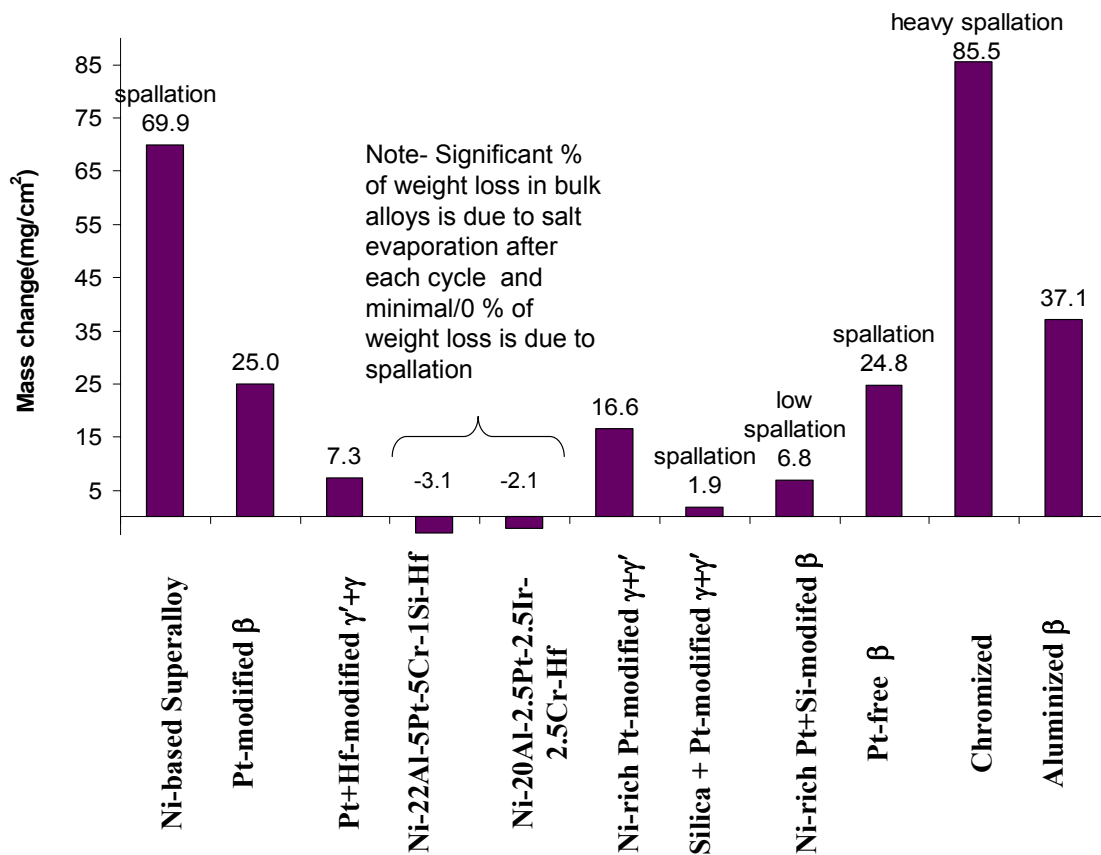


**Figure 132.** Weight gains after 100h HTHC of various coatings and alloys with a pre-oxidation treatment (air-1080°C-6h).

Semi-quantitative analysis of the extents of HTHC attack is summarized in the form of histograms in figure 134. There was more than 50% high corrosion in the Ni-based superalloy and the Pt-modified  $\beta$ , Pt-free  $\beta$ , Chromized and Aluminized  $\beta$  coatings. The coatings that exhibited a greater proportion of low corrosion were Pt+Hf-modified  $\gamma'+\gamma$  and Silica+Pt-modified  $\gamma+\gamma'$ , together with the  $\gamma'+\gamma$  alloys. The maximum depth of penetration

was lowest for the Pt+Hf-modified  $\gamma'+\gamma$  coating and Ni-22Al-5Pt-5Cr-1Si-Hf  $\gamma'+\gamma$  alloy, while Ni-rich Pt+Si-modified  $\gamma+\gamma'$  also showed a comparatively low depth of maximum penetration (figure 135). The Silica+Pt-modified  $\gamma+\gamma'$  coating showed a relatively high maximum depth of penetration due to localized attack; however, those regions of the coating away from the localized attack exhibited excellent HTHC resistance.

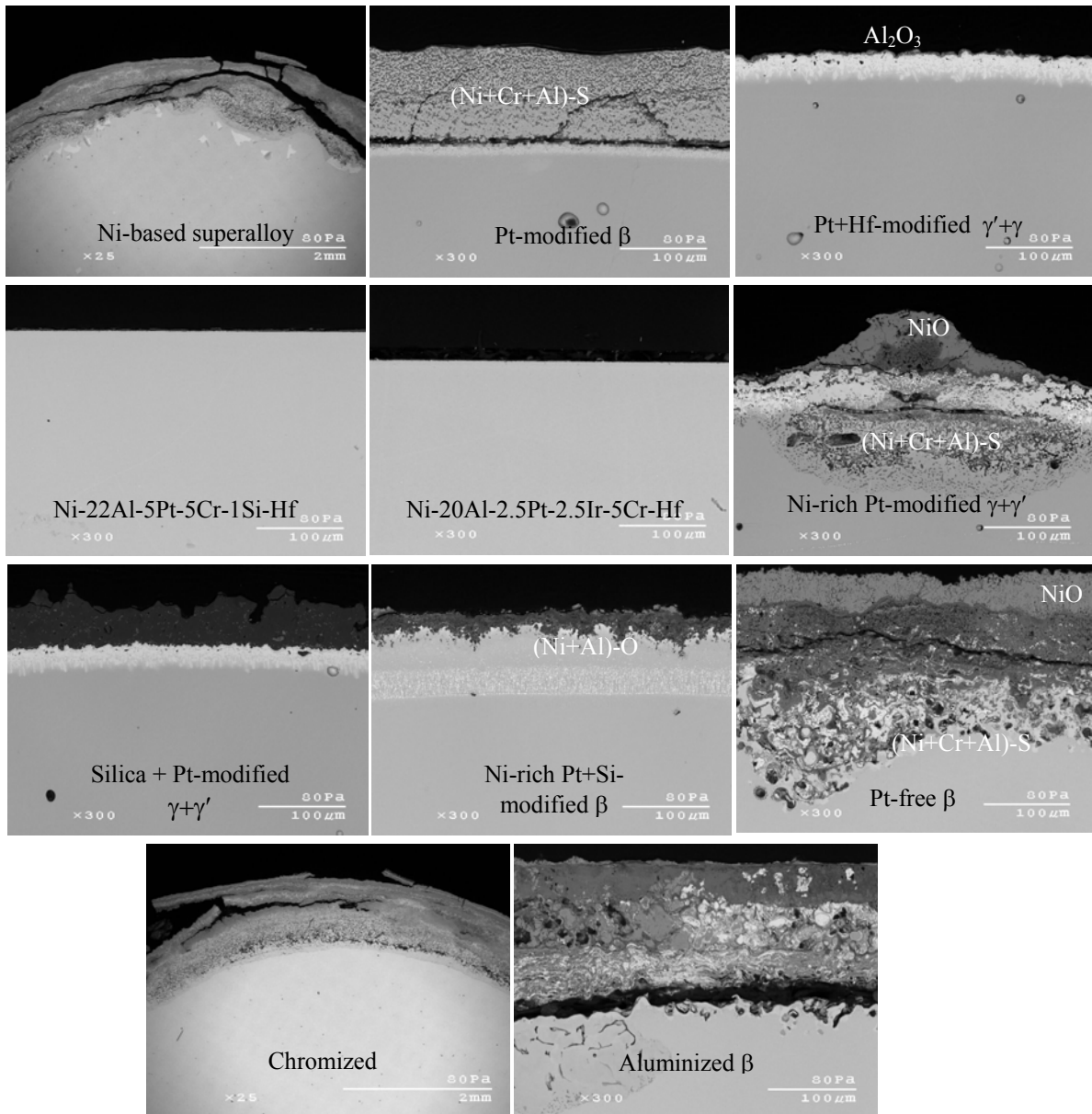


**Figure 133.** Cross-sectional SEM images after 100h HTHC of various coatings and alloys with a pre-oxidation treatment (air-1080°C-6h).

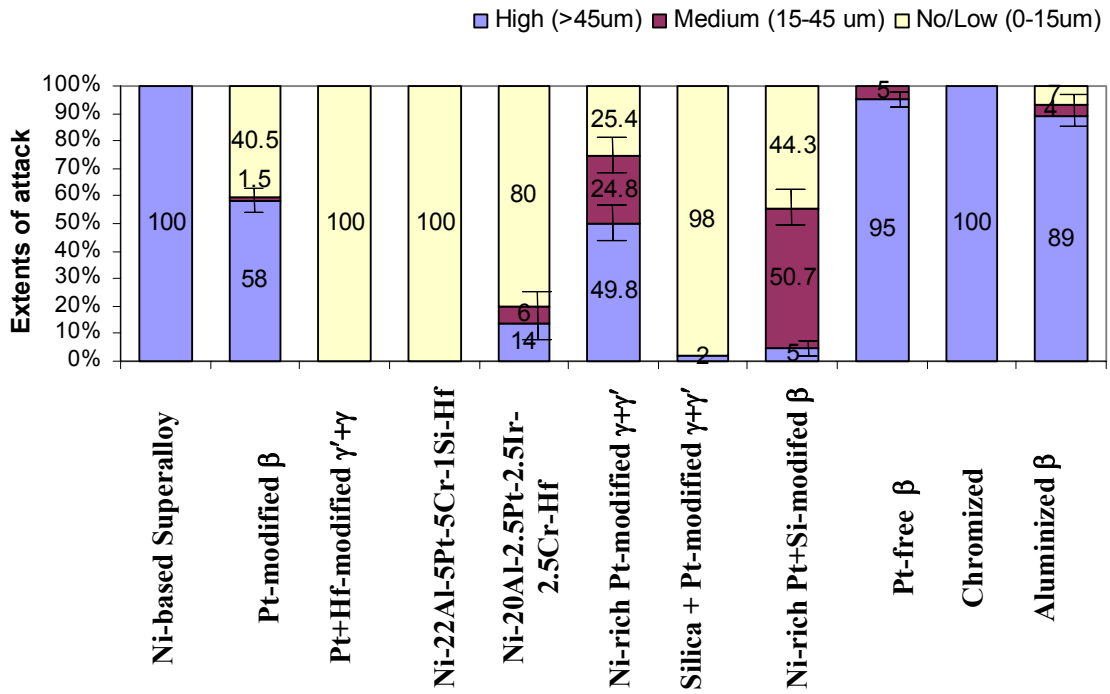


**Figure 134.** Extents of attack after 100h HTHC of various coatings and alloys with a pre-oxidation treatment (air-1080°C-6h).

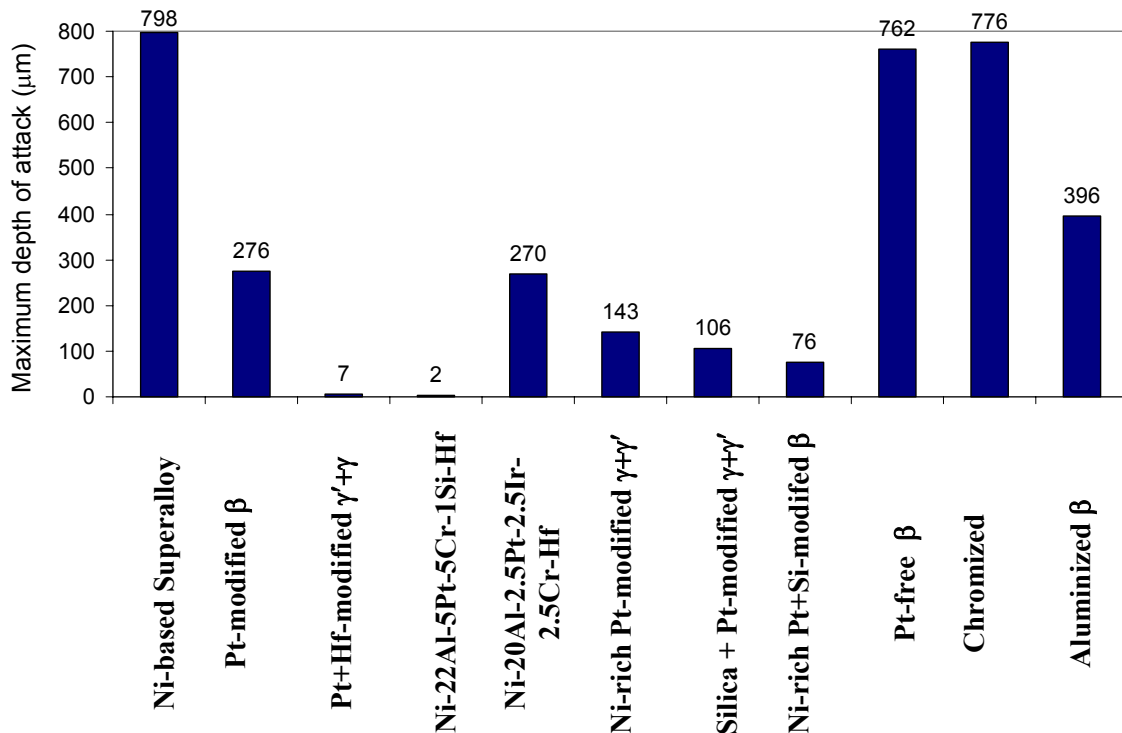


**Figure 135.** Maximum depth of attack after 100h HTHC of various coatings and alloys with a pre-oxidation treatment (air-1080°C-6h).

The six coatings/alloys that were selected for further LTHC testing were also selected for 200 h HTHC testing (w/ pre-oxidation). The resulting weight change behavior and cross-sectional SEM images after this extended HTHC testing are shown in figures 136 and 137. The Pt+Hf-modified  $\gamma'+\gamma$  and Silica+Pt-modified  $\gamma+\gamma'$  coatings, together with the  $\gamma'+\gamma$  alloys, showed improved HTHC performance; however, these coatings/alloys also showed localized regions of attack, as seen from the SEM images in figure 137. The extents of attack and maximum depth of attack measurements also confirmed that these coatings/alloys exhibited excellent HTHC compared to other coatings/alloys (figures 138 and 139). The other coatings were completely attacked after the 200 h of HTHC exposure.

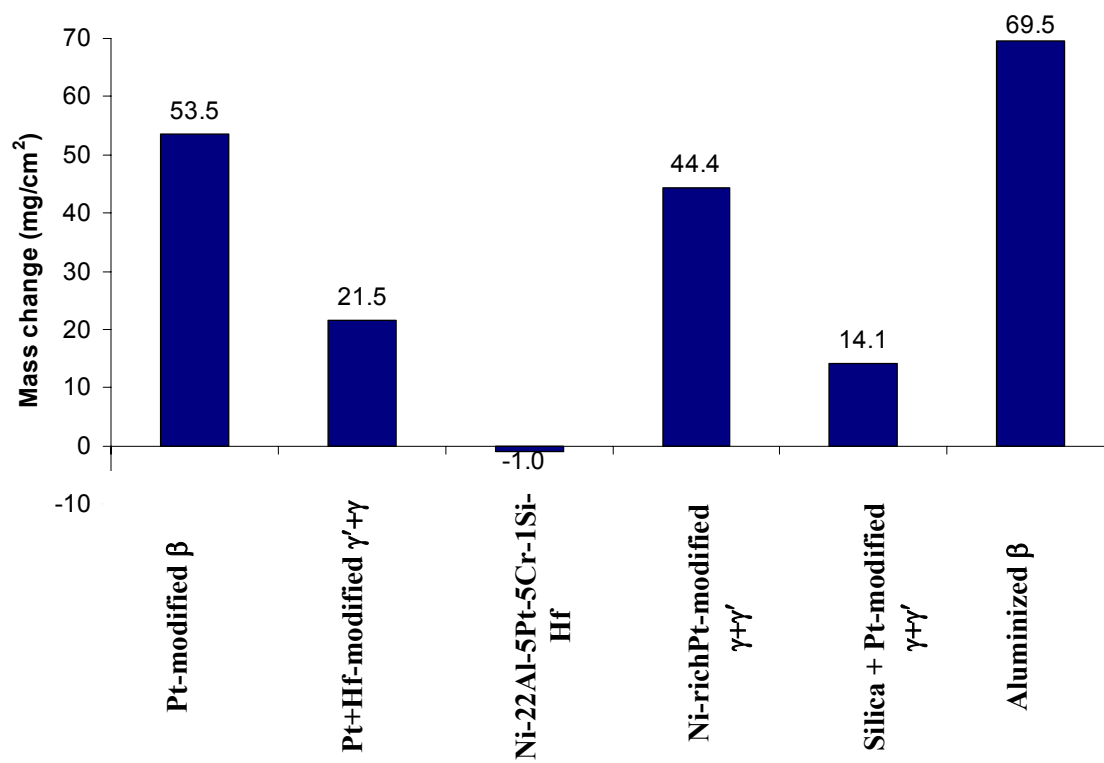


**Figure 136.** Weight gains after 200h LTHC of six selected coatings/alloy with a pre-oxidation treatment (air-1080°C-6h).

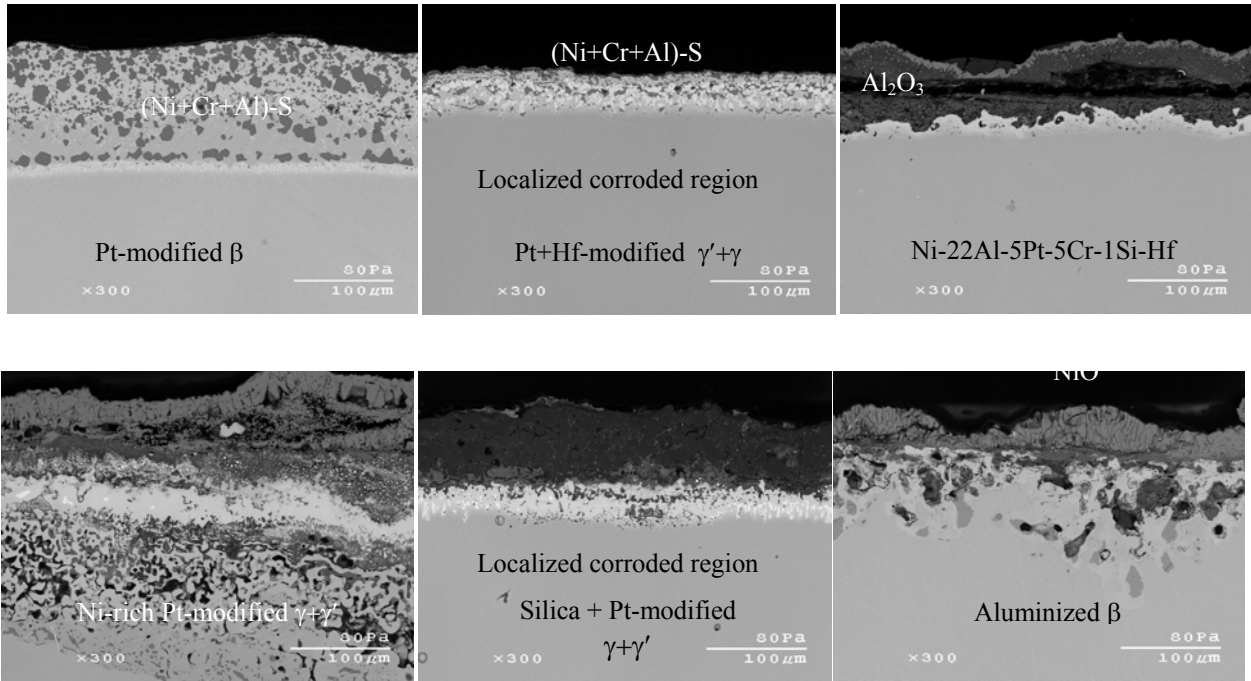


**Figure 137.** Cross-sectional SEM images after 200h HTHC of six selected coatings/alloy with a pre-oxidation treatment (air-1080°C-6h).

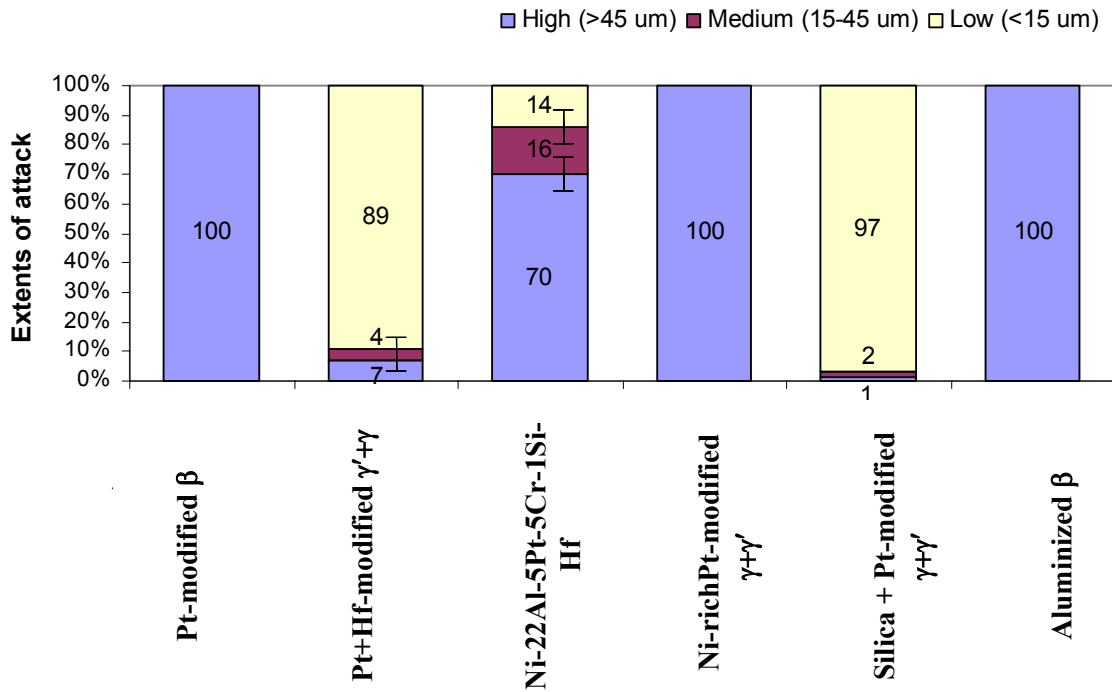


**Figure 138.** Extents of attack after 200h HTHC of six selected coatings/alloy with a pre-oxidation treatment (air-1080°C-6h).

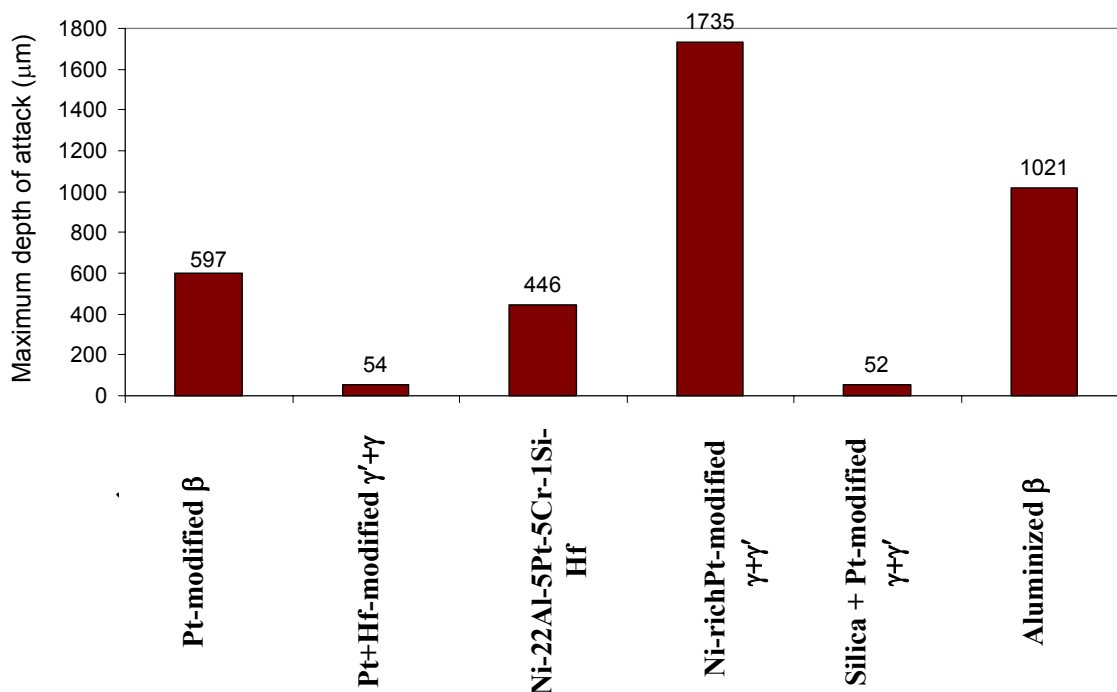


**Figure 139.** Maximum depth of attack after 200h HTHC of six selected coatings/alloy with a pre-oxidation treatment (air-1080°C-6h).

The overall ranking after 100 and 200 h of HTHC testing (w/ pre-oxidation) was in the following order from best to worst: Silica+Pt-modified  $\gamma+\gamma'$  > Pt+Hf-modified  $\gamma'+\gamma$  coating  $\approx$  Ni-22Al-5Pt-5Cr-1Si-Hf  $\gamma'+\gamma$  alloy > Ni-20Al-2.5Pt-2.5Ir-5Cr-Hf  $\gamma'+\gamma$  alloy > Ni-rich Pt+Si-modified  $\beta$  > Ni-rich Pt-modified  $\gamma+\gamma'$   $\approx$  Pt-modified  $\beta$  > Pt-free  $\beta$   $\approx$  Aluminized  $\beta$  > Ni-based superalloy  $\approx$  Chromized.

#### 6.3.4 HTHC (900 °C) with No Pre-oxidation Treatment

The HTHC testing was carried out for a total of 100 h on selected untreated coatings/alloys and their weight change after the testing is shown in figure 140. In general, the absence of a pre-oxidation treatment resulted in higher weight gains for all coatings except for the Silica+Pt-modified  $\gamma+\gamma'$ . The Ni-rich Pt-modified  $\gamma+\gamma'$  coating exhibited extremely poor HTHC resistance and the coating completely spalled just after 80 h of exposure. SEM images of the corroded regions of the coatings are shown in figure 141.

Semi-quantitative analyses of the extents of attack (figure 142) and maximum depth of penetration (figure 143) also confirmed that only the Silica+Pt-modified  $\gamma+\gamma'$  coating exhibited excellent HTHC resistance for the test duration studied. The Ni-rich Pt+Si-modified  $\beta$  also showed comparatively good performance, with varying levels of high, medium and low corrosion. The untreated Pt+Hf-modified  $\gamma'+\gamma$  and Pt-modified  $\beta$  coatings exhibited rather poor HTHC resistance. The order of performance of the various coatings/alloys (w/ no pre-oxidation) under HTHC conditions from best to worst are as follows: Silica+Pt-modified  $\gamma+\gamma'$  > Ni-rich Pt+Si-modified  $\beta$  > Ni-22Al-5Pt-5Cr-1Si-Hf  $\gamma'+\gamma$  alloy > Aluminized  $\beta$  > Pt-modified  $\beta$   $\approx$  Pt+Hf-modified  $\gamma'+\gamma$  coating > Pt-free  $\beta$  > Chromized > Ni-rich Pt-modified  $\gamma+\gamma'$   $\approx$  Ni-based superalloy.

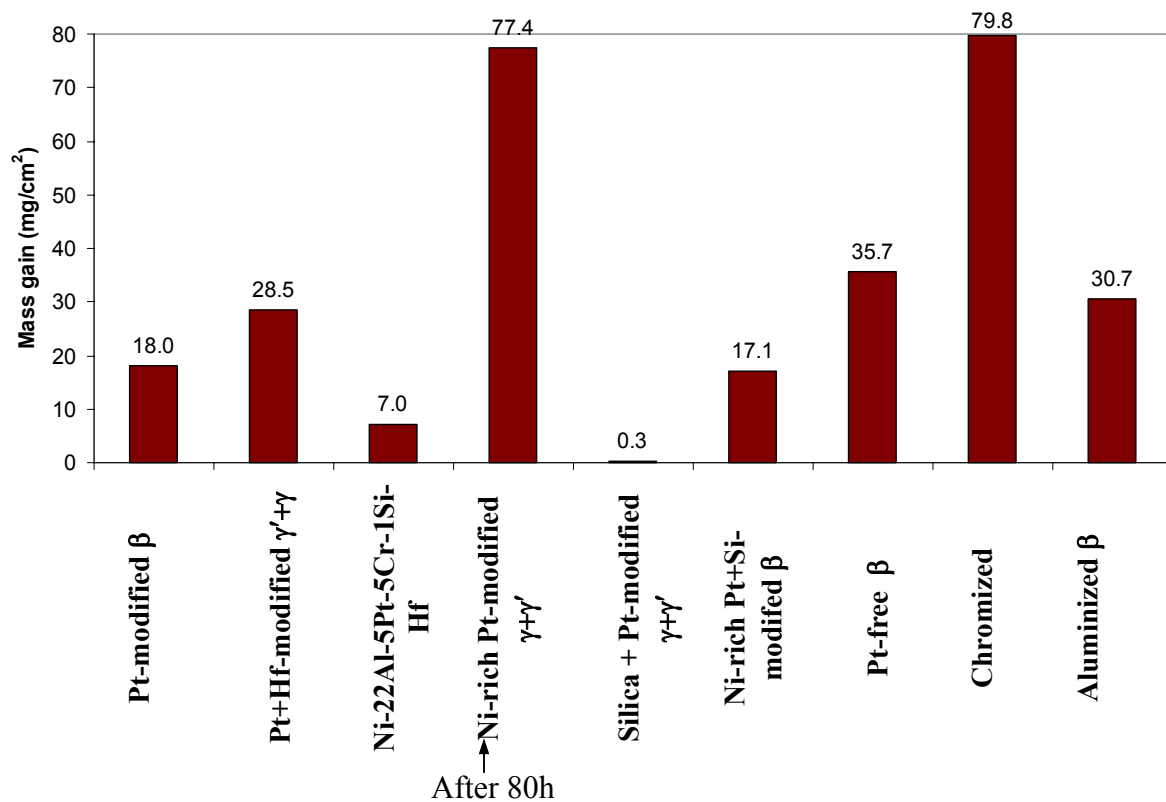


**Figure 140.** Weight gains after 100h HTHC of various coatings and alloys with no pre-oxidation treatment.

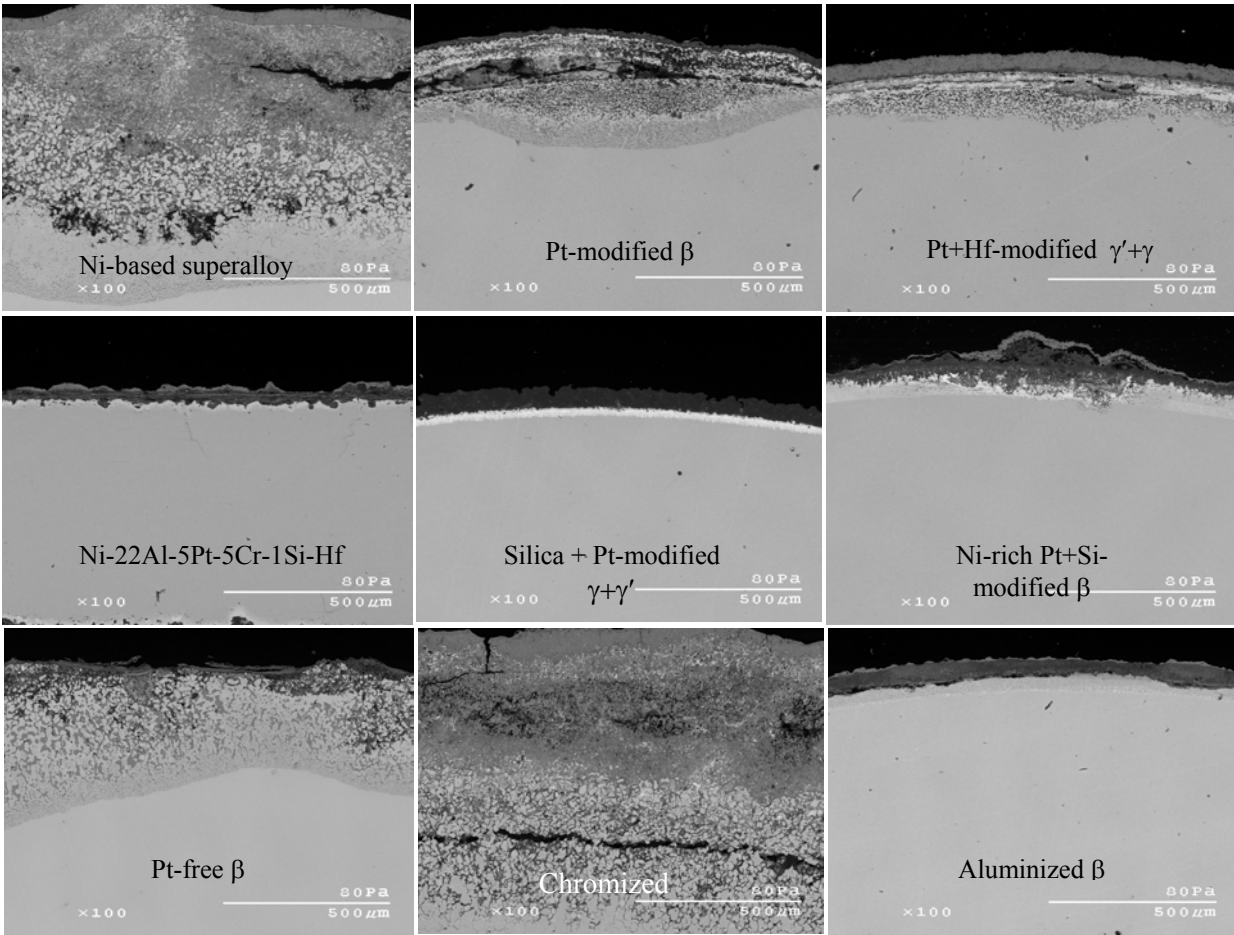


**Figure 141.** Cross-sectional SEM images after 100h HTHC of various coatings and alloys with no pre-oxidation treatment.

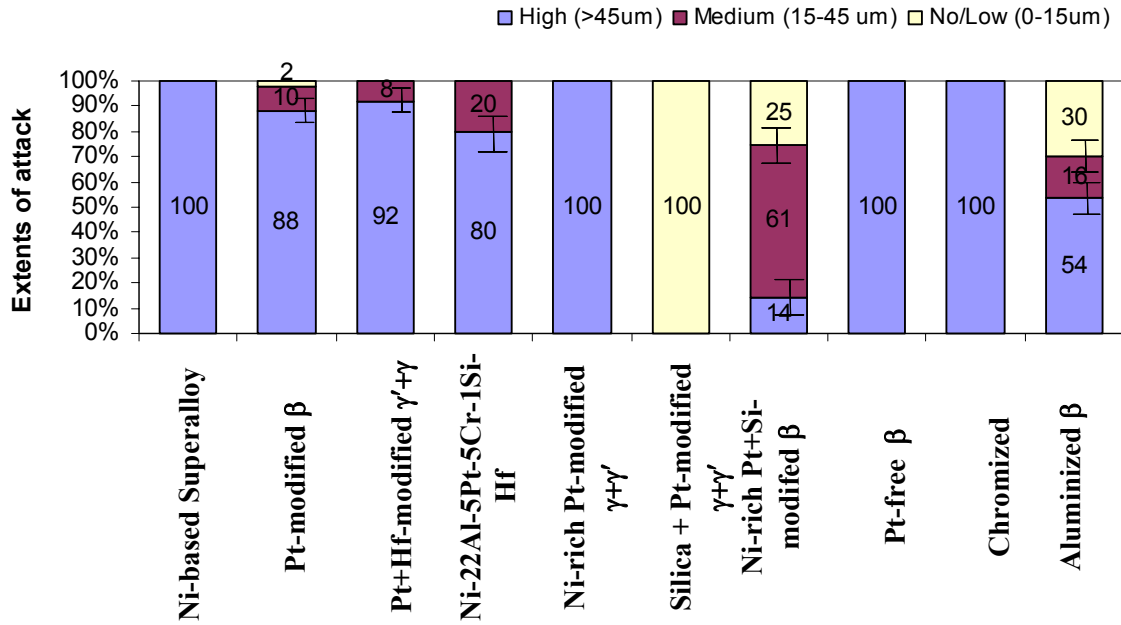


**Figure 142.** Extents of attack after 100h HTHC of various coatings and alloys with a pre-oxidation treatment.

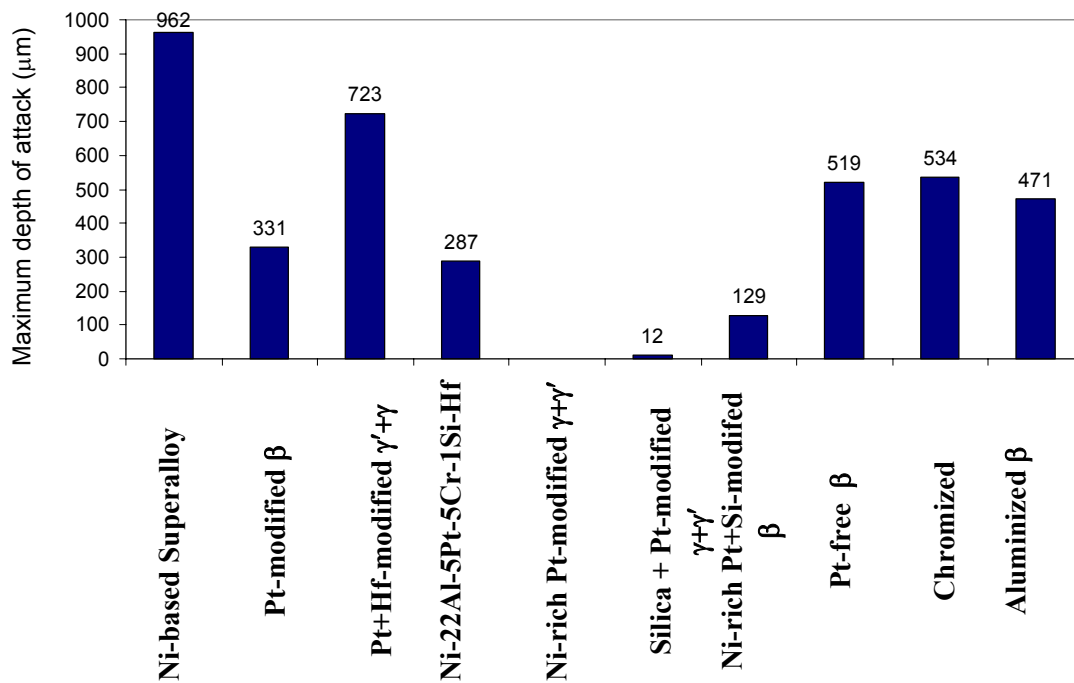


**Figure 143.** Maximum depth of penetration after 100h HTHC of various coatings and alloys with a pre-oxidation treatment.

### 6.3.5 Hot Corrosion Resistance: Pt+Hf-Modified $\gamma'+\gamma$ vs. $\gamma+\beta$ -CoCrAlY

It was found that the Pt+Hf-modified  $\gamma'+\gamma$  exhibited excellent HTHC and LTHC resistance with pre-oxidation treatment; hence its hot corrosion resistance was compared with the MCrAlY-type coating having excellent hot corrosion resistance. The overlay CoCrAlY and diffusion aluminide coatings were applied on Ni-based superalloy substrates that will be designated A and B. The nominal compositions of these alloys (in at %) are as follows:

Superalloy A: 59.6Ni-14.6Cr-8.9Co-6.9Al-5.1Ti-1.3W-1.3Nb-1.2Mo-1C-0.1B-0.06Zr

Superalloy B: 63.5Ni-13.9Al-8.2Co-8.1Cr-2.3Ta-1.6W-1.3Mo-1Re-0.07Hf

The average chemical composition (in at %) of each coating was measured via energy dispersive spectroscopy (EDS), and the results for selected constituents are summarized below:

- $\gamma+\beta$ -CoCrAlY (65-75  $\mu\text{m}$ ) on superalloy A: Co-26Cr-18Al-7Ni-0.7Y-others;
- Pt+Hf-modified  $\gamma'$ -Ni<sub>3</sub>Al +  $\gamma$ -Ni (20-25  $\mu\text{m}$ ) on superalloy B: Ni-20Al-22Pt-7Co-7Cr-0.7Hf-others.

The  $\gamma+\beta$ -CoCrAlY coating was deposited via physical vapor deposition (PVD) to an actual vane airfoil made of superalloy A. The Pt+Hf-modified  $\gamma'$ -Ni<sub>3</sub>Al +  $\gamma$ -Ni coating, with  $\gamma'$ -Ni<sub>3</sub>Al being primary phase, was deposited on superalloy B by Pt electroplating followed by a proprietary Al+Hf co-deposition pack cementation CVD process.

The hot corrosion experiments were carried out for 100 hours exposure on coated samples that were given a pre-oxidation treatment. The pre-oxidization treatment involved exposing the samples for 24 h at 1100°C in 3% H<sub>2</sub>+Ar atmosphere to pre-form an Al<sub>2</sub>O<sub>3</sub>-rich scale. SEM micrographs of pre-oxidized  $\gamma+\beta$ -CoCrAlY and Pt+Hf modified  $\gamma'+\gamma$  coatings, after 200 hours Type I hot corrosion, are shown in figure 2. It was found that the CoCrAlY and Pt+Hf modified  $\gamma'+\gamma$  coatings were only marginally attacked; although, some attack involving nickel sulfide formation (as determined by EDS) was initiated at the edges of this latter coating. The Pt+Hf modified  $\gamma'+\gamma$  coating in particular showed very little Type I hot corrosion attack. The excellent performance of the Pt+Hf modified  $\gamma'+\gamma$  coating is attributable to the presence of a protective  $\alpha$ -Al<sub>2</sub>O<sub>3</sub> scale after the pre-oxidation treatment.

Cross-sectional micrographs of the  $\gamma + \beta$ -CoCrAlY (mid-chord section), and Pt+Hf modified  $\gamma' + \gamma$  coatings after 100 hours of LTHC are shown in figure 144 (a-c). From these micrographs it is evident that the CoCrAlY coating was attacked while the Pt+Hf modified  $\gamma' + \gamma$  coatings showed excellent LTHC resistance. The poor performance of CoCrAlY coatings in LTHC conditions is attributed to the formation of  $\text{Na}_2\text{SO}_4$ - $\text{CoSO}_4$  eutectic ( $T_{\text{melt}} = 565^\circ\text{C}$ ) [49, 50]. Co-based alloys and coatings are more susceptible to Type II hot corrosion attack than the Ni-based alloys and coatings because  $\text{CoSO}_4$  is more stable than  $\text{NiSO}_4$ . As a consequence,  $\text{CoSO}_4$  can form at a lower  $\text{P}_{\text{SO}_3}$  than  $\text{NiSO}_4$ . Visual observations of these coatings confirmed that the salt was indeed in liquid state on the CoCrAlY coating just after 60h of testing, while it was in solid state on the Pt+Hf modified  $\gamma' + \gamma$  coatings even after 100h of testing. A further contributing factor to the liquid formation on to CoCrAlY coating may be the fact that this coating formed less protective TGO scale than those formed on the Pt-modified  $\beta$  and Pt+Hf modified  $\gamma' + \gamma$  coatings.

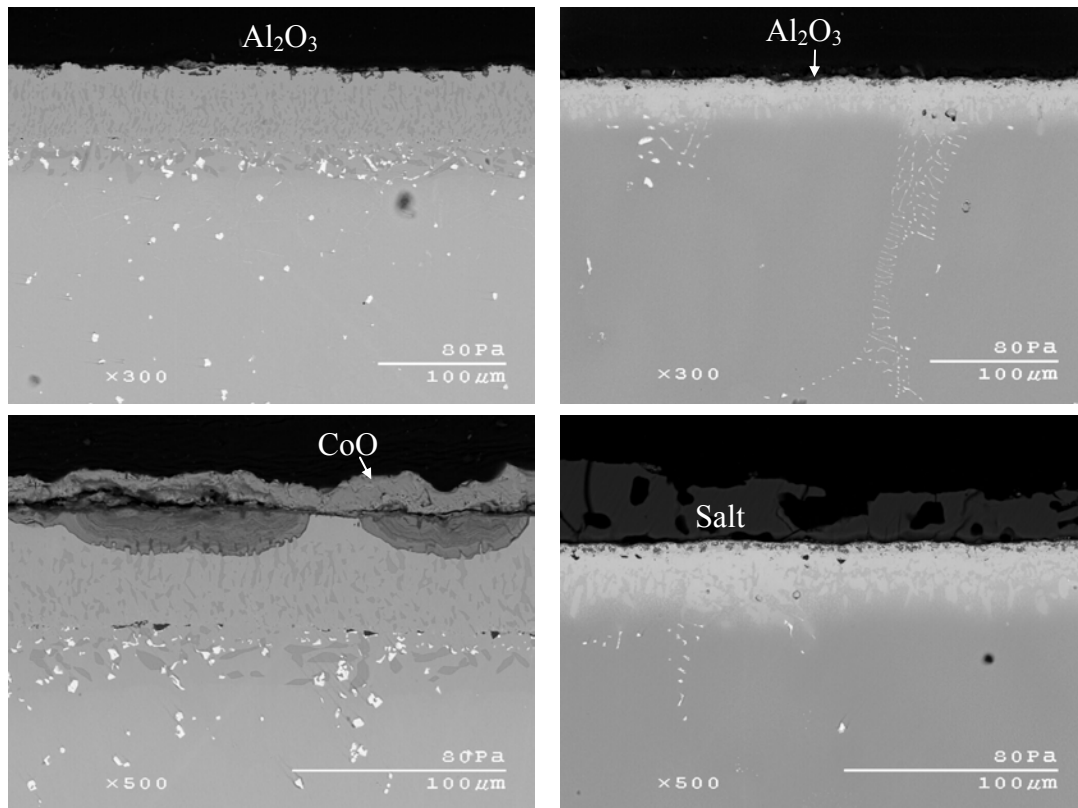


**Figure 144.** Cross-sectional SEM micrographs of (a)  $\gamma + \beta$ -CoCrAlY (b) Pt+Hf-modified  $\gamma' + \gamma$  coatings after 200h of HTHC testing at  $900^\circ\text{C}$  and 100h of LTHC testing at  $705^\circ\text{C}$ .

## 6.4 Summary and Conclusions

1. The order of performance under LTHC conditions of various coatings/alloys (w/ pre-oxidation) from best to worst is as follows: Pt+Hf-modified  $\gamma'+\gamma$  coating  $\approx \gamma'+\gamma$  alloys (Ni-22Al-5Pt-5Cr-1Si-Hf and Ni-20Al-2.5Pt-2.5Ir-5Cr-Hf)  $>$  Pt-modified  $\beta$   $>$  Silica+Pt-modified  $\gamma+\gamma'$   $>$  Aluminized  $\beta$   $>$  Ni-rich Pt+Si-modified  $\beta$   $>$  Pt-free  $\beta$   $>$  Ni-rich Pt-modified  $\gamma+\gamma'$   $>$  Chromized  $>$  Ni-based superalloy.
2. The overall ranking of the untreated (*i.e.* w/ no pre-oxidation) coatings and alloys from best to worst after 100h of LTHC testing is as follows: Pt-modified  $\beta$   $>$  Ni-22Al-5Pt-5Cr-1Si-Hf  $\gamma'+\gamma$  alloy  $>$  Aluminized  $\beta$   $>$  Pt-free  $\beta$   $>$  Ni-rich Pt+Si-modified  $\beta$   $>$  Chromized  $\approx$  Pt+Hf-modified  $\gamma'+\gamma$  coating/Silica+Pt-modified  $\gamma+\gamma'$   $>$  Ni-based superalloy  $\approx$  Ni-rich Pt-modified  $\gamma+\gamma'$ .
3. The overall ranking after 100 and 200h of HTHC testing (w/ pre-oxidation) was in the following order from best to worst: Silica+Pt-modified  $\gamma+\gamma'$   $>$  Pt+Hf-modified  $\gamma'+\gamma$  coating/Ni-22Al-5Pt-5Cr-1Si-Hf  $\gamma'+\gamma$  alloy  $>$  Ni-20Al-2.5Pt-2.5Ir-5Cr-Hf  $\gamma'+\gamma$  alloy  $>$  Ni-rich Pt+Si-modified  $\beta$   $>$  Ni-rich Pt-modified  $\gamma+\gamma'$   $\approx$  Pt-modified  $\beta$   $>$  Pt-free  $\beta$   $\approx$  Aluminized  $\beta$   $>$  Ni-based superalloy  $\approx$  Chromized.
4. The order of performance of various untreated (*i.e.* w/ no pre-oxidation) coatings/alloys under HTHC conditions from best to worst are as follows: Silica+Pt-modified  $\gamma+\gamma'$   $>$  Ni-rich Pt+Si-modified  $\beta$   $>$  Ni-22Al-5Pt-5Cr-1Si-Hf  $\gamma'+\gamma$  alloy  $>$  Aluminized  $\beta$   $>$  Pt-modified  $\beta$   $\approx$  Pt+Hf-modified  $\gamma'+\gamma$  coating  $>$  Pt-free  $\beta$   $>$  Chromized  $>$  Ni-rich Pt-modified  $\gamma+\gamma'$   $\approx$  Ni-based superalloy.
5. The Pt+Hf-modified  $\gamma'+\gamma$  coating exhibited excellent resistance to both types of hot corrosion when given a 6 h pre-oxidation treatment in air at 1080°C; while, the Pt-modified  $\beta$  coating exhibited best LTHC hot corrosion resistance when no pre-oxidation treatment was given.
6. The LTHC attack in Ni-based aluminide coatings and alloys is believed to be due to the formation of eutectic  $\text{Na}_2\text{SO}_4\text{-NiSO}_4$  ( $T_{\text{melt}} = 671^\circ\text{C}$ ) liquid. The presence of Co

and other refractory elements may have further exacerbated the performance of coatings.

7. The improved performance under HTHC and LTHC conditions of Pt+Hf-modified  $\gamma'+\gamma$  coating and  $\gamma'+\gamma$  alloy (w/ pre-oxidation) is believed to be attributable to the presence of a protective  $\alpha$ - $\text{Al}_2\text{O}_3$  scale which was pre-formed at  $1080^\circ\text{C}$ . The low temperatures of the LTHC and HTHC testing – LTHC in particular – are apparently insufficient for the  $\gamma'+\gamma$  coatings to kinetically establish a protective and continuous  $\text{Al}_2\text{O}_3$  scale, which is necessary for prolonged HC resistance.
8. Addition of Pt is beneficial in improving hot corrosion resistance of  $\beta$  coatings. A pre-oxidation of Pt-modified  $\beta$  coating was not beneficial in improving LTHC hot corrosion resistance, it is believed due to Al depletion in the coating during the pre-oxidation treatment.
9. A Pt+Hf modified  $\gamma'$ - $\text{Ni}_3\text{Al}$  +  $\gamma$ -Ni coating outperformed commercially used  $\gamma+\beta$ -CoCrAlY coatings from the standpoint of combined resistance both types of hot corrosion.

## 7. SUMMARY AND OUTCOMES

### 7.1 Hot Corrosion Behavior of Commercial Ni- and Co-Based Metallic Coatings

- Under HTHC and LTHC testing conditions Al-Pt-rich  $\beta$  aluminide was the best amongst the commercial coatings tested for the marine gas turbine engine components. This is attributable to the presence of higher Al and Pt content in this coating promoting the formation of a more protective alumina scale. It was inferred that this protection is a result of the alumina scale being homogeneous and having little to no transient oxides rich in Ni and/or Co.
- The diffusion aluminide coatings exhibited better HTHC resistance when applied on the superalloy 792 substrate than on the superalloy 247. The improved performance in the superalloy 792 substrate is due to the presence of higher Cr content and lower amount of refractory elements, which, in turn, affect the “quality” (*i.e.*, homogeneity, adherence and continuity) of the alumina scale.
- The reliability of Dean rig testing was confirmed by comparing the HTHC results with burner rig testing; however, Dean rig testing is more aggressive than burner rig testing.
- The presence of porosity and reduction in Pt content considerably decreased the longer-term hot corrosion resistance (LTHC and HTHC) of the Al-Pt-rich aluminide coating.
- LTHC attack of the CoCrAlY coatings is attributed to the formation of eutectic  $\text{Na}_2\text{SO}_4\text{-CoSO}_4$  ( $T_{\text{melt}} = 565^\circ\text{C}$ ) liquid; while the LTHC attack in diffusion Pt-modified  $\beta$  coatings was possibly due to the eutectic  $\text{Na}_2\text{SO}_4\text{-NiSO}_4$  ( $T_{\text{melt}} = 671^\circ\text{C}$ ).
- A highly mixed ( $\text{CoO} + \text{Al}_2\text{O}_3 + \text{Cr}_2\text{O}_3$ ) TGO scale formed on Pt-modified CoAl, while primarily CoO formed on CoCrAlY during exposure to the LTHC conditions. The tendency for the latter to form a simpler scale is believed to contribute to its better corrosion resistance. Pt-modified CoAl was more brittle than the CoCrAlY coating, which may have further contributed to the inferior performance of the former.

### 7.2 Hot Corrosion and Oxidation Behavior of Novel $\gamma'+\gamma$ Alloys

- The establishment of an adherent, intact and homogeneous  $\alpha\text{-Al}_2\text{O}_3$  scale is critical in providing high temperature protection from hot corrosion and oxidation. The novel

Pt+Hf-modified  $\gamma'+\gamma$  alloys have excellent oxidation resistance; however, addition of only “low Pt” (up to 10%) to  $\gamma'+\gamma$  alloys improved HTHC resistance and addition of Pt >10% exhibited rather poor HTHC resistance. This is because Pt decreases  $a_{Al}$  and increases  $a_{Ni}$  to the extent that  $Ni_3S_2$ , which is liquid above about 787°C, forms in preference to  $Al_2S_3$  with increasing Pt content.

- The formation of a protective  $\alpha-Al_2O_3$  scale on “low Pt” Ni-22Al-(5-10)Pt-0.4Hf  $\gamma'+\gamma$  alloys is achieved by Cr addition up to 10%. Pre-oxidation treatment applied to the Pt+Cr+Hf-modified  $\gamma'+\gamma$  alloys resulted in the formation of continuous and adherent  $\alpha-Al_2O_3$  scale. In the case of “low Pt” (up to 10%)  $\gamma'+\gamma$  alloys, the present results suggest that addition of Cr should be either equal to or greater than Pt content for optimum HTHC and oxidation resistance. The Pt+Cr+Hf-modified  $\gamma'+\gamma$  alloy (Ni-22Al-5Pt-5Cr-Hf) also exhibited excellent cyclic oxidation resistance.
- Pre-oxidation of Pt+Cr+(Si)+Hf-modified  $\gamma'+\gamma$  alloys (*i.e.* Ni-22Al-5Pt-5Cr-Hf, Ni-22Al-5Pt-5Cr-2.5Si-Hf, Ni-22Al-5Pt-10Cr-Hf, and Ni-22Al-10Pt-10Cr-Hf) and Pt+Si+Hf-modified  $\gamma'+\gamma$  alloy (Ni-22Al-10Pt-5Si) also resulted in the formation of a continuous and adherent  $Al_2O_3$  scale, which prevented these alloys from HTHC attack. These modified versions of  $\gamma'+\gamma$  alloys also possessed improved HTHC and oxidation resistance than the Ni-50Al-15Pt  $\beta$  and  $\gamma+\beta$ -NiCrAl alloy. The Pt+Si+Hf-modified  $\gamma'+\gamma$  alloy (*i.e.* Ni-22Al-10/20Pt-5Si-Hf) showed lowest weight gain amongst the alloys tested under cyclic conditions.
- Higher Cr-content (20%) alloys with varying Pt content (5-20%), *e.g.*, Ni-22Al-5Pt-20Cr-Hf, Ni-22Al-10Pt-20Cr-Hf, Ni-22Al-20Pt-20Cr-Hf gave the best performance of the alloys not given a pre-oxidation treatment. These particular alloys showed excellent HTHC resistance, better than Pt-modified  $\beta$  and MCrAl alloys, but their oxidation resistance is rather poor.
- Statistical analyses of the oxidation and Type I hot corrosion results from the various Ni-22Al-based alloys studied gave an optimized coating composition of (in at%) Ni-22Al-5Pt-5Cr-(0-2.5)Si-0.5Hf.

- Addition of Pt (up to 30%) improved LTHC resistance of  $\gamma'+\gamma$  alloys; however, it could not completely prevent LTHC after 100 h exposure. The LTHC in the  $\gamma'+\gamma$  alloys is due to the formation of  $\text{NiSO}_4+\text{Na}_2\text{SO}_4$  liquid at  $705^\circ\text{C}$ .
- Chromium addition to Pt+Hf-modified  $\gamma'+\gamma$  alloys considerably improved LTHC resistance of  $\gamma'+\gamma$  alloys with a pre-oxidation treatment. The Ni-22Al-5Pt-5Cr-Hf  $\gamma'+\gamma$  alloy with an optimum HTHC and oxidation resistance also exhibited excellent LTHC resistance with a pre-oxidation treatment.
- Addition of Si to high Pt-containing  $\gamma'+\gamma$  alloys resulted in excellent LTHC resistance even without pre-oxidation treatment. This is attributable to the relatively rapid establishment of a protective alumina-rich scale during early stages of oxidation/corrosion.
- Most of the untreated  $\gamma'+\gamma$  alloys exhibited rather poor LTHC when compared with the Pt-modified  $\beta$  alloys. Addition of Pt is quite beneficial in improving LTHC resistance  $\beta$  alloys; while, a decrease in Al content and additions of Co and other refractory elements in  $\beta$  alloys significantly decreased LTHC performance due to increased stabilization of eutectic  $\text{Na}_2\text{SO}_4\text{-CoSO}_4$  ( $T_{\text{melt}} = 565^\circ\text{C}$ ) liquid.
- Pre-oxidation of the Ni-22Al-20Pt-5Cr-Hf and Ni-22Al-5Pt-5Cr-Hf  $\gamma'+\gamma$  alloys in air at high temperature ( $> 1050^\circ\text{C}$ ) and for a short time (1-6h) results in excellent LTHC resistance.

### 7.3 Hot Corrosion Evaluation of Developmental $\gamma'+\gamma$ Coating and Commercially Available Coatings

- The Pt+Hf-modified  $\gamma'+\gamma$  coating exhibited excellent resistance to both types of hot corrosion when given an optimum pre-oxidation treatment (*i.e.* 6 h in air at  $1080^\circ\text{C}$ ); while, the Pt-modified  $\beta$  coating exhibited best LTHC resistance when no pre-oxidation treatment was given.
- The LTHC attack in Ni-based aluminide coatings and alloys is believed to be due to the formation of eutectic  $\text{Na}_2\text{SO}_4\text{-NiSO}_4$  ( $T_{\text{melt}} = 671^\circ\text{C}$ ) liquid. The presence of Co and other

refractory elements may have further exacerbated the performance of coatings by promoting liquid-salt formation.

- The improved performance under HTHC and LTHC conditions of Pt+Hf-modified  $\gamma'+\gamma$  coating and  $\gamma'+\gamma$  alloy (w/ pre-oxidation) is believed to be attributable to the presence of a protective  $\alpha$ - $\text{Al}_2\text{O}_3$  scale which was pre-formed at 1080°C. The low temperatures of the LTHC and HTHC testing – LTHC in particular – are apparently insufficient for the  $\gamma'+\gamma$  coatings to kinetically establish a protective and continuous  $\text{Al}_2\text{O}_3$  scale, which is necessary for prolonged HC resistance.
- Addition of Pt is beneficial in improving hot corrosion resistance of  $\beta$  coatings. A pre-oxidation of Pt-modified  $\beta$  coating was not beneficial in improving LTHC hot corrosion resistance, it is believed due to Al depletion in the coating during the pre-oxidation treatment.
- A Pt+Hf modified  $\gamma'+\gamma$  coating outperformed commercially used  $\gamma+\beta$ -CoCrAlY coating from the standpoint of combined resistance to both types of hot corrosion.

**References**

1. F.S. Pettit and G.H. Meier, *Superalloys 1984*, Metallurgical Society of AIME, Warrendale, PA, 651-87, (1984).
2. F.S. Pettit and G.W. Goward, *Applied Science Publishers*, (1983).
3. N. Eliaz, G. Shemesh, R.M. Latanision, *Engineering Failure Analysis*, 9, (2002), 31-43.
4. G.W. Goward, 30<sup>th</sup> International Gas Turbine Conference and Exhibit, Paper No. 85-GT-60, ASME, (1985).
5. Y. Tamarin, "Protective Coatings for Turbine Blades," ASM International, (2002).
6. N.P. Padture, M Gell, and E.H. Jordan, *Science*, Vol. 296, (2002), 280.
7. U. Schulz, C. Leyens, K. Fritscher, M. Peters, B. Saruhan-Brings, O. Lavigne, Jean-Marc Dorvaux, M. Poulain, R. Mevrel, *Aerospace Science and Technology* 7, (2003), 73-80.
8. B. Gleeson, W. Wang, S. Hayashi, and D. Sordelet, *Materials Science Forum*, 461-464, (2004), 213.
9. A.S. Radcliff, *Mater. Sci. Technol.*, Vol. 3, (1987), 554.
10. J.R. Strife and J.E. Sheehan, *Ceramic Bulletin*, 67, (1988), 369-374.
11. J.H. Wood and E.H. Goldman, "Protective Coatings," in *Superalloys II*, C.T. Simms, N.S. Stoloff and W.C. Hagel (eds.), Chapter 13, (1987), 359-384.
12. R. Marvel, *Materials Science and Engineering*, A 120 (1989), 13-24.
13. R. Sivakumar and B.L. Mordike, *Surface and Coatings Technology*, 37, (1989), 139-160.
14. J.R. Nicholls, *MRS Bulletin*, (September 2003), 659-670.
15. G.W. Goward, *Surface and Coatings Technology*, 108-109, (1998), 73-79.
16. S.J. Grisaffe, "The Superalloys," C.T. Simms and W.Hagel (eds.), Wiley, NY, 1972.
17. M.P Brady, B. Gleeson, and I.G. Wright, *Journal of Metals*, (January 2000), 16-21.
18. J.A. Haynes, B.A. Pint, W.D. Porter, I.G. Wright, *Materials at High Temperature*, 21, (2004), 87-94.
19. B.A. Pint, I.G. Wright, W.Y. Lee, Y. Zhang, K. Prubner, and K.P. Alexander, *Materials Science and Engineering*, A245, (1998), 201-211.
20. B.A. Pint, *Oxidation of Metals*, 49 (5-6), (1998), 531-560.

21. S. Alperine, P. Steinmetz, A.F. Constantini, P. Josso, *Surface and Coatings Technology*, 43/44, (1990), 347.
22. P. Kuppusami and H. Murakami, *Surface and Coatings Technology*, 186, (2004), 377-388.
23. P.C. Patnaik, R. Thamburaj, and T.S. Sudarshan, *Surface Modification Technologies III*, T.S. Sundarshan, D.G. Bhat, eds, TMS, Warrendale, (1990), 759.
24. Y. Zhang, W.Y. Lee, J.A. Haynes, I.G. Wright, B.A. Pint, K.M. Cooley, P.K. Liaw, *Metallurgical and Materials Transaction*, 30A, (1999), 2679.
25. M.C. Meelu, B.G. McMordie, M.H. Loretto, and A. Jones, *Processing and Properties of Materials*, (1992), 1250.
26. B. Gleeson, B. Li, D. Sordelet, W.J. Bridley U.S. 2006127695, (2006).
27. D.H. Boone and J.W. Fairbanks, *Specialized Cleaning, Finishing and Coating Processes*, Conference Proceedings, CA, ASM, Metals Park, Ohio, (1980), 357.
28. W.F. Schilling, NATO Advanced Workshop, *Coatings for Heat Engines*, Italy, April 1984.
29. G.E. Creech., S.K. Naik, P.S. Korinko, U.S. Patent No. 6406561, (2002).
30. B. Gleeson, *Journal of Propulsion and Power*, 22(2), (2006), 375-383.
31. H.C. Scott, *Journal of Materials Science*, Vol. 10, (1975), 1527-1535.
32. B.J. Zimmerman, "Rumpling Phenomenon in Platinum-Modified Ni-Al Alloys," MS Thesis, Iowa State University, (2005).
33. D.S. Rickerby, S.R. Bell and R.G. Wing, U.S. patent No. 5,981,091
34. M.A. DeCrescente and N.S. Bornstein, *Corrosion-NACE*, 24 (5), (1968), 127-133.
35. N.S. Bornstein, *JOM* 48, (November 1996), 37-39.
36. P. Hancock, *Materials Science and Technology*, 3 (7), (1987), 536-544.
37. "Phase Diagrams for Ceramists", vol. II (Westerville, OH: American Ceramic Society, (1969), fig. 2923.
38. J. Stringer, *Materials Science and Technology*, 3(7), (1987), 482-493.
39. P. Kofstad, "High Temperature Corrosion" Elsevier Applied Science, (1988), 468.
40. D.K. Gupta and R.A. Rapp, *Journal of Electrochemical Society*, 127, (1980), 2194.

41. N.S. Bornstein and M.A. DeCrescente, Transactions of Metallurgical Society, AIME, 245, (1969), 1947.
42. N.S. Bornstein and M.A. DeCrescente, Corrosion, 26, (1970), 209.
43. N.S. Bornstein and M.A. DeCrescente, Metallurgical Transactions, 2, (1971), 2875.
44. J.A. Goebel and F.S. Pettit, Metallurgical Transactions, 1, (1970), 1943.
45. J.A. Goebel and F.S. Pettit and G.W. Goward, Metallurgical Transactions, 4 (1973), 261.
46. R.A. Rapp and K.S. Goto, Proc. 2<sup>nd</sup> Int. Symp. On Molten Salts, J. Braunstein and J.R. Selman, (eds.), Electrochemical Society, Pennington, NJ, (1981), 81.
47. D.A. Shores, NACE-6, R.A. Rapp (ed.), Houston, TX, (1983), 493.
48. R.A. Rapp, Corrosion Science 44, (2002), 209-221.
49. K.L. Luthra and D.A. Shores, Journal of Electrochemical Society, 127 (1980), 2202-2210.
50. K.L. Luthra, Metallurgical Transactions, 13A, 1647, (1982), 1843.
51. K.L. Luthra, Journal Electrochemical Society, 132, (1985), 1293.
52. K.L. Luthra and J.H. Wood, Thin Solid Films, 119, (1984), 271.
53. N. Otsuka and R.A. Rapp, Journal of Electrochemical Society, (1990), 46.
54. K.P. Lillerud and P. Kofstad, Oxidation of Metals, Vol. 21, Nos. 5/6, (1984), 233-270.
55. K. Holthe and P. Kofstad, Corrosion Science, 20, (1980), 919.
56. B. Sand and P. Kofstad, MS Thesis by B. Sand, University of Oslo, 1980.
57. K.L. Luthra and D.A. Shores, Journal of Electrochemical Society, 127, (1980), 2202-2210.
58. R.H. Barkalow and F.S. Pettit, Proceedings of the 14<sup>th</sup> conference on gas turbine materials in a marine environment, Annapolis, MD, 1979, 493.
59. A.K. Misra, Journal of Electrochemical Society, 133, (1986), 1038.
60. F.S. Pettit and C.S. Giggins, " Hot Corrosion" in Superalloys II, C.T. Simms, N.S. Stoloff and W.C. Hagel (eds.), Chapter 12, (1987), 327-358.
61. P. Singh and N. Birks, Werkstoff Und Korrosion, 32(1980), 682.

62. G.M. Kim and G.H. Meier, in Z.A. Munir, D. Cubicciotti and H. Tagawa (eds.), "High Temperature Materials Chemistry IV", The Electrochemical Society, Pennington, NJ, (1988), 79.
63. Y.K. Kim, K. Przybylski and G.J. Yurek, in D.A. Shores and G.H. Yurek (eds.), "Fundamental Aspects of High Temperature Corrosion II" The Electrochemical Society, Pennington, NJ, (1986), 259.
64. F.H. Stott and M.F. Chong, in D.B. Meadowcroft and M.I. Manning (eds.), "Corrosion Resistant Materials for Coal Conversion Systems", Elsevier, Amsterdam, (1983), 491.
65. F.H. Stott, F.M. Chiang and C.A. Stirling, in M.F. Rothman (eds.) "High Temperature Corrosion in Energy Systems" AIME, Warrendale, PA, (1985), 253.
66. P. Deb, D.H. Boone and R. Streiff, *Journal of Vacuum Science and Technology*, A 3 (6), (1985), 2578-2581.
67. R. Streiff and O. Cerclier, *Surface and Coatings Technology*, 32, (1987), 111-126.
68. H. L. Du, J. Kipkemoi, D.N. Tsipas and P.K. Datta, *Surface Coatings and Technology*, 86/87, (1996), 1-8.
69. K. Godlewski and E. Godlewska, *Materials Science and Engineering*, 88, (1987), 103-109.
70. K. Shirvani, M. Saremi, A. Nishikata, and T. Tsuru, *Materials Science Forum*, 461-464, (2004), 335-342.
71. G. R. Krishna, D.K. Das, V. Singh and S.V. Joshi, *Materials Science and Engineering*, A 251, 1-2, (1998), 40-47.
72. D. K. Das, V. Singh and S.V. Joshi, *JOM*, 52/1, (2000), 41-48.
73. J.A. Haynes, Y. Zhang, W.Y. Lee, B.A. Pint, I.G. Wright, K. M. Cooley, "Elevated Temperature Coatings: Science and Technology III", N. B. Dahotre, J.M. Hampikian (eds.), Warrendale, PA: TMS, (1999), 185.
74. R.E. Malush, P. Deb and D. H. Boone, *Surface Coatings and Technology*, 36, (1988), 13-26.
75. M. Dust, P. Deb D.H. Boone and S. Shankar, *Journal of Vacuum Science and Technology*, A, 4 (1986), 2571.

76. K. L. Luthra and O. H. LeBlanc, Jr., *Materials Science and Engineering*, 87 (1987), 329-335.
77. H. Singh, D. Puri, S. Prakash, *Metallurgical and Materials Transactions A*, (2005), 36A(4), 1007.
78. E. Rocca, L. Aranda, M. Vilasi, P. Steinmetz, *Materials Science Forum* (2004), 461-464 (Pt. 2, High Temperature Corrosion and Protection of Materials 6, Part 2), 917-925.
79. M.R. Jackson, J.R. Rairden, *Metallurgical Transactions, A* 8, (1977), 1697.
80. J. Schaeffer, G.M. Kim, G.H. Meier, F.S. Pettit, E. Lang (ed.), Elsevier, Amsterdam, 231-267, (1989).
81. Y. Cadoret, M.-P. Bacos, P. Josso, V. Maurice, P. Marcus, S. Zanna, *Materials Science Forum*, 247, (2004), 461-464.
82. Y. Cadoret, D. Monceau, M.-P. Bacos, P. Josso, V. Maurice, P. Marcus, *Oxidation of Metals*, 64 (314), (2005), 185-205.
83. S. Hayashi, T. Narita, B. Gleeson, "Early-Stage Oxidation Behavior of  $\gamma'$ -Ni<sub>3</sub>Al-based alloys with and without Pt addition," *Materials Science Forum*, 522-523, (2006), 229.
84. D. Clemens, W.J. Quadackers, L. Singheiser, *High Temperature Corrosion and Materials Chemistry*, ed. P.Y. Hou *et al.* (Electrochemical Society, 1998), 134.
85. S.G. Young and D.L. Deadmore, *Thin Solid Films*, 73 (1980), 373-378.
86. M.W. Brumm and H.J. Grabke, *Corrosion Science*, 33(11), (1992), 1677-1690.
87. B.A. Pint, K.L. More, and I.G. Wright, *Oxidation of Metals*, 59(3/4), (2003).
88. M.A. Phillips and B. Gleeson, *Oxidation of Metals*, 50, (1998), 399-429.
89. C. Leyens, B.A. Pint, I.G. Wright, *Surface and Coatings Technology*, 133-134, (2000), 15-22.
90. G.J. Smeggil, A.W. Funkenbush, and N.S. Bornstein, *Metallurgical Transactions, A* 17, 923, (1986).
91. J.L. Smialek, *The minerals* (Metals & Materials Society, 1989), 425.
92. B.A. Pint, *Surface and Coatings Technology*, 188-189, (2004), 71-78.
93. D.R. Coupland, C.W. Hall, I.R. McGill, *Platinum Metal Review*, 26, (1982), 186.
94. D.R. Coupland, I.R. McGill, C.W. Corti, and G.L. Selman, *Environmental Degradation of High Temperature Materials*, 2 (1980), 26-29.

95. G.J. Tatlock and T.J. Hurd, *Oxidation of Metals*, 22, 5/6, (1984), 201-226.
96. G.J. Tatlock and T.J. Hurd, *Werkstoffe und Korrosion*, 41(12), (1990), 710-715.
97. G.J. Tatlock and T.J. Hurd, *Platinum Metals Review*, 31(1), (1987), 26-31.
98. E.J. Felten, *Oxidation of Metals*, Vol.10, No. I, (1976).
99. B.A. Pint, J.A. Haynes, K.L. More, I.G. Wright and C. Leyens, in T.M. Pollock, R.D. Kissinger, R.R. Bowman, K.A. Green, M. McLean, S. Olson and J.J. Shirra eds., *Superalloys 2000*, TMS, Warrendale, PA, p.629-38.
100. Y. Zhang, B.A. Pint, J.A. Haynes, I.G. Wright, *Surface and Coatings Technology*, 200 (5/6), (2005), 1259-1263.
101. A. V. Dean "Investigation into the resistance of various nickel and cobalt base alloys to sea salt corrosion at elevated temperatures" NGTE report, January 1964.
102. E.W. Ross, *Journal of Metals*, 12, (December 1967).
103. D. Shifler, Office of Naval Research, Personal communication, 2006.
104. K.T. Chiang, F.S. Pettit, and G.H. Meier, in R.A. Rapp (ed.), *High Temperature Corrosion Engineers*, NACE-6, Houston, TX, (1983), 519-30.
105. Zhu Rizhang and Zheng Xiaoguang, *Journal of Chinese Society of Corrosion Protection*, 7, (1987), 207.
106. L.P. Kostin, L. L. Pluzhnikov, A. N. Ketov; Perm. Farm. Inst., USSR. *Zhurnal Fizicheskoi Khimii*, 49(9), (1975), 2235-7.
107. T.R. Ingraham, M.C.B. Hotz; *Can. Metall. quarterly*; Vol. 7 (3), (1968), 139-146.
108. J.J. Grisik, R. G. Miner and D. J. Wortman, *Thin Solid Films*, 73 (1980), 397-406.
109. T. Izumi and B. Gleeson, *Materials Science Forum*, 522-523, (2006), 221.
110. I. Barin, Weinheim; New York: VCH, V1-2, 3<sup>rd</sup> edition, 1995.
111. E. Copland, "Partial Thermodynamic Properties of  $\gamma'$ -(Ni,Pt)<sub>3</sub>Al in the Ni-Al-Pt System", *Journal of Phase Equilibria and Diffusion*, (2007) in press.
112. Z. F. Gulvanitskaya, N. M. Pavlyuchenko, L. I. Blokhina, and G. N. Zviadadze, *Izvestiya Akademii Nauk SSSR, Neorganicheskie Materialy*, Vol.15-11, (1979).
113. S. Hayashi, S.I. Ford, D.J. Sordelet, M.F. Besser, B. Gleeson, *Acta Materialia*, 53, (2005), 3319.
114. C. Jiang, D.J. Sordelet, B.Gleeson, *Acta Materialia*, 54, (2006), 1147.

115. T. Izumi and B. Gleeson, Unpublished results, Iowa State University.
116. C. Barrett, "A Statistical Analysis of Elevated Temperature Gravimetric Cyclic Oxidation Data of 36 Ni- and Co-Base Superalloys Based on an Oxidation Attack parameter", NASA Technical memorandum, 105934, (1992).
117. D. Monceau, F. Crabos , A. Malié, B. Pieraggi, Materials Science Forum, 369-372, (2001), 607-614.
118. I. Spitsberg and K. More, Materials Science and Engineering A, 417, (2006), 322-333.
119. T.J. Nijdam and W.G. Sloof, Surface and Coatings Technology, 201(7), (2006), 3894-3900.
120. V. Deodeshmukh, N. Mu, B. Li, B. Gleeson, Surface and Coatings and Technology, 201(7), (2006), 3836-3840.
121. G.C. Rybicki and J.L. Smialek, Oxidation of Metals, 31(3-4), (1989), 275-304.
122. M.W. Brumm and H.J. Grabke, Corrosion Science, 33(11), (1992), 1677-1690.
123. H.J. Grabke, Intermetallics, 7, (1998), 1153-1158.
124. H.J. Grabke, M.W. Brumm, B. Wagemann, Materials and Corrosion, 47(12), (1996), 675-677.